Development of copolymer based nanocarriers for imaging and therapy

Alexandra Arranja

UNIVERSITÉ DE STRASBOURG

ECOLE DOCTORALE pcp

ÉCOLE DOCTORALE DE PHYSIQUE ET CHIMIE-PHYSIQUE

Institut Charles Sadron

THÈSE

présentée par:

Alexandra ARRANJA

soutenue le: **20 Novembre 2015**

pour obtenir le grade de: **Docteur de l'université de Strasbourg**

Discipline/ Spécialité: Physique et Chimie-Physique

Développement de nanovéhicules à base de copolymères pour l'imagerie et la thérapie

THÈSE dirigée par :

M. SCHOSSELER François	Directeur de thèse, Université de Strasbourg
M. MENDES Eduardo	Codirecteur de thèse, TUDelft

RAPPORTEURS :

M. TILLEMENT Olivier	Rapporteur externe, Université Claude Bernard
M. CHASSENIEUX Christophe	Rapporteur externe, Université du Maine

---

AUTRES MEMBRES DU JURY :

M. SCHAAF Pierre	Examinateur interne, Université de Strasbourg
M. LAMMERS Twan	Examinateur, RWTH Aachen University Clinic

Alexandra ARRANJA

Développement de nanovéhicules à base de copolymères pour l'imagerie et la thérapie

Résumé

Le développement de nanomédicaments pour l'imagerie et le traitement du cancer a suscité un intérêt croissant à cause de leur grand potentiel. En particulier les vecteurs à base de polymères et de micelles polymères sont très intéressants, car ils peuvent être conçus avec des fonctionnalités adaptées aux besoins.
Nous avons utilisé des copolymères amphiphiles triséquencés pour développer de nouveaux nanovecteurs moléculaires (unimères) et supramoléculaires (micelles stabilisées par photo-réticulation). Nous les avons fonctionnalisés avec un marqueur fluorescent ou radioactif pour permettre leur imagerie in vitro et in vivo. Les interactions in vitro et in vivo ont été étudiées pour comprendre l'influence des propriétés des copolymères sur les interactions biologiques.
Cette thèse présente le développement complet de nanovecteurs depuis les premières étapes de la caractérisation physico-chimique fondamentale jusqu'à l'évaluation de leur intérêt pour différentes applications cliniques.

Nanovéhicules; Pluronic; Unimères; Micelles stabilisées; Radiomarquage; Marquage fluorescent; In vitro; In vivo.

Résumé en anglais

The interest in developing new nanocarriers for imaging and therapy of cancer has been growing due to their high potential. Particularly nanocarriers based on polymers and polymeric micelles are very interesting because they can be tailor-made with certain functionalities to meet our needs.
We have used amphiphilic triblock copolymers to develop new molecular (unimers) and supramolecular (micelles stabilized by photo cross-linking) nanocarriers. The carriers were then functionalized with fluorescent or radioactive markers to enable their in vitro and in vivo imaging. The in vitro and in vivo interactions were then studied to understand the influence of the copolymers properties on the biological interactions.
This thesis presents the complete development of the nanocarriers from the early stages of fundamental physicochemical characterization up to the evaluation of their interest for different clinical applications.

Nanocarriers; Pluronic; Unimers; Stabilized micelles; Radiolabeling; Fluorescent labeling; In vitro; In vivo.

Development of copolymer-based nanocarriers for imaging and therapy

Alexandra ARRANJA

Master of Science in Pharmaceutical Sciences,
Faculty of Pharmacy, University of Lisbon, Portugal

This research has been funded by the People Programme (Marie Curie Actions) of the European Union's Seventh Framework Programme (FP7/2007-2013) under the REA grant agreement no. PITN-GA-2012-317019 "TRACE'nTREAT".

The research leading to these results has been carried out in the following institutions:

Table of Contents

Acknowledgments

It is a pleasure to thank to the many people who made this thesis possible.

I have been indebted in the development and preparation of this thesis to my supervisor, Dr. François Schosseler, who made me feel always welcome, and whose experience, wise words and availability enabled a critical and positive discussion of the work. My supervisor gave me the support and encouragement to overcome the main challenges and difficulties, which was definitely preponderate for my career progression and life experience.

I would like to gratefully acknowledge the co-supervision of Prof. Dr. Eduardo Mendes. His vast academic experience and creative ideas were essential to ensure the success of this work.

I would also like to acknowledge the contribution of the many collaborators at the Institut Charles Sadron, the Reactor Institut Delft and the ChemE/TUDelft, whose help in the laboratory work and scientific discussions were important for the progress of this thesis. A special thanks to Gilles Waton, Adrie Laan, Astrid van der Meer, Marcel Bus, André Schroder, Mark Schmutz, Philippe Mesini, Yves Guilbert, Catherine Foussat, Mélanie Legros and Jean-philippe Lamps.

The "TRACE'nTREAT" consortium was a fundamental collaboration group that greatly motivated the success of this thesis. I would like to particularly acknowledge Dr. Antonia Denkova for her patient, supervision during my secondment in Delft, and fruitful scientific discussions.

The colleagues and ultimately friends that I have made during these 3 years in France and in The Netherlands were a crucial part for the development of this thesis and myself. A special thanks to Laurence Jennings, Frank Paulus, Paul Rouster, Maria Alice Witt, Yasmine Micheletto, Alliny Naves, Heveline Follmann, Christiane Davi, Pierre Ayoub, Vallín Cruz, Robin De Kruyff and Laura Bogers.

I also want to thank the informal support of my friends from Portugal which has been invaluable to me.

Lastly, and most importantly, I wish to thank my family. They have been a constant source of support (emotional and moral) and encouragement to achieve my goals. To them I dedicate this thesis.

General overview of the thesis and outline

This thesis project was funded by the People Programme (Marie Curie Actions) of the European Union's Seventh Framework Programme (FP7/2007-2013) under the framework of the "TRACE'nTREAT" project. This Initial Training Network combines academic and industrial partners from different countries with a great variety of complementary expertise.

The work reported in this thesis is a result of 3 years research mainly performed in Strasbourg (Institute Charles Sadron, University of Strasbourg), including 6 months abroad in Delft (Reactor Institute Delft, Technical University of Delft) and in Utrecht (MILabs). The fruitful discussions from the collaboration between the different partners, the research periods abroad, and the intense multi-disciplinary training were crucial for the completion of this thesis.

The mains objectives of the "TRACE'nTREAT" project are to produce radionuclides for nuclear imaging and/or radionuclide therapy, their incorporation in newly designed polymeric molecular and supramolecular carriers, and their preclinical evaluation.

In the context of this project, the main goal of this thesis is the development, characterization and preclinical evaluation of molecular and supramolecular polymeric nanocarriers with different physicochemical properties.

The specific goals are:

(i) Achieve a deeper understanding on the fundamental growth and decay dynamics of Pluronic micelles, when they evolve from single unimers to complex structured morphologies.
(ii) Develop nanocarriers based on Pluronic copolymers that can be used to study the effects of PEO block length and aggregation state, from molecular to supramolecular arrangements.
(iii) Understand the roles of these physicochemical parameters on the interactions with 2D/3D *in vitro* models, and on the *in vivo* biodistribution.

The thesis outline is as follows:

Chapter 1 introduces general concepts required for a better understanding of the different aspects explored in this thesis. We introduce the importance of nanomedicine and imaging technologies, the properties of Pluronic block copolymers, and we finalize with the main concepts of dynamic light scattering.

Chapter 2 explores the sphere-to-rod transition kinetics of Pluronic copolymers with increasing molecular weight and constant hydrophobic/hydrophilic ratio.

Chapter 3 describes the development of molecular (unimers) and supramolecular (stabilized micelles) Pluronic nanocarriers with different PEO block length. We also describe the functionalization of the nanocarriers with appropriate moieties for fluorescence and radioactive imaging.

Chapter 4 analyses the *in vitro* interactions of the different nanocarriers using 2D and 3D cell culture. We specifically study the cytotoxicity, internalization kinetics and retention in 2D cell culture, while 3D tumor spheroids are used to evaluate the penetration and toxicity potential of the carriers.

Chapter 5 focuses on the *in vivo* biodistribution evaluation of the radiolabeled nanocarriers in healthy mice, and the influence of the different physicochemical aspects (PEO block length and aggregation state).

Outline scheme

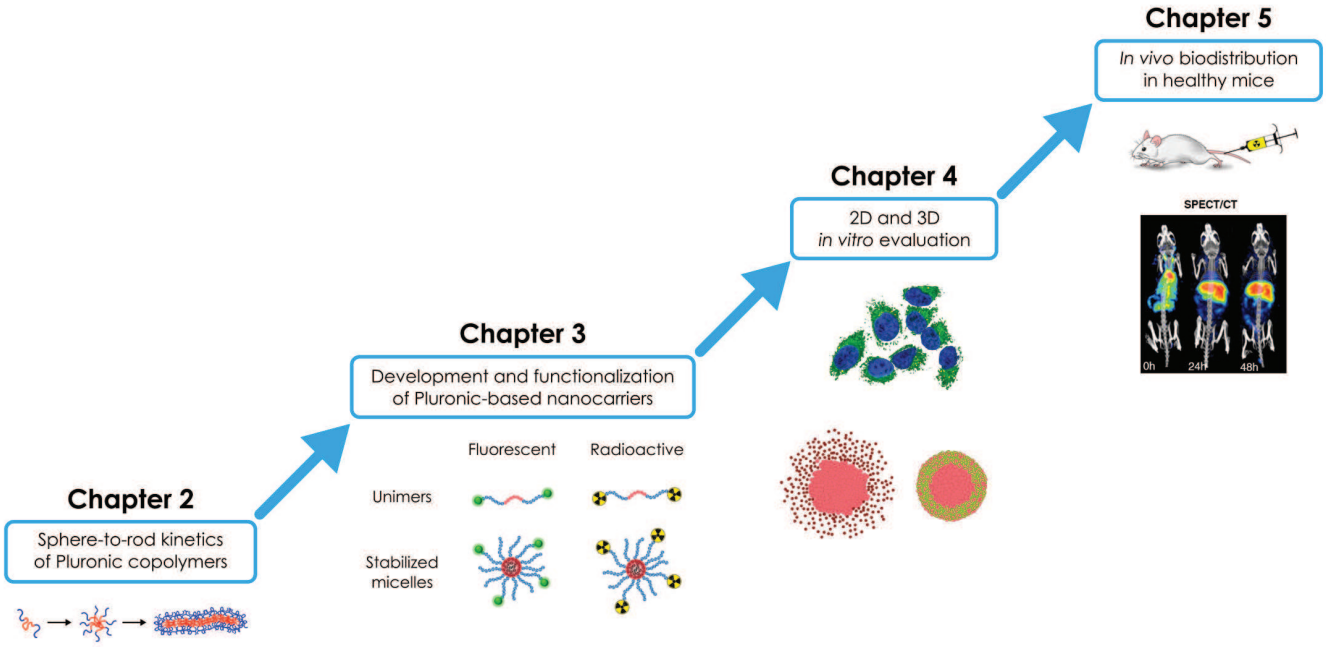

CHAPTER 1

Background and Introduction

1.1 Nanocarriers for biomedical applications

There is a continuing interest in the use of nanocarriers for diagnostics and therapy of diseases, particularly in the field of oncology.

The conventional chemotherapeutic drugs present several disadvantages due to their low molecular weight and general high hydrophobicity. First, they display a fast clearance from the body and suffer enzymatic degradation after intravenous (i.v.) administration. Second, they have a high volume of distribution which leads to high accumulation and toxicity in healthy tissues, and low accumulation in the target sites.[1] In Figure 1 (left) this effect can be visualized through the distribution of the chemotherapeutic drugs within the whole body with low specificity for the tumor site. Moreover, the clearance of the drugs from the body occurs very fast (Table 1) which reduces the efficiency of the treatment, while still presenting serious side effects.

To overcome these major drawbacks, a great variety of higher molecular weight carriers including polymers, micelles, liposomes and metallic nanoparticles have been proposed and are currently being investigated.[2]

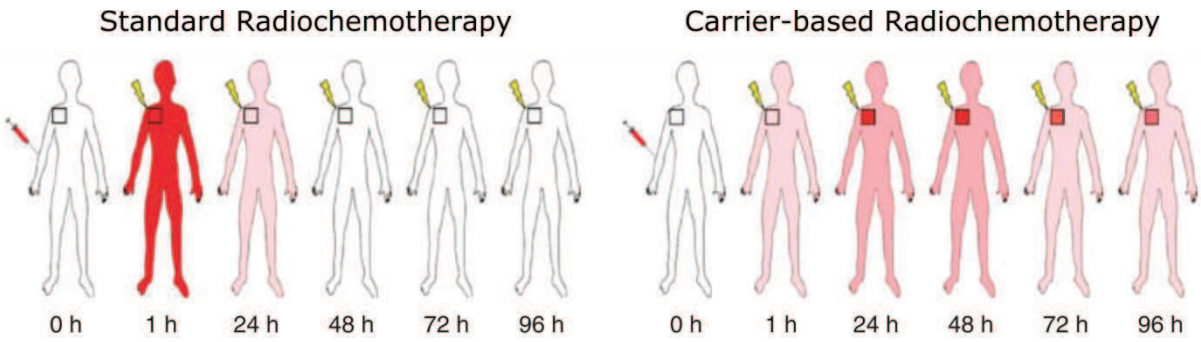

Figure 1. Schematic representation of the *in vivo* interaction between radiochemotherapy using standard (conventional) and carrier-based medicines. The carrier-based nanomedicines improve the temporal and spatial interaction of radiochemotherapy with the patient compared to the standard treatment. Image adapted from Ref.[3].

Higher molecular weight agents, with a size larger than the intact endothelial fenestrations, will distribute in the blood circulation and only reach the tissues when the endothelium is defective. Moreover, if their size is larger than the renal cut-off (> 5.5 nm)[4], clearance by renal filtration will also be avoided. This results in higher blood concentration and longer retention for these carriers (Figure 1 right). The reduced volume of distribution leads to lower accumulation in healthy tissues and therefore less toxicity and side effects[5] (Table 1). Moreover, they accumulate preferentially in targeted areas such as solid tumors by passive diffusion[1, 5, 6] (for details on this effect see section 1.2.2.2 of this Chapter).

The general aim of modern nanomedicine is to develop nanocarriers that can selectively target diseased sites by active or passive mechanisms in order to reduce side effects and improve treatment efficacy. Particularly well-known examples of this success[1, 7] are the formulations Doxil®[8] and Abraxane®,[9] which are able to improve the pharmacokinetics of doxorubicin and paclitaxel respectively.

Table 1. Pharmacokinetics of low and high molecular weight (M_w) agents.

Low M_w drugs	**High M_w carriers**
Rapid elimination: ↗ Clearence	Slow elimination: ↘ Clearence
Short circulation: ↘ $t_{1/2}$	Long circulation: ↗ $t_{1/2}$
Wide distribution : ↗ V_d	Limited distribution : ↘ V_d
Poor accumulation: ↘ C_{max}	Good accumulation: ↗ C_{max}
Poor retention : ↘ AUC	Good retention: ↗ AUC

$t_{1/2}$: blood circulation half-life; V_d: volume of distribution; C_{max}: maximum blood concentration; AUC: Area Under the Curve (concentration×time).

1.1.1 Nanocarriers for imaging and therapy

Although the most common use of nanocarriers is to improve the pharmacokinetics and delivery of drugs to tumor site, they have also been used for other therapeutic approaches and disease imaging. Other applications include tissue engineering, gene delivery and radiotherapy. The ideal multifunctional nanocarriers should allow detection of the diseased sites, while improving drug or radionuclide delivery to cellular and sub-cellular targets. Ultimately, an overall improvement of the treatment efficacy and monitoring of treatment progression is expected.

In the context of this thesis, the use of radionuclides is very interesting because they can enable combination of therapy[10] (via Auger electrons or alpha particles) and imaging[11] (through photon detection).

1.1.2 Strategies exploited by nanocarriers for tumor targeting

Diseased cells and their microenvironment differ markedly from healthy cells in respect to their gene expression, growth rate, morphology, cell-to-cell interactions and cytoskeleton organization.[12, 13] By taking advantages of these variations, nanocarriers can selectively target defective sites by either active or passive mechanisms.

1.1.2.1 Active targeting

In active targeting, a natural or synthetic molecule is used as a ligand to target specific components expressed in diseased cells, normally surface receptors. A great number of molecules have been developed, including protein ligands, synthetic peptides, carbohydrates, antibodies, antibody fragments and aptamers,[14] and have received approval for clinical therapy.[15, 16] The use of molecules that bind surface receptors can be used to directly block surface receptors (such as Herceptin)[17] or to promote the binding and internalization of drugs or nanocarriers.[18] It has been shown that their incorporation in nanocarriers does not increase their concentration in the targeted sites,[19] but only improves the cellular internalization and retention. Therefore, the higher costs of the production of actively targeted nanocarriers will most likely not justify their implementation in the clinical practice.

1.1.2.2 Passive targeting

The most important factor for the success of the nanocarriers is based on a passive mechanism inherent to the characteristics of the tumor cells and the microenvironment. Cancer cells grow at a much faster rate than healthy cells, which requires the formation of new blood vessels (angiogenesis) to supply the demanding oxygen and nutrients. Due to the abrupt vasculature formation, the new blood vessels are immature and highly permeable with a poor line of smooth muscle and a discontinuous endothelial cell layer (Figure 2).[20] Therefore, holes in the vasculature are created which enable the passive convection of nano-sized materials with sizes below the fenestrations cut-off.[21] Moreover, due to the excessive disorganization of the cellular growth, the lymphatic drainage is also impaired which causes the retention of the nanocarriers in the tumor site. The combination of both mechanisms is known as the Enhanced Permeability and Retention (EPR) effect.[18, 20]

The reliance of the nanocarriers on this passive effect is very limiting because of the high variation of the EPR phenomenon. This heterogeneity has been observed in different tumor types, and even between patients with the same tumor. On the one hand, sarcomas,[22] glioblastomas[23] and head and neck[24] tumors have demonstrated high EPR effect with high retention of various nanocarriers in these tumors. On the other hand, due to the stromal nature of

breast tissue, breast cancer has shown low EPR effect.[24] In these cases, the use of nanocarriers to deliver drugs has only shown to be advantageous in reducing the side effects by decreasing the drug accumulation in healthy tissues, while the drug concentration in the tumor remains the same as compared to injection of the free drug. The differences in the EPR effect have been mostly related to the tumor type and the microenvironment, particularly the angiogenesis, hypervascularity, irregularity of blood flow, vascular permeability, abnormal lymphatic drainage and tissue inflammation.[24-26]

The EPR effect in animal models has also been studied by some groups.[27-30] The angiogenesis, anatomical and functional evaluation of tumor vasculature, and the size of endothelial fenestrations have been assessed with several tumor types.

1.1.3 Biophysical barriers to nanocarriers delivery

As discussed, the mechanism used to target nanocarriers to the tumor site is based on the EPR effect. However, to achieve the EPR effect, a critical requirement is a prolonged blood circulation of the nanocarriers. The circulation half-life time and tissue distribution is largely influenced by the biophysical barriers encountered, which include anatomical, physiological, chemical and clinical barriers.[31-33] The most important hurdles that nanocarriers face when injected intravenously are exemplified in Figure 2.

The primary barrier is the blood circulation where nanomaterials are exposed to the blood components (e.g. albumin) and opsonins that can bind to their surface (opsonisation). This will activate the complement system and increase their clearance mechanisms. Therefore, high accumulation of the nanocarriers in the main clearance organs (liver and spleen) is often observed. The high accumulation of nanocarriers in these organs is also related to the EPR effect inherent to these organs, since they possess endothelial holes for blood filtration and elimination of pathogens from the circulation.[6, 34]

Some of these barriers can be overcome by changing the physicochemical properties of the nanocarriers such as composition, size, surface charge and shape.[6, 35-39] For instance, one of the interests of using larger nanocarriers (like micelles and nanoparticles) is to avoid rapid kidney clearance thus achieving

higher *in vivo* circulation, and preventing the early release of incorporated hydrophobic drugs. This will increase the chances of tumor uptake[40] and, simultaneously, provide a selective accumulation of the encapsulated drugs at the tumor site.[41]

The most common strategy to avoid clearance by the immune system is to cover the nanocarriers with a layer of poly(ethylene oxide) (PEO).[6] This creates a steric barrier that prevents interaction with serum proteins resulting in less activation of the immune system. The PEO block length, density and conformation have also been shown to determine the opsonization rate.

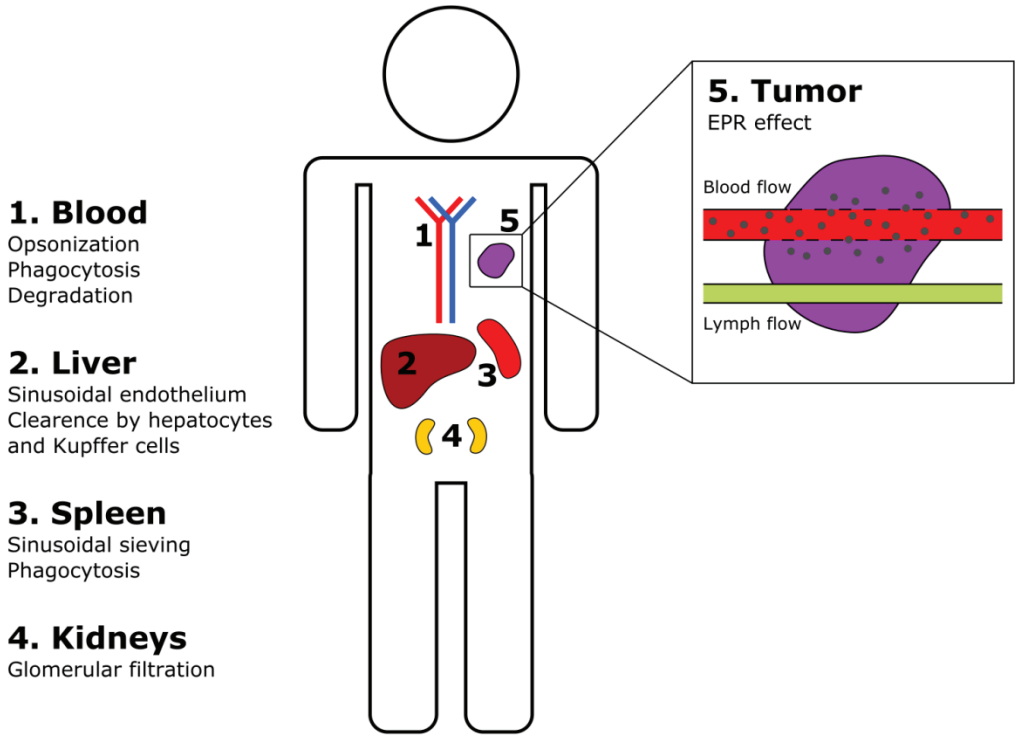

Figure 2. Biophysical barriers for intravenously administered nanomedicines (left) and the EPR effect (right).

After reaching the desired place, the nanocarriers still need to be internalized by the target cells, to accumulate in the appropriate cellular target, to have appropriate retention and ultimately they should be eliminated without causing toxicity. The interaction of the nanocarriers with the cancer cells will have a major impact on their retention at the tumor site, penetration and distribution across the tumor interstitium, and on their overall therapeutic efficacy.

This interaction occurs firstly by their attachment to the cell surface, followed by internalization through specific pathways (endocytic or non-endocytic), trafficking inside the cells, and finally their intracellular retention or exocytosis.[42-45] The cellular interaction mechanisms of the nanocarriers can also be modulated according to the intended application by varying their physicochemical properties.[46-48] For example, associating targeting moieties on the nanocarriers surface (as described in section 1.2.2.1 of this chapter) will activate specific tumor-associated cell surface receptors which will increase the internalization of the nanocarriers, their subcellular localization and ultimately their retention inside the cell. Varying other properties such as size, aggregation state,[49, 50] composition[51, 52] and cross-linking,[53, 54] also influence their uptake and intracellular trafficking, leading to distinct subcellular localizations and retention. For instance, if a nuclear localization of the nanocarriers is intended, they should be designed in order to be able to escape endosomal trapping and possess appropriate targeting peptides to be transported to the nucleus.[55]

1.1.4 Remaining challenges and limitations

Enormous progress has been made on the development of more efficient nanocarriers, and some of them appear to be very promising due to high tumor accumulation and decrease of chemotherapy side effects,[24] thus improving pharmacokinetics of conventional chemotherapeutic drugs. However, there are still several challenges that need to be addressed.

The main mechanism for their accumulation in diseased sites is based on the EPR effect, and therefore on the blood vessel density, vascular permeability and lack of lymphatic drainage. Due to the high heterogeneity of tumors, their use in several tumor types is hampered and, in some cases, solely relies on reducing the side effects of chemotherapeutic drugs. Moreover, the passive accumulation is driven by many factors associated to the nanocarriers (e.g. composition, size, shape) and the ideal parameters are still far from discovery. Although the addition of targeting moieties to the nanocarriers appears interesting, the accumulation of actively targeted nanocarriers in the tumor site still depends on their passive diffusion to those leaky sites.[19]

Another issue is the evaluation of their potential through the development of appropriate imaging modalities that should enable the visualization of their biodistribution and the eventually encapsulated drugs. Commonly, researchers analyze the biodistribution of the incorporated drugs rather than the nanocarriers themselves resulting in their inability to track the nanocarriers biodistribution and verify the *in vivo* drug release. The most efficient technique to perform this qualitative and quantitative determination is nuclear imaging.[33, 56, 57] However, exposure to radiation and instability of the metal complexation in the blood circulation are also limitations of this technique.

Finally, the biggest challenges of nanomedicines remain their interactions with the biological barriers. Overcoming or limiting these encounters before reaching the desired target place is the main goal of nanomedicine. Few strategies have been proposed to reduce these interactions. Specifically, reducing the clearance by the main organs of the immune system (liver and spleen) is still the major challenge.

1.2 Imaging modalities

The most widely used imaging technologies for disease detection are based on anatomic and functional imaging, which are most of the times nonspecific and detect the diseases at late stages. The direct detection of diseases with specific imaging probes has a great potential because they enable earlier detection and a more precise diagnostics. This will allow an efficient monitoring of the disease progression, and the controlled detection of the therapies effects.

With the progress of nanomedicines, there is an emergent need to develop new imaging technologies that can non-invasively detect and monitor the circulation and biodistribution of the nanomedicines. This will primarily assess their potential use as effective and safe nanomedicines using animal models (pre-clinical), and ultimately monitor their use in humans (clinical).

Imaging modalities include Computed Tomography (CT), Magnetic Resonance Imaging (MRI), Optical Molecular Imaging (OMI), Ultrasound (US), Positron Emission Tomography (PET) and Single Photon Emission Computed tomography (SPECT). These modalities differ in terms of spatial and temporal

resolution, sensitivity in probe detection, resolution and signal penetration depth. Each modality has its own advantages and disadvantages, and the choice of the appropriate imaging system will depend on the type of information required. For example, CT relies on the photoelectric absorption of x-rays to provide high spatial resolution. However, the x-rays absorption is very sensitive to the atomic number of the absorbing material. Therefore, this technique often requires the use of contracts agents to image the liver, vasculature, spleen, kidney, intestine and bladder, while other organs do not require (bone, lean tissue, fat and lung). Due to the low sensitivity for ligand detection of the most used imaging techniques (CT, MRI and US), they are commonly combined with nuclear imaging techniques and co-registered in multi-modal imaging.

Multi-modality imaging combines two or more modalities with images being registered in space and in time to provide anatomic, functional and molecular imaging information. The combination of OMI with MRI, and SPECT or PET with CT has represented major clinical advances in oncology, cardiology, orthopedics and metabolic diseases. In particular, pre-clinical PET/CT and SPECT/CT have been critical for the understanding of pathological processes, nanomedicines development (pharmacokinetics and pharmacodynamics) and for the assessment of treatment responses. The full exploitation of image information requires a series of complex computing tasks such as image registration, image segmentation, tracking and motion analysis, quantitative image analysis and image visualization and fusion.

1.3 Nuclear Imaging

The advantages of the non-nuclear techniques are that they are non-invasive procedures that do not require exposure to ionizing radiation, while providing high spatial resolution and anatomic information. However, they have a very low sensitivity for ligand detection. Therefore, molecular imaging technologies with high sensitivity for ligand detection have been developed and represent one of the most emerging technologies.

Positron Emission Tomography (PET) and Single Photon Emission Computed tomography (SPECT) are the most used nuclear imaging techniques. Both rely on the use of radioelements that emit radiation in specific ranges to enable

their detection. These radioelements are often conjugated to ligands (called tracers) like (deoxy)glucose, hormones, vitamins, RGD, VEGF-R, amino acids, polymers and nanoparticles, according to the desired target and application (imaging or therapy). The advantages of these techniques are the non-invasiveness, the ability to perform 3D whole-body scans and the high quantification sensitivity (pM-nM). Disadvantages are the poor spatial resolution and the poor anatomic details. A comparison of PET and SPECT properties is presented in Table 2.

Table 2. Comparison of PET and SPECT.

	PET	**SPECT**
Resolution	2 mm	< 1 mm
Sensitivity	pmol	nmol
Quantification	++	+
Tracer half-life	sec, hours	hours, days
Early kinetics (min)	+++	+
Late kinetics (hours)	+/-	++

1.3.1 Radioisotopes

Radioisotopes are elements used for nuclear imaging. Isotopes are atoms ${}^{A}_{Z}X$ with equal atomic number (Z = number of protons) but different mass number (A = number of protons + neutrons). A radioisotope is an atom with an unstable nucleus that will disintegrate/decay spontaneously by emitting radiation. The radionuclide chart (Figure 3) provides information on the available radioisotopes, their atomic and mass number, half-life time ($t_{1/2}$) and specific decay processes. This detailed information can be visualized for some elements in Figure 3 (right).

Radioactive decay can occur through different processes, the most common being β^- or β^+ decay, alpha particles emission or electron capture (EC). Other processes that usually occur in combination with the most common decay mechanisms include isomeric transition, internal conversion, spontaneous fission, and emission of gamma-rays, x-rays and Auger electrons.[58]

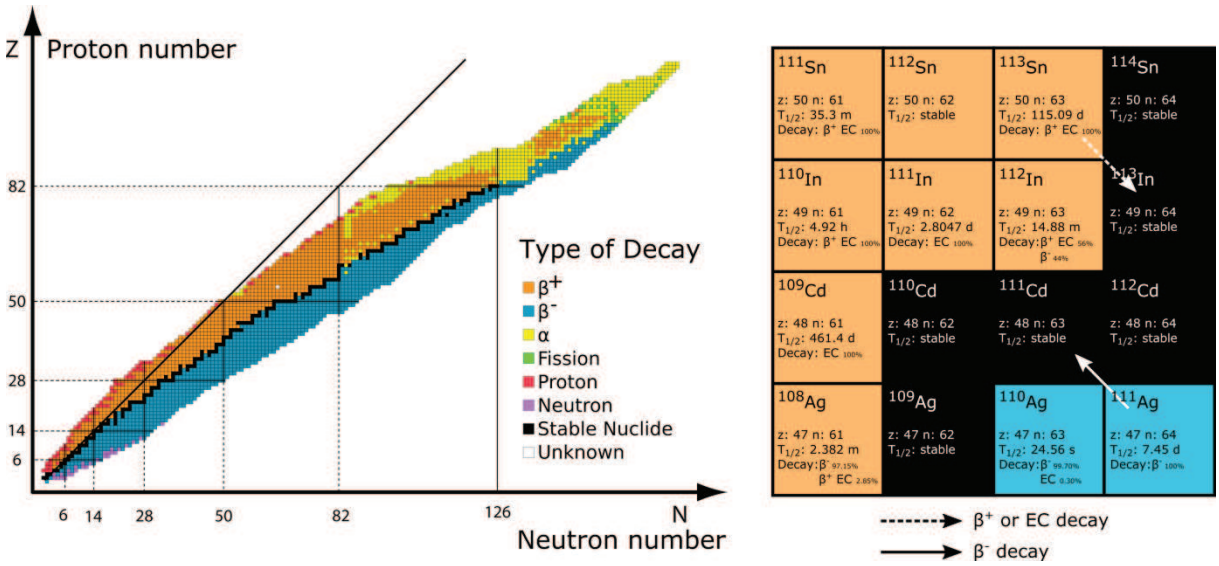

Figure 3. Typical arrangement of a radionuclide chart adapted from[59] and detailed information provided by the chart for some elements. Arrows show the decay of elements and the stable elements originated from their decay.

In the case of an excess of neutrons in the atom nucleus, the decay will progress by β^- decay, where a neutron (n) is transformed into a proton (p^+) and emits an electron (β^-) and an anti-neutrino (ν), according to the following scheme:

$$n \rightarrow p^+ + \beta^- + \nu$$

When there is a lack of neutrons in a small nucleus with at least 1022 keV, a proton is transformed into a neutron through emission of a β^+ particle (positron) and a neutrino (ν):

$$p^+ \rightarrow n + \beta^+ + \nu$$

The positron will collide with an electron and two high energetic gamma photons (2 × 511 keV) are emitted, in a process called annihilation.

If β^+ decay is not possible, an atom with lack of neutrons will decay by EC where an orbital electron (e^-) combines with a proton to form a neutron and emit a neutrino:

$$p + e^- \rightarrow n + \nu$$

Disintegration of the isotopes via β decay and EC are often accompanied by the emission of gamma radiation that can be detected for imaging purposes.

Atoms with lack of neutrons can also decay via emission of alpha particles, which are in fact helium nucleus, but this only occurs in atoms with heavy nuclei. Alpha particles have a very short path and quickly lose their energy in a short distance, which means that several MeV are deposited in a small volume of material. This results in a high damage potential particularly to the DNA strands via double-strand breaks or clustered damage.[58] Isotopes can also emit Auger electrons, which are very similar to alpha particles in terms of ability to damage DNA.[60] Although they have much lower energy (<25 keV), their path-length is much shorter and thus their linear energy transfer (LET) approaches that of alpha particles. Therefore, to be effective, the nuclides emitting Auger electrons need to be as close as possible (nm-μm) to the nuclear DNA.[61] The use of Auger electron emitters (like ^{111}Indium) has been proposed for *in situ* radiotherapy of cancer using monoclonal antibodies and peptides.[62, 63] However, delivering Auger electrons to the cancer cell nucleus remains a big challenge.[64]

The decay exponential law of radionuclides (Figure 4) is defined as follows:

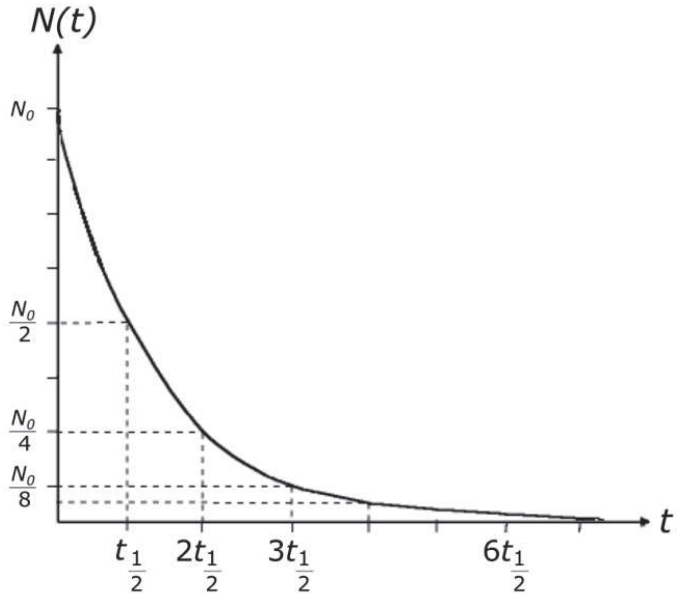

$$A(t) = -\frac{dN(t)}{dt} = \lambda \cdot N(t)$$

$$N(t) = N(o) \cdot e^{-\lambda t}$$

$$A(t) = A(o) \cdot e^{-\lambda t}$$

$$t_{\frac{1}{2}} = \frac{ln\,2}{\lambda}$$

$$A(t) = A(o) \cdot e^{-\frac{ln\,2}{t_{\frac{1}{2}}} \cdot t} = A(o) \cdot \frac{1}{2}^{\frac{t}{t_{\frac{1}{2}}}}$$

Figure 4. Exponential decay and most important equations characterizing the decay process.

where $N(t)$ is the number of unstable nuclei at a specific moment t (s), $dN(t)/dt$ corresponds to the change in the number of unstable nuclei overtime, and λ is the exponential decay constant (s^{-1}).

The activity $A(t)$ is commonly expressed in Bequerel (Bq) and corresponds to the decay rate: it is the number of atoms that disintegrate per second (dps) at a moment t. The $t_{1/2}$ is specific for each isotope and is defined as the time required for its activity to reduce to half of its initial value (Figure 4).

Radionuclides are produced in a reactor (using neutrons) or in a cyclotron (using charged particles like protons). In the cyclotron, protons are in a magnetic field and are used to `bombard´ targets like $^{18}O(p,n)^{18}F$, $^{16}O(p,\alpha)^{13}N$ or $^{69}Ga(p,2n)^{68}Ga$.

1.3.2 Positron Emission Tomography (PET)

PET is based on the detection of the two annihilation photons (2 × 511 keV) originated from the β^+ decay. These are synchronously detected as coincidence events when they strike opposing detectors simultaneously (Figure 5). A 3D distribution of the radionuclides is then generated.

Examples of PET isotopes are: ^{15}O, ^{13}N, ^{11}C and ^{18}F with 2.05 min, 9.96 min, 20.4 min and 110 min of half-life times respectively. Examples of PET tracers are: F-18-Fluorodeoxyglucose F18 (^{18}F-FDG), F-18 Fluorothymidine (FLT), F-18 Fluoromisonidazole (^{18}F-FMISO) and ^{11}C-thymidine.

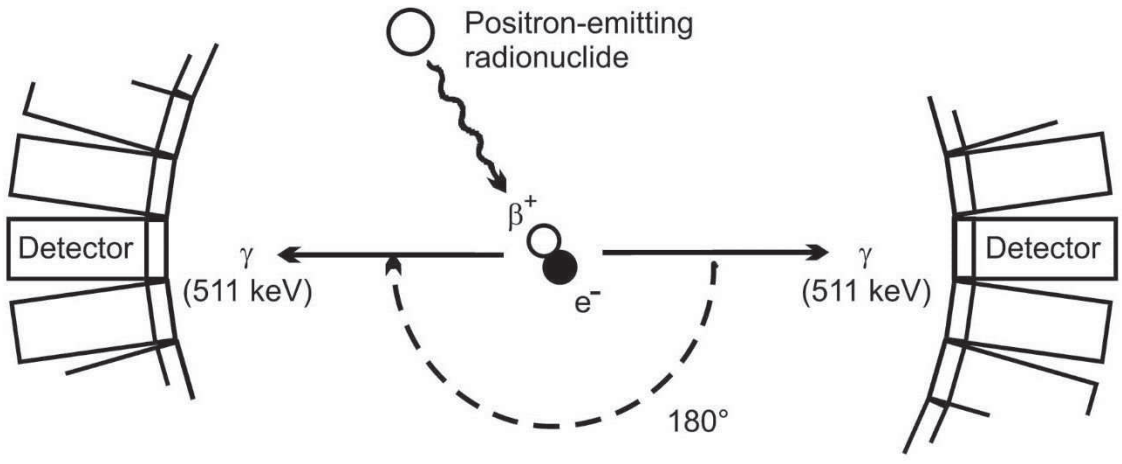

Figure 5. Positron Emission Tomography: positron emission, annihilation, and coincidence detection.[65]

1.3.3 Single Photon Emission Computed tomography (SPECT)

In the case of SPECT, the photon detection is based on the emission of single gamma-rays per radionuclide disintegration, e.g. ^{99m}Tc, ^{123}I, ^{67}Ga and ^{111}In. As opposed to PET, SPECT can be used for dual-tracer imaging by using gamma-emitters with different energies, usually within the range ~100-250keV.

Detectors with focused collimators are used and, by reconstructing cross-sections images acquired at different positions, it is possible to obtain 3D whole body images. The collimator, a slab of lead with holes (pinholes), selects the photons based on their travel direction, and a correspondence between the emission and the detection positions is established. The use of multi-pinholes increases the resolution of the detector (the smaller the pinhole the higher the resolution), but reduces sensitivity because the number of photons that reach the detector is also decreased (Figure 6).

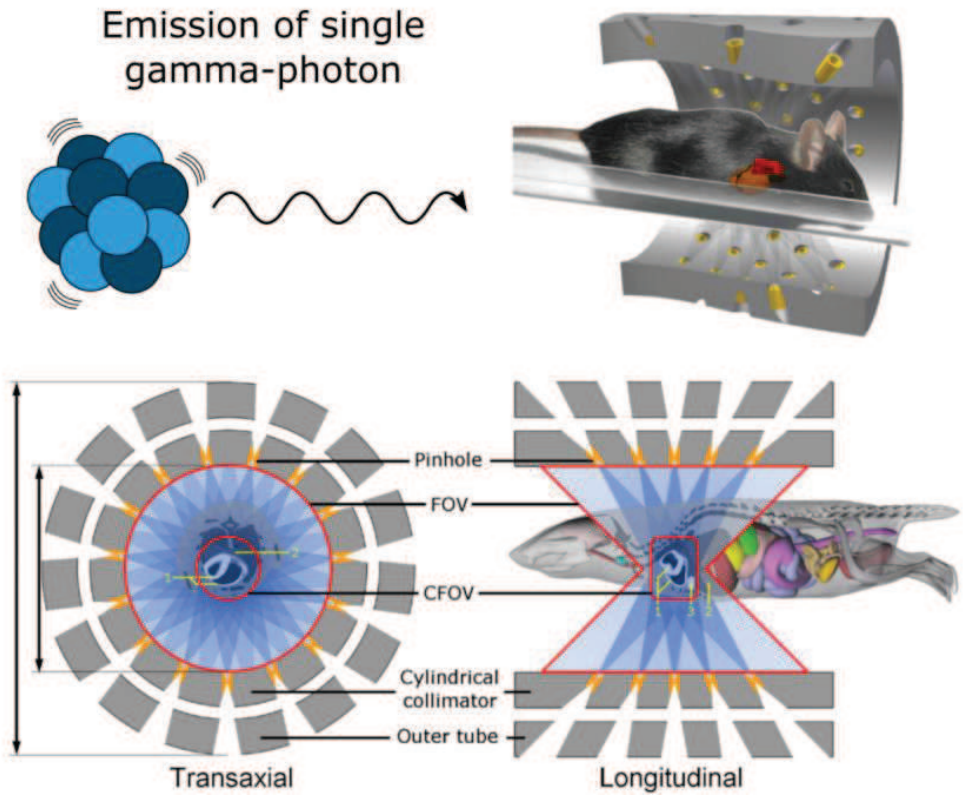

Figure 6. Schematic representation of pre-clinical SPECT. A radioisotope emitting single gamma-photons is used as a tracer (top left). The tracer is injected and the animal placed inside a mouse collimator (top right). Cross-sections of field-of-view (FOV) and central-field-of-view (CFOV) (center) are acquired. Image adapted from [66].

1.3.4 ^{111}Indium

In this work, we have selected ^{111}Indium (^{111}In) to radiolabel the developed nanocarriers due to its prolonged $t_{1/2}$ of 2.83 days (67.9 h), and the fact that it can be simultaneously used for imaging and therapy. The isotope ^{111}In is produced commercially in a cyclotron by irradiation of a natural cadmium source with energetic protons according to the following reaction: ^{112}Cd(p,2n)^{111}In.[67] After production, ^{111}In decays exclusively by electron capture (EC) into ^{111}Cd through the emission of two gamma photons of 171 and 245 keV (Figure 7-A). Overtime, the concentration and activity of ^{111}In decreases and the concentration of ^{111}Cd increases exponentially according to Figure 7-B. The emission of the two photons is perfect for SPECT imaging because of the ideal SPECT energy detection range of 100-250 keV.[68] Moreover, ^{111}In emits Auger electrons which have the potential to be used for radiotherapy (details on Auger electrons are given in section 1.3.1).

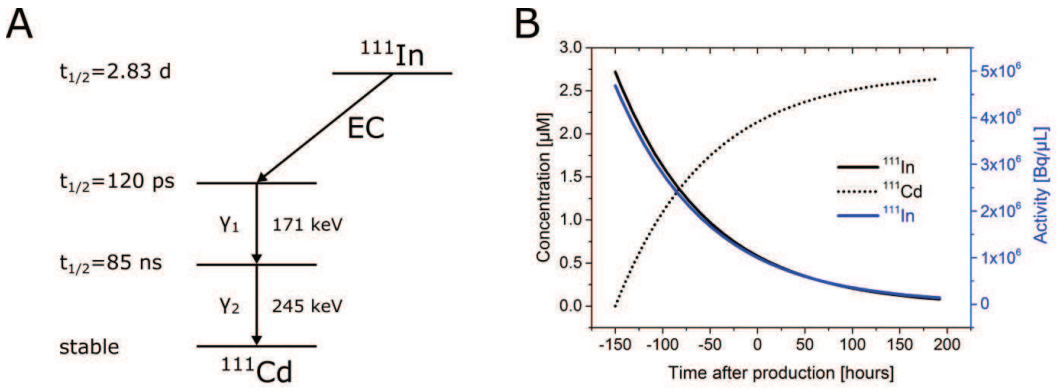

Figure 7. (A) Decay scheme of ^{111}In and (B) evolution of ^{111}In activity and concentration, and ^{111}Cd concentration after production in the cyclotron.

1.3.5 Complexation of isotopes

In order to use metallic isotopes for clinical applications, the isotopes need to be complexed to suitable chelators. Moreover, to radiolabel nanocarriers, the chelator needs to be attached to the carriers. Therefore, the selection of a chelator depends mostly on the stability constant of the formed complexes to ensure chelation stability with complex mediums such as the blood, and on the

possibility to attach it to the nanocarriers which often requires functionalized chelators.[69] The most used chelators are diethylene triamine pentaacetic acid (DTPA) and tetraazacyclododecane-tetraacetic acid (DOTA), and a great variety of functionalized versions of these chelators to attach to nanocarriers are commercially available. For example, in this thesis, we use active ester derivatives (p-SCN-Bn-DTPA and p-SCN-Bn-DOTA) that readily react with amine functionalized polymers through covalent bonding.

The metallic complexes formed by DOTA have higher thermodynamic stability compared to the ones formed with DTPA. However, while complexation with DTPA occurs rapidly at room temperature, complexation with DOTA is slow and difficult requiring usually a heating step,[70] which can represent a problem for the nanocarriers stability.

The chelator DTPA has high affinity to metal cations and is a potential octadentate ligand due to eight available positions for coordination (three center nitrogens and five COO^- groups). For detailed structure of DTPA see Figure 42.

In the case of ^{111}In, the only stable aqueous oxidation state is +3. Due to its large size (62-95 pm), it presents common coordination numbers (CN) of 4-8.[68] DTPA is able to form complexes with ^{111}In with a CN of 7 forming a pentagonal bipyramid with a log K_{ML} = 29.5 (K_{ML}= [ML]/[M][L], where M=metal=^{111}In and L=ligand=DTPA)[68] (Figure 8).

Figure 8. Complexation geometry of DTPA-^{111}In.[68]

1.4 General aspects of block copolymers

Nanocarriers composed by amphiphilic block copolymers have shown to be promising nanosystems for tumor imaging and drug delivery applications.[71, 72] Block copolymers consist of at least two covalently bonded polymer blocks with chemically different monomers.[73] They are generally composed by two blocks A-B (diblock) or three blocks A-B-A (triblock) arranged linearly. Most polymers of different nature tend to be incompatible and to segregate for large enough molecular weights. With copolymers, the macroscopic segregation is prevented by the covalent bond between the blocks and segregation can only occur locally through the formation of self-assembled supramolecular structures with different morphologies such as spheres or rods.[74-79] In the context of this thesis, it is important to define some parameters that govern the aggregation and dynamics of block copolymers in a solvent.

The solvent quality determines the conformation that a polymer assumes in solution, which is related to the strength of the interactions between the polymer segments and the solvent molecules. This has been assessed by the Flory parameter (χ). The smaller the χ value, the more favorable are the interactions between the polymer and the solvent. When the solvent is good for one of the blocks but poor for the other, it is said to be a selective solvent of one of the blocks.[80] Amphiphilic block copolymers built with hydrophilic and hydrophobic blocks are an important class of block copolymers because they can form in water supramolecular assemblies with hydrophobic core and hydrophilic corona structures, which can be potentially used as nanocarriers for pharmaceutical applications.

The kinetic stability of the structures formed depends largely on the glass transition temperature (T_g) of the hydrophobic block as it directly influences the mobility of the block in the micellar structures. In the case of poly(styrene), the T_g is ~100ºC which makes the hydrophobic block kinetically frozen below this temperature. For poly(propylene oxide) (PPO), the value is much lower (~ -60ºC).[81] When the temperature of the solution is above the T_g of the hydrophobic block, the structures formed are in thermodynamic equilibrium, which means they can disassemble and reassemble continuously according to the solution properties. However, this does not mean that the

formed structures are in equilibrium. The polymerization index (*P)* and the Flory parameter of the insoluble block (χ_B) are key parameters that govern the dynamics. Thermodynamic equilibrium can be achieved only for not too large values of the product $\chi_B P_B$ that determines the precipitation of the insoluble block. Also large values of P_B increase dramatically the characteristic time for the equilibration of the micellar core. The incompatibility between the two components, as measured by $\chi_{AB} P_A P_B$ plays also a major role in the dynamics.[82] Here, χ_{AB} is the interaction parameter between the two components. Thus, by varying all these parameters, a continuum of behaviors can be obtained between polymer micelles at full thermodynamic equilibrium and frozen micelles that can be assembled only through progressive solvent exchange.[83]

1.5 Pluronic block copolymers

1.5.1 Properties and applications

Among the several block copolymers tested for the development of polymer-based nanocarriers, Pluronics are probably the most broadly investigated and have superior advantages over other systems.[84-86] Pluronics are amphiphilic triblock copolymers composed of PEO-PPO-PEO, where PEO stands for poly(ethylene oxide) and PPO denotes poly(propylene oxide).[73] They are widely studied and used because of their low-cost and commercial availability in a very broad composition and molecular weight range (from 1000 to 15000 Da and from 10 to 80 wt% of PEO). They have been primarily used as surfactants in different industries[73] and, after the assessment of their *in vivo* low toxicity profile,[87] their use in the design of pharmaceutical and cosmetic products has emerged.[88] Some of them are even approved by the Food and Drug Administration (FDA) for use in i.v. pharmaceutical formulations.[89]

Due to their amphiphilic nature, Pluronic unimers aggregate and self-assemble into supramolecular structures (micelles) composed by a hydrophobic PPO core and a hydrophilic hydrated PEO corona.[85] The self-assembling mechanism and dynamics depend on many parameters such as the solution temperature, composition (e.g. salts and proteins) and the polymer concentration. Above a certain critical micelle temperature (cmT) and/or a critical micelle concentration (cmc), unimers aggregate and micelles are formed. The core of

the micelles has shown to be able to incorporate hydrophobic anticancer drugs which cannot be administrated intravenously due to their water insolubility. An increase of their solubility and improvement of the *in vivo* drug bioavailability has been observed when they are incorporated in Pluronic micelles.[85, 86, 90-94] At the same time, the PEO corona contributes to the micelles stability and prevents unwanted opsonization by serum proteins, thus avoiding recognition of the nanocarriers by the immune system. Pluronic copolymers have also shown to induce significant sensitizing effects in multidrug resistant (MDR) cancer cells,[95-97] which have shown to depend mainly on the PEO and PPO composition of the copolymers and were well-established in previous studies.[84, 96-103]

All of these advantages offer great potential for the development of improved nanomedicines based on Pluronics for oncology applications. However, due to the dynamic nature of Pluronic micelles (see section 1.5.3), further studies dedicated to micellization and to the development of innovative strategies for micelles stabilization are required.

1.5.2 Micellization and phase transitions

An important feature of Pluronic solutions is their temperature dependent self-assembling and thermo-gelling behavior. Concentrated aqueous solutions of Pluronic copolymers are liquid at low temperature and form a gel at higher temperature in a reversible process. The transitions that occur in these systems depend on the polymer composition (molecular weight and PEO/PPO molar ratio), and have been extensively studied in the past.[79, 104-106] Different phase diagrams have been constructed for most of the Pluronics by using a great variety of experimental techniques (e.g. SAXS, DSC, viscosity, light scattering).

Typical phase diagrams of Pluronic copolymers are given in Figure 9. In the given examples, we can observe that at low temperatures and concentrations (below cmT and cmc) individual block copolymers (unimers) are present in solution. Above these values, aggregation of individual unimers occurs in a process called micellization. This aggregation is driven by the dehydration of the hydrophobic PPO block that becomes progressively less soluble as the polymer concentration or temperature increases.[107] It is associated with a

large endothermic heat (heat of micellization).[79] The aggregation of several unimers occurs to minimize the interactions of the PPO blocks with the solvent. Thus, the core of the aggregates is made from the insoluble blocks (PPO) while the soluble portion (PEO) forms the shell of the micelles. Spherical Pluronic micelles contain on average 10 to 300 unimers per aggregate and have average hydrodynamic radii of 2-10 nm.[79] Besides spherical micelles, elongated or wormlike micelles can also be formed. The final geometry will depend on the entropy costs of stretching the blocks, which is directly related to their composition (size and PEO/PPO ratio). In particular, Pluronic copolymers with intermediate PEO block composition (40%) have shown to form micelles at high temperatures with a core diameter nearly the size of the fully stretched PPO chain, thus causing the transition from a spherical to a wormlike structure.[73] With higher increments of the temperature and/or concentration, other phenomenon can occur such as the formation of highly ordered mesophases (cubic, hexagonal and lamellar). Eventually, a complete dehydration of the PPO and the collapse of the PEO chains will lead to clouding and/or macroscopic phase separation.[73] This is due to the fact that hydrogen bonding between the PEO and the water molecules breaks down at high temperature and PEO becomes also insoluble in water.

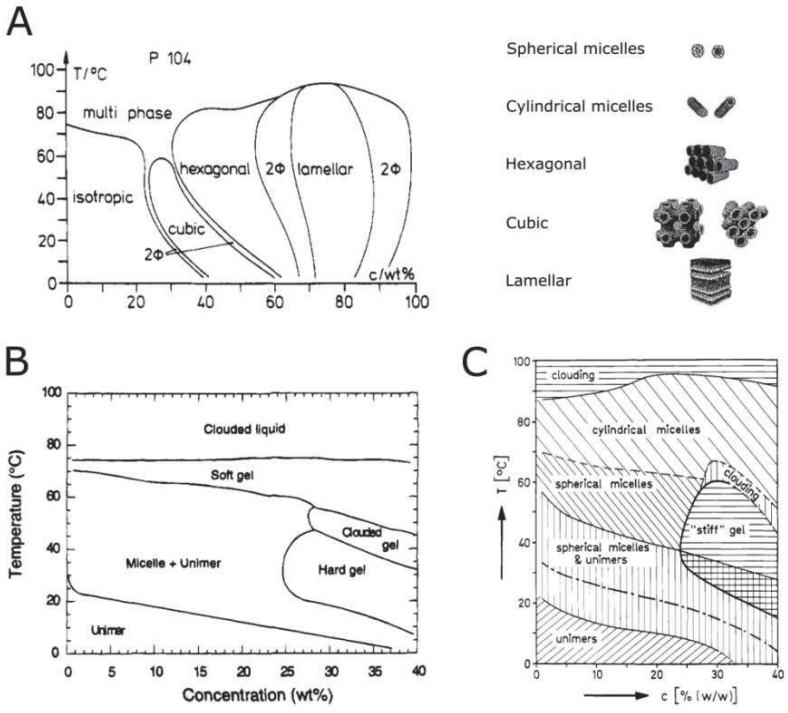

Figure 9. Phase diagrams of aqueous solutions of (A) Pluronic P104,[79] (B) Pluronic P94[104] and (C) Pluronic P85.[105]

The phase transitions can also be largely influenced by the use of additives such as salts[108-113] and alcohols.[109, 114-117] The interactions with salts are related to their ability to act as water structure makers (salting-out) or water structure breakers (salting-in). Salting-out salts increase the self-hydration of water through hydrogen bonding and reduce the hydration of the copolymers, thus reducing the cmc and cmT. Salting-in electrolytes reduce the water self-hydration and increase the polymer hydration, therefore increasing the cmc and cmT.[118] The different salts have been categorized by the Hofmeister or lyotropic series according to their 'salting-out' power.[119] For anions the series is: $CO_3^{2-} > SO_4^{2-} > H_2PO_4^- > F^- > Cl^- > Br^- > NO_3^- > I^- > SCN^-$.[120, 121]

The simultaneous use of a salt (NaCl) and an alcohol (butan-1-ol) has even recently been shown to induce sphere-to-rod transitions of the highly hydrophilic Pluronic F127.[122] Addition of other additives such as methyl paraben to Pluronic P105 and P104 solutions induced the sphere-to-rod transition, while butyl paraben avoided the sphere-to-rod transition and aggregates of spherical micelles were observed.[123] In other studies, addition of ibuprofen to Pluronic P104[124] and salicylic acid to Pluronic P85[125] also induced the sphere-to-rod transition.

1.5.3 Micelles stability

Pluronic-based nanosystems have shown to successfully enhance the anti-tumor efficacy of anticancer drugs through their incorporation in the micellar core. Particularly, a combination of two types of Pluronic (F127 and L61 in a ratio 1:8) designed to deliver doxorubicin showed superior anti-tumor activity *in vitro* and *in vivo* compared to the free drug.[126, 127] This formulation (SP1049C) has completed Phase II clinical trials[128-130] for the treatment of advanced adenocarcinoma of the esophagus and gastroesophageal junction, and has shown improved efficacy as a single-therapy agent and an acceptable safety profile.[126, 127]

However, unlike kinetically stable polymeric micelles with 'glassy' cores, micelles composed from Pluronic block copolymers are thermodynamically stable ('soft' cores) which leads to their disassembly upon variations in concentration and/or temperature. The formulation SP1049C contains micelles that are not stabilized which means that there is a constant thermodynamic

equilibrium between the single polymer chains and the micelles. Therefore, once the system is extremely diluted in the bloodstream, a fast release of the encapsulated doxorubicin can occur. The observed overall blood concentration of incorporated doxorubicin was similar to that of free drug hinting at *in vivo* micelles dissociation and premature release of the drug.[129]

Therefore, the main concern regarding the clinical use of these polymeric micelles is the extreme dilution they undergo once they are in the bloodstream. This dilution can easily reach a total concentration below the cmc, which will result in micelles dissociation into unimers in vivo.[85, 90-93, 96, 131, 132]

Due to this micellar instability, the *in vitro* and *in vivo* studies of Pluronic micelles as supramolecular carriers have been limited. However, through the use of different concentrations of polymer solution (in order to be below or above the cmc), researchers have shown that the association state, unimers versus micelles, has a very important effect on the circulation half-time life, biodistribution and intracellular fate of the carriers.[42, 56, 96, 98, 131]

Therefore, in order to use Pluronic micelles for *in vivo* applications, further stabilization strategies are needed to prevent dissociation caused by severe dilution in the bloodstream after i.v.. To this goal, one can imagine either to slow down the dissociation with an appropriate choice of the Pluronic characteristics, or to freeze the micelles via chemical routes, like cross-linking of their core or their shell.

1.5.4 Dynamics and kinetics of Pluronic micelles

The stability and morphology of the nanomedicines has shown to largely influence their efficacy.[133-135] Due to the wide range of biomedical applications of Pluronic copolymers and the growing interest in stable systems with different morphologies, understanding the dynamics of micellization and kinetics of shape transformation is crucial. This might open new opportunities to develop Pluronic-based system with varying morphologies and increased stability.

There have been many studies dedicated to investigate the dynamics and kinetics of Pluronic micelles. However, the complexity of these phenomena makes it a controversial topic.[136-141]

The mechanisms on the micellization at equilibrium have been particularly analyzed, and two relaxation times are involved in this process: (1) the first and fastest (in the microseconds range) corresponds to the unimers exchange between micelles and the bulk solution and follows the Aniansson-Wall model[142] (step-by-step insertion and expulsion of single polymer chains), and (2) the second and much slower one (in the millisecond range) is attributed to the formation and breakdown of whole micellar units leading to the final micellar size equilibration.[136-141]

The sphere-to-rod transition and its kinetics have been much less investigated.[141, 143] The mechanisms involved in the shape transformation are different compared to the dynamics of micellization. Figure 10 shows two proposed mechanisms for the sphere-to-rod transitions of block copolymer micelles, in which the micellar growth can occur by (A) fusion/fragmentation of micelles or (B) concomitant fusion/fragmentation of micelles and unimer exchange, followed by smoothing of the rod-like structures.[141]

The life-time of the micelles and the time to reach system equilibration has shown to vary a lot, taking days or even month before equilibrium is reached.[109, 140] The dominant mechanisms are expected to depend on many parameters such as the length of both the hydrophilic and hydrophobic blocks, the PEO/PPO ratio, the affinity for the solvent, and the swelling degree of the core.[141] In particular, the effects of the copolymer length have not been investigated so far. By modulating these parameters, one can expect to increase or decrease the kinetic stability of the structures formed.

However, due to the large variety of experimental settings between the different studies (measurement technique, equilibration time scales, polymer composition, concentration and the use of additives), a consensus has been difficult to achieve. Dynamic light scattering is a characterization technique that provides the means to analyze the kinetics and mechanisms of these structural transitions. Details on this technique are given in the following section.

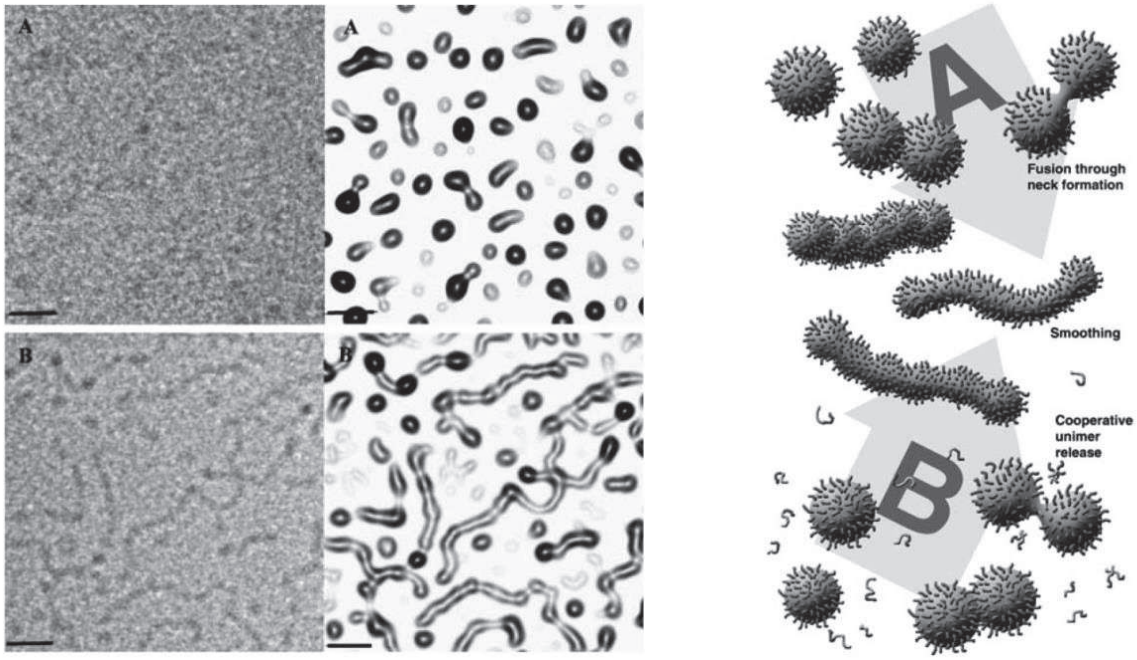

Figure 10. On the left: cryo-EM images of Pluronic P123 with added salt (KCl) and alcohol (ethanol) after (A) 5 minutes and (B) 2 hours. On the right: schematic representation of the proposed mechanisms for the sphere-to-rod transition of block copolymer micelles.[141]

1.6 Dynamic Light Scattering

Although dynamic light scattering (DLS) appears now to be a standard and powerful technique widely used to study the properties of solutions with different components such as proteins, macromolecules, polymers and nanoparticles, its specific application to the analysis of growing micellar aggregates requires some caution.

The sample is inserted in a small quartz cell, which is placed in a bath filled with a solvent which has a refractive index (n) similar to glass e.g. toluene (n=1.496). Through illumination of the sample with a laser beam, this technique is able to measure time-dependent fluctuations of the scattered intensity that arise from the species present in solution (Figure 11).

The principle of the technique is based on the fact that light is scattered by fluctuations in the dielectric constant of the medium. Those in turn are proportion to the fluctuations in the concentration of the solutes. The latter are linked to the Brownian motion of the particles (translational and rotation).[144]

The measured fluctuations are then translated into characteristic times, which are associated with the diffusion coefficient of the particles, and can further be correlated to the particles size.

These phenomena are followed theoretically and experimentally with correlation functions. An intensity correlation function (ICF) is used to determine how long the intensity signal stays correlated. The incoming data is processed in real time by a correlator and the autocorrelation function of the scattered light intensity fluctuations in the microsecond range is obtained as a function of delay time (t).

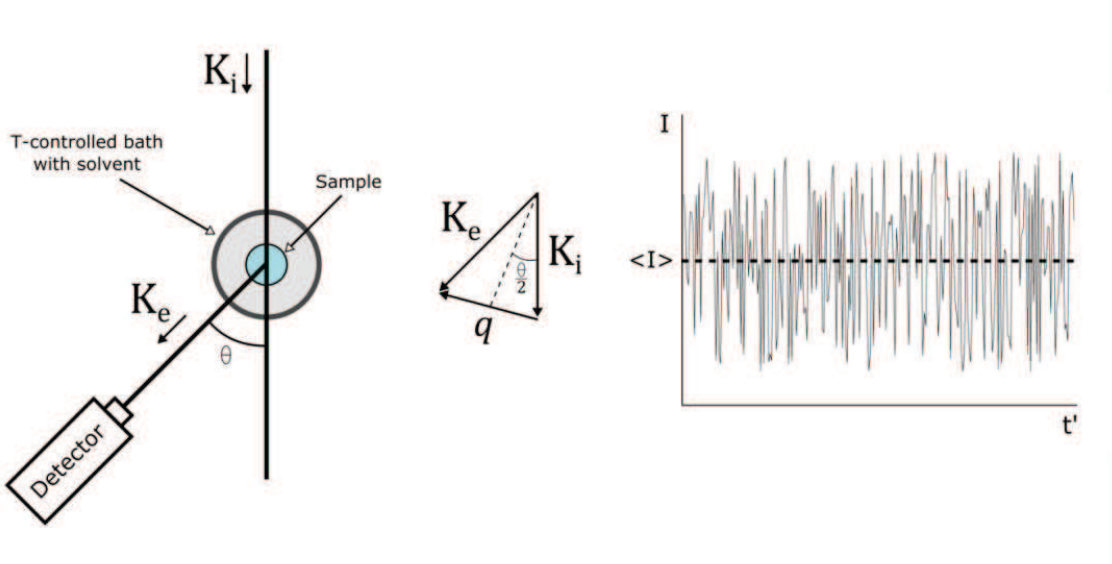

Figure 11. Scheme of a typical light scattering experiment (left), definition of the scattering vector *q* (center), and detection of intensity fluctuations of the scattered intensity overtime (right).

The normalized intensity correlation function of the scattered intensity $g^{(2)}(t)$ describes therefore the rate of change in scattering intensity by comparing the intensity at a time t' to the intensity at a later time $(t' + t)$, and is written as:

Equation 1

$$g^{(2)}(t) = \frac{\langle I(t') \cdot I(t' + t) \rangle}{\langle I(t') \rangle^2}$$

The autocorrelation function $g^{(1)}(t)$ of the scattered electric field $E(t)$ is defined similarly as:

Equation 2
$$g^{(1)}(t) = \frac{\langle E(t' + t) \cdot E^*(t') \rangle}{\langle I(t') \rangle^2}$$

The $g^{(2)}(t)$ and $g^{(1)}(t)$ are related through the Siegert equation:

Equation 3
$$g^{(2)}(t) = 1 + \left| \beta \, g^{(1)}(t) \right|^2$$

where $\beta \leq 1$ is a numerical factor close to unity that depends on geometry of detection.[144]

The analysis of the data is then processed using the cumulant method or the CONTIN fitting for monomodal or polymodal systems respectively.

In monodisperse systems, $g^{(1)}(t)$ decays in a single exponential:

Equation 4
$$g^{(1)}(t) = e^{-\Gamma t}$$

$$\Gamma = D_g \cdot q^2 = \tau^{-1}$$

$$g^{(1)}(t) = e^{-D_g q^2 t}$$

where Γ is the decay rate and the inverse of correlation time, and D_g is the translational diffusion coefficient determined for each single object with a defined mass center and undergoing Brownian motion.

The hydrodynamic radius R_H can then be determined using the Stokes-Einstein equation which determines the diameter of a sphere with the same D_g as the measured particles:

Equation 5
$$R_H = \frac{k_B T}{6\pi\eta D_g} = \frac{q^2 k_B T}{6\pi\eta}\tau$$

where k_B is the Boltzmann constant, T is the absolute temperature, and η is the solvent viscosity.

For polydisperse systems, there is a distribution of relaxation times $p(\tau)$. The $g^{(1)}(t)$ can then be written as the integral over the exponential decay with $p(\tau)$ as the distribution function of the relaxation times. Formally, $g^{(1)}(t)$ is the Laplace transform of $p(\tau)$ as follows:

Equation 6
$$g^{(1)}(t) = \int_0^\infty p(\tau)\, e^{(-t/\tau)} d\tau$$

Equation 7
$$g^{(2)}(t) = 1 + \left|\beta\, g^{(1)}(t)\right|^2 = 1 + \left(\beta \int_0^\infty p(\tau)\, e^{(-t/\tau)} d\tau \right)^2$$

Due to data noise, trying to numerically inverse Laplace transform of $g^{(1)}(t)$ to obtain $p(\tau)$ is not possible without very large numerical errors. A different approach has been proposed by S.W. Provencher using the CONTIN method, by discretizing the pseudo-distribution of relaxation times $P(\tau_i)$ on a number of N_g grid point values:

Equation 8
$$\beta\, g^{(1)}(t) = \tilde{g}^{(1)}(t) = \sum_{i=1}^{N_g} P(\tau_i)\, e^{(-t/\tau_i)}$$

The resolution of this equation by least squares minimization is an ill-posed problem and demands the use of a regularizer that puts high penalties on unphysical solutions. The solution provided by the CONTIN method is only likely and must always be checked for consistency with a priori knowledge about the physical system under investigation. It is still sensitive to experimental noise and its robustness should be checked by repeated measurements and analysis.

1.6.1 Multi-angle analysis

In more complex samples, the scattered light signal can be collected with the detector positioned at different scattering angles in relation to the incident beam laser (Figure 11). The scattering vector $|\vec{q}|$ is defined as the difference between $\vec{K_i}$ and $\vec{K_e}$ wave vectors and its magnitude is defined by the following equation:

Equation 9

$$q = \frac{4\pi n}{\lambda} \sin\frac{\theta}{2}$$

where λ is the laser wavelength in vacuum, n is the refractive index of the solution and θ is the scattering angle.

Depending on its magnitude, the scattering vector (q) enables to measure the the correlations of the scattering intensity on different length scales $\sim 1/q$ as sketched in Figure 12.

The collection of ICFs at different scattering angles enables the determination of the decay rate Γ at different scattering vectors. This allows one to check that $\Gamma \sim q^2$ and that the motion of the scatters is due to the Brownian diffusion. However, in some difficult cases, even a diffusive motion can yield a departure from this q^2 dependence (see below).

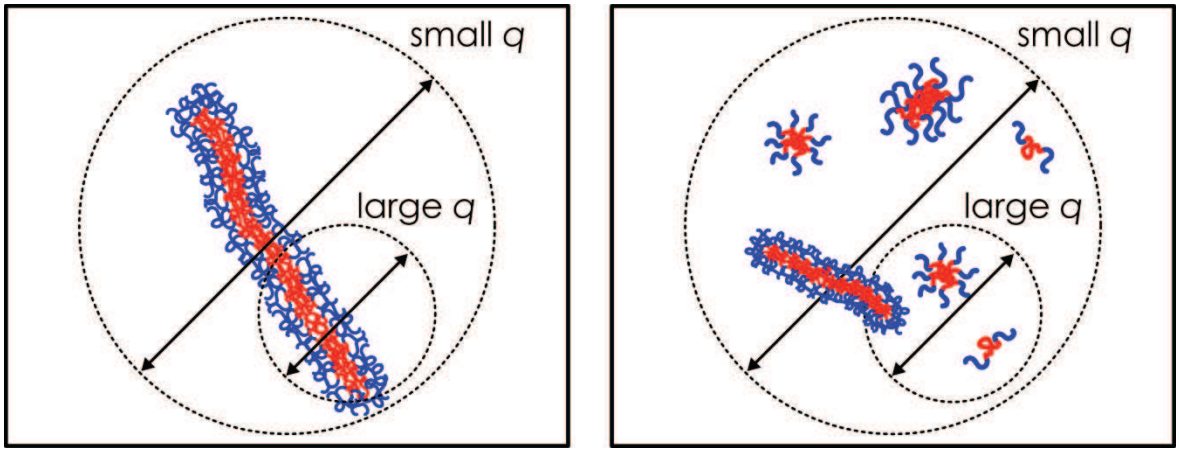

Figure 12. Scheme of the different scales measured according to the magnitude of the scattering vector q. In the left the scattered intensity is not related to the true size of the objects at large scattering vector. On the right we can observe how the effect of sample polydispersity can contribute to the detection of different species according to the q vector.

1.6.2 Guinier and out of Guinier regimens

The intensity scattered by a dilute solution of particles can be approximated as:

Equation 10 $$I(q) \sim nM^2P(q)$$

where $P(q)$ is the form factor of the particles, n their density number in the solution and M their molecular weight. For not too large particles, $P(q)$ can be approximated by the first two terms of a series expansion:

Equation 11 $$P(q) \approx 1 - \frac{q^2R_g^2}{3} + O\left(q^4R_g^4\right)$$

The condition $q \cdot R_g \ll 1$ (or equivalent $q \cdot R_H \ll 1$) defines the Guinier regime where the higher order terms can be neglected. In the Guinier regime, the Brownian translation motion of the individual particles is probed.[144, 145] Both D and R_H will be independent of the angle (Equation 10 and Equation 11).

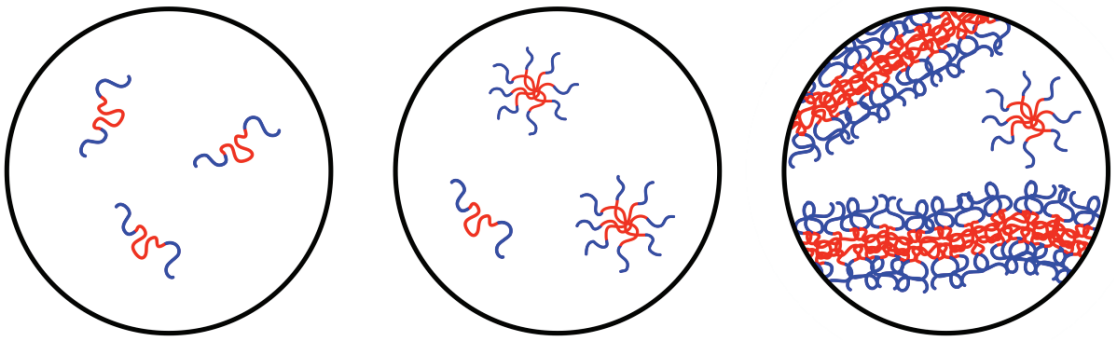

Figure 13. Schematic representation of transition of Pluronic copolymer systems from the Guinier regime (left and center) to out of the Guinier range (right) upon sphere to rod transition.

Out of the Guinier range ($q \cdot R_H \gg 1$) in dilute conditions and for polymer chains or elongated micelles, the fluctuations of concentrations measured at the length scale q^{-1} are mainly driven by the wiggling of these flexible objects and the measured intensity fluctuations are due to the internal dynamic motions of the chains.[145] In this case, the classical result for Zimm-like dynamics is:

Equation 12 $$\Gamma = D_g \cdot q^3 \cdot R_g$$

Equation 13 $$g^{(1)}(t) = e^{-D_g q^3 R_g t}$$

Since $D_g \cdot R_g \sim 1$, Γ becomes independent of R_g in this regime:

Equation 14 $$\Gamma = 0.0788 \frac{k_B T}{\eta} q^3$$

Therefore, the apparent R_H calculated using Equation 4 and Equation 5 will not be related to the real dimension of the objects but will be simply proportional to q^{-1}. Thus, measurements at different scattering angles in this regime will give q dependent apparent R_H. The q exponent in Equation 13 depends on the specific internal dynamics of the investigated system.

1.6.3 Semi-dilute range

The transition from a dilute to a semi-dilute system occurs above the so-called overlap concentration c*. At this concentration, the species in solution start to overlap, which can be schematically visualized in Figure 14.

Entering this regime can also occur with initially dilute solutions of growing species. For instance, the average hydrodynamic radius R_H of polymerizing units will progressively increase as the reaction proceeds. However, as R_H becomes of the same order of magnitude as the mean distance between the chains, the polymers start to entangle and one enters the semi-dilute regime.

In this regimen, the dynamics of the transient network are no longer characterized by the size of the constituting chains R_H but by a mesh size ξ, and the Brownian motion corresponds to the collective fluctuations of concentration of the temporary network formed by the entangled chains.[146]

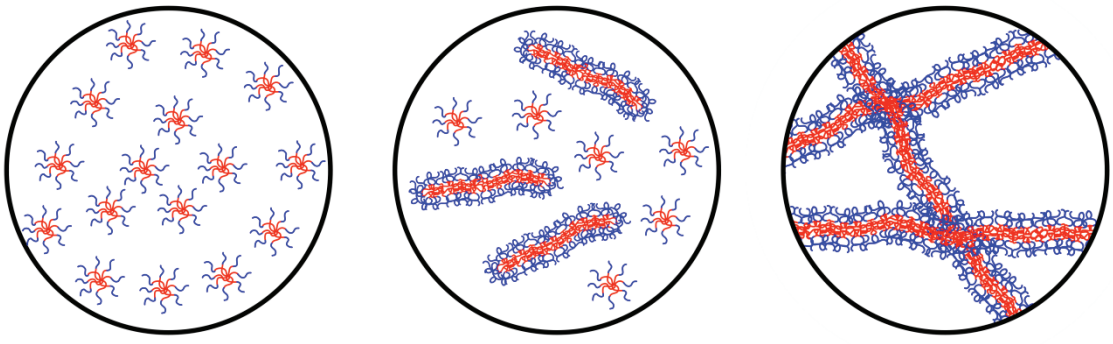

Figure 14. Transition from dilute to semi-dilute range.

The corresponding collective diffusion coefficient is then related to the characteristic mesh size ξ of the entangled solution and no longer to the molecular dimensions of the entangled chains.

During the polymerization or the growth transition of polymer micelles, there will be a crossover from the dilute regime ($D_g \sim {R_H}^{-1}$) to the semi-dilute regime, where $D \sim \xi^{-1}$ becomes a constant depending on the polymer concentration. Thus, there will be an apparent levelling of the apparent R_H even if the micellar growth is still occurring.

1.6.4 Polydispersity effects

One peculiar and often neglected aspect of dynamic light scattering is the fact that the contribution of species to the fluctuations of the scattering intensity is weighted by their contribution $I(M,q)$ (Equation 10) to the average scattering intensity. This means that the relative contribution of species with widely different sizes will be weighted differently depending on the scattering angle (Figure 12). In particular, the contribution of large aggregates will be smaller at larger scattering vectors and the contribution of small aggregates will be dwarfed by that of large aggregates, especially at small scattering vectors. Therefore, the distribution of relaxation times $p(\tau)$ or $P(\tau_i)$ in Equation 6 and Equation 8 is in principle q dependent.

For small size polydispersities, this is often unnoticeable. However, for large polydispersities, the intensity correlation function is not measured with a constant $p(\tau)$ when q is varied. This can yield a departure from the q^{-2} dependence expected for the measured $<\tau>$, and to apparent R_H values depending on the scattering angle. In this case, only the values obtained by extrapolation to $q = 0$ keep a precise meaning during the growth process.

To conclude, while investigating the growth of micellar aggregates, any dependence of the apparent hydrodynamic radius on the scattering vector should ring a bell and warn us that we are no longer measuring the size of the growing aggregates in a meaningful way.

CHAPTER 2

Lack of a unique kinetic pathway in the growth and decay of Pluronic micelles

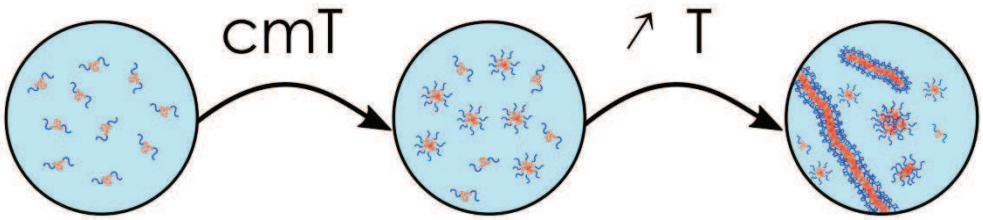

In this chapter, we report kinetic experiments on dilute brine solutions of P84, P94 and P104 Pluronic copolymer micelles. The growth and the decay of micelles after temperature steps are measured by non-standard time resolved multi-angle photon correlation spectroscopy. Several concurrent mechanisms are at work during the very slow equilibration of the solutions, namely insertion/expulsion of unimers, aggregation/dissociation of micellar aggregates, and fusion/budding of micellar aggregates. Their relative rates determine both the kinetic pathways and the morphologies of the micellar assemblies, which depend markedly on modest changes in the copolymer molecular weight. For the typical Pluronic copolymers investigated here, none of these elementary processes can be neglected if the resulting morphology is to be explained. This feature imposes multiple kinetic behaviors where growth and decay of Pluronic micelles become strongly dependent on the thermal history. We point to some possible shortcomings in previous studies of micellar growth kinetics by light scattering techniques, and demonstrate that extensive time-resolved multi-angle measurements are a prerequisite to avoid these pitfalls.

2.1 Introduction

The dynamics of block copolymer micelles in selective solvent of one block (A) has been the subject of intensive work in the past two decades.[141, 147, 148]

At thermodynamic equilibrium, there is a fast exchange of unimers between micelles and the bulk solution through insertion/expulsion steps like in short surfactant solutions.[142] In comparison, fusion/fission of micelles are relatively much slower and play also a role in equilibrium dynamics.[149-151]

After small temperature jumps, the concentration of free surfactant molecules (cmc) goes to a new value and the size and number of copolymer micelles achieve new average values. The cmc is equilibrated rapidly through the fast exchange of unimers between the bulk solution and the micelles.

The equilibration of the average number density of micelles is slower by two or three orders of magnitude and its mechanism was the subject of many discussions.[136-138, 150, 152-159] Two different routes based on the equilibrium dynamics have been proposed: step by step association of individual unimers or successive fusion/fission steps between micellar aggregates.

For appropriate block length ratios, spherical micelles can grow reversibly into wormlike micelles upon changes in temperature[112, 140, 143, 160-165] or solvent composition.[166, 167] The equilibration times vary widely in the range 1-100 h with experimental conditions and various kinetic pathways were proposed for the growth transition: fusion/fission coexisting with unimer exchange,[143] random fusion/fragmentation of spherical and rodlike micelles,[140] or aggregation of spherical micelles followed by transformation into smooth cylinders.[166] The worm-to-sphere decay transition is consistently faster than the growth[160, 163, 166] and facilitated by higher polymer concentration.[163] Mechanisms proposed for the decay transition were either a sequential budding at rod ends followed by spherical micelles release growth[163, 166] or fast random fragmentation followed by equilibration through unimer exchange.[148]

While each of these mechanisms has been proposed and validated for specific systems, only few systematic variations of molecular parameters, like e.g. molecular weight or composition, have been performed to determine how the latter affect the relative importance of these mechanisms. Moreover, some

light scattering studies did not separate properly the growth kinetics from the crossover to the entangled regime and/or out of the Guinier regime for the growing micelles. Therefore, conclusions, e.g. about concentration effects on the kinetics, could be strongly biased by these approximations.

In this chapter we address these issues by studying the growth kinetics of dilute Pluronic micelles with multi-angle light scattering experiments. We start by characterizing the copolymers, particularly their purity and composition, and we also determine their critical micelle temperature (cmT) at a fixed copolymer concentration in 2M NaCl. Then, we study specifically the effect of the total molecular weight of the copolymers, while keeping their PEO/PPO composition constant. We started by performing large temperature jumps (T-jumps) but verified that the evolution of the systems was very complex. Therefore, we carried out small T-jumps in the transition region where the spherical micelles start to grow into elongated cylinders before entering the semi-dilute range or out of the Guinier regimen.

The main goal was to verify if, by varying the molecular weight of the copolymers, (1) different morphologies are obtained and (2) if it is possible to modulate their stability for their use as nanomedicines.

2.2 Experimental section

2.2.1 Polymers purification and characterization

Pluronics P84, P94 and P104 were kindly provided by BASF. Then, their composition was analyzed by size exclusion chromatography (SEC) and proton nuclear magnetic resonance (^{1}H-NMR). The cmT was determined by micro Differential Scanning Calorimetry (microDSC).

For the SEC, samples were dissolved in HPLC quality tetrahydrofuran and the chromatograms were recorded using a differential refractive index detector (Shimadzu SPD 10Avp UV). The columns were filled with PLgel of 4 different porosities (50Å, 100 Å, 500 Å and 1000 Å), and nine homopolymers of PEO (194-18380 g/mol) were used as standards for the calibration curve. This analysis revealed the presence of satellite peaks in the distributions of molecular weights for the three samples. The lower molecular weight impurities were removed by dyalisis. Concentrated aqueous solutions of the copolymers (10 wt%) were prepared and dialyzed against distilled water using regenerated cellulose membranes (cut-off 3.5 kDa, Roth). Dialysis was performed for 7 days, and the water was changed 4 times in the first three days, and then twice-daily. After purification, the water in the polymer solution was removed by vacuum drying, and the obtained products were analyzed by SEC. The composition of the block copolymers was determined by ^{1}H-NMR. A small amount of Pluronic sample (5-10 mg) was dissolved in 1 mL of $CDCL_3$ and the ^{1}H-NMR spectrum recorded in a Bruker 400 Ultrashield. Additionally, to dislocate the signal of the terminal hydroxyl group, 10 µL of trichloroacetyl isocyanate (TAIC, Sigma-Aldrich) were added to the solution of Pluronic in $CDCL_3$ for ≈ 10 minutes before ^{1}H-NMR analysis for complete reaction.

MicroDSC experiments were performed in a Micro DSC III Setaram calorimeter. Stock solutions of all triblock copolymers were prepared in the presence of 2M NaCl to final concentrations of 0.5 wt%. Solutions were kept in the fridge for at least 24h and filtered (0.45 µm, Millipore Co.). Heating scans were performed with heating rates of 0.2ºC/min, respectively. The data were analyzed using SETSOFT 2000 (Setaram).

2.2.2 Samples preparation

Solutions were prepared at polymer concentration c_p = 0.5 g/L by weighing purified polymer in 2M NaCl brine prepared with MilliQ water. Gentle manual shaking was applied to facilitate dispersion and samples were immediately put in the fridge (ca. 4ºC) before use.

2.2.3 Dynamic Light Scattering

All samples were filtered (Millipore hydrophilic PTFE 0.45mm) in the cylindrical scattering cells (diameter 20 mm) prior to the DLS experiments, which were performed with a compact ALV/CGS-8 goniometer system equipped with an He-Ne laser (14 mW, λ=632.8 nm, vertically polarized), an ALV-7002/USB-25 autocorrelator and an automatic attenuator driven by the proprietary ALV software. The temperature of the matching index fluid (toluene) was controlled with a circulating water bath (Huber) and measured with a Pt probe. Temperature was stable within ±0.1ºC and temperature jumps were achieved after about two minutes. Measurements were done by looping repeatedly on nine scattering angles ($20º \leq \theta \leq 120º$) and measuring the intensity correlation function (ICF) and the average scattering intensity I_{meas} for typically 180 s at each angle. The effective incident intensity I_0 was measured by a diode placed after the attenuator. For very strong scattering intensities, the incident intensity was attenuated further by neutral filters with known transmission values T_r. The total scattering intensities were calculated as $I_{tot} = I_{meas}/I_0/T_r$ and further normalized with respect to the average intensity $I_{tot} = I_0$ scattered by a toluene standard. All intensities are given and plotted in these units.

Kinetics were investigated for typically 1 day up to 20 days at a given temperature. Unless otherwise specified, samples were kept in place for the whole duration of the experiment. Therefore most gaps in the data are only due to random unattended crash of the acquisition software during measurements, with no consequence on the thermal regulation of the sample. Total duration for a complete thermal history lasted typically a few weeks.

2.2.4 Data analysis

Each ICF was analyzed with CONTIN software. In most cases, one or two decay modes were obtained that were very well described by log-normal curves. Thus the peaks in the distributions of relaxation times could be easily fitted and deconvoluted. Peak areas were then calculated and gave the relative contribution of each decay mode to the decay of the ICF and to I_{tot}.[168-170]

The position of each peak maximum was used as the value of the corresponding relaxation time τ. The latter was converted into an apparent hydrodynamic radius (AHR) with the Stokes-Einstein relationship (see Equation 5 in Chapter 1) to factor out any trivial temperature dependence due to the Boltzmann factor and to the solvent viscosity. This relation also ensures q-independent AHRs for diffusive decay modes. However, this is not always the tru in some specials conditions like e.g. out of the Guinier regime when $q \cdot R > 1$ and internal dynamic modes come into play for long wormlike micelles, or when the size polydispersity is large (see Chapter 1 section 1.6 for further details on these effects). The results of the deconvolution were checked by biexponential fits when the overlap of decay modes was important. Further details on data analysis and on peaks identification and sorting are given in Appendix I.

2.3 Results and Discussion

2.3.1 Polymers characterization

2.3.1.1 Size exclusion chromatography and purification

All block copolymers used in this study were characterized by Size exclusion Chromatography (SEC). Samples were dissolved in tetrahydrofuran and the chromatograms were recorded using a differential refractive index detector. The analysis of the commercial triblock copolymers revealed two main peaks (Figure 15 left). The strong peak is attributed to the triblock copolymers, while the small peak corresponds to low molecular weight impurities. These copolymers are often used without purification despite the fact that such impurities have been reported to critically modify the micellization dynamics of the block copolymers.[104, 152, 171, 172]

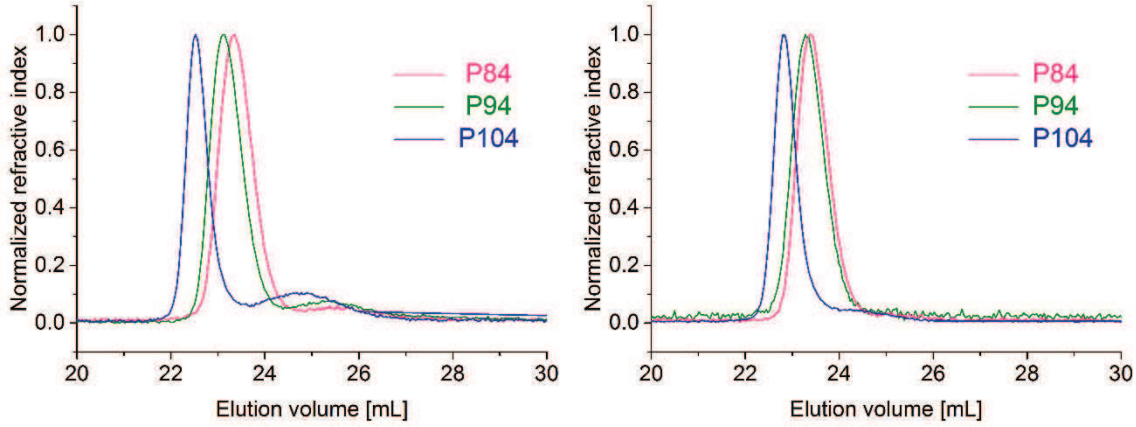

Figure 15. Size exclusion chromatograms of commercial P84, P94 and P104 samples analyzed as received (left) and after purification (right).

The low molecular weight impurities can be either smaller triblock copolymers, diblock copolymers (PEO-PPO) or homopolymers of PEO or PPO. Therefore, in order to avoid the use of unspecific methods in relation to the variety of contaminants that may be present and also to avoid the use of organic solvents, the samples were purified by dialysis.

After purification, the water in the polymer solution was removed by vacuum drying, and the obtained products were analyzed by SEC (Figure 15 and Table 3) and further by ^{1}H-NMR (see example of Pluronic P94 on Figure 16).

SEC analysis of the products demonstrated that purification by dialysis was successful as revealed by the disappearance of the satellite peak (Figure 15 right). Gravimetric analysis revealed that most of the water was removed by vacuum drying (water content < 1%).

Table 3. Contents of low molecular weight impurities of commercial Pluronic copolymers before and after purification determined by SEC analysis.

	Before purification			**After purification**		
	M_w	Pdi[(a)]	%[(b)]	M_w	Pdi[(a)]	%[(b)]
P84	4600	1.16	8	4800	1.09	0
P94	4800	1.23	15	5200	1.07	2
P104	6700	1.43	25	7500	1.17	7

(a) M_w/M_n for the main peak
(b) % (w/v) of low molecular weight impurities

2.3.1.2 ^{1}H-NMR

The precise composition of the block copolymers, namely the molecular weight and the number of repeating unimers in each block, was determined by ^{1}H-NMR.

Propylene oxyde/ethylene oxyde (PO/EO) ratio determination

The PO/EO ratio was determined by dissolving a small amount of purified Pluronic copolymers in deuterated chloroform and recording the ^{1}H-NMR spectrum. The PO units (–CH_3 group) are characterized by a narrow signal at about 1.1 ppm. The CH_2O/CHO units cause a multiplet between 3.2 and 3.8 ppm (Figure 16 above). The % of EO was calculated using Equation 15:[173]

Equation 15

$$\% \text{ EO} = \frac{3300 \cdot \alpha}{33\alpha + 58}$$

$$\text{with } \alpha = \frac{\text{area } (CH_2/CHO)}{\text{area } (CH_3)} - 1$$

Determination of the Number of repeating units

To determine the number of repeating units, Equation 16 was used:[174]

Equation 16

$$n_x = \frac{a_x \,.\, m_y \,.\, n_y}{a_y \,.\, m_x}$$

n_x = number of repeating units
a_x = area of unknown sequence (PO or EO)
m_x = number of protons
a_y = peak area of end group
n_y = number of repeating units
m_y = number of protons

The protons of the end groups (–OH) are not well discriminated in the ^{1}H-NMR because they arise in the same area as the signals from the non-terminal EO and PO groups. Thus, to determine the peak area of the end group (a_y), the signal was displaced. For this, the polymers were reacted with trichloroacetyl isocyanate[175] which readily reacts with terminal hydroxyl groups according to Figure 17. After the reaction with the displacement reagent, a new signal arises in the ^{1}H-NMR spectra at 4.4-4.5 ppm (see ^{1}H-NMR for Pluronic P94 before and after reaction with TAIC on Figure 16 below).

Molecular weight determination

The total molecular weight was determined using the respective number of repeating units (n_{PPO} and n_{PEO}) determined using Equation 16, the molecular mass of each unit, and the molecular mass of the end groups.

The results obtained from the ^{1}H-NMR are represented in Table 4 along with the information provided by the manufacturer. Similar results to ours were obtained before using ^{1}H and ^{13}C NMR for Pluronic P94[104] and MALDI-TOF MS for Pluronic P104[124] which also differ from the information provided by the manufacturer.

2.3.1.3 Micro Differential Scanning Calorimetry (MicroDSC)

Figure 18 presents the MicroDSC heating scans of 0.5% solution of Pluronic P84, P94 and P104 in 2M NaCl. The first and fairly broad peak is assigned to the aggregation of unimers into micelles (micellization). The cmT was determined after integration of the peaks and it decreases as the molecular weight increases as expected. The cmT values are 10, 9 and 2°C for Pluronic P84, P94 and P104 respectively.

The following transitions with much smaller amplitude are probably related to the sphere-to-rod transition. Different behaviors were observed with all the copolymers: with P84 we observed a small transition at around 31°C after micellization has ended, with P94 the micellization does not end and several steps of transition are observed, and with the P104 almost no transition was observed.

According to the slow kinetics of micellar growth described in the sections below, the MicroDSC technique is not suitable for the micellar growth analyses. The heating scans lasted in general 5 hours, which is not enough time to observe the slow transitions. The last abrupt transition corresponds to the beginning of a phase separation process which is not complete at these temperatures, and does not start for the P104 copolymer

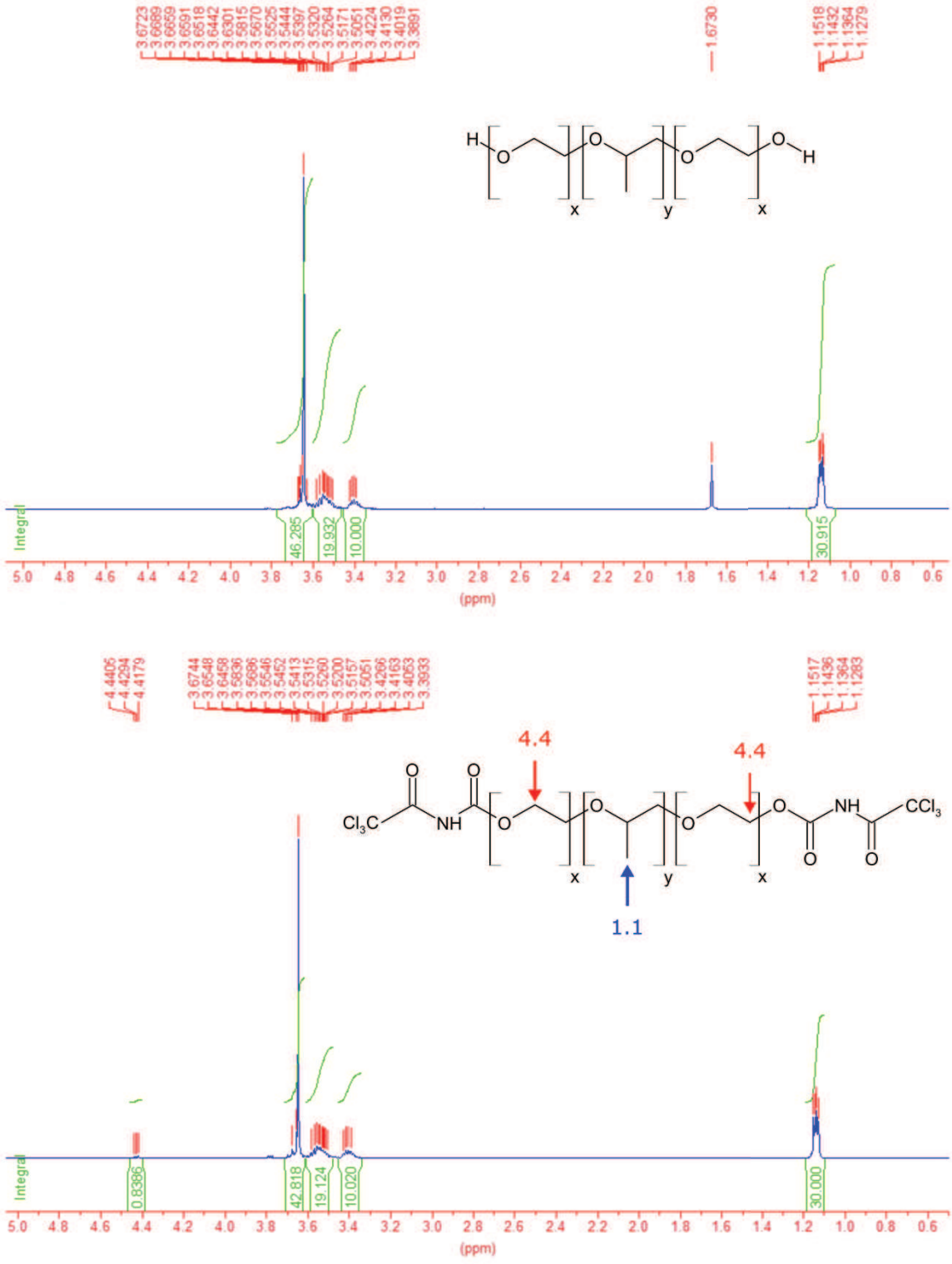

Figure 16. ^{1}H-NMR spectrum of purified Pluronic P94 before (above) and after (below) reaction with the displacement reagent (TAIC).

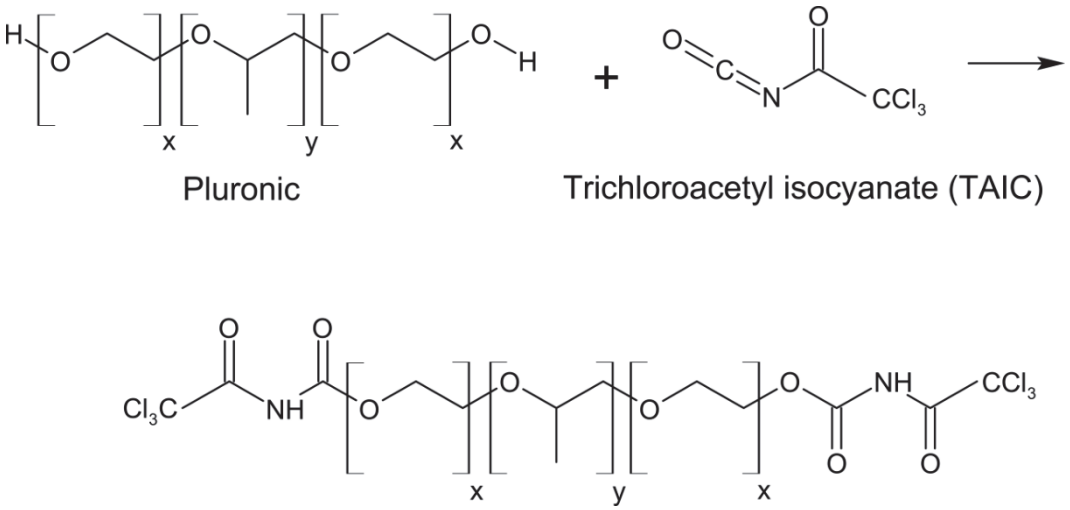

Figure 17. Reaction between Pluronic and trichloroacetyl isocyanate.

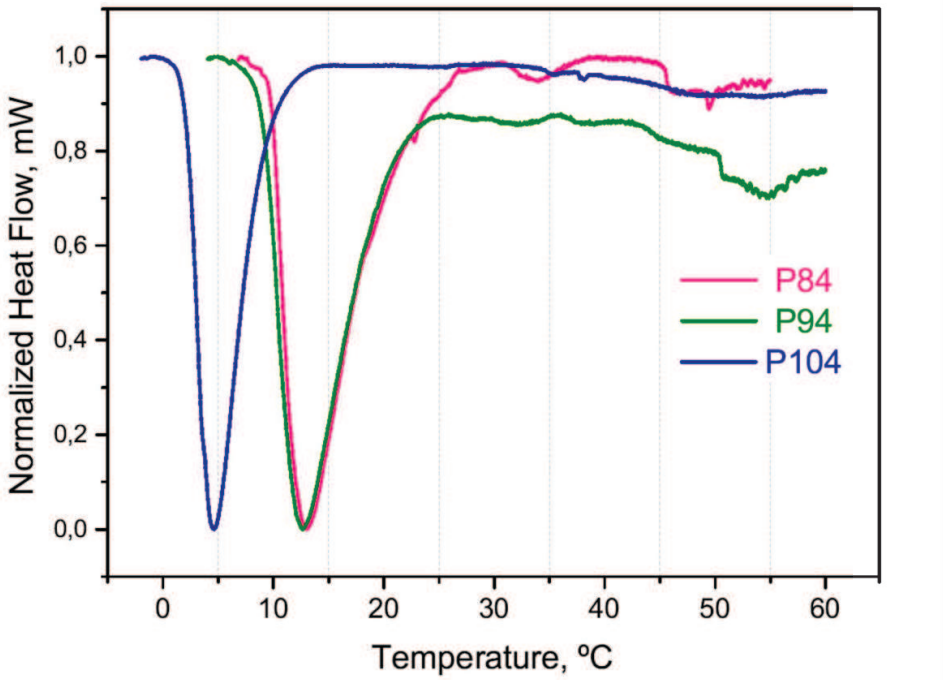

Figure 18. MicroDSC heating scans for the three Pluronic triblock copolymers.

Table 4. Characterization of purified Pluronic block copolymers by ^{1}H-NMR and comparison with information provided by the supplier (BASF).

	% PEO			n_{PEO}		M_w PEO	
	^{1}H-NMR						
	Without TAIC[b]	With TAIC[c]	Supplier[a]	^{1}H-NMR[c]	Supplier[a]	^{1}H-NMR	Supplier[a]
P84	44	43	40	46	38	2020	1670
P94	45	45	40	51	42	2240	1850
P104	39	39	40	56	53	2440	2350

	% PPO			n_{PPO}		M_w PPO	
	^{1}H-NMR						
	Without TAIC[b]	With TAIC[c]	Supplier[a]	^{1}H-NMR[c]	Supplier[a]	^{1}H-NMR	Supplier[a]
P84	56	57	60	46	43	2670	2510
P94	55	55	60	48	47	2770	2750
P104	61	61	60	66	61	3830	3530

	Total molecular weight		Formula	
	^{1}H-NMR	Supplier[a]	^{1}H-NMR	Supplier[a]
P84	4700	4200	$EO_{23}PO_{46}EO_{23}$	$EO_{19}PO_{43}EO_{19}$
P94	5000	4600	$EO_{26}PO_{48}EO_{26}$	$EO_{21}PO_{47}EO_{21}$
P104	6300	5900	$EO_{28}PO_{66}EO_{28}$	$EO_{27}PO_{61}EO_{27}$

[a] Values provided by BASF.
[b] PO/EO ratio determination (see Equation 15).
[c] Number of repeating units (see Equation 16).

2.3.2 Micellar growth and decay stability of Pluronic micelles

The main characteristics of the studied samples are given in Table 5.

Table 5. Characteristics of purified Pluronic copolymers.

	M_w[a]	M_n[a]	M_n[b]	% PEO[b]	n_{PPO}[c]	cmT[d]	T_1[d]	T_2[d]
P84	4800	4430	4700	43	46	10	31	-
P94	5200	4900	5000	45	48	9	28	32
P104	7500	6375	6300	39	66	2	30	34

[a] SEC; [b] ^{1}H-NMR; [c] polymerization index of PPO block;
[d] ºC at 0.5 g/L with 2M NaCl

Samples stored in the fridge were first brought to 25ºC. As this temperature is above the critical micellar temperature (cmT) for the three copolymers at this concentration in this solvent (2M NaCl) (Table 5), spherical micelles are expected. Interestingly, the total scattering intensity I_{tot} can exhibit very slow nonmonotonic transients depending markedly on the scattering angle. It can take several hours up to days to stabilize. The kinetics of micellization depends on both the molecular weight and the thermal history of the samples. Its detailed study is ongoing and is not discussed in this thesis.

The hydrodynamic radii of the spherical micelles (R_{sm}) measured before the subsequent temperature steps rank as expected with the molecular weight of the unimers: R_{sm} ≈ 7.1±0.1 nm for P84, R_{sm} ≈ 8.0±0.5 nm for P94 and R_{sm} ≈ 9.3±0.2 nm for P104. Their weight averaged aggregation numbers N_{sm} obtained from the light scattering intensities are about 70, 80, and 110 for P84, P94, and P104, respectively.

We used a brine solvent (2M NaCl) to study the micellar growth and the decay kinetics because it is known that its presence shifts the transition temperatures down closer to room temperature.[176] The dynamics of Pluronic copolymers with increasing molecular weight and constant PEO/PPO ratio was then analyzed by step increases of the temperature and by acquiring the total scattered intensity and the intensity correlation functions using DLS.

2.3.2.1 Total scattered intensity

For the three copolymers, an increase of I_{tot} by about two orders of magnitude is obtained for temperature increases of about a few degrees (Figure 19). First moderate, the increase becomes much more pronounced above a temperature T_1 (Table 5) where the onset of angular dependence also indicates the progressive appearance of large objects in the solution. Thus T_1 corresponds roughly to the onset of micellar growth. Then, above a temperature $T_2 > T_1$, I_{tot} becomes insensitive to temperature and the angular dependence stops increasing with temperature. This can be due to a crossover to either the entangled regime of wormlike micelles or the intermediate scattering regime of large aggregates ($q \cdot R_H > 1$) (see Chapter 1 section 1.6.2 and 1.6.3 for details on these effects). In both cases, the scattering intensity should become independent of the aggregate sizes.[177] For P84 this regime was not obtained in the temperature range investigated, but for P94 and P104 the T_2 is about 32ºC and 34ºC respectively. Therefore, in the following, we restricted our analysis of the growth to a limited range of temperature above T_1, shown by the gray rectangles in Figure 19. Although T_1 depends weakly on the copolymer molecular weight (Table 5), there are other striking differences between the behaviors of the three copolymers.

The most evident is the stepped increase of I_{tot} for P84 as compared to the continuous increase observed for P94 and P104. After each temperature jump applied above 30ºC to the P84 solution, there is first a step increase of I_{tot} followed by a slower and smaller increase, which does not reach a real steady state even after 24 hours (≈1500 min). Conversely, in the same conditions, P94 and P104 solutions do not depart from a smooth increase of I_{tot} and display merely a faster rate of intensity increase at higher temperatures. The time evolution of the angular dependence follows the same pattern as that of I_{tot}: it varies abruptly for P84 (see Figure 83 in Appendix I) but very progressively for P94 (see Figure 84 and Figure 85 in Appendix I) and P104 (see Figure 86 in Appendix I) after each temperature change.

2.3.2.2 Analysis of the Intensity Correlation Functions (ICFs)

CONTIN analysis of the ICFs measured in the range $T_1 \leq T \leq T_2$ shows that the onset of growth is associated with the presence of two decay modes for all

three copolymers. However, the behavior of these two decay modes as a function of temperature and time depends strikingly on the molecular weight. These decay modes, labeled for convenience as fast and slow, corresponds to two different populations of micellar aggregates.

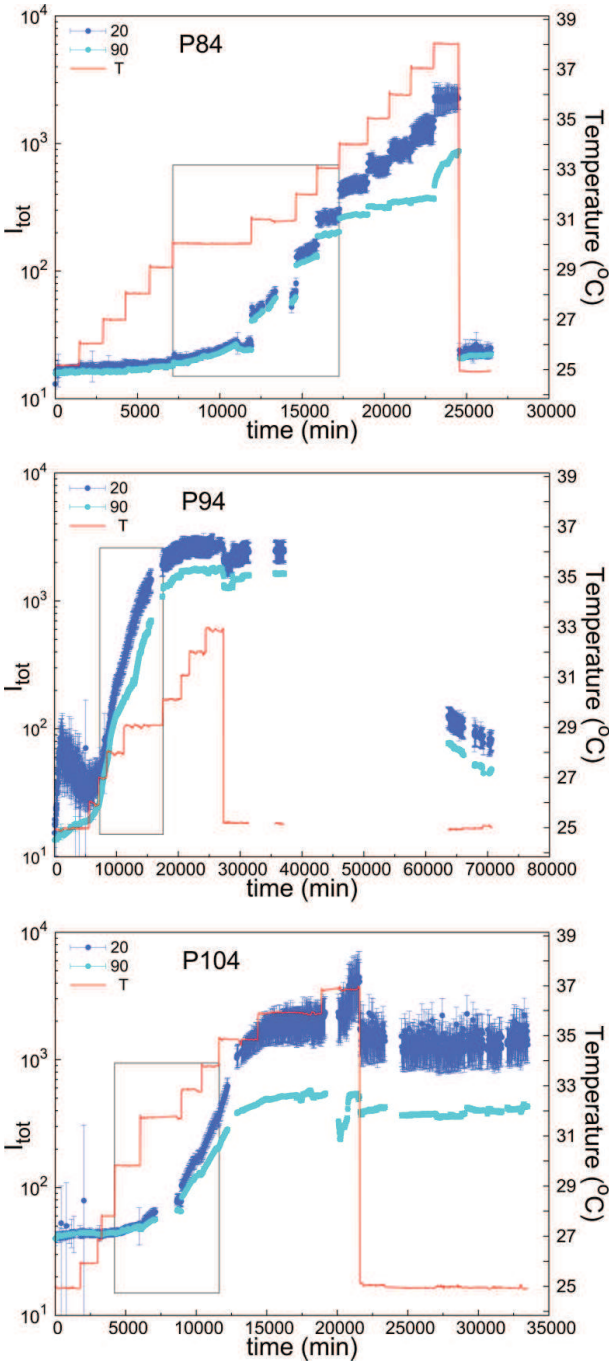

Figure 19. Evolution of the total scattering intensity with time and temperature for copolymer P84 (top), P94 (middle), and P104 (bottom) for two scattering angles (20º and 90º). The red lines are the temperature steps. Grey rectangles show the regions used for the growth analysis. Error bars are the standard deviation in I_{tot} during ICF measurement.

For P84 (Figure 20), after a moderate continuous increase of both the scattering intensity and the hydrodynamic radius between 25ºC and 30ºC, there is a sudden jump in these quantities at 31ºC (≈12000 min). When the temperature is increased further to 32ºC (≈14500 min), a second slower decay mode with a much larger and q-dependent scattering intensity appears almost instantaneously. At 33ºC (≈ 16000 min), the scattering intensity of the slow mode and its q-dependence are increasing further while the associated apparent hydrodynamic radius (AHR) becomes also q-dependent.

The faint fast decay mode persisting above 31ºC (≈14700 min) corresponds to smaller scattering intensities (≈2 a.u.) and hydrodynamic radii (≈5 nm) than measured for the spherical micelles before the onset of growth, resp. ≈16 a.u. and ≈7 nm before ≈12000 min. At T=31ºC, it is likely that the respective contributions of spherical micelles and growing micelles could not be separated by CONTIN. Indeed, for this temperature, bi-exponential fits yielded satisfactory results as well with R_{fast} ≈8 nm and R_{slow} ≈20 nm.

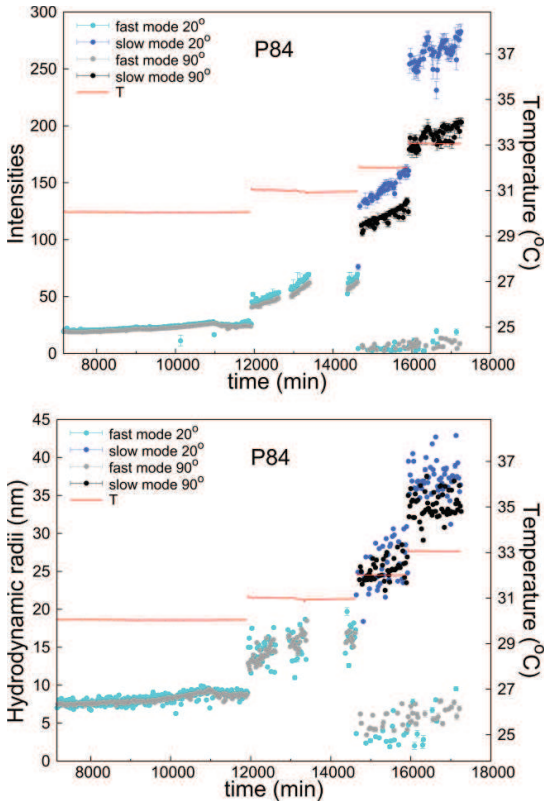

Figure 20. Evolution with time and temperature of the intensities (top) and apparent hydrodynamic radii (bottom) associated with the fast and the slow decay modes for P84.

For P94 (Figure 21), no jump is observed in the scattering intensity, which increases smoothly at a rate that grows with temperature. At 28ºC (≈8500 min), a second slower mode appears: its associated scattering intensity and hydrodynamic radius as well as its q-dependence increase progressively with time. This behavior becomes more pronounced at 29ºC (≈11000 min). When R_{slow} increases above 30-40 nm its values become progressively q-dependent and T-independent. This occurs first for the largest angle and then progressively at smaller angles. At elapsed time around 13000 min, the rate of intensity increase becomes suddenly larger for the largest scattering angles and the q-dependence that was steadily increasing strikingly shrinks back at its value at the beginning of the temperature step. Thus, the micelles start their growth and enter the entangled regime in a very narrow temperature interval of about 1-2ºC.

As the relative contribution of the slow decay mode increases, the reliable characterization of the fast decay mode becomes more difficult. Although rather dispersed, values for I_{fast} ≈15 a.u. and R_{fast} ≈5-10 nm remain still mostly consistent with those measured at 25ºC.

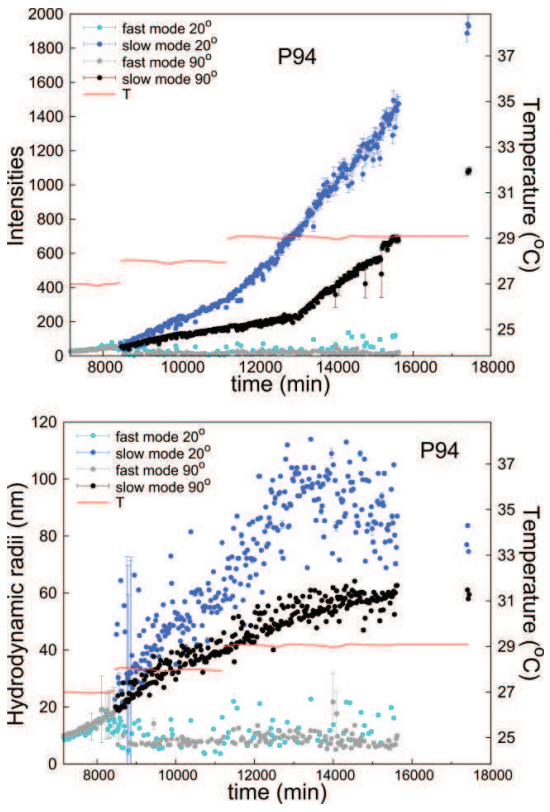

Figure 21. Same as Figure 20 for sample P94.

Although P104 exhibits the same continuous intensity increase as P94, the behavior of the decay modes is very different (Figure 22). The slow decay mode appears progressively at 32ºC (≈6000 min). Since it corresponds immediately to a large apparent hydrodynamic radii (R_{slow} ≈100 nm), it can only be detected first at small scattering angles (see details on multi-angle analysis in Chapter 1 section 1.6.1). At 33ºC (≈9000 min) and 34ºC (≈10500 min), it is clearly seen at all scattering angles and the associated R_{slow} values show a marked q-dependence (see also Figure 85 in Appendix I). For these two temperatures, the results shown are obtained with bi-exponential fits of the ICFs, which reduce the dispersion of the data points. In contrast with P84 and P94, both I_{fast} and R_{fast} still increase slightly in this regime. They decrease only at higher T (not shown) to values I_{fast} ≈15 a.u and R_{fast} ≈7-8 nm slightly smaller than those measured at 25ºC (respectively ≈40 a.u. and ≈9 nm). Neglecting the fraction of unimers in the spherical micelles, we get rough lower estimations for the mean aggregation numbers of the large objects about 1100, 8900, and 650 for P84 (33ºC), P94 (29ºC), and P104 (34ºC), respectively.

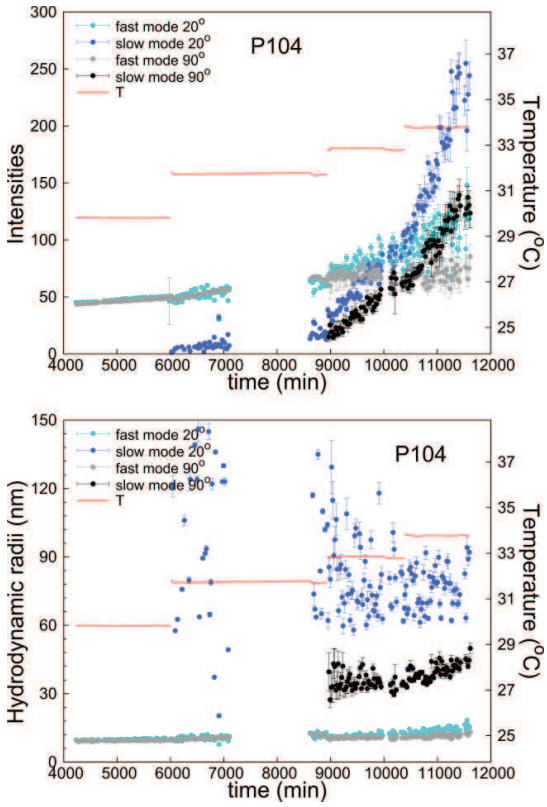

Figure 22. Same as Figure 20 for sample P104. Plotted results from CONTIN analysis except those at 33 and 34ºC (bi-exponential fits).

2.3.2.3 Stability after temperature decrease

We also tested the evolution of the solutions when they were cooled down to 25ºC. Again the three copolymer solutions showed strikingly different evolutions (Figure 19).

In the P84 solution (Figure 19 top), I_{tot} values measured at all angles decreased back to values close to the ones measured at the beginning of the experiment in the time needed to cool down the sample (a few minutes) with only one decay mode and $R_{fast} \approx 8$ nm, slightly larger than before the T-steps (≈ 7 nm).

In the P94 solution (Figure 19 middle), the intensity and radius values associated with each decay mode remained nearly constant for one week, with only a small 10% decrease in I_{slow}. After this time, the sample was kept at 25ºC in a different bath for 18 days and then measured again for 5 days. Even after one month at T=25ºC, this sample did not fully return back to its initial state at this temperature. The I_{tot} values were still about one order of magnitude larger than the initial ones and two decay modes were present: the faster one with characteristics corresponding to the initial state and the slowest one, which is responsible for the excess of intensity, corresponding to $R_{slow} \approx 150$ nm, larger than the value measured at T = 33ºC.

The total scattering intensity and the two decay modes in the P104 solution displayed the same stability as in the P94 solution during 8.5 days after cooling down (Figure 19 bottom).

2.3.3 General remarks about crossover artefacts

As micellar aggregates start to grow, I_{tot} becomes progressively q-dependent, as expected, and this angular dependence is entirely due to I_{slow} contribution. For large enough aggregates, R_{slow} values also show a q-dependence (Figure 20, Figure 21 and Figure 22), which can be due to flexibility and/or size polydispersity.

For flexible objects, both the conformational fluctuations as well as their translational diffusive motion contribute to the fluctuations of concentration. The former contribution dominates for large objects with low translational

diffusion coefficient and the decay rate of the ICFs crossover to a q^3 scaling[144, 145] as discussed in Chapter 1 in section 1.6.2, which yields a q-dependent apparent hydrodynamic radius (AHR) $R_{slow} \approx q^{-1}$ unrelated to the true size of the Brownian objects.

Large size polydispersity can also yield q-dependent AHRs since the relative contributions of the Brownian objects to the ICF are weighted by their scattering intensity: the largest objects contribute more at smaller q values while the smallest objects are the major contributors at larger q values. Therefore, the sampling of the objects shifts with their growth and only average values extrapolated at q = 0 keep a precise definition while those measured at fixed angles are poorly defined.

Whatever the reason, q-dependent AHRs are the warning sign that the measured values are loosely related to the true average size of the aggregates. Therefore, following the kinetics of growth with intensity or radius values measured at a fixed and large scattering angle can be misleading. These aspects were overlooked in former studies.[112, 140, 143, 161, 162]

Above a certain temperature and/or after a certain time, all samples become insensitive to further T-steps with constant I_{tot}, I_{slow}, and R_{slow} values within experimental errors. This behavior can mark the transition to an entangled regime (discussed in Chapter 1 section 1.6.3) where the elongated micelles overlap and I_{tot} becomes independent of their length.[177] The single characteristic length is then the mesh size of the entangled solution ($\xi \sim c_p^{-3/4}$),[82] which decreases with polymer concentration (c_p). T-jump experiments bringing the solutions into this regime will display faster relaxations to $R_{slow} \approx \xi$ independent of the true micellar size. These effects were also neglected in some earlier studies[112, 140] at higher concentrations. Significantly, in one case,[112] the viscosity, which is sensitive to the size of the entangled micelles, still increased after I_{tot} reached a stationary value.

For these reasons, we have based our discussion to the T range ($T_1 \leq T \leq T_2$) where the samples displayed a clear sensitivity to temperature steps, and on values measured at the smallest scattering angles, which can be considered as good approximations to values extrapolated at q = 0.

2.3.4 Kinetic pathways of micellar growth

Figure 20, Figure 21 and Figure 22 show a first clear difference between P84 solutions on one hand, and P94 or P104 solutions on the other hand. After each temperature step, the P84 solutions display a sudden increase of intensities and radii followed by a moderate increase on much longer time scales. Therefore, mean micellar sizes corresponding to some close-to-equilibrium state can be defined as a function of temperature. On the other hand, for P94 and P104 solutions, the growth appears continuous with rates increasing with temperature. Even P94 solution at 25ºC does not reach thermodynamic equilibrium after 5000 min (Figure 19). It seems that no equilibrium state is achieved for P94 and P104 within days, at least for this polymer concentration. All samples are very sensitive to temperature in the range $T_1 \leq T \leq T_2$ and small 1ºC degree steps induce a noticeable change in the behavior.

It can be emphasized that the hydrodynamic radius of P84 and P94 unimers is about the same (respectively 1.9±0.2 nm and 1.6±0.2 nm) and the diffusion of the unimers cannot explain the different orders of magnitude for the equilibration times. The structure function of either P94 or P104 solutions depends on their thermal history, hence on the experimental protocol. This feature allows only a qualitative comparison of their growth kinetics and morphologies but the design of an experimental protocol that would allow a more quantitative comparison between the three different copolymers would be very difficult to define. For these reasons, we chose a reasonable duration of the order of 24 hours for P94 and P104 solutions. For P84 solutions, the duration of each temperature step does not really matter as long as it allows a close to equilibrium state.

Despite the strong difference in kinetics, all solutions share the same feature: small spherical micelles can still be detected while larger species appear in the solution. The spherical micelles are about the same size as before the micellar growth (R_{sm}) in P104 solutions and slightly smaller in P84 and P94 solutions. Within experimental accuracy, the associated I_{fast} values remain the same order of magnitude as the contribution of spherical micelles before the growth transition. Therefore, the number density of small micelles remains the same

order of magnitude as below the growth transition. This remains true at higher temperatures even above T_2 (results not shown). This suggests that the phase diagram region explored in this study corresponds to the coexistence of spherical micelles and larger aggregates.

The population of growing aggregates is clearly different for the three copolymers. With increasing T, solutions of P84 and P94 show a progressive splitting of the two decay mode intensities (Figure 20 and Figure 21 respectively), both being comparable at the onset of growth. There is also a progressive increase of R_{slow} and of the q-dependence of the slow mode characteristics. These features indicate a progressive increase of the micellar size, through either unimer exchange or fusion of spherical micelles.

In contrast, the onset of intensity growth in P104 is due to the appearance of a slow mode characterized by a large $R_{slow} \approx 100$ nm associated with a small but strongly q-dependent intensity contribution $I_{slow}/I_{fast} \approx 0.1$ (Figure 22). As I_{slow} increases R_{slow} keeps about the same values. At the same time, there is a modest increase of I_{fast} and R_{fast}. At later time (≈10000 min) I_{fast} starts to display a small q-dependence. This suggests two concurrent processes triggered by the temperature increase, the progressive formation of large spheroidal aggregates composed by many spherical micelles and the growth of slightly elongated micelles. There are only few large spheroidal aggregates and the growth of spherical micelles (R_{fast} ≈9 nm) yields only weakly elongated micelles (R_{fast} ≈12 nm).

The different morphologies of the large aggregates are further confirmed by the ratio of their radius of gyration to their hydrodynamic radius (R_g/R_H). It is about 1.6±0.2, 1.9±0.3, and 1.2±0.2 for, respectively, P84 (33ºC), P94 (29ºC), and P104 (34ºC). The smaller value for P104 is consistent with a more compact structure of the large aggregates in this sample.

The above findings can be rationalized by the effect of unimer molecular weight on the prevailing kinetic pathway of the sphere-to-rod transition. Previous studies on spherical copolymer micelles have shown that the faster and dominant dynamical process at thermodynamic equilibrium is the unimer exchange[149-151] and this is also true for elongated micelles.[178] On the other

hand, fusion/fission events, although much slower, must be present to explain some results.[136, 139, 140, 143, 164, 171]

As the molecular weight of the unimers increases, their exchange will be slowed down by the smaller concentration of free unimers[179] and/or the higher energy barrier experienced by them to cross the shell.[154, 178] Here the latter one should be proportional to the polymerization degree of the insoluble block (n_{PPO}).[178] Then the much slower fusion/fission of micellar aggregates can become a significant competitor.[153] However, with further increase of the molecular weight of the insoluble block, the aggregation number of the spherical micelles N_{sm} increases and the equilibration of aggregated spherical micelles into smooth cylinders[166] should become progressively very difficult because it involves many intramicellar rearrangements.

These features can well explain the shift in the behaviors displayed by the three copolymers with increasing molecular weight. After T-jumps the smaller P84 displays a fast adjustment of the average size of the micellar aggregates followed by a much slower equilibration (Figure 20). This is consistent with previous measurements with a classical T-jump setup.[136, 138] For P84 solutions with low salt concentration, the characteristic time for unimer exchange was shown to be a few 10 ms and a second longer relaxation time (≈ 1 s) was attributed to fusion/fission. In high salt condition, an additional slow size variation could be attributed to small intramicellar rearrangements.[136, 138] Thus, for sample P84 with n_{PPO}≈46 and N_{sm}≈70, all these processes occur concurrently and allow the two step relaxation observed in our experiments. For the slightly larger P94, the insertion/expulsion of the unimers becomes more difficult and fusion/fission events occur with much fewer intervening insertion/expulsion events. Because fusion/fission involves much larger transfer of matter between aggregates, the time scale of the kinetics becomes the one of the fusion/fission events although unimer exchange is still faster. The equilibration time is longer than for P84 because both n_{PPO}≈48 and N_{sm}≈80 are larger than for P84. For P104 micelles, still larger values n_{PPO}≈66 and N_{sm}≈110 make the intramicellar rearrangements so difficult that the fusion of two micelles becomes very unlikely. Therefore, in order to decrease the PEO/water interface, the micelles form large spheroidal aggregates without fusion.

In parallel, only a modest and very slow increase in the size of the small spherical micelles can be obtained after a long time through slowed down unimer exchange.

Thus, several concurrent mechanisms are at work during the equilibration of the solutions and their relative rates determine both the kinetic pathways and the morphologies of the micellar assemblies. Figure 23 summarizes the evolution of the kinetic pathways as a function of increasing unimer molecular weight. The corresponding kinetic equations should therefore consider both unimer exchange and fusion/fission, as proposed in Ref. [140], but should further distinguish the two steps in a fusion event: collision/aggregation and fusion itself, as well as in a fission event: budding of micellar aggregates and separation of aggregated buds. This complexifies considerably the model and its resolution since, as argued here, there are only few experimental cases where some mechanisms can be neglected, like for polymer micelles at thermodynamic equilibrium where unimer exchange is the dominant process.[178, 180-188] The full set of coupled equations should be solved with longer time series for a meaningful analysis of the present systems. This is out of the scope of this thesis.

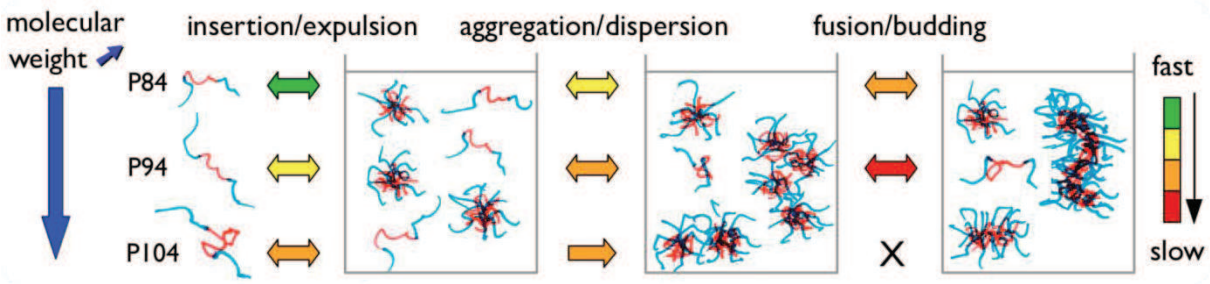

Figure 23. Schematic representation of the concurrent mechanism and resulting kinetic pathway for increasing unimer molecular weight.

2.3.5 Stability of micellar structures after temperature decrease

The surprising stability of wormlike morphologies after a decrease of the temperature back in the spherical micelles regime has already been reported for Pluronic P123 in the presence of salt.[109, 170] Here, the elongated micelles of P84 return back to their spherical morphology in a time shorter than the experimental resolution, which confirms that the fast unimer exchange plays also a role in the equilibration kinetics of P84 after temperature decrease.

On the other hand, the elongated micelles of P94 take much longer times to decay to their spherical shapes. After dilution of P94 samples following specific procedures,[112, 161] this stability is still present but for shorter times. Only when the samples were diluted to a polymer concentration lower than the cmc at the given temperature and salt concentration did the long micelles disappear very rapidly (results not shown). These features are consistent with the much slower fusion/fission process being the prevailing mechanism for P94.

Finally the large spheroidal aggregates of spherical micelles formed in P104 solutions appear to be very stable after temperature decrease and do not redisperse easily at low T once formed at high T. This might be due to the difficulty for water to repermeate the spheroids and to rehydrate the collapsed PEO shells.

It is worth noticing that the kinetic pathways involved in the T-jump from high to low temperature for P104 and P94 are likely to depend on the structure of the micellar aggregates achieved during their thermal history. For P104 aggregates, the peculiar structure deduced from the analysis of their growth introduces a new parameter, i.e. the permeation of water inside the spheroidal aggregates. The permeability of these spheroids depends on their compactness and thus on the PEO dehydration state achieved at a given high temperature. One might expect that these spheroidal aggregates would be less stable if formed at a lower temperature and/or for shorter duration. For the wormlike aggregates formed by P94, this is not as likely since rehydration of the PEO corona can be achieved more easily. In this case, our results are consistent with a slow expulsion of the unimers from the core and rare fission events hindered by the lower mobility of the unimers in the core but more

experiments would be needed to clarify the effect of the thermal history on their decay.

Finally P84 wormlike aggregates can decay very rapidly because a new equilibrium can be achieved rapidly through the fast escape of individual unimers from the core. In this case the involved cooperativity is smaller than the one necessary to create two micellar caps in a fission event and the faster process dominates the followed kinetic pathway.

2.3.6 Comparison with previous studies

Such a comparison is not straightforward since many experimental aspects are different.

Growth kinetics for Pluronic micelles have been reported for copolymers P103,[112, 140, 162] P104,[162] P123,[143, 161, 162] or F127[162] that have equal or larger PPO nominal block length than the samples investigated here. Therefore, only our P104 sample has been studied before. However, in all previous studies, samples were used as received despite the fact that impurities have been known for a long time to have an effect on the aggregation of these copolymers. Since our P104 sample had the largest amount of smaller molecular weight impurities that was almost completely eliminated in our purification process (see section 2.3.1.1 of this Chapter), a direct comparison is not possible even in this case.

Almost all previous studies were performed in the presence of added salt[112, 143, 161] and/or added alcohol,[143, 162] with the exception of Ref. [140] that was done in pure water solutions. Qualitatively, all previous results converge to the conclusion that the growth proceeds faster for higher alcohol content[143, 162] and lower salt content,[112] with the nature of salt being an important parameter.[112]

Our measurements techniques differ also from those in previous studies. Here we used a combination of static and dynamic multi-angle light scattering measurements. While dynamic light scattering technique, mostly at a single scattering angle, was also used previously,[112, 140, 143, 161, 162] only small angle neutron scattering intensities have been performed in Refs. [112, 161, 162] i.e. in a scattering vector range where the growth of large objects cannot be

measured. Only Ref. [140] has reported light scattering intensities but mostly at a single scattering angle.

Analysis of dynamic light scattering data was previously done by cumulants[140, 143] or modified cumulants method[112, 161] although partial checks with CONTIN methods revealed in some cases[140, 143, 162] two decay modes in the intensity correlation functions. In Ref. [162], a forced bi-exponential fit was used. This contrasts with our approach where the number of decay modes was systematically checked for all angles and all times, thanks to extensive software writing. As explained above, a priori assumptions on the number of decay modes can easily yield biased results.

For the above technical reasons, no experimental evidence for systematic coexistence between small spherical micelles and larger aggregates was provided by any of these previous studies. Here we show that during the growth transition of samples P84, P94, and P104, spherical micelles always coexist with larger aggregates although they can be very difficult to detect, especially at small scattering angles, due to the large intensity scattered by the larger aggregates. Moreover there is a clear size gap in the size distributions except in the very vicinity of the transition temperature.

Only one previous study[140] attempted a detailed mechanistic description of the growth with analytical kinetic models. The growth of P103 in pure water was reported by static and dynamic light scattering measurements at a single scattering angle. Consistently with their cumulants analysis used a priori, the authors concluded that the growth mechanism was random fusion-fragmentation, yielding an exponential size distribution with no gaps, clearly inconsistent with our data. A second striking difference is the very large scattering intensity increases measured during the growth in our systems compared to a mere factor 5 measured for P103.[140] Although part of the difference can be assigned to intensity measurements performed at 90º scattering angle in the latter case, this suggests that P103 aggregates might be more similar to the ones formed by P104 than to the true elongated micelles formed by P84 and P94.

The previous studies have reported much faster relaxations to equilibrium after T-jumps in the growth regime.[112, 140, 143, 161, 162]

Several features could explain our findings:

a. As detailed above, our copolymer samples have a different composition and have been purified from low molecular weight impurities.
b. Our experiments are performed at high NaCl concentration with no added alcohol, conditions that slow down the kinetics. Also our samples were not stirred like in some previous studies.[140, 143]
c. Sometimes higher polymer concentrations[140, 143, 161] have likely made the leveling of intensity and AHR faster due to the transition to the entangled regime as discussed above. This feature calls for increased caution when characterizing the kinetic constants as a function of copolymer concentration, as attempted in Ref. [140].
d. Also the AHR of large aggregates, either flexible or with a large size polydispersity, cannot be measured accurately out of the Guinier regime and the erroneous values show a misleading apparent saturation. Some previous results might have been affected by this effect,[112, 140] which starts to show up for AHRs about 30 nm at q = 90º with our experimental setup.

To conclude this comparison, there is convincing evidence that copolymer micelles made from P84, P94, P104, P103, P123, and even F127, can form at high temperature larger aggregates in appropriate conditions of added salt and/or alcohol. However the lack of homogeneity in the experimental conditions and in the analysis methods prevents any definitive comparisons between the exact morphologies of these aggregates. Based on our results, we suspect however that some diversity in the kinetic pathways and in the resulting morphologies are hidden behind the generic features, e.g. increased viscosity, light scattered intensity or apparent hydrodynamic radius reported so far. This diversity can only be unraveled by detailed measurements with the methods reported here.

2.4 Conclusions

We studied the effect of copolymer molecular weight on the kinetics of growth and decay of Pluronic micelles after T-jumps using time-resolved multi-angle photon correlation spectroscopy.

Our results demonstrate that increasing by a factor less than two the length of the insoluble PPO block at fixed PEO/PPO composition has dramatic effects on both the kinetics of equilibration and the morphologies of resulting aggregates after a T-jump in the growth regime: while P84 can form equilibrium wormlike micelles, the wormlike micelles formed by P94 are likely never at full equilibrium on the time scale of our experiments. With P104, only large spheroidal aggregates of spherical micelles and, on longer time scales, slightly elongated micelles are obtained.

Upon cooling the solutions down to the spherical micelles regime, wormlike micelles made from P84 return very rapidly to spherical micelles while P94 solutions stay for very long times in their high temperature state. The large spheroidal aggregates formed in P104 solutions do not redisperse easily at low temperature. For all copolymers, spherical micelles are still present at all temperatures and their concentration remains of the same order of magnitude as below the growth transition.

These results are explained by several elementary processes working concurrently to equilibrate the population of micellar assemblies after a T-jump, namely insertion/expulsion of unimers, aggregation/dissociation of micellar aggregates, and fusion/budding of micellar aggregates. The rates of these elementary processes depend markedly on the copolymer molecular weight at a fixed polymer concentration. In the cases investigated here, none of these processes can be safely neglected when attempting to solve the corresponding set of coupled kinetic equations, if the resulting morphology is to be taken into account. We suspect that this might also hold true for previous studies where the morphology of the micellar aggregates was not investigated thoroughly enough to distinguish a possible departure from the assumed wormlike morphology. Extensive time-resolved multi-angle measurements are a prerequisite for this purpose.

Our results also point to some possible shortcomings in studies of micellar growth kinetics where the crossover to the entangled semi-dilute regime and/or out of the Guinier regime might yield an apparent saturation of the total scattering intensity or the hydrodynamic radius. Moreover, analysis of intensity correlation functions with a priori assumed number of decay modes is bound to produce unreliable results.

Owing to the marked effect of modest molecular weight changes on the kinetic pathways, consensus about the equilibration mechanisms of copolymer micelles has been difficult to achieve on the grounds of results obtained from copolymers with different natures, compositions, architectures and molecular weights. This reflects the nature of a system that laks a unique kinetic behavior and that is the reason why the formulation of "one" T-jump protocol that will capture all the features (mechanisms) of the growth or decay of Pluronics or equivalent systems cannot be easily carriers out.

Based on these results, a series of trials were performed to form and stabilize Pluronic wormlike micelles. Details on these attempts are described in Appendix II.

CHAPTER 3

Development and functionalization of Pluronic nanocarriers

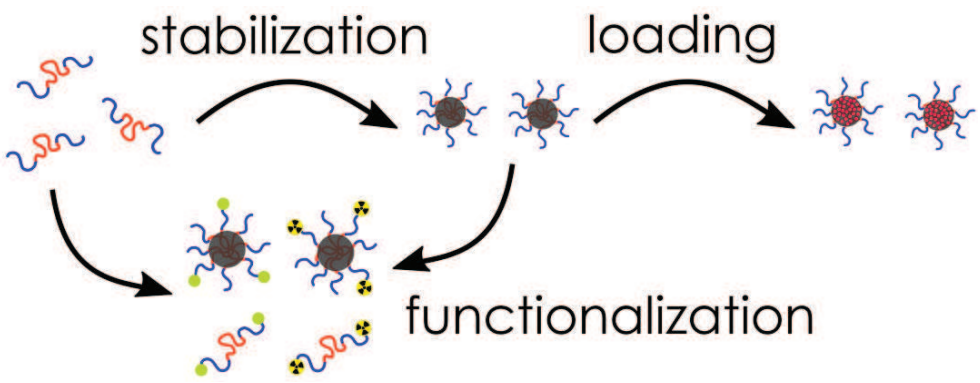

In this chapter, we present the development and functionalization of molecular and supramolecular Pluronic nanocarriers. Two triblock copolymers of PEO-PPO-PEO (P94 and F127) with different molecular weight and hydrophilic/hydrophobic ratio enable the preparation of nanocarriers with different PEO block length. The supramolecular carriers are obtained through the stabilization of dynamic micelles via core cross-linking. The physicochemical characterization of both molecular (unimers) and supramolecular (stabilized micelles) nanostructures is described. The hydrophobic capacity of the micellar core to physically incorporate hydrophobic molecules is also investigated using a hydrophobic dye.

Finally, the molecular and supramolecular Pluronic systems are functionalized through covalent attachment of a fluorescent probe and a hydrophilic chelator for further radiolabeling with the radioisotope ^{111}Indium.

3.1 Introduction

3.1.1 Molecular and supramolecular nanocarriers

We selected Pluronic triblock copolymers to create molecular and supramolecular nanocarriers. Due to the dynamic nature of these copolymers, they can be used as both molecular (unimers) and supramolecular (micelles) nanocarriers within an acceptable temperature range. In terms of nanocarriers, this will ultimately provide valuable information on the effects of important parameters such as the aggregation state and composition, while keeping the same triblock copolymer structure.

As molecular nanocarriers, they were chosen taking into account the selection criteria of polymers for biomedical applications, which include controlled stability, biocompatibility, aqueous solubility and availability to attach chemical groups that can be used for targeting, imaging or therapy.[189, 190] They are available in a wide range of molecular weight and PEO/PPO ratio, thus enabling comparison of different properties.

Regarding the supramolecular carriers (micelles), they are not stable against temperature and dilution (see Chapter 1 section 1.5.3). Therefore, in this chapter we address the stabilization of the micelles structure, crucial for the biological evaluation performed in Chapters 4 and 5. The stabilization and consequent 'freezing' of the nano-sized structure is expected to prevent unimers disassociation caused by dilution in the bloodstream after intravenous injection. This will delay the release of the hydrophobic entrapped molecules and improve the chances of reaching the tumor site by the EPR effect.

3.1.2 Stabilization strategies of dynamic micelles

A key point on choosing a strategy to stabilize the micelles structure is to assure the integrity of PEO corona. In a first stage, this will provide colloidal stability to the system. In a later stage, the shielding properties of the PEO corona will prevent *in vivo* unwanted interactions such as opsonization and uptake by the reticuloendothelial system (RES).[90, 91, 191]

The stabilization of micelles through the cross-linking of the corona involves the chemical introduction of cross-linkable groups in the hydrophilic portions of the copolymers. Since the cross-linking chemistry is on the shell, the individual micelles need to be sufficiently far from each other so that cross-linking occurs only within the same micelle. Hence, they require high dilution conditions, which often results in very low efficiency. Moreover, the chemical groups added to the polymer may contribute to increased toxicity, affect micelles formation and stability, and also hinder the further functionalization with active moieties in the corona.[192-194] Therefore, the ideal stabilization strategy should be confined to the micelles core without compromising the structure and flexibility of the PEO corona.

Core cross-linking involves the creation of a matrix in the hydrophobic micellar core, which can simultaneously stabilize the micelles structure and entrap a drug. For this strategy, we can either have cross-linkable groups in the hydrophobic blocks, or use a non-covalent interpenetrating polymer network (IPN). Such an approach is very interesting because the integrity of the hydrophilic shell is kept rendering micelle stability and availability of the terminal groups for the attachment of functionalization groups like chelators or targeting agents.[192, 194]

3.1.3 Stabilization of Pluronic micelles

The stabilization of micelles based on Pluronic copolymers has been addressed by different groups in the last years. To our knowledge, Rapoport and co-workers were the first to explore three different mechanisms to stabilize Pluronic micelles: direct radical crosslinking of the micelle core with a hydrophobic radical initiator (benzoyl peroxide), introduction of low concentrations of a vegetable oil, and formation of an IPN.[191] The third route was the most successful and was based on the polymerization of a temperature-responsive low critical solution temperature (LCST) hydrogel (N-isopropylacrylamide, NiPAAm) inside the micelles core. The diameters of the micelles ranged from 30 to 400 nm depending on the Pluronic P105 concentration. This formulation was named Plurogel®.[191]

Pruitt et al. in collaboration with Rapoport used the same principle to polymerize N,N-diethylacrylamide (NNDEA) in the Pluronic P105 micelles core. The size of the stabilized micelles depended on the Pluronic concentration and temperature. The diameters ranged from 120 to 490 nm at 25ºC, and from 50 to 390 nm at 37ºC.[195] The major problems of this cross-linking method are related to the toxicity of the acrylamide derivatives, the toxic potential of the other cross-linking agents and radical initiators used, the large increase in the micellar size compared to the pure Pluronic micelles, and the limited stability of the obtained micelles (days to weeks).[93, 191, 196, 197]

More recently, Petrov et al. 2005 used the same approach to create an IPN of poly(pentaerythritol tetraacrylate) (PETA) in the micelle core.[198] Stabilized micelles of Pluronic F68 had average diameters ranging from 32 to 50 nm depending on the concentration of Pluronic and cross-linking temperature. Yoncheva et al. in collaboration with Petrov also stabilized Pluronic F38 micelles using the same approach to deliver the anticancer hydrophobic drug Paclitaxel. In this study, the micelles diameters obtained were considerably larger (180 nm).[199]

Other groups have focused on the chemical modification of the PEO[101, 200-204] or PPO[205, 206] blocks in order to covalently cross-link the micelle structure. However, in some of these studies, the introduction of chemical modifications appears to influence the micellization properties of Pluronics, since the reported sizes are much larger than the pure micelles, which is inconsistent with the structure of a core/shell Pluronic micelle.

In this chapter, we present a non-covalent approach to cross-link the core of Pluronic micelles by adapting the protocol developed by Petrov et al..[198] Two copolymers with different molecular weight and different PEO/PPO composition were chosen (Pluronics F127 and P94). Pluronic F127 was selected due to its known biocompatibility, wide use in pharmaceutical formulations and FDA approval for intravenous use in humans. Pluronic P94 has a lower molecular weight due to a shorter PEO block length and a much higher PPO content than Pluronic F127. In this way, the applicability of the cross-linking process on stabilizing Pluronic micelles with different molecular weight and PPO/PEO composition was assessed. The efficiency of the cross-linking technique was

evaluated by studying the physical stability of the cross-linked micelles below the cmT and cmc, in the presence of serum proteins, and upon freeze-drying.

The potential of the stabilized micelles to load and deliver a hydrophobic anticancer drug was also evaluated by loading pre-stabilized micelles with a highly hydrophobic fluorescent dye (Nile Red).

3.1.4 Functionalization of nanocarriers

A prerequisite for the evaluation of the nanocarriers performance and their future clinical utilization is the development of strategies and methods to conjugate chemical moieties to the nanocarriers. This will enable their pharmaceutical and biomedical application especially for tumor detection and therapy.

In this chapter, two general approaches were developed to enable labeling of the nanocarriers with fluorescence and gamma-emission. The modification strategies were applied to the molecular polymeric unimers and to the supramolecular stabilized micelles. Both functionalities were introduced in the terminal hydroxyl groups of the PEO blocks.

In the case of the fluorescent probe, this strategy was chosen as the supramolecular carriers need to be modified after their stabilization due to degradation of the fluorescent probe in the micelles stabilization process. Moreover, the hydrophilic shell is more readily available for the post-chemical reaction.

In the case of the modification with the chelator, this can be achieved at different block positions such as the hydrophilic terminal block,[207, 208] the block junction[209] or the hydrophobic block.[210] The introduction of the chelator in the block junction and hydrophobic block raises problems regarding the orientation of the chelator which are critical for complexation with the radioisotopes. Moreover, the accessibility of the radioisotopes to the chelator will be hindered by the PEO shell. The attachment of the chelator to the hydrophilic block avoids these problems but will most likely result in a lower stability of the complexes formed due to higher interactions with the surrounding fluids.

3.2 Experimental section

3.2.1 Preparation of pure polymer solutions

Purification of Pluronic F127 (M_w=11700 g/mol) and P94 (M_w=5000 g/mol) from low molecular weight impurities was performed by Dean Stark distillation in toluene and by dialysis (described in section Chapter 2 section 2.2.1) respectively.

For the preparation of pure polymer solutions, aqueous solution of 2.5% (w/v) of purified Pluronic P94 or F127 (BASF) were prepared and stored for at least 48h in the fridge in order to be below the cmT for this polymer concentration. Upon increasing the temperature, unimers self-assembled into micelles above the critical micelle temperature (cmT), or remained as unimers below the cmT.

3.2.2 Stabilization of Pluronic micelles by core cross-linking

To prepare core cross-linked micelles, an aqueous solution of 2.5% Pluronic P94 or F127 was mixed with a small amount of pentaerythritol tetraacrylate (PETA, Sigma-Aldrich) below the cmT. PETA was dissolved in acetone (50 mg/mL) before mixing with the Pluronic aqueous solution, and was added to achieve a 6% weight ratio relative to the amount of Pluronic.

To promote the solubilisation of PETA in the micelles core, the temperature of the solution was increased well-above the cmT (60ºC) for 1 hour. This solution was then degassed with nitrogen for 1 hour, and PETA was polymerized through irradiation with a full spectrum UV light for 1 hour in a closed reactor with a cooling system under a constant nitrogen flow.

The sample was stirred at approximately 100 rpm during all the procedure. The quartz glass cooling pipe, the UV lamp (Medium Pressure Mercury Lamp TQ 150 W) and the power supply were acquired from UV-Consulting Peschl (Heraeus). The reactor vessel was tailor-made by Verlabo 2000.

3.2.3 Physicochemical characterization

Samples were filtered through membrane filters with a pore size of 0.45μm (Millex LCR hydrophilic, Millipore Co.) before the physicochemical characterization. Moreover, samples containing cross-linked micelles were purified from free remaining unimers by diafiltration at 5ºC using Amicon® Ultra-4 30K devices (Millipore).

Dynamic Light Scattering (DLS)

The average size of pure polymer solutions and cross-linked micelles was determined by DLS as described in Chapter 2 section 2.2.3.

Zeta potential

The superficial charge of the stabilized micelles was measured through the zeta potential (mV) determination (Zetasizer Nano ZS, Malvern Instruments, UK).

Fourier Transformed Infrared Spectroscopy (FT-IR)

Raw polymers, functionalized unimers with primary amines and cross-linked micelles were freeze-dried and analyzed by FT-IR (Vertex 70, Bruker).

Cryo-Transmission Electron microscopy (Cryo-TEM)

Samples of stabilized P94 or F127 Pluronic micelles were vitrified before observation. The vitrification of the samples was prepared in our home-made vitrification system. The chamber was held at 22 °C and at a relative humidity of 80%. A 5 μl drop of the sample was deposited onto a lacey carbon film covered grid (Ted Pella) rendered hydrophilic using a ELMO glow discharge unit (Cordouan Technologies). The grid was automatically blotted to form a thin film which is plunged in liquid ethane hold at -190°C by liquid nitrogen. In that way, a vitrified film is obtained in which the native structure of the assemblies is preserved. The grid was mounted onto a cryo holder (Gatan 626) and observed under low dose conditions in a Tecnai G2 microscope (FEI) at 200 kV. Images were acquired using a Eagle slow scan CCD camera (FEI). Average core diameters were determined from the images using ImageJ software.

Scanning Electron microscopy (SEM)

Pluronic unimers and purified cross-linked Pluronic micelles were also visualized by SEM. The samples were diluted in water to a final concentration of 0.25% and a droplet of each solution was placed on 5x5 mm silicon chips previously washed with ethanol and treated with plasma, and the solution was vacuum dried. Then, the silicon chips were imaged using a SU8000 UHR Cold-Emission FE-SEM Scanning Electron Microscope (Hitachi, Japan). The samples were imaged at 1kV acceleration voltage and without the addition of a conductive coating.

Atomic force microscopy (AFM)

The morphology and homogeneity of cross-linked Pluronic micelles were analyzed by AFM using a NTMDT Ntegra AFM in tapping mode. The samples were diluted in water to final concentrations of 0.05% (SPM-F127) and 0.25% (SPM-P94) and a droplet of each solution was placed on silicon chips previously washed with ethanol and treated with plasma. To obtain thin films of micelles, the chips with the sample droplet were placed in a IBIS spin coater at 3000 rpm for 1 minute.

3.2.4 Stability of Pluronic cross-linked micelles

The stability of cross-linked micelles was evaluated below and above the cmT, below the cmc, in the presence of serum proteins, and upon freeze-drying.

The size distribution at different temperatures near the cmT (15, 25 and 37ºC) was analyzed by DLS.

The stability below the cmc was analyzed by DLS after dilution in water and compared with the pure polymer solutions.

For the evaluation of the serum proteins effect, a small amount of micelle solution was diluted in freshly prepared cell culture medium (DMEM) supplemented with 10% NCS to a final polymer concentration of 0.5% (w/v). The obtained solution was incubated at 37ºC for approximately 72 hours. The hydrodynamic size distribution was analyzed by DLS continuously during the incubation period. Contributions from the medium components and from the

stabilized micelles were distinguished by the use of CONTIN analysis and of the methods described in in Chapter 2 section 2.2.3.

Finally, the stability of cross-linked micelles was analyzed after freeze-drying solutions containing 2.5% SPM-P94 or SPM-F127 in a FreeZone 4.5L lyophilizer. From the obtained powder, solutions of 0.5% were prepared from both cross-linked micelles in water, acetone, tetrahydrofuran and chloroform, and the hydrodynamic size distribution was recorded by DLS.

3.2.5 Loading of cross-linked micelles with hydrophobic dye

Pre-stabilized micelles were loaded with a lipophilic dye (Nile Red) through non-covalent interactions. A concentrated stock solution of Nile Red in ethanol was prepared (1mg/mL) and a small amount of this solution was added to the aqueous solutions containing 2.5% (w/v) of stabilized Pluronic micelles. The concentration of fluorescent probe in relation to the concentration of Pluronic was 0.25% (w/w). The obtained mixture was stirred at 300 rpm at room temperature for 24 hours.

After the loading period, the fluorescently stabilized micelles were separated from the non-incorporated Nile red: the solution was firstly filtered (0.45µm, Millex LCR hydrophilic, Millipore Co.) to remove the precipitated Nile Red, and secondly purified by size exclusion chromatography (SEC) using prepacked PD10 columns (GE Healthcare). To determine the eluted fractions containing the loaded micelles, volumes of 500µl from the chromatographic column were collected and the scattered intensity of each fraction was analyzed by DLS. A solution containing free Nile Red was also eluted.

3.2.6 Functionalization of Pluronic unimers with p-SCN-Bn-DTPA and FITC

The purified copolymers were modified with 1,1-carbodiimidazole (CDI-Pluronic) followed by primary amines (F127-NH_2 and P94-NH_2) using a procedure similar to the one reported by Lu *et al.* for Pluronic F68.[211] For the CDI activation, the purified Pluronic (P94 or F127) was dissolved in dry THF (8 mM) and added dropwise during one hour in a 1:10 molar ratio to a solution of CDI in dry THF (0.08 mM) at room temperature under argon

atmosphere. The reaction mixture was stirred overnight. The solution was concentrated to 2 mL under vacuum and added to 30 mL of diethyl ether. The precipitate was isolated via filtration and redissolved in THF, followed by precipitation in an excess amount of diethyl ether. This process was repeated three times to remove unreacted CDI. The CDI-activated Pluronics (Pluronic-CDI) were obtained as white powders after drying under vacuum at room temperature.

For the amine modification, the Pluronic-CDI was dissolved in dry THF (4 mM), and added dropwise to ethylenediamine (1:394 ratio) at room temperature during one hour. The mixture was left to react overnight. The unreacted ethylenediamine was removed by vacuum distillation and the residue was dissolved in water and dialyzed against water using a membrane with a 1 kDa molecular weight cut-off to yield the amine-terminated triblock copolymers (Pluronic-NH_2) as white powders after freeze-drying.

The purification of Pluronic F127 and amine modification of the copolymers were performed by the project partners in the University of Ghent (Polymer Chemistry and Biomaterials Group).

The reactive isothiocyanate groups in the chelator p-SCN-Bn-DTPA (S-2-4-isothiocyanatobenzyl-diethylenetriamine pentaacetic acid, Macrocyclics) and in the fluorescent FITC (Fluorescein Isothiocyanate, Life Technologies) were then conjugated to the amine terminated copolymers (F127-NH_2 or P94-NH_2) as previously reported for the diblock PEG-PCL.[212] The *p*-SCN-Bn-DTPA or FITC were dissolved in DMSO (50 mg/mL) and added in a 1:1 molar ratio to a 25 mg/mL solution of F127-NH_2 or P94-NH_2 in sodium bicarbonate buffer (0.1 M, pH 8.5) or MilliQ respectively. The solutions were stirred at room temperature for at least 4 hours. Purification from unreacted p-SCN-Bn-DTPA and FITC was performed by SEC using prepacked PD10 columns and MilliQ water as the eluent. After purification, aqueous solutions containing Pluronic unimers modified with the chelator p-SCN-Bn-DTPA (F127-DTPA and P94-DTPA) and FITC (F127-FITC and P94-FITC) were obtained. Characterization of the raw and amine modified copolymers was performed by FT-IR as described in section 3.2.3.

3.2.7 Conjugation efficiency of p-SCN-Bn-DTPA to Pluronic unimers

The conjugation efficiency of p-SCN-Bn-DTPA to the amine-terminated polymers was determined by thin layer chromatography (TLC) before purification by SEC. The nanocarriers F127-DTPA and P94-DTPA diluted in PBS were labelled with 1 MBq of $^{111}InCl_3$ and incubated for 30 min at room temperature. The radioactive isotope $^{111}InCl_3$ (^{111}In-chloride) was provided by IDB Holland.

TLC was done using a stationary phase of aluminum sheets of silica gel 60 and a mobile phase of sodium acetate buffer (0.1 M, pH 5.8). A spot (5 µL) with the radiolabeled samples was placed in the bottom of a TLC strip (1×10 cm) and developed in the buffer. After elution, the TLC strips were imaged with a Storage Phosphor system (Cyclone, Packard), which enabled an appropriate sectioning of the TLC strip for the quantitative analysis through gamma-scintillation counting (2480 Wizard^2 Automatic Gamma Counter, Perkin Elmer).

3.2.8 Preparation of functionalized cross-linked micelles

Stabilized polymeric micelles containing the chelator p-SCN-Bn-DTPA in the corona were prepared from a mixture of DTPA functionalized copolymers (P94-DTPA or F127-DTPA) with regular copolymers (P94 or F127), using 10% of F127-DTPA and 3.65% of P94-DTPA to a final copolymers concentration of 2.5% w/w. Then, the Pluronic micelles were cross-linked as previously described in section 3.2.2).

Functionalization of the stabilized micelles with FITC was performed after micelles stabilization. Aqueous solutions with 10% of F127-NH_2 and 3.65% of P94-NH_2 were prepared, and self-assembled micelles with amine groups in the corona were cross-linked as described above (see section 3.2.2). After cross-linking, a solution of FITC in DMSO (10 mg/mL) was added to the cross-linked micelles at room temperature for reaction with the primary amine in the micelles surface. Purification from free p-SCN-Bn-DTPA or FITC was performed by SEC using prepacked PD10 columns and MilliQ water as the eluent.

3.2.9 Radiolabeling of Pluronic nanocarriers with ^{111}In and purification

We assessed the speed of complexation of DTPA-^{111}In in PBS at room temperature. Analysis was performed by TLC using the mobile phase of sodium acetate buffer (0.1 M, pH 5.8). Then, radiolabeling of the Pluronic nanocarriers was performed by diluting the carriers in PBS buffer (pH 7.4) and adding an appropriate activity of $^{111}InCl_3$ according to their further application, and incubation at room temperature for 30 minutes.

Labelling efficiency was verified using SEC columns (1cmx50 cm) filled with Sephadex G25 (1x30 cm). Radiochemical purity was evaluated by TLC using a mixture of EDTA and NH_4Ac (1:1) (v:v) (0.1 M, pH 5.5) as the eluent. Samples that presented a labeling efficiency of more than 95 percent (F127-DTPA and P94-DTPA) were used without further purification, while samples with a coupling efficiency less than 95 percent (SPM-F127-DTPA and SPM-P94-DTPA) were further purified.

Purification was achieved by adding free DTPA and subsequent purification over a prepacked PD10 column using PBS 1X as the eluent. Elution profiles of free ^{111}In and DTPA-^{111}In were performed with both columns to optimize the purification procedure.

3.2.10 Radiostability in mouse serum and PBS

Radiostability of F127-DTPA-^{111}In, P94-DTPA-^{111}In, SPM-F127-DTPA-^{111}In and SPM-P94-DTPA-^{111}In was measured *in vitro* by incubation of 50µL of radiolabeled samples with 350µL of PBS or mouse serum at 37^{o}C for 72 h. At various time points, 5 µL aliquots of the solutions were spotted in the bottom of TLC strips and developed in the EDTA:NH_4Ac (1:1) (v:v) (0.1 M, pH 5.5) eluent to evaluate the dissociation of ^{111}In from the samples. In this system, it is possible to assess transchelation to serum proteins as the Retention factor (R_f) [Pluronic-DTPA-^{111}In]=0.0, R_f [Proteins-^{111}In]=0.5 and R_f [free ^{111}In]=1.0. Free ^{111}In and *p*-SCN-Bn-DTPA-^{111}In were used as controls.

3.3 Results and Discussion

3.3.1 Stabilization of Pluronic micelles by core cross-linking

Pluronic triblock copolymers aggregate into dynamic micelles, which are highly sensitive to variations in concentration and temperature. The physical stability of the micelles is fundamental to withstand premature dissociation after entry into the bloodstream and to be used as a safe and effective delivery system. Therefore, to prevent the unimers dissociation, the stabilization of the Pluronic micelles was obtained through incorporation of a hydrophobic cross-linking agent in the micelles core and subsequent photo-polymerization. A scheme of the procedure used is depicted in Figure 24, and a more detailed description of the photo-polymerization set-up is presented in Figure 25. We selected Pluronics P94 ($PEO_{26}PPO_{48}PEO_{26}$) and Pluronic F127 ($PEO_{96}PPO_{56}PEO_{96}$), and prepared cross-linked micelles from both copolymers.

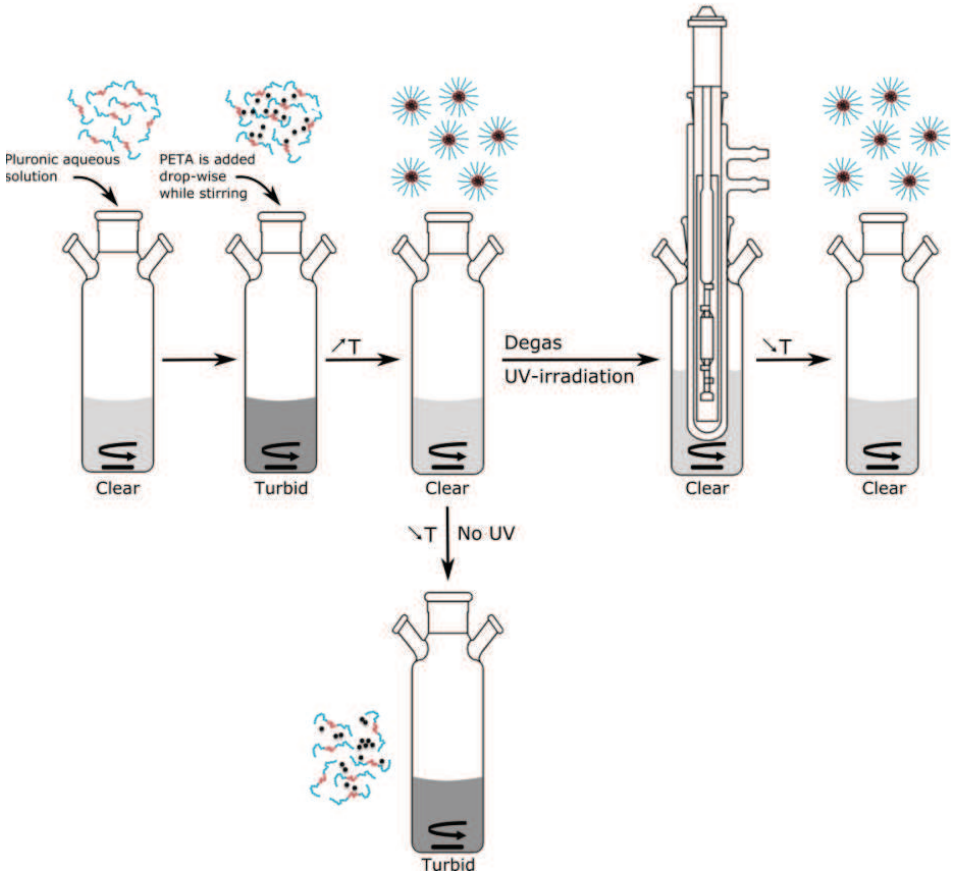

Figure 24. Scheme of the preparation of cross-linked Pluronic micelles by UV-polymerization.

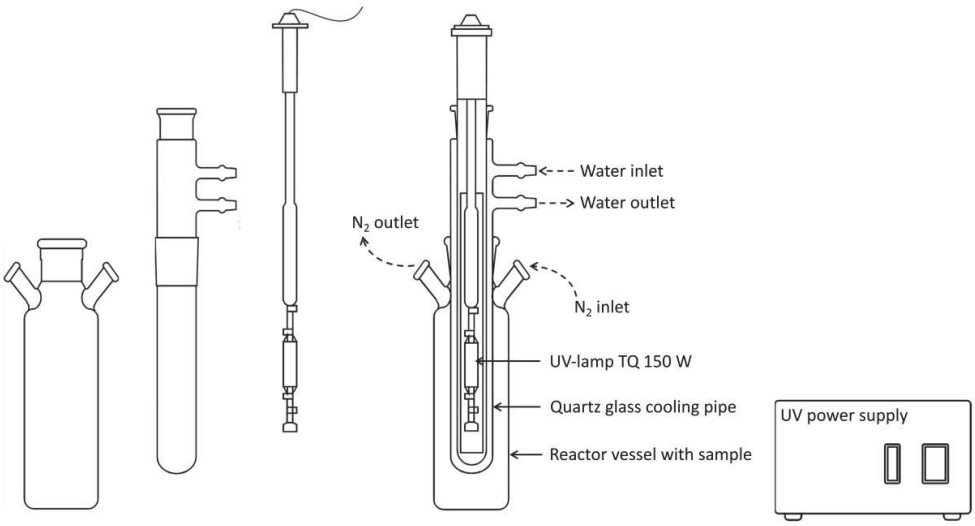

Figure 25. UV experimental set-up. The sample is inside the reactor vessel. A quartz glass cooling pipe is placed inside the reactor vessel and is connected to a water in/outlet for cooling of the UV-lamp. A continuous nitrogen flow is provided during the UV polymerization reaction. The temperature inside the reactor vessel is controlled externally by a magnetic stirrer with heating plate and internally by the cooling pipe.

Firstly, a mixture between the Pluronic aqueous solution and the hydrophobic cross-linking agent PETA was prepared below the cmT. Secondly, the temperature of the mixture was increased to 60ºC to promote the formation of micelles (micellization) and consequent incorporation of the hydrophobic PETA in the micelles core (Figure 24). At this high temperature and polymer concentration (2.5 wt%), it is expected that most of the Pluronic unimers have self-assembled into micelles with only a small percentage of polymer unimers is left in solution.[179] Lastly, the dispersion was exposed to UV light in order to initiate the polymerization reaction. The cross-linking of PETA molecules is initiated by UV-light and proceeds according to Figure 26 inside the micelles core. This network formed inside the micelles is able to retain the Pluronic unimers together, which results in the stabilization of the micelles structure.

If no UV light is used, the polymerization of PETA will not occur and micelles will disassemble upon decrease in temperature below cmT. This will lead to the release of PETA molecules and the formation of aggregates rendering turbidity to the solution. If polymerization is successful, micelles will retain the PETA network, and the final solution with the stabilized micelles will be clear upon decrease in temperature (see Figure 24).

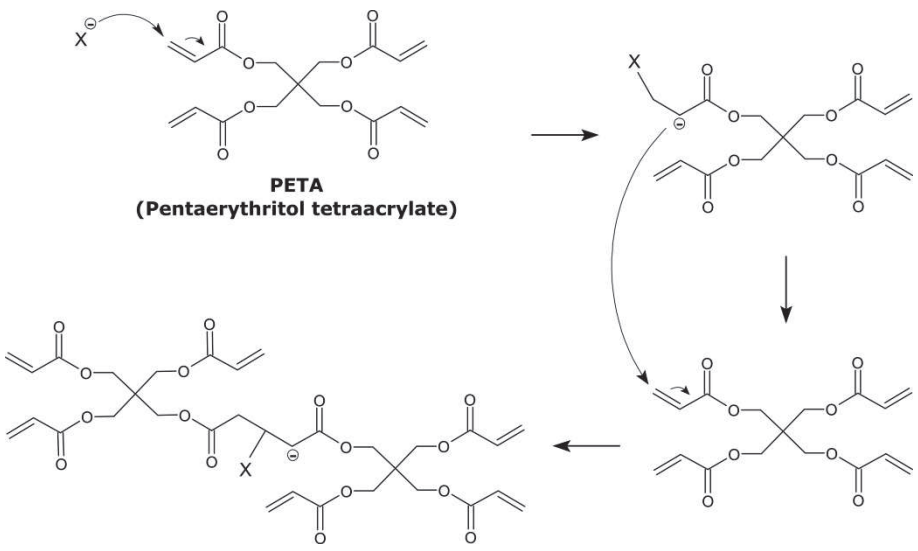

Figure 26. Polymerization reaction of pentaerythritol tetraacrylate.

The presence of the C=O double bonds from the presence of poly(PETA) was confirmed by Fourier transform infrared spectroscopy (FT-IR) after freeze-drying of the cross-linked micelles. The detected IR absorptions at 1900-1600 cm^{-1} are associated to the carbonyl groups of the PETA, and are clearly visualized by the presence of a corresponding peak in the cross-linked sample (Figure 27), which is absent in the pure polymer (F127). Moreover, we can see that the main copolymer structure was kept after micelle stabilization.

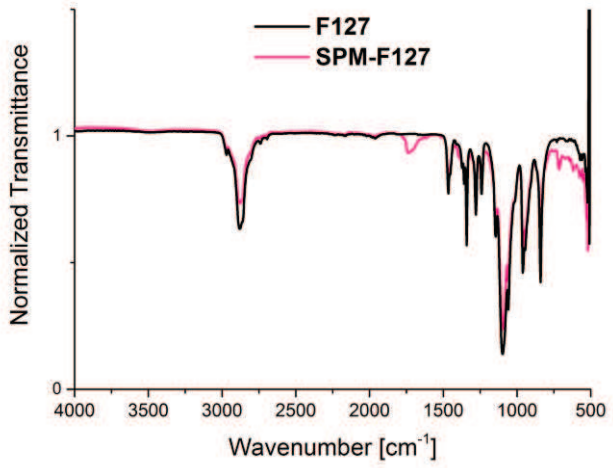

Figure 27. FT-IR spectrums of pure Pluronic F127 and respective cross-linked micelles (SPM-F127).

3.3.2 Physicochemical characterization of Pluronic nanocarriers

The characterization of the Pluronic molecular (unimers) and supramolecular (cross-linked micelles) nanocarriers employed in this thesis was performed by Dynamic Light Scattering (DLS), Cryo-Transmission Electron Microscopy (Cryo-TEM), Atomic Force Microscopy (AFM) and Scanning Electron Microscopy (SEM).

The DLS measurements were performed at different temperatures below and above the cmT (15, 25 and 37ºC) for both molecular and supramolecular nanocarriers (see Table 6).

The hydrodynamic size distribution of the pure polymer solutions (F127 and P94) follows as expected (Figure 28). At 2.5% (w/v) polymer concentration in water, both Pluronic P94 and F127 present a cmT of approximately 21ºC. Therefore, at lower temperatures (15ºC) only unimers are found, and are expected to be highly compact possibly with the PEO block forming a tight shell around the non-hydrated PPO core.[73] Due to the larger length of the PEO block, Pluronic F127 exhibits a slightly larger hydrodynamic diameter than Pluronic P94. When the temperature is larger than the cmT (25ºC), unimers start to self-assemble spontaneously into micelles. At temperatures much higher than the cmT (37ºC), only micelles are detected by DLS. These effects can be clearly observed in the size distribution plots in Figure 28A for Pluronic F127, and Figure 28B for Pluronic P94.

After incorporation of the photo-cross-linking agent in the core of the Pluronic micelles, and cross-linking by photo-polymerization, the DLS measurements reveal that the obtained supramolecular structures are monodisperse systems with well-defined populations of nanometric sizes for both polymers (Table 6 and Figure 29).

Moreover, comparatively to the pure polymer solutions, the micelles remain "intact" in solution below (15ºC) and above (25ºC) the cmT as observed in Table 6 and Figure 29, revealing the effectiveness of the cross-linking method in stabilizing Pluronic micelles against temperature effects.

Table 6. Hydrodynamic radii (R_H) and zeta potential (ζ) of Pluronic F127 and P94 pure polymer solutions, and cross-linked polymeric micelles of Pluronic F127 (SPM-127) and Pluronic P94 (SPM-P94). The parameters were analyzed at 2.5% (w/v) in water and different temperatures. The R_H and ζ of cross-linked micelles after purification by diafiltration is also shown.

	F127[a]	**SPM-F127[b]**	**P94[a]**	**SPM-P94[b]**
$R_{H,15ºC}$	2.9 ± 0.2	24.5 ± 1.3	2.1 ± 0.2	21.5 ± 0.5
$R_{H,25ºC}$	16.4 ± 0.4	23.3 ± 0.8	8.8 ± 3.5	20.5 ± 0.2
$R_{H,37ºC}$	10.4 ± 0.2	13.5 ± 0.7	6.7 ± 0.3	14.4 ± 0.4
ζ (mV)	[c]	Neutral	[c]	Neutral
$R_{H,15ºC}$[d]	-	16.2 ± 1.2	-	14.6 ± 0.5
$R_{H,25ºC}$[d]	-	18.8 ± 0.7	-	13.1 ± 0.9
$R_{H,37ºC}$[d]	-	17.9 ± 0.2	-	13.8 ± 0.9
ζ (mV)[d]	-	-13.3 ± 1.3	-	-9.9 ± 0.3

[a] Pure polymer solution.
[b] SPM - Stabilized Polymeric Micelles.
[c] Not measurable by equipment.
[d] Measured after purification by diafiltration.

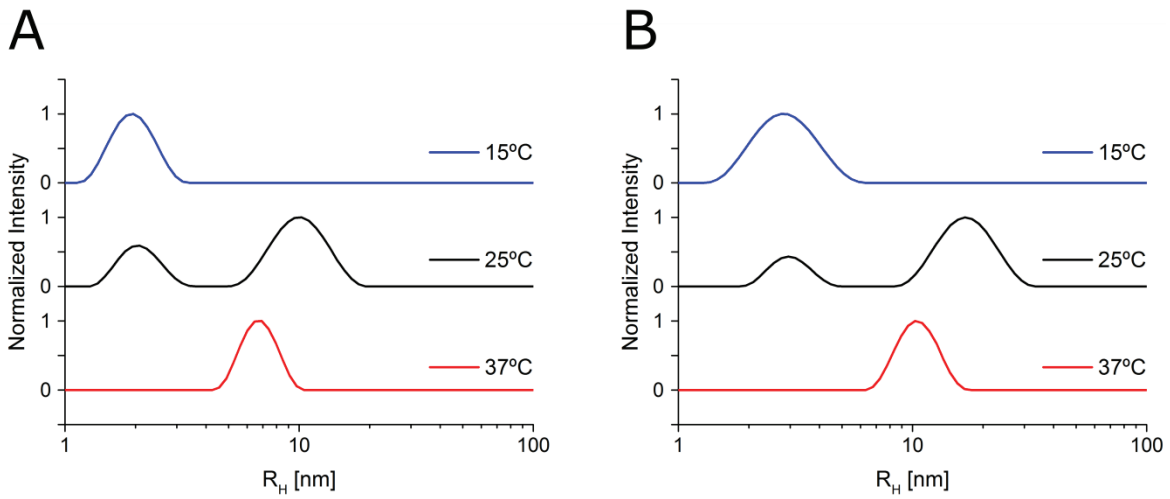

Figure 28. Intensity weighted hydrodynamic radii distribution (θ=90º) of 2.5% (w/v) pure (A) Pluronic F127 and (B) Pluronic P94 in water at increasing temperatures (15ºC, 25ºC and 37ºC).

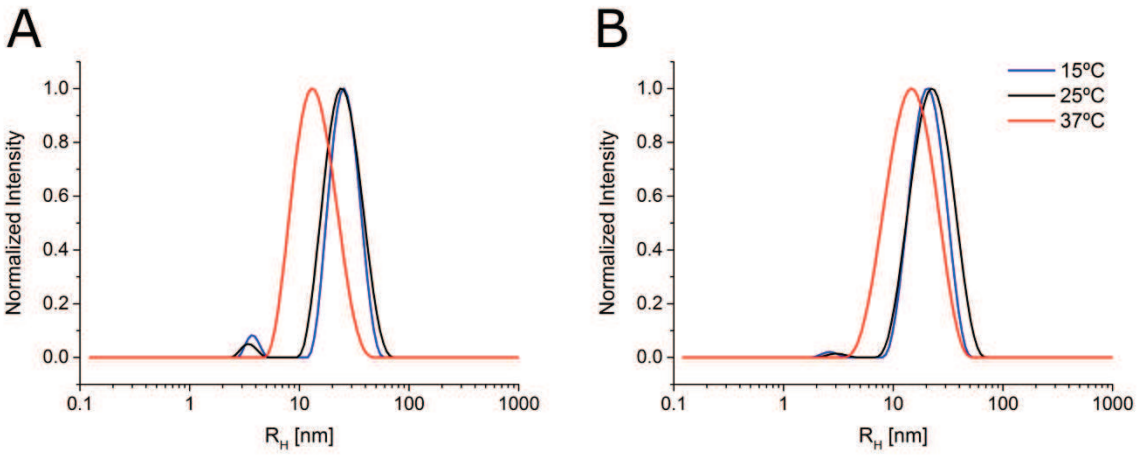

Figure 29. Intensity weighted hydrodynamic radii distribution (θ=90º) of 2.5% (w/v) stabilized polymeric micelles in water of (A) Pluronic F127 (SPM-F127) and (B) Pluronic P94 (SPM-P94) at increasing temperatures (15ºC, 25ºC and 37ºC) before purification from unimers.

The facts that the size of the cross-linked micelles decreases at 37ºC (Table 6) and the presence of a small peak of unimers below 37ºC (Figure 29) are indications that there is still a contamination with free unimers in the cross-linked micelles solution. The full characterization of the cross-linking reaction efficiency is still underway. Preliminary results can be consulted in the Appendix III. Polymer unimers that were not incorporated and cross-linked in the micelles were removed by diafiltration at low temperature using Amicon® filters with 30 kDa membrane. This centrifugation device enables the passage of components smaller than the membrane cut-off and retains larger ones according to Figure 30. Three to five washing steps were required to purify 1 mL of 2.5% of SPM-P94 and SPM-F127 respectively.

After purification, the size of the micelles does not practically change with temperature (Table 6) and the small peak of unimers is not detected at any of the analyzed temperatures (Figure 31).

The purified SPM-F127 and SPM-P94 present hydrodynamic diameters of ~36 and ~28 nm respectively at 37ºC, while non-stabilized micelles of Pluronic and F127 and P94 present smaller diameters of ~21 and ~13 nm. Two factors are responsible for the increased size of the nanoparticles cross-linked at 60°C compared to the size measured at 37°C for the micelles.

First the micellar size at 60°C will be larger since the aggregation number of Pluronic micelles is known to increase with temperature. Second the micelle core is swollen by the presence of PETA. Therefore, the crosslinking at 60ºC stabilizes larger micelles than those observed at 37°C.

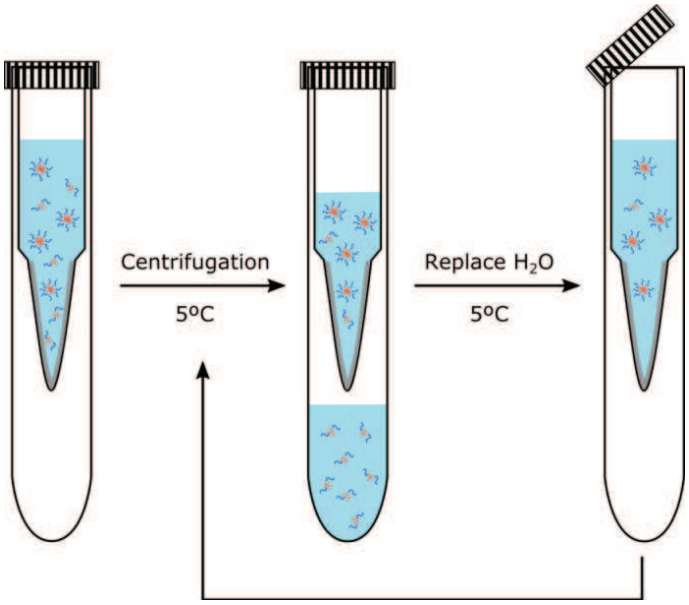

Figure 30. Purification process of cross-linked micelles from free unimers using Amicon® Ultra centrifugal filters. Regenerated cellulose membrane (Ultracel®) presented in light grey with a molecular weight cut-off of 30 kDa.

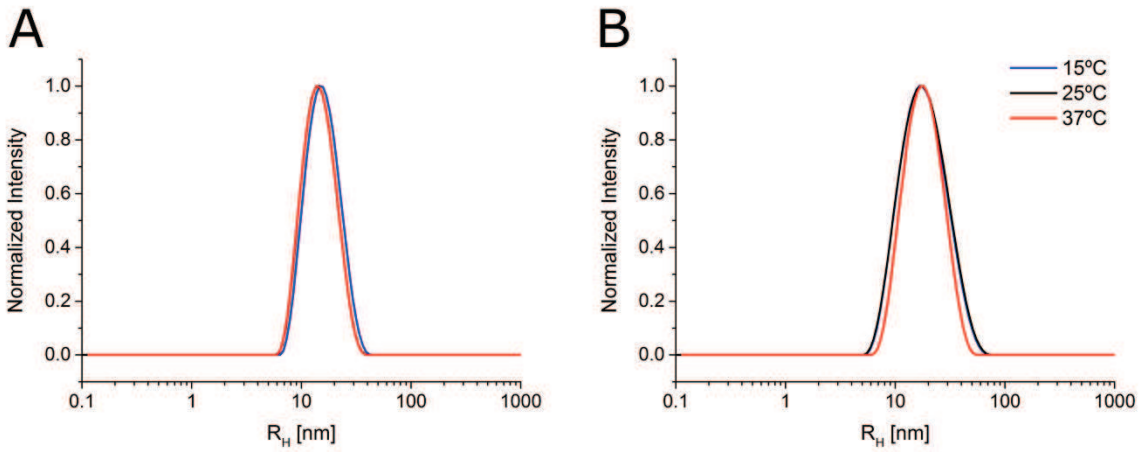

Figure 31. Intensity weighted hydrodynamic radii distribution (θ=90º) of 2.5% (w/v) stabilized polymeric micelles in water of (A) Pluronic F127 (SPM-F127) and (B) Pluronic P94 (SPM-P94) at increasing temperatures (15ºC, 25ºC and 37ºC) after purification by diafiltration.

Cryo-TEM analysis of the cross-linked micelles revealed a homogenous dispersion of spherical objects (Figure 32). The diameters of the objects (≈ 11-17 nm) differ from the light scattering measurements. This is most likely related to the fact that Pluronic micellar systems have low contrast to the electron beam which makes visualization of the micelles very difficult.[213-216] The dark dots observed in Figure 32 are most probably the hydrophobic micellar cores containing PETA, while the PEO chains (corona) are not visible due to the low inherent contrast between the PEO polymer chains and water. In fact, the diameters of the micelles core determined from the images (using imageJ software) are approximately 11-15 nm for SPM-F127, and slightly larger for SPM-P94 (13-17 nm). Previous studies using cryo-TEM have determined an approximate diameter of 5-7 nm for the PPO core of pure F127 micelles.[214] This increase of the PPO core size is consistent with the incorporation of the hydrophobic PETA in the core and the larger aggregation number of micelles at 60ºC.

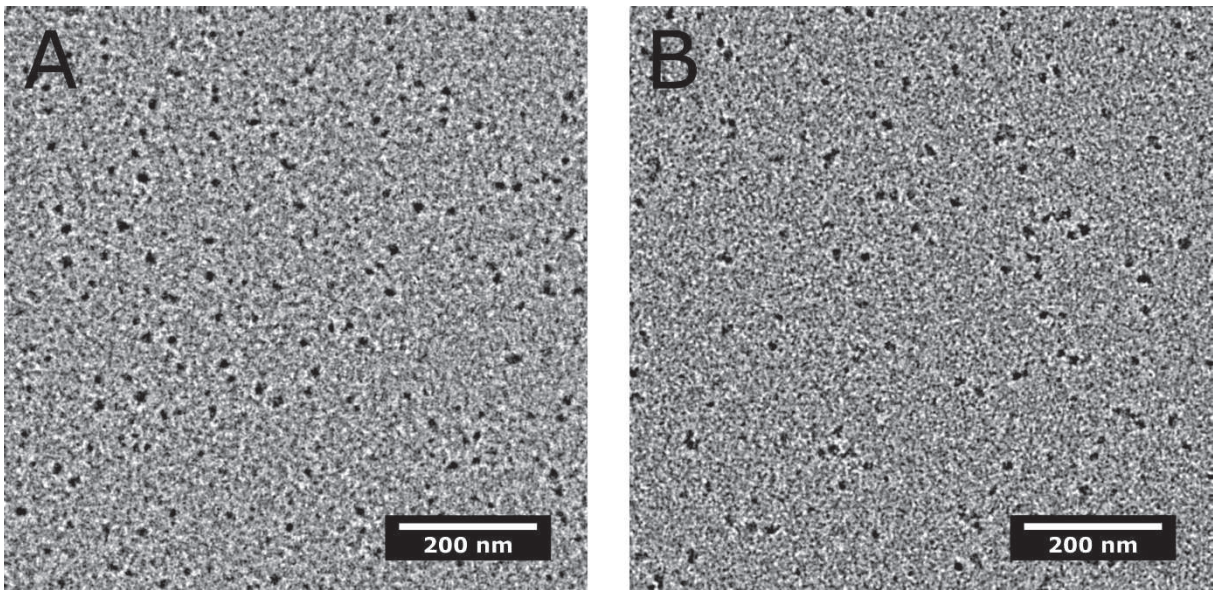

Figure 32. Cryo-TEM microphotographs of 2.5% cross-linked polymeric micelles of (A) Pluronic F127 (SPM-F127) and (B) Pluronic P94 (SPM-P94).

While Cryo-TEM revealed to be a crucial technique to analyze the core of the cross-linked micelles because of the low electron density of the PEO block and higher density of the cross-linked core, it does not allow visualization of the whole structures. SEM enables visualization of the surface topography since

the electrons from the beam interact with the atoms in the sample and, even if the sample has a very low electron density, this technique enables visualization of the whole structures. We determined by SEM that SPM-F127 (Figure 33) and SPM-P94 (Figure 34) present a spherical structure and have average diameters of 29.2±4.7 nm and 24.4±4.3 nm respectively (determined using ImageJ). These values are more consistent with the light scattering measurement than the ones calculated with Cryo-TEM. Using SEM we were also able to image the F127 unimers even though their size is very small (< 6 nm) (Figure 33), while the P94 unimers were not possible to distinguish (Figure 34). We can also verify that the F127 unimers are not present in the sample of cross-linked micelles (Figure 33), which also confirms that the purification process by diafiltration to remove free unimers was successful.

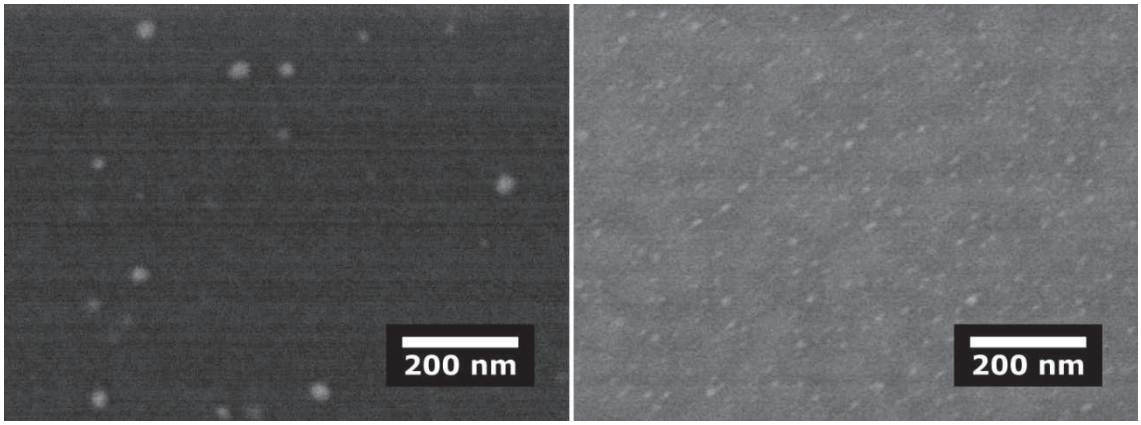

Figure 33. SEM of (left) cross-linked polymeric micelles of Pluronic F127 after diafiltration, and (right) Pluronic F127 unimers.

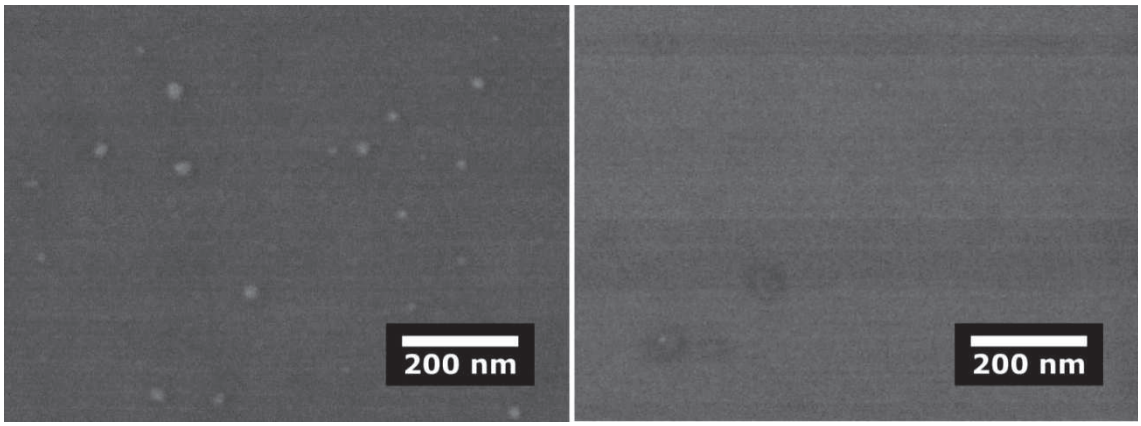

Figure 34. SEM of (left) cross-linked polymeric micelles of Pluronic P94 after diafiltration, and (right) Pluronic P94 unimers.

Lastly, the purified samples were analyzed by Atomic Force Microscopy (Figure 35). AFM images of stabilized polymeric micelles were acquired with samples prepared below the cmc and reveal spherical nanostructures with high homogeneity.

Based on the cryo-TEM and AFM analysis, it also appears that the Pluronic F127 cross-linked micelles are more spherically homogeneous than the ones obtained with the Pluronic P94. This can be related to the aggregation of the different copolymers when forming spherical micelles. The unimers aggregation depends on their molecular weight and hydrophilic/hydrophobic ratio, in particular the shorter PEO block length of Pluronic P94 unimers might hinder the formation of perfect spherical structures and therefore results in less organized structures.

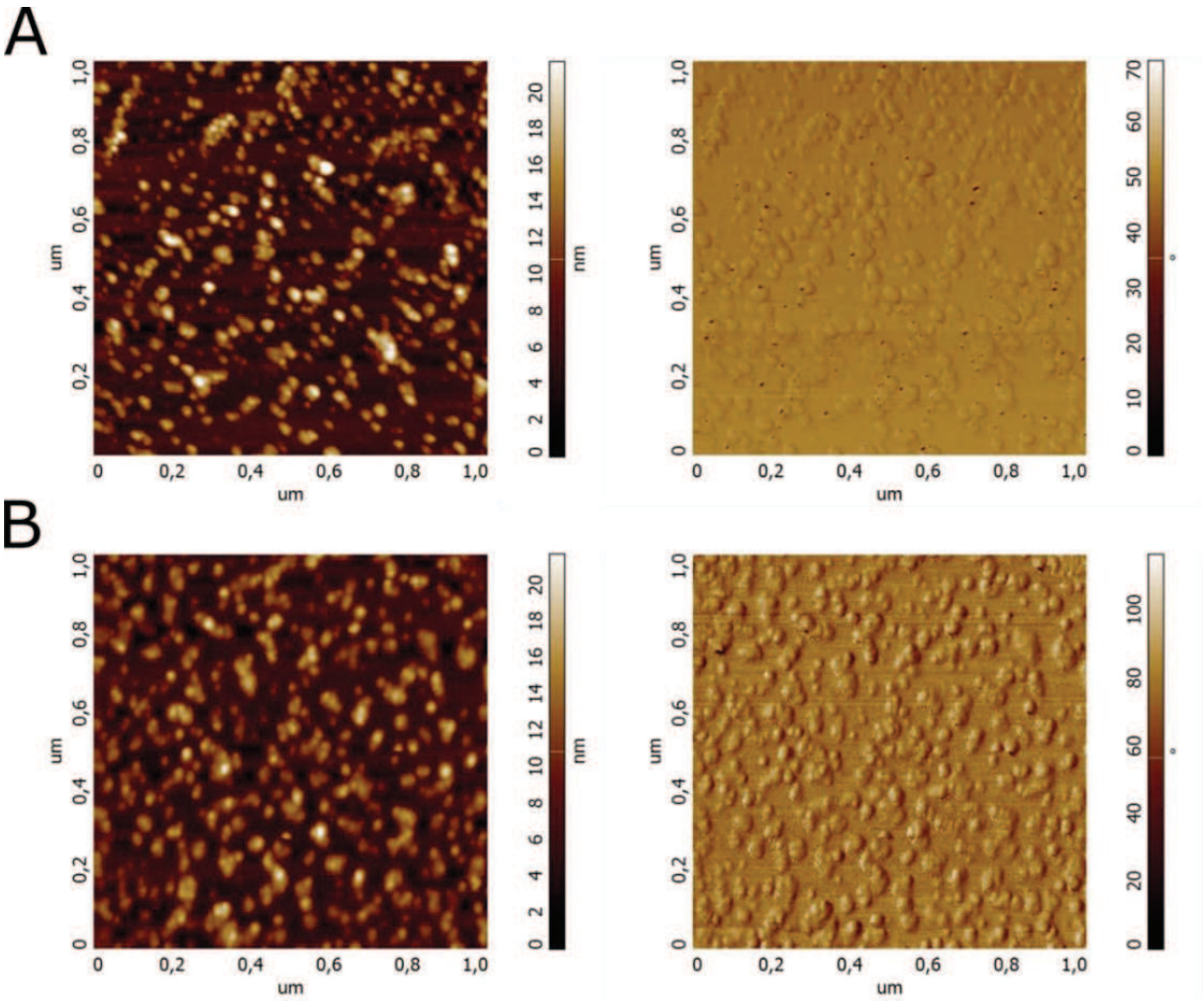

Figure 35. AFM of cross-linked polymeric micelles of (A) Pluronic P94 and (B) Pluronic F127 after diafiltration.

3.3.3 Stability of Pluronic cross-linked micelles

Below cmc

The stability of cross-linked micelles below the cmc was analyzed and compared with the pure polymer solutions. Samples were diluted in water at room temperature and immediately analyzed by DLS at 25ºC (Figure 36). The cmc at 25ºC for both pure polymers solutions is approximately 0.7% (w/v). Immediately after 1:2 dilution of the polymer solutions (Pluronic P94 and F127), a final concentration of 1.25% (w/v) was reached and the major contribution of the scattered intensity corresponds already to the unimers peak (R_H ≈ 2 nm). The second peak corresponding to the micelles was not present at dilution factors higher than 2. On the contrary to the unimers, the cross-linked micelles remained stable at all tested dilutions, with only a small decrease of the hydrodynamic radii, which is likely due to virial effects (Figure 36).

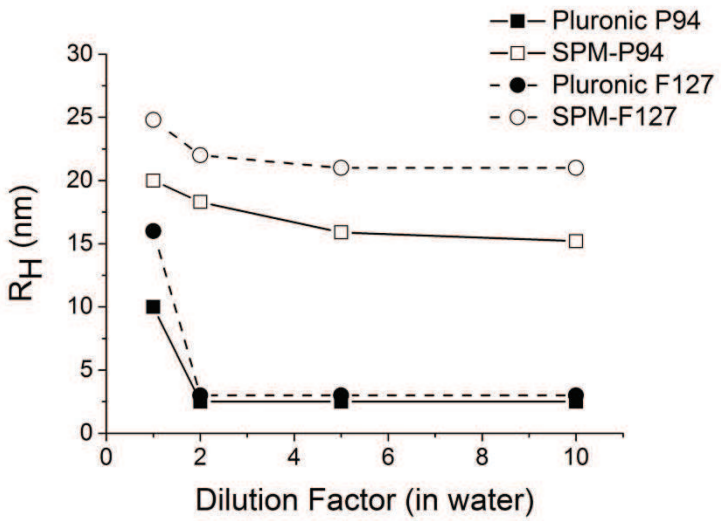

Figure 36. Hydrodynamic radii of non-cross-linked Pluronic P94 and F127, and cross-linked micelles of Pluronic P94 (SPM-P94) and Pluronic F127 (SPM-F127) at 25ºC after dilution in water.

Micellar stability in the presence of serum proteins

In addition to dilution and temperature variations, nanocarriers are exposed to the complex composition of the blood after intravenous administration. The expected *in vivo* performance of the nanocarriers will be affected by the

interactions with the blood components before reaching their target. It is well-known that the presence of the PEO chain acts as a steric barrier that avoids the adhesion of specific proteins to the micelles surface (opsonization)[6, 94, 217] and provides colloidal stability to the system. Hence, the integrity of the PEO corona after cross-linking is critical for the biological use of the carriers.

The influence of serum proteins on the micelles stability was investigated in the presence of cell culture medium (DMEM) supplemented with 10% Newborn Calf Serum. The samples were analyzed continuously by light scattering and the hydrodynamic radii of the micelles (Figure 37) and total scattered intensity (Figure 38) in the cell medium was obtained every 2 minutes.

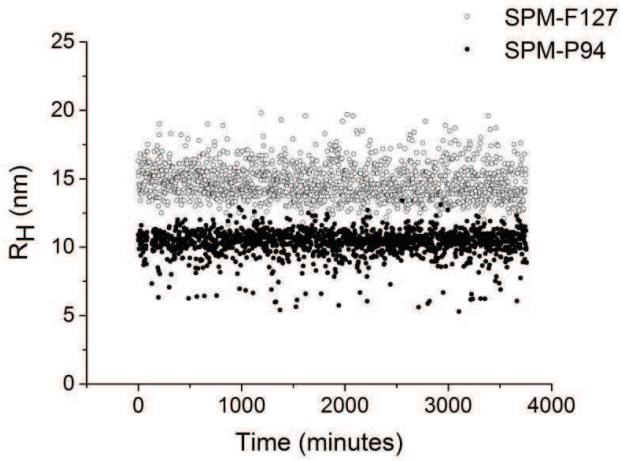

Figure 37. Apparent hydrodynamic radius of stabilized cross-linked Pluronic micelles in complete culture medium as a function of time. Samples incubated at 37ºC at a concentration of 0.5% (w/v).

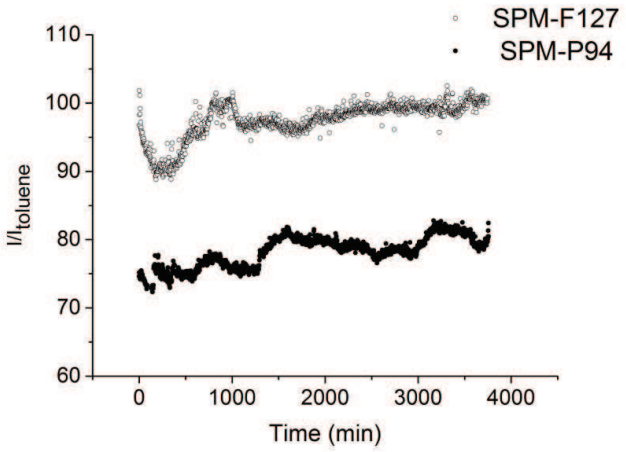

Figure 38. Evolution of the total scattered intensity of cross-linked Pluronic micelles in complete culture medium as a function of time. Samples incubated at 37ºC at a concentration of 0.5% (w/v).

No significant change in the micelles radii (Figure 37) was observed, which indicates that no adsorption of serum proteins on the micelles corona occurred. Moreover, no significant variations of the total scattered intensity (Figure 38) were observed revealing that the number of cross-linked micelles remained stable during the assay without the formation of aggregates. This stability effect is consistent with the importance of the PEO chain to maintain the steric hindrance and reduce the formation of aggregates with serum proteins.

Upon freeze-drying and dispersion in water and organic solvents

Cross-linked micelles were freeze-dried and a very fine white powder was obtained for both SPM-F127 and SPM-P94. Then, the obtained powders were dispersed in aqueous and organic solvents (water, acetone, tetrahydrofuran and chloroform), and the hydrodynamic size distribution was determined by DLS. This allowed the assessment of the stability of cross-linked micelles in different solvents, which is particularly interesting as it opens new possibilities for their post-modification via chemical reactions. Moreover, this test is determinant in evaluating the effectiveness of the cross-linking method as the cross-linking agent is soluble in most of these solvents. An immediate dissolution of the powders was observed in all the tested solvents without the requirement of stirring. Moreover, after analysis by DLS, we observed that micelles remained intact in all the tested solvents.

3.3.4 Loading of cross-linked micelles with a hydrophobic dye

Several studies have been conducted to develop more efficient delivery systems, especially for the delivery of poorly water soluble anticancer drugs. On designing these systems, the nanocarriers should be capable of incorporating hydrophobic molecules and, at the same time, possess characteristics that favor the delivery of the drug to the cancer site.

The ability of the cross-linked micelles to incorporate a hydrophobic molecule in their core and transport it across the cellular membrane was assessed by loading the stabilized micelles with a small photo-stable lipophilic dye (Nile Red, M_w=318.37g/mol). Nile Red dissolved in ethanol was added to the aqueous solutions containing 2.5% of stabilized Pluronic micelles

(0.25% w/w Nile Red/Pluronic ratio). The obtained mixture was stirred at 300 rpm at room temperature for 24 hours. After the incubation period, the solution was filtered (0.45µm) to remove precipitated Nile Red (amount that was not incorporated by the micelles and precipitated in the water phase).

Nile red is poorly soluble in water (0.2 mg/mL) but in order to avoid any unspecific *in vitro* labelling, a solution of fluorescently loaded micelles without Nile Red solubilized in the water was obtained after purification. For this, samples containing the stabilized Pluronic micelles were eluted using a chromatographic PD10 column to identify the fractions where micelles were eluted. The fractions were analyzed by Light Scattering to determine the scattered intensity and correlate with the concentration of micelles in each fraction. Moreover, a small amount of Nile Red in ethanol was eluted to identify in which fractions the Nile Red soluble in the water phase was eluted (Figure 39).

After this study, purified fluorescently loaded stabilized Pluronic micelles were obtained after eluting a sample volume of 2 mL, and collecting the volumes between 3.5 and 5.5mL (which showed to contain the stabilized micelles and no free dye). This solution was further analyzed by light scattering to verify the influence of the fluorescent dye on the hydrodynamic diameter of the micelles. The determined hydrodynamic radii were 20.3±0.5 and 21.2±0.7 for SPM-P94 and SPM-F127 at 25ºC respectively.

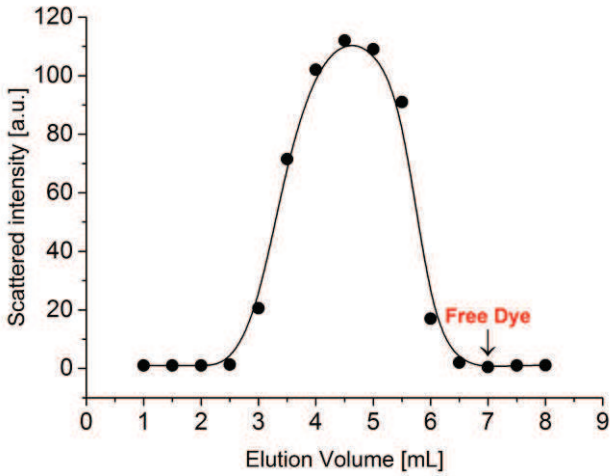

Figure 39. Elution profile of SPM-P94 in chromatographic PD10 columns. The elution region of free dye (Nile Red) is depicted by the arrow.

3.3.5 Functionalization of nanocarriers with FITC and p-SCN-Bn-DTPA

After the development and physicochemical characterization of molecular and supramolecular nanocarriers based on Pluronic copolymers, the carriers were modified with appropriate fluorescent and metallic chelator moieties to allow their further biological evaluation.

The molecular carriers (F127 and P94 unimers) were first modified with primary amines after CDI-activation according to Figure 40. This was performed by the University of Ghent in the framework of the "TRACE'nTREAT" project.

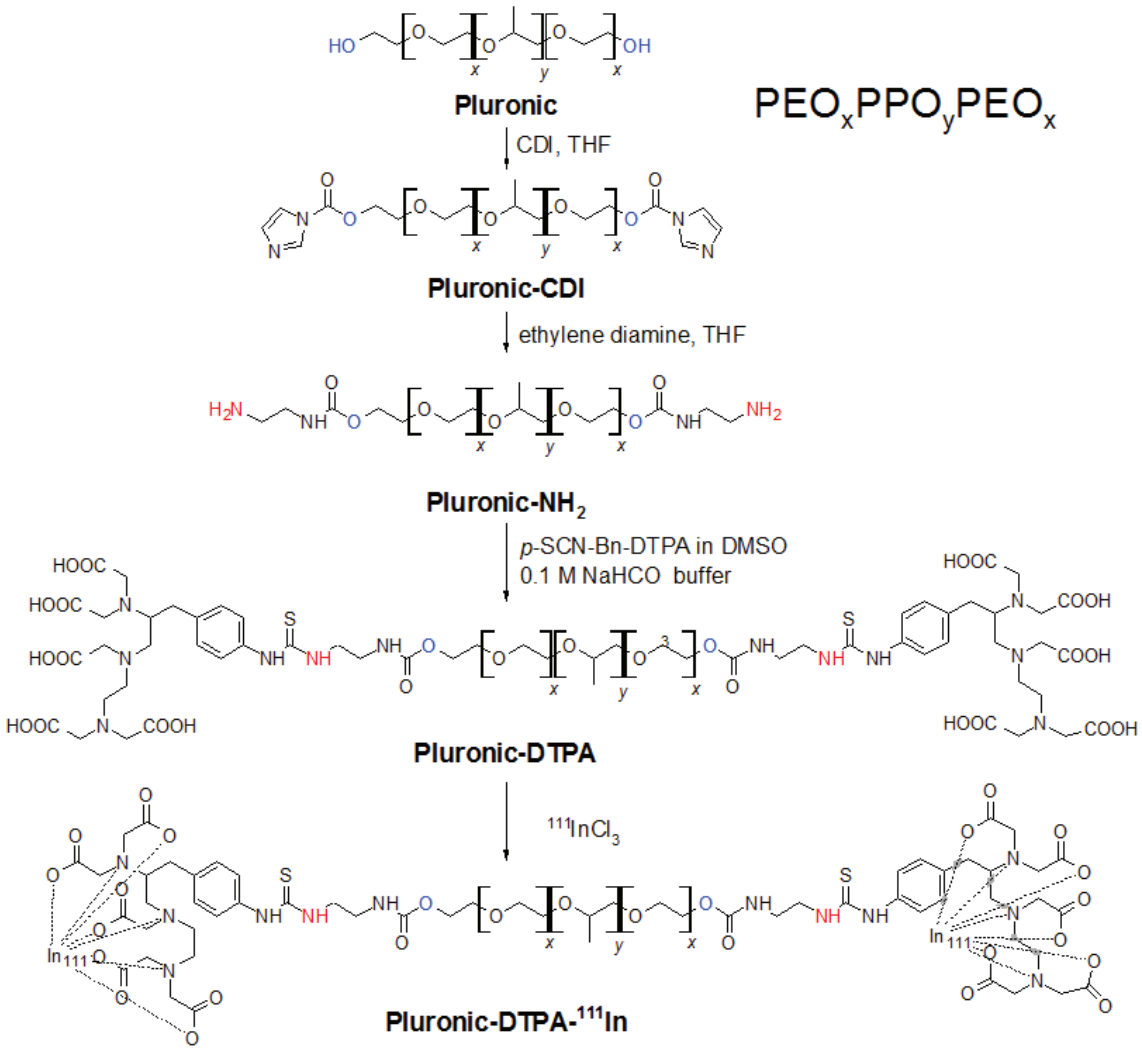

Figure 40. Synthesis of DTPA-modified Pluronic unimers and radiolabeling with ^{111}Indium.

The presence of primary amines in the Pluronic hydroxyl terminal groups was determined by FT-IR (Figure 41) and by measuring the solution pH (Table 7). Primary amines (C-NH_2 bonds) are responsible for a characteristic absorbance at 1650-1580 cm^{-1} that corresponds to the sharp peak in Figure 41. The protonation of the amines will lead to an increased pH of the solutions. On the one hand, we can observe in Table 7 that samples not modified with primary amines present pH's of ~6.5 or ~5.8 for Pluronic F127 and P94 respectively. On the other hand, samples containing the amine groups have pH > 8 due to the amines protonation in water ($RNH_2 + H_20 \rightarrow RNH_3^+ + OH^-$). The decreased pH observed once the Pluronic micelles were cross-linked with the amine groups on their corona (Table 7) might be related to a reduced solvation of the micelles corona in comparison to the free unimers. This basicity is important for amines solubility, stability and further binding to moieties.

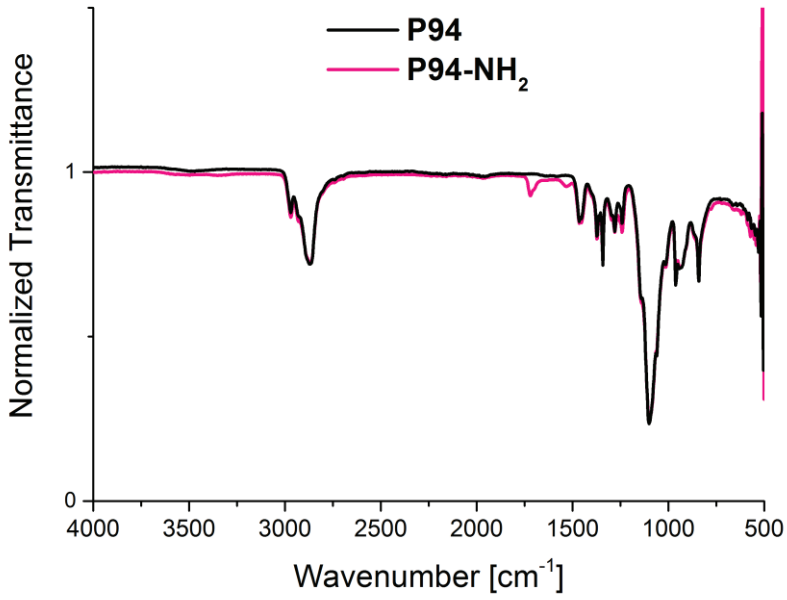

Figure 41. FT-IR spectrums of (black) pristine and (pink) primary-amine modified Pluronic P94.

Table 7. pH of aqueous solution made from unmodified copolymers or cross-linked polymeric micelles (SPM), and from their amine-modified analogs.

	pH
F127	6.6
SPM-F127	6.4
F127 + F127-NH_2[a]	8.2
F127-NH_2[b]	9.7
SPM-F127-NH_2[a]	6.4
P94	5.8
SPM-P94	5.7
P94 + P94-NH_2[c]	8.9
P94-NH_2[d]	9.5
SPM-P94-NH_2[c]	6.3

[a] Obtained from a mixture of Pluronic F127 with 10% F127-NH_2
[b] 0.25% of pure Pluronic F127-NH_2
[c] Obtained from a mixture of Pluronic P94 with 3.65% P94-NH_2
[d] 0.09% of pure Pluronic P94-NH_2

The fluorescent probe (FITC) and the chelator (p-SCN-Bn-DTPA) (Figure 42) were then conjugated to the molecular and supramolecular nanocarriers by reaction of the primary amine with the reactive isothiocyanate groups to form a stable thiourea bond. The detailed reaction of the Pluronic-NH_2 with the p-SCN-Bn-DTPA is depicted in Figure 40.

The unimers (F127 and P94) were functionalized directly with FITC and DTPA, while cross-linked micelles were functionalized with DTPA and FITC either before or after micelle stabilization respectively, according to Figure 43.

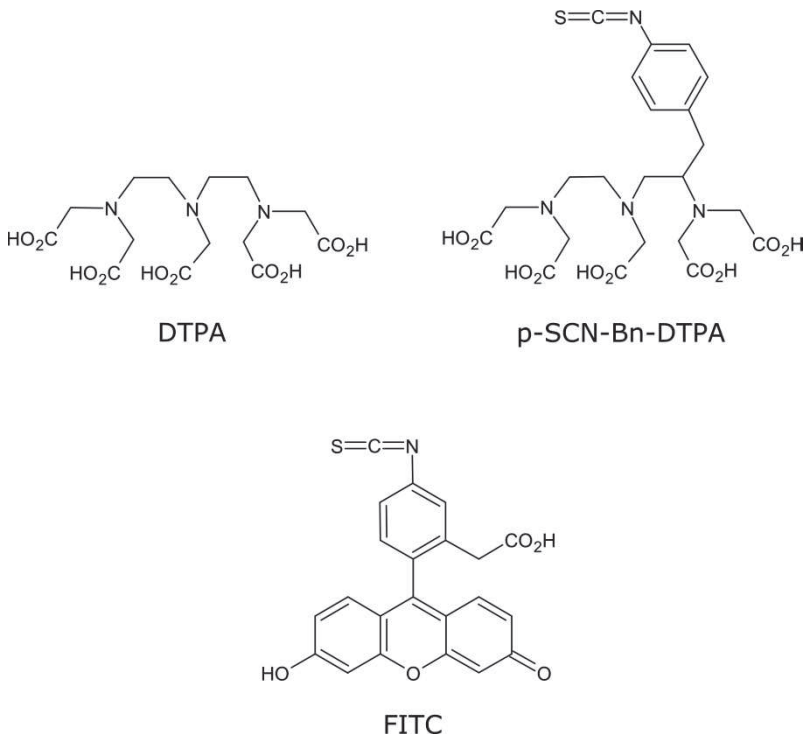

Figure 42. Structures of DTPA and reactive p-SCN-Bn-DTPA and FITC with the isothyocianate groups.

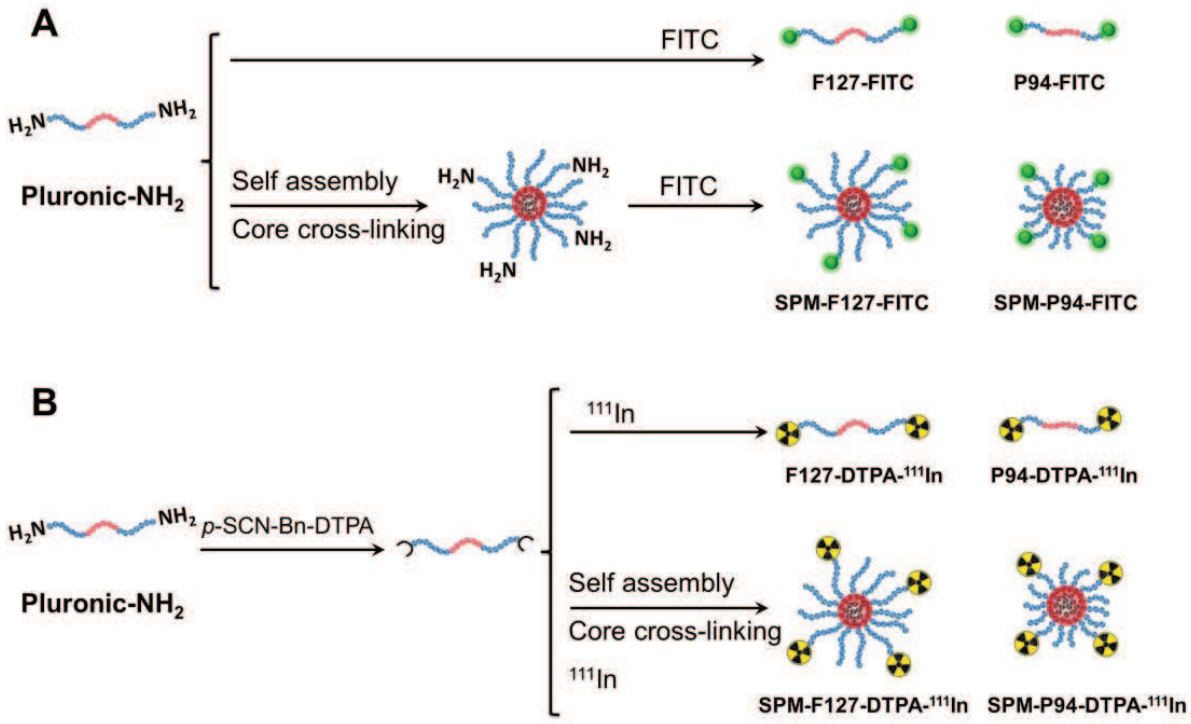

Figure 43. Synthetic routes developed for the functionalization of molecular and supramolecular nanocarriers with (A) the fluorescent probe FITC, and (B) the chelator DTPA for further complexation with the radioisotope ^{111}In.

Table 8 summarizes the characteristics of the employed Pluronics and the corresponding functionalization degrees.

Table 8. Characteristics of the selected PEO-PPO-PEO copolymers and functionalization degrees of modified copolymers.

	Pluronic F127	**Pluronic P94**
Chemical Formula[a]	$PEO_{96}PPO_{56}PEO_{96}$	$PEO_{26}PPO_{48}PEO_{26}$
Mn (Da)[a]	11700	5000
Mn PEO blocks (Da)[a]	8500	2200
Mn PPO block (Da)[a]	3200	2800
CDI activation efficiency[b]	86%	67%
NH_2 modification efficiency[b]	91%	82%
p-SCN-Bn-DTPA conjugation efficiency[c]	82%	81%

[a] Determined by ^{1}H-NMR
[b] Determined by ^{1}H-NMR (University of Ghent)
[c] Determined by TLC and gamma-counter

3.3.6 Radiolabeling of Pluronic nanocarriers with ^{111}Indium

After attachment of the metallic chelator DTPA (see section 3.3.5), the nanocarriers can then be labelled with different radioisotopes (^{44}Sc, ^{90}Y, ^{89}Zr, ^{177}Lu, ^{68}Ga and ^{111}In)[68] via complexation. The selection of the isotope depends on the half-life time ($t_{1/2}$), the emitted radiation, and whether therapeutic and/or diagnostic properties are required.

We have selected ^{111}In because of its prolonged $t_{1/2}$ of 2.83 days (67.9 h), and the fact that it can be simultaneously used for imaging and therapy due to emission of two gamma photons and Auger electrons.

3.3.6.1 Chelation speed of DTPA-^{111}In

We first started by assessing the chelation speed between DTPA and ^{111}In in PBS buffer. For this, the radioactive $InCl_3$ obtained commercially was added to a solution of DTPA in PBS at room temperature and, at different time points, 5 µL of the sample were collected and spotted in a thin layer chromatographic plate. The plates were then eluted in an appropriate eluent (sodium acetate buffer, see Table 9) that enables separation of free ^{111}In and DTPA-^{111}In (Figure 44). After elution, the plates were imaged with a storage phosphor screen and then appropriately sectioned for gamma-scintillation counting.

We can see that the complexation is very fast: almost immediately (after 3 minutes) all the ^{111}In was complexed to the DTPA and no alteration on the stability is detected for the next 40 minutes.

Table 9. Retention factors (R_f) of ^{111}In radiolabeled samples in different eluents. R_f are determined by measuring the distance traveled by the sample divided by the distance traveled by the eluent.

	Eluent	
Compound	**NaOAc 0.1 M, pH 5.8**	**EDTA:NH_4Ac 1:1, 0.1 M, pH 5.5**
$^{111}InCl_3$	0	1
DTPA-^{111}In	1	1
SCN-Bn-DTPA-^{111}In	0.5-1	0.5-1
Proteins-^{111}In	-	0.5
Nanocarrier-^{111}In	0	0

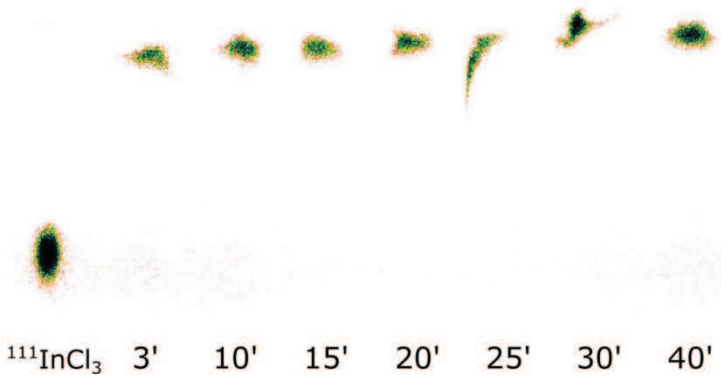

Figure 44. Radio-TLC of $^{111}InCl_3$ and DTPA-^{111}In in sodium acetate buffer after incubation for different times (3 to 40 minutes).

3.3.6.2 Conjugation efficiency of p-SCN-Bn-DTPA to Pluronic unimers

The next step was to assess the modification efficiency of the reaction between the amine-modified Pluronic unimers with the chelator p-SCN-Bn-DTPA. For this, we incubated unpurified samples (F127-DTPA and P94-DTPA) in PBS with $^{111}InCl_3$ for 30 minutes at room temperature.

The modification efficiency was analyzed by TLC using an adequate eluent. We require an eluent that separates between ^{111}In attached to the nanocarriers and attached to the contaminants. In this case, the contaminants will be unreacted p-SCN-Bn-DTPA-^{111}In, unfunctionalized DTPA (DTPA-^{111}In) that is present in the commercial sample of p-SCN-Bn-DTPA, and free ^{111}In. The appropriate eluent is the EDTA:NH_4Ac system (Table 9). The nanocarriers will not travel by capillarity through the plate due to the small pore size of the Silica gel (particles of 40-63 μm and pore size < 6 nm) and will therefore have a R_f=0. The p-SCN-Bn-DTPA-^{111}In and DTPA-^{111}In will be eluted by polarity, and the free ^{111}In will be chelated by the EDTA present in the eluent (log K(EDTA-^{111}In)≈25[68]) and will also travel by polarity. The contaminants will therefore present Retention factors (R_f's) in the range 0.5-1 (Table 9).

After elution, the plates were imaged and sectioned for gamma-scintillation counting. The conjugation efficiencies of the p-SCN-Bn-DTPA to P94-NH_2 and F127-NH_2 were calculated based upon the relative amount of ^{111}In attached to F127-DTPA or P94-DTPA and the amount of ^{111}In bound to the contaminants, and are presented in Table 8.

In Figure 45D, an example of the TLC profile of the unpurified Pluronic F127-DTPA-^{111}In can be seen. Similar profiles were obtained for Pluronic P94-DTPA-^{111}In. Since the conjugation efficiency of the bifunctional chelator p-SCN-Bn-DTPA to the Pluronic unimers was ≈80%, the samples (F127-DTPA, SPM-F127-DTPA, P94-DTPA and SPM-F127-DTPA) were purified from free chelator by SEC using PD10 columns prior to the radiolabeling.

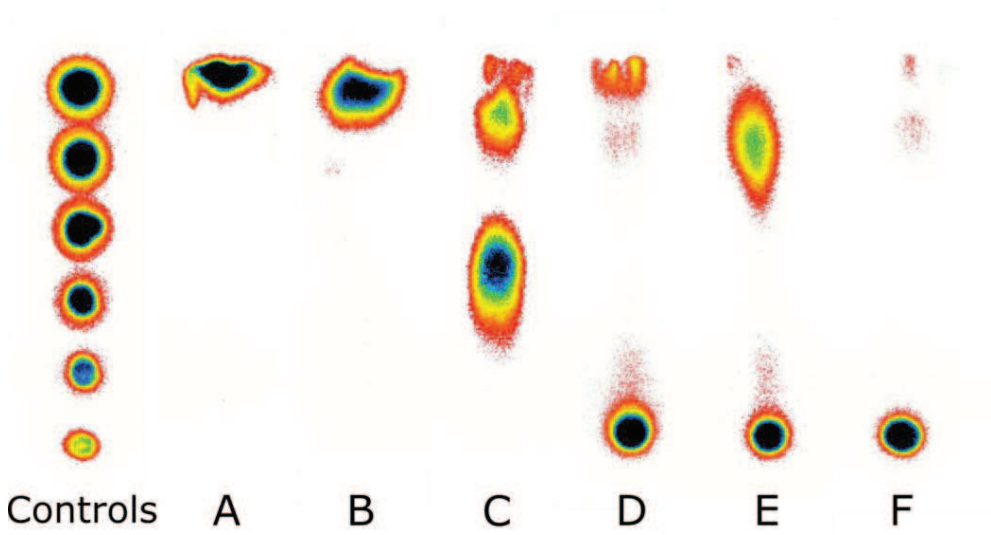

Figure 45. Example of radio-TLC in ammonium acetate. Imaging controls were prepared by adding increasing amounts of activity in 10 µL (0.5, 1, 2, 3, 4 and 5 kBq), (A) $^{111}InCl_3$, (B) DTPA-^{111}In, (C) p-SCN-Bn-DTPA-^{111}In, (D) F127-DTPA-^{111}In before purification, (E) SPM-F127-DTPA-^{111}In before purification, (F) SPM-F127-DTPA-^{111}In after purification.

3.3.6.3 Radiolabeling efficiency of Pluronic nanocarriers

Radiolabeling of the nanocarriers was performed under standard labelling conditions for DTPA and ^{111}In (PBS and room temperature). The radiolabeling efficiencies were analyzed by TLC coupled to gamma-scintillation, and by SEC.

The radiolabeling efficiencies determined by TLC are presented in Table 10. The purified DTPA modified copolymers (P94-DTPA and F127-DTPA) presented high labelling efficiencies (>95%), while radiolabeling of cross-linked micelles (SPM-F127-DTPA and SPM-P94-DTPA) was less efficient (~50%). In the latter, we can observe in Figure 45E that the contamination corresponds mostly to free DTPA.

The SEC was performed in 1cm×30cm columns filled with Sephadex G25 and using PBS as eluent. The elution profiles of 1 mL of the molecular and supramolecular nanocarriers, represented by F127-DTPA-^{111}In and SPM-F127-DTPA-^{111}In respectively, can be seen in Figure 46A. Appropriate controls were also used with the SEC to verify the suitability of the characterization method (Figure 46B). We can see that the contaminant DTPA-^{111}In and the major part of free ^{111}In are eluted after 16 mL.

However, a considerable amount of free ^{111}In (~15%) is also eluted earlier (between 9 and 13 mL). These larger compounds are insoluble aggregates formed by ^{111}In in PBS and are eluted in the same region of the radiolabeled nanocarriers (9 to 13 mL). Therefore, special care needs to be taken when purifying radiolabeled nanocarriers as free ^{111}In aggregates can be collected in combination with the carriers.

After assessing the radiolabeling efficiency of the different nanocarriers using TLC and SEC, we verified that the molecular carriers (P94-DTPA and F127-DTPA) could be used without further purification, while the supramolecular carriers (SPM-F127-DTPA and SPM-P94-DTPA) required a final purification step.

Table 10. Radiolabeling efficiencies of DTPA-modified Pluronic nanocarriers.

	^{111}In labelling efficiency[(a)]	**^{111}In labelling efficiency[(a)] after purification**
F127-DTPA-^{111}In	95%	[(b)]
SPM-F127-DTPA-^{111}In	45%	99%[(c)]
P94-DTPA-^{111}In	99%	[(b)]
SPM-P94-DTPA-^{111}In	53%	97%[(c)]

[(a)] Determined by TLC and gamma-counter
[(b)] No purification needed
[(c)] Purification with PD10 column

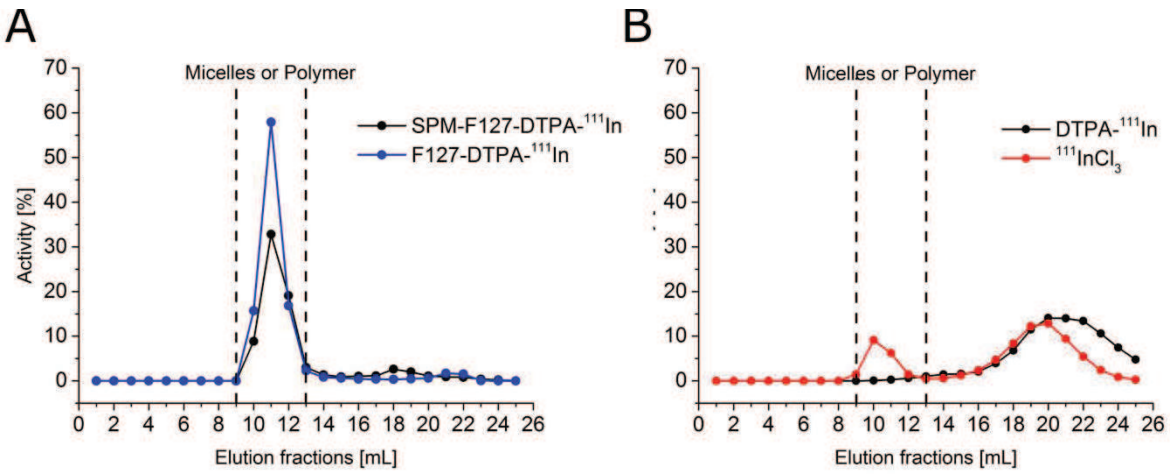

Figure 46. Elution profiles in G25 columns (30cm×1cm) of (A) radiolabeled molecular (SPM-F127-DTPA-^{111}In) and supramolecular (F127-DTPA-^{111}In) nanocarriers, and (B) the controls (DTPA-^{111}In and $^{111}InCl_3$).

3.3.6.4 Purification of radiolabeled cross-linked Pluronic micelles

Purification of the supramolecular carriers was performed by SEC using smaller SEC columns (PD10) to enable a faster purification and avoid sample dilution for their direct *in vitro* and *in vivo* use. The elution profiles of 700µL of the cross-linked micelles (SPM-F127-DTPA-^{111}In) is presented in Figure 47A. We can observe the elution of two components: 1 mL of cross-linked micelles (from 3-4 mL), and contaminants (after 6 mL).

The suitability of smaller PD10 columns to purify the samples was also analyzed by eluting DTPA-^{111}In and $^{111}InCl_3$ using PBS as eluent (Figure 47B). We can see that we have the same problem of contamination with ^{111}In aggregates that are eluted in the same fractions as the micelles. Therefore, to enable purification, free DTPA is added to the radiolabeled samples to chelate the ^{111}In aggregates and to enable the longer retention of DTPA-^{111}In in the column.

The purification efficiency of the eluted fractions was also confirmed by TLC using the EDTA:NH_4Ac (1:1) (v:v) (0.1 M, pH 5.5) eluent (Figure 45F). We verified that this process enables the purification of radiolabeled nanocarriers using PD10 columns and PBS as the eluent. The radiolabeling efficiencies were nearly 100% (Table 10), which are suitable to perform further studies.

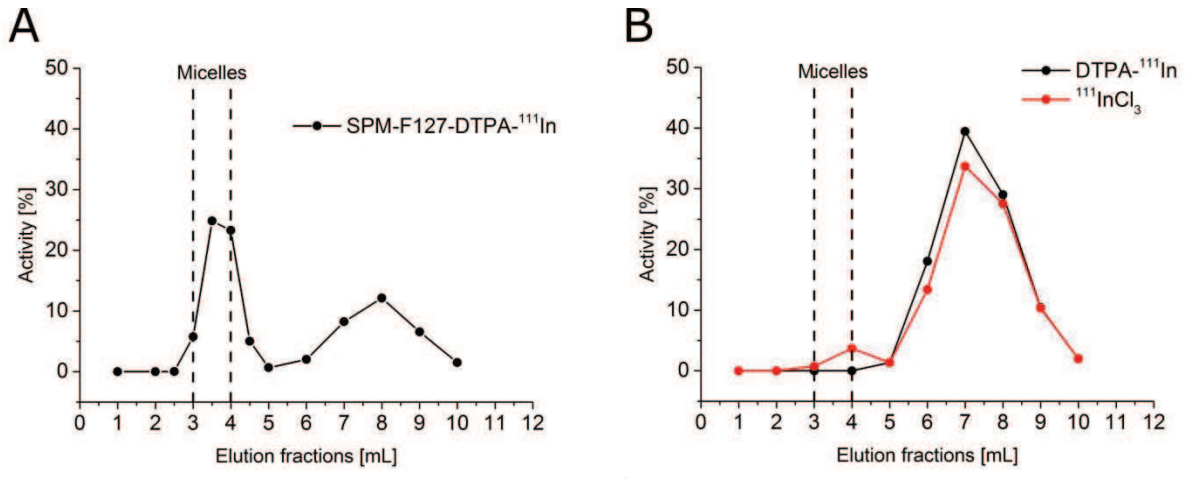

Figure 47. Elution profiles in PD10 columns of (A) radiolabeled supramolecular nanocarriers (SPM-F127-DTPA-^{111}In), and (B) the controls (DTPA-^{111}In and $^{111}InCl_3$) using PBS as the eluent.

3.3.7 Radiostability in mouse serum and buffer

Finally, the stability of the DTPA-^{111}In complex in all the nanocarriers was evaluated at 37ºC in both mouse serum (Figure 48A) and PBS (Figure 48B). The comparison between the two solvents allows to assess the role of chelating proteins present in the serum (e.g. transferrin) on the complex stability. The latter was quantified by using TLC and gamma-scintillation counting up to 72h.

For all nanocarriers, loss of ^{111}In occurred in two steps in both media, with a rapid drop in the first few hours followed by a gradual decrease. After 72h, the loss of ^{111}In remained low, about 5-7% for F127-DTPA-^{111}In, SPM-F127-DTPA-^{111}In and P94-DTPA-^{111}In. However, the cross-linked micelles with the shorter PEO corona (SPM-P94-DTPA) were less stable revealing a 24% ^{111}In loss after 2h in the presence of mouse serum. Complex instability was also observed in PBS but at a slower rate. TLC analysis showed that the ^{111}In released from the SPM-P94-DTPA-^{111}In was present in its free form in PBS, and chelated to proteins in the mouse serum.

It is known that complexes of DTPA-^{111}In present some *in vivo* instability and can dissociate at a rate of 5-9% loss per day for low molecular weight compounds,[218-220] and up to 20% loss in 24h for e.g. polymersomes with the DTPA-^{111}In complexes on their surface.[221] In comparison, the present nanocarriers have a better overall labelling stability. The three nanocarriers with the highest labelling stabilities (F127-DTPA-^{111}In, SPM-F127-DTPA-^{111}In and P94-DTPA-^{111}In) do not show significantly different ^{111}In loss in the presence of mouse serum or buffer.

The SPM-P94-DTPA-^{111}In show both higher ^{111}In loss and sensitivity to the medium. Since we observed also instability in PBS, we hypothesize that the DTPA-^{111}In complexes formed at the SPM-P94-DTPA-^{111}In surface might have a lower coordination number and/or different complexation geometry. This would correspond to lower stability for the complexes that could dissociate in the presence of strong competitors in the serum (e.g. log K(transferrin-^{111}In) = 18.5)[222] or simply for entropic reasons in the case of PBS buffer.

The fact that the loss of ^{111}In with SPM-P94-DTPA seems to stabilize after a few hours in the serum suggests that only a finite fraction of the complexes formed at the surface are weakly bound. In the case of PBS medium, there is no competition with proteins and the dissociation kinetics are slower, i.e. the 25% of ^{111}In loss observed for SPM-P94-DTPA-^{111}In in the serum is not reached after 3 days in PBS buffer.

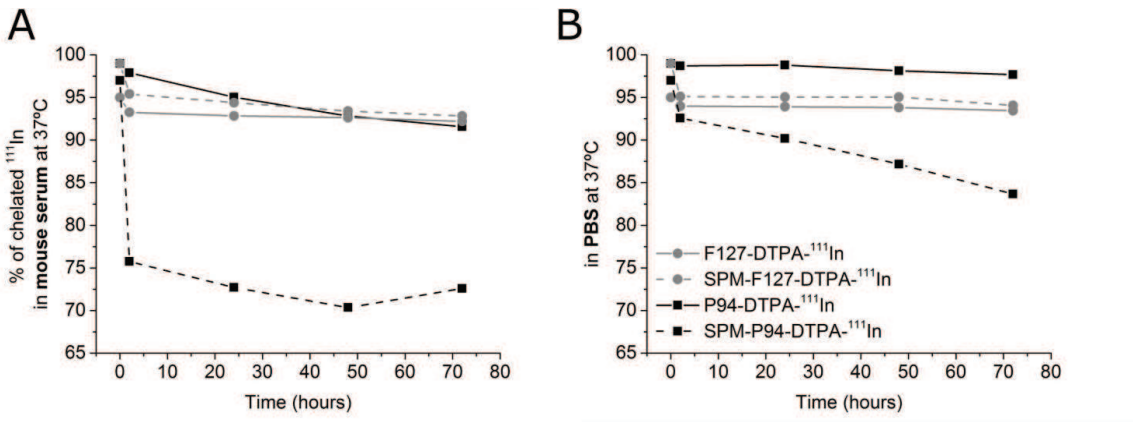

Figure 48. In vitro stability of ^{111}In-radiolabeled Pluronic nanocarriers at 37ºC after dilution in (A) mouse serum and (B) PBS for 72h.

3.5 Conclusions

We developed molecular and supramolecular nanocarriers based on Pluronic block copolymers. Molecular unimers present average diameters of ~4 to 6 nm with increasing PEO block masses (1100 and 4250 g/mol) and a constant PPO block mass of ~3000 g/mol.

Due to the dynamic nature of supramolecular Pluronic assemblies, we developed an easy and effective strategy to prevent the disintegration of Pluronic micelles into unimers by incorporating a hydrophobic cross-linking agent in the micelles core. Photo-polymerization of the cross-linking agent resulted in the creation of an interpenetrating polymer network of poly(PETA). After purification of the cross-linked solutions from free unimers, the obtained stabilized micelles present hydrodynamic diameters ranging from 26 to 38 nm for PEO masses of 1100 or 4250 g/mol. The obtained sizes are within the appropriate range to avoid both rapid clearance of the nanocarriers by the kidneys and retention in the liver.[6, 223] The cross-linked micelles were stable below and above the cmT, below the cmc, in the presence of serum proteins, and upon freeze-drying and dispersion in aqueous and organic solvents. Moreover, this method could retain the micelle structure in a much longer time scale than the stabilization procedures developed by other groups.[191, 195] This stability is most likely related to the presence of the unaltered PEO block in their corona, which demonstrates that this stabilization strategy seems promising on maintaining the *in vivo* stealth properties of PEO-PPO-PEO micelles. To test the ability of the PPO core in incorporating hydrophobic molecules, cross-linked micelles were also loaded with a hydrophobic fluorescent dye.

We also described strategies to functionalize the molecular and supramolecular Pluronic nanocarriers with fluorescent probes and hydrophilic metallic chelators. Functionalization with the fluorescent probes enables their visualization, while attachment of the chelator enabled the complexation with radioisotopes. We used the radionuclide ^{111}In to obtain radiolabeled nanocarriers that can be further used for imaging, therapy or quantification purposes. In the following chapters, the *in vitro* (Chapter 4) and *in vivo* (Chapter 5) interactions of the nanocarriers herein developed are evaluated.

CHAPTER 4

In vitro investigation of Pluronic nanocarriers

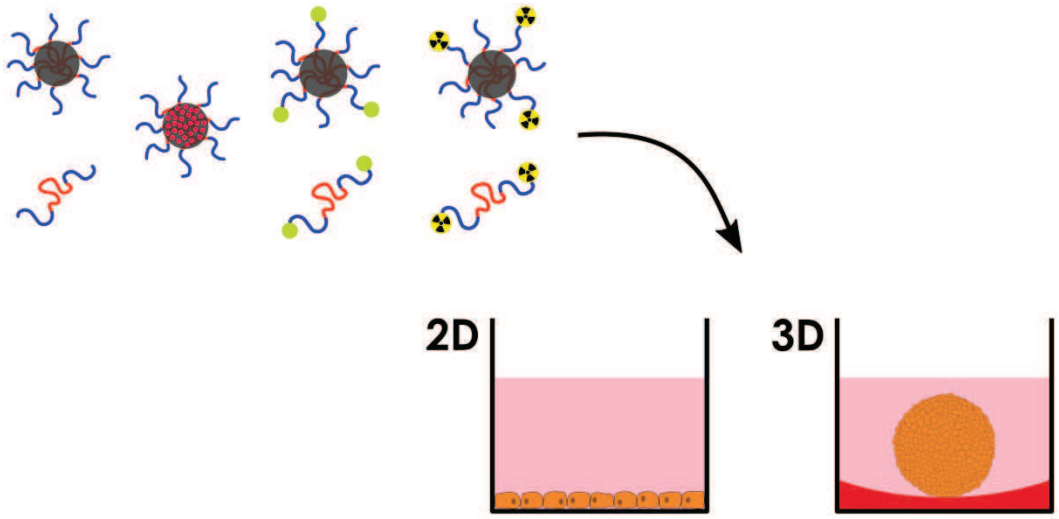

Two-dimensional (2D) and three-dimensional (3D) cell culture models were used to investigate the interactions of Pluronic carriers with different PEO block length and aggregation state (unimers *versus* stabilized micelles) in healthy and cancer cells. Monolayer cell cultures were used to study the nanocarriers cytotoxicity, ability to transport hydrophobic molecules, intracellular localization, uptake and exocytosis, and the clonogenic potential. The penetration and toxicity of the different nanocarriers were investigated in 3D tumor spheroids.

This chapter reveals how the physicochemical properties of Pluronic block copolymers influence significantly their interactions with healthy and cancer cells, whether in monolayer or spheroid cultures, and how distinct clinical applications can be foreseen.

4.1 Introduction

It has been shown that Pluronic micelles behave differently compared to the free unimers *in vitro*[41, 102, 103, 224-227] and *in vivo.*[228, 229] These previous studies evaluated the different interactions of unimers and micelles through the use of different polymer concentrations in order to be below (unimers) or above (micelles) the cmc. However, this strategy does not prevent that unimers and micelles coexist even at high polymer concentrations. Due to the self-assembling process in thermodynamic equilibrium of Pluronic micelles, there is a constant exchange of free unimers between the self-assembled micelles and the bulk solution, which results in the simultaneous presence of both aggregation states. Additionally, the use of different carrier concentrations is also known to induce different biological responses. All the referred processes can cause misleading conclusions on the relation between the aggregation state of the copolymers and their biological effects. Therefore, new approaches are needed for an appropriate assessment of these properties. Moreover, the effect of hydrophobicity in molecular and supramolecular systems has been showed to influence significantly the nanocarriers behavior.[51, 230] Therefore, it seems interesting to investigate specifically these parameters in a set of systematic comparisons.

In this chapter, we report the cellular interactions of Pluronic nanocarriers with varying PEO block mass (1100 and 4250 g/mol) and aggregation state (unimers *versus* stabilized micelles) (Figure 49 and see Table 8).

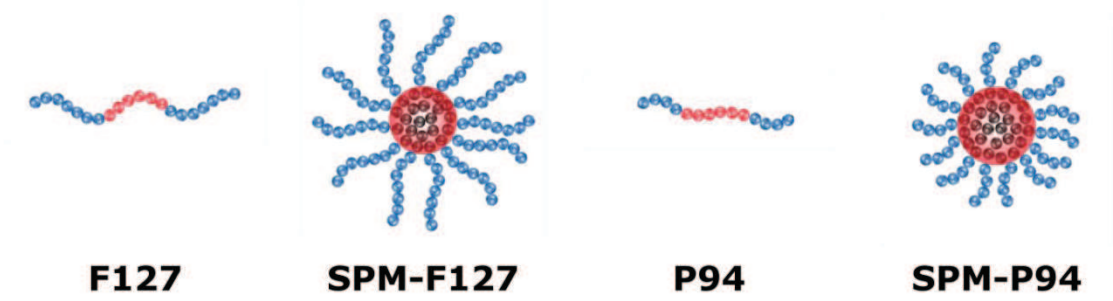

Figure 49. Pluronic molecular (F127 and P94) and supramolecular (SPM-F127 and SPM-P94) nanocarriers with varying PEO block length and aggregation state.

We started by assessing the cytotoxicity of the nanocarriers in a healthy cell line of mouse fibroblasts. Then, pre-stabilized micelles were loaded with the fluorescent Nile Red to mimic the incorporation of a poorly water-soluble drug. After loading, the internalization and intracellular localization of Nile red was studied by confocal microscopy at different incubation times.

The chemically modified nanocarriers with the fluorescent probe and the chelator were used to evaluate more specific interactions with HeLa and U87 cancer cells. The functionalization of the carriers with FITC enabled the visualization of the nanocarriers themselves by confocal microscopy. The use of common molecular biology techniques to label cellular organelles along with the fluorescently labelled nanocarriers provided valuable information for their potential clinical use. The nanocarriers modified with the chelator DTPA were radiolabeled with the radioisotope ^{111}In and also evaluated *in vitro*. This radionuclide is very interesting for the *in vitro* assessment of the nanocarriers' potential due to its prolonged half-life of 2.8 days, and simultaneous emission of gamma-radiation and Auger electrons. On the one hand, the long half-life and the emission of gamma radiation provide a substantial advantage since it allows the use of low radiation doses and to quantitatively determine the uptake and exocytosis of the nanocarriers by scintillation. On the other hand, this radio-metal can also be used for therapy due to the emission of Auger electrons (see Chapter 1 section 1.3.1). The therapeutic effect of ^{111}In has not yet been widely explored when associated to nanocarriers. In this work, we also evaluated the clonogenic potential of the nanocarriers, particularly the P94-DTPA-^{111}In unimers.

For the complete *in vitro* assessment of the developed Pluronic nanocarriers, different cell culture conditions were used. 2D monolayer cell culture systems were used for the evaluation of their cytotoxicity, internalization kinetics and clonogenic potential. This system was particularly useful to study single cell interactions and to discover potential intracellular targets. 3D multicellular tumor spheroids were generated to investigate more complex interactions such as the penetration and toxicity of the nanocarriers into multicellular aggregates. This system provides a realistic approach to predict the clinical efficacy of the carriers for solid tumor therapy, since it mimics the pathophysiological conditions of tumors in vivo.[231-234]

4.2 Experimental section

4.2.1 Cell culture conditions

NIH/3T3 mouse embryonic fibroblast cells were obtained from ATCC and cultured in Dulbecco's Modified Eagle's Medium (DMEM) supplemented with 10% Newborn Calf Serum (NCS) and 0.5% (v/v) Penicillin-Streptomycin. HeLa cells were cultured in a 50/50 mixture of DMEM and Ham's F10 supplemented with 10% Fetal Bovine Serum (FBS) and 0.5% (v/v) Penicillin-Streptomycin. U87 cells were cultured in Ham's F10 supplemented with 10% FBS and 0.5% (v/v) Penicillin-Streptomycin.

For the experimental studies, cell cultures were prepared from deep-frozen stock vials and seeded in 25 cm^2 (HeLa and U87) or 75 cm^2 (NIH/3T3) culture bottles (Cellstar, Greigner bio-one). Cells were incubated under standard cell culture conditions (37ºC, 5% CO_2 and 95% humidity) and maintained until sub-confluence was reached (70-80%).

4.2.2 Generation of fibroblasts growth curves

To determine the optimal seeding density for cell culture and sub-culture, the growth profile of NIH/3T3 fibroblasts was determined. Cells in 75 cm^2 culture bottles were trypsinized, counted with a hemocytometer, and seeded in 24-well plates (1.9 cm^2/well) at two different seeding densities (2.6×10^3 and 5.3×10^3 cells/cm^2). Cells were allowed to attach overnight and the cell culture medium was renovated every 2 days. The cell density in each well was determined using the MTT colorimetric assay and a calibration curve during a total period of 8 days. The calibration curve was also obtained using the MTT colorimetric assay. For this, cells were trypsinized, counted and seeded at increasing concentrations from 2.5×10^3 to 1×10^6 cells. On the following day, 0.2 mg/ml of MTT reagent were added to each well and incubated for 4 hours at 37ºC. Then, the solution containing unreacted MTT was carefully removed from each well. The remaining blue formazan crystals formed by living cells were solubilized with 500 µL of isopropanol. The reaction was

spectrophotometrically measured at 570 nm using a microplate reader (Xenius, SAFAS, Monaco).

The Population Doubling time (PDL) of NIH/3T3 fibroblasts was determined using Equation 17, where T corresponds to the incubation time (in any units) and X_e and X_b correspond to the cell number at the end and beginning of the incubation time respectively:

Equation 17

$$\mathrm{PDL} = \frac{\mathrm{T} \cdot ln\, 2}{ln\, \frac{\mathrm{X_e}}{\mathrm{X_b}}}$$

4.2.3 *In vitro* cytotoxicity of Pluronic nanocarriers

The effect of pure polymer solutions and cross-linked micelles on the viability of NIH/3T3 fibroblasts was determined qualitatively by phase contrast microscopy and quantitatively by the MTT colorimetric assay. The phase contrast microscope was a Nikon Eclipse TS 100 equipped with a Spot Insight Camera and images were analyzed with Spot Software (Diagnostics Instruments).

To determine the optimal cell density to perform the quantitative cytotoxicity test, cells were seeded in 96-well culture plates at increasing densities from 3.1×10^3 to 2.3×10^3 (1000 - 7500 cells/well), and the cell number was determined in the following 4 days. Similarly to section 4.2.2, calibration curves relating the cell number to the absorbance at 570 nm were obtained for the 96-well plates. After determining the optimal cell seeding density, fibroblasts were seeded at a density of 5000 cells/well and allowed to attach overnight. They were then incubated with increasing concentration of pure aqueous polymer solutions of Pluronic P94 and F127, and stabilized polymeric micelles of Pluronic P94 (SPM-P94) and F127 (SPM-F127). A wide range of concentrations from 2.5 μg/mL to 5000 μg/mL was tested. All samples were sterilized prior to use by filtration using Acrodisc® sterile syringe filters with 0.22μm Supor® membrane (Pall Corporation). Un-treated cells (no-exposure) were used as controls.

After the exposure period (24 or 48 hours), the medium was removed and 100 µL of DMEM (without phenol red and serum) with 0.2 mg/ml of MTT reagent were added to each well and incubated for 4 hours at 37ºC. After the incubation period with the MTT reagent, the medium was carefully removed, 100 µL of isopropanol were added to each well and the absorbance was measured at 570 nm. Cell viability was determined using Equation 18:

Equation 18 $$\text{Cell viability } [\%] = \frac{\text{A}_{570} \text{ of exposed cells}}{\text{A}_{570} \text{ of control cells}} \times 100$$

Results are expressed as the mean viability percentage ± standard error mean. Experiments were performed in quadriplicate. The statistical analysis of the results was carried out by one-way ANOVA (*p<0.05, **p<0.001) using Origin 9 software.

4.2.4 Internalization of Nile Red-loaded stabilized Pluronic micelles and co-localization with the mitochondria

Cells were seeded at a density of 2×10^4 cells/cm^2 in 12 mm coverslips placed in a 24-well plate and cells were allowed to attach overnight. Then, Nile Red-loaded stabilized micelles of either Pluronic P94 or F127 were added at a concentration of 0.025% (w/v) in 500 µL of complete cell culture medium. The cells were incubated with the stabilized micelles for different periods (30 min and 1, 2 and 4h). After the incubation period, cells were washed once with DMEM without phenol red. Then, cells were fixed with pre-warmed 3.7% formaldehyde in PBS for 10 min. Cells were washed again with PBS followed by incubation with 2 µg/mL of Hoescht 33342 solution in PBS for 15 min at room temperature. Then, the cells were washed three times with PBS and mounted with aqueous mounting medium.

For cell imaging, we used an inverted TE 2000 microscope (Nikon, Japan), equipped with a 60x Water Immersion 1.2 NA Plan Apo DIC objective. We performed confocal laser scanning imaging (Nikon C1 scanhead), and images were captured using EZ-C1 software (Nikon, version 3.50). All confocal images were taken with a unique set of the following parameters: laser power

(one specific power for each of the excitation wavelength mentioned above), PMT amplification (one specific gain for each of the two emission wavelength ranges mentioned above), pinhole size, pixel dwell, image size and number of pixels per image. Therefore, qualitative comparison in terms of fluorescence emission intensity between images could be performed throughout the whole study.

To determine the co-localization of Nile Red-loaded stabilized micelles with the mitochondria, we used a green-fluorescent mitochondrial stain (MitoTracker® Green FM, Life Technologies). After incubation with each of the stabilized micelles for 4 h, cells were further incubated for 30 min at 37ºC with a 100 nM solution of MitoTracker® in complete DMEM. Then, cells were fixed and imaged as previously described.

4.2.5 Internalization and intracellular localization of FITC-labelled nanocarriers and co-localization with the lysosomes

For the internalization experiments, 1×10^5 of HeLa or U87 cells were seeded on 20×20 mm borosilicate glass slides placed inside 6-well plates (Corning) and cells were allowed to attach overnight. Then, FITC-labelled unimers and stabilized micelles of either Pluronic P94 or F127 were added at a concentration of 250 µg/mL in 2 mL of cell culture medium. After 4 h incubation, the lysosomes were labelled with a 50nM solution of LysoTracker® Red DND-99 in complete cell culture medium for 45 min at 37ºC. Then, cells were washed twice with PBS and fixed with 3.7% formaldehyde in PBS for 15 min. Cells were washed again thrice with PBS and mounted with DAPI Vectashield (Vector Laboratories) for confocal microscopy. Images were captured with a Carl Zeiss LSM710 microscope using a Fluar 40x/1.30 Oil M27 objective and were superimposed to determine the co-localization of the nanocarriers with the lysosomes. Experiments were performed in triplicate.

4.2.6 Cellular uptake and exocytosis

HeLa cells were seeded in 96-Stripwell™ plates (TC treated, flat bottom) at a density of 5000 cells/well and allowed to attach overnight. Then, cells were incubated with ^{111}In radiolabeled compounds at a concentration of 25 µg/mL.

For the exocytosis experiments, cells were incubated with the radiolabeled samples for 24 h. After this period, the medium containing the samples was removed, the wells cleaned twice with PBS, and new medium was added to each well.

At different time points, the wells were stripped, the medium was removed from each well, and the wells containing the HeLa cells attached were rinsed twice with PBS. The activity in the medium and the cleaning PBS (activity not internalized), and in the wells (activity internalized by the cells) was counted through gamma-scintillation counting (2480 Wizard^2 Automatic Gamma Counter, Perkin Elmer).

4.2.7 Clonogenic assay

The clonogenic potential of Pluronic P94 was determined by the colony-forming assay to evaluate the ability of single cells to replicate and form colonies (>50 cells). Diluted HeLa cell suspensions were plated in 6-well plates at a density of 1000 cells/well in 2 mL of culture medium. Cells were allowed to attached overnight and, on the following day, 0.1, 1 and 10 MBq of P94-DTPA-^{111}In were added to each well (200 µL of sample + 1.8 mL of cell culture medium). PBS, non-radioactive P94-DTPA and 0.1, 1 and 10 MBq of DTPA-^{111}In (free chelator) were used as controls. The samples P94-DTPA-^{111}In and P94-DTPA were added to a final concentration of 25 µg/mL of modified polymer, and a concentration of DTPA-^{111}In of 5.77 µM.

After incubation with the samples for 6 days, the cell medium was removed and the formed cell colonies were washed with PBS. Then, they were fixed and colored with coomassie blue solution for 5 min. The staining solution was removed and the wells were rinsed under a slow streaming of demineralized water. The wells were air dried and images of the wells and colonies were acquired with optical microscopy.

4.2.8 Spheroids penetration and toxicity

Spheroids of HeLa and U87 cells were prepared using the agarose method. Briefly, the wells of a 96-well plate (flat bottom) were coated with a heated (60°C) 1.5% agarose solution in complete DMEM (50 µL/well) to provide a

nonadhesive surface. The coating also provides a concave bottom which forces cells to accumulate in the center of the well and increases cell-to-cell interactions.

To the agarose-coated wells, 200µL of cells suspension containing 7500 U87 cells or 5000 HeLa cells was added per well. After 4 days, well-defined single spheroids with approximately 500-600 µm in diameter were obtained and further studies were conducted.

The morphology of the spheroids was analyzed by optical and confocal microscopy (Carl Zeiss LSM710). The cell nuclei were labelled with 20 µg/mL of Hoescht 33342 solution in complete cell culture medium during 1 h. To observe the cell density in the spheroids, the confocal images of the nuclei stain were analyzed by ImageJ software using the Shape Index Map.

The penetration of F127 unimers and SPM-F127 was evaluated by incubation with the FITC-labelled carriers for different incubation times at a concentration of 2500 µg/mL.

For confocal imaging, the tumor spheroids were collected, rinsed with PBS twice, transferred to perfusion chambers (CoverWell™, Grace Bio-Labs) and then analyzed by confocal microscopy (Carl Zeiss LSM710) at a penetration depth of 80-100 µm and a section thickness of 10 µm. Considering the average size of the spheroids (500 µm), the confocal images correspond to a cross section that does not intersect the center of the spheroids. All images were acquired in the same conditions to allow a quantitative comparison of fluorescence intensities. The penetration depth into the tumor spheroids was measured using ImageJ software and the plugin Radial Profile Angle. A section of the spheroids was selected and the radial fluorescence intensity profiles were obtained.

The toxicity of P94 unimers and SPM-P94 micelles in the tumor spheroids was evaluated by incubating the spheroids with toxic concentrations of the samples (2500 µg/mL) (see Chapter 4 section 4.3.1.2). Growth inhibition was monitored by measuring the size of the U87 tumor spheroids by optical microscopy. Images of the spheroids were acquired and the spheroid volume was calculated using the formula: $V = 4/3\pi(d/2)^3$. Experiments were performed in quadruplicate.

4.3 Results and Discussion

4.3.1 *In vitro* 2D studies

4.3.1.1 Optimization of NIH/3T3 cell culture

In order to optimize the culture of NIH/3T3 fibroblasts in monolayer, growth curves were obtained which enabled determination of optimal cell seeding density for culture and subculture (cells/cm^2 substrate). The most important parameter is the development of an appropriate calibration method to determine the cell number. In this work we used the MTT colorimetric assay. MTT is a yellow water-soluble tetrazolium dye that is reduced to a purple water-insoluble product (formazan) (Figure 50). This reaction occurs in living cells in the mitochondria via the mitochondrial succinate dehydrogenase enzyme. The amount of formazan produced by the cells correlates with the amount of metabolically active cells, which is directly proportional to the number of living cells. After solubilization of the formazan crystals in an appropriate solvent (e.g. DMSO, isopropranol), the absorbance of the solutions can be determined spectrophotometrically at 570 nm. In Figure 51 we can observe the formation of the formazan crystals that, once formed, disrupt the cellular membrane and can be easily visualized by optical microscopy.

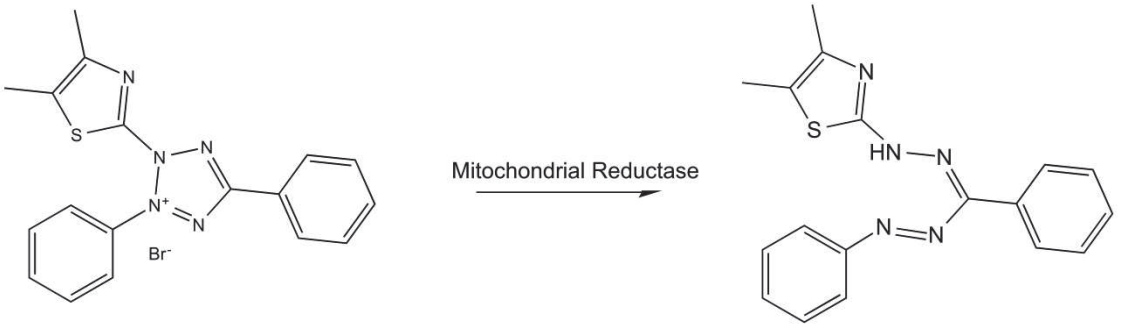

Figure 50. Reaction of MTT to Formazan.[235]

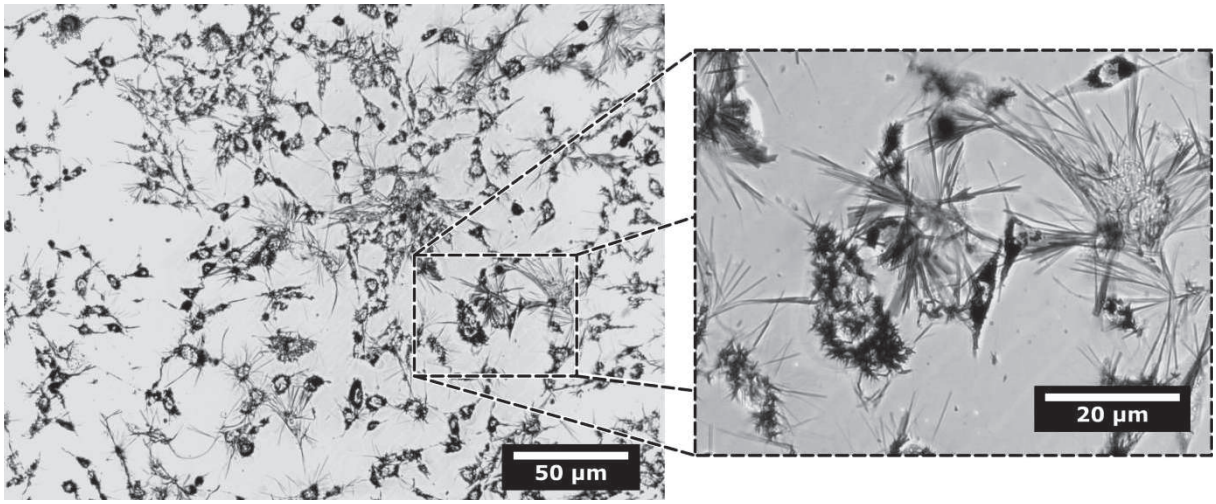

Figure 51. NIH/3T3 fibroblasts after 4 hours incubation with the MTT reagent. The formation of formazan crystals from the metabolization of MTT and disruption of the cellular membranes can be seen.

To determine the cell number, a calibration curve is obtained (Figure 52) by seeding increasing number of cells that were previously counted manually using the hemocytometer. The calibration curve was then obtained by fitting a second degree polynomial.

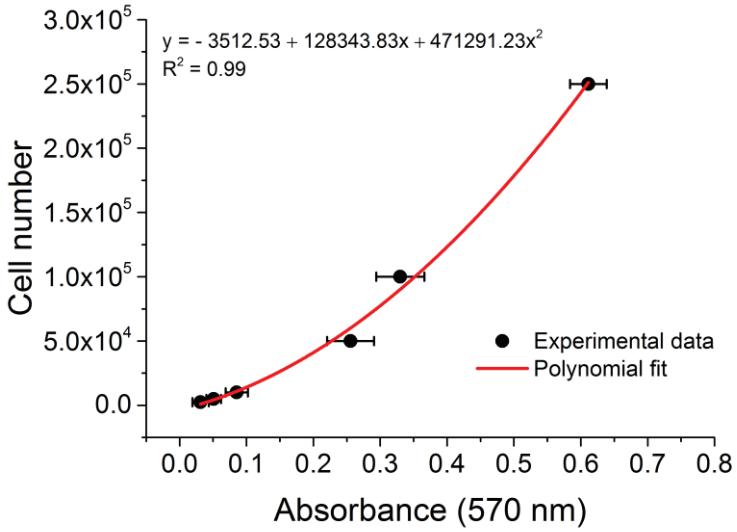

Figure 52. Calibration curve correlating the absorbance with the number of NIH/3T3 cells in 24-well plates.

To obtain the growth profile curves, two seeding densities were tested (Figure 53) and the cell concentration at different time points was determined by the MTT assay and the previously obtained calibration curve. The growth profiles were fitted with the Logistic fit.[236] We can observe in the growth curve the presence of three distinct growth patterns: lag phase, exponential phase and stationary phase.

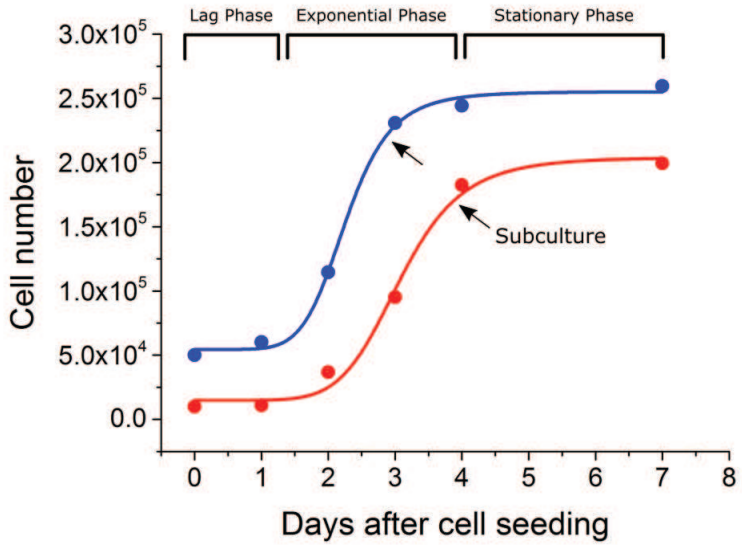

Figure 53. Growth profile curves of NIH/3T3 fibroblasts after initial seeding density of • 2.6 × 10^3 cells/cm^2 and • 5.3 × 10^3 cells/cm^2, and respective Logistic fits.

The lag phase corresponds to the time immediately after seeding where there is no increase in cell number. In this period, cells are adapting to the new conditions and replacing the components in the cell surface and extracellular matrix that were lost during trypsinization in order to be able to attach to the substrate and spread. After this phase, the growth increases exponentially and the population of cells doubles at defined time intervals (exponential phase). We have determined that the population doubling time of NIH/3T3 fibroblasts is around 16 hours. The duration of the exponential phase depends on the seeding density and the growth rate which is specific to each cell line. When most of the growth surface starts to become occupied, cells become confluent and the growth rate is reduced or ceases completely. In this stationary phase, cells start to contact with each other and their growth and spreading is inhibited through contact inhibition. If cells are transformed, they are

insensitive to close contact and will overgrow.[237] At this point, the cells need to be sub-cultured, which is achieved by seeding an appropriate amount this cellular population in a new culture flask.

4.3.1.2 Cytotoxicity of Pluronic nanocarriers

An appropriate *in vitro* cytotoxicity screening of the nanocarriers must be performed before their clinical use. Cytotoxicity experiments were performed following the International Standard Organization (ISO 10993-5:2009) recommendations concerning the biological evaluation of medical devices, which comprises a series of criteria for evaluating the biocompatibility of a medical device prior to an *in vivo* study. One of the critical parameters in determining the cytotoxicity of nanomaterials is the optimal cell seeding density. Cells should be seeded in the semi-confluence state and exposure to the nanomaterials needs to be performed in the logarithmic phase of cell growth. The exponential phase ensures that the cell population is at its most uniform phase and that the cell viability is high (90-100%). In the case the control cells are already in the stationary phase (Figure 53), the MTT reading will be false because cells will have a slow growth and cannot therefore be compared to cells exposed to toxic materials. At the same time, if cells are seeded at too low density, they will remain in the lag phase during the treatment and cells will not grow exponentially, which will lead to false positives.

Therefore, different seeding densities were tested in order to determine the optimal seeding density that allows studying the toxicity up to a period of 48 hours. In this case, cells need to remain in the exponential phase for a period of 72 hours after seeding to ensure the exponential growth during all the treatment. A new calibration curve to optimize cell counting was also performed for the 96-well plates (Figure 54). Then, different cell seeding densities were tested, and the number of cells for the following 4 days was determined.

In Figure 55, we can see that too low seeding density results in a very delayed cell growth, while too high density results in the reach of stationary phase very early.

According to the observed growth profiles, we have defined that the optimal seeding density to perform cytotoxicity experiments in NIH/3T3 fibroblasts is 1.6×10^4 cells/cm^2. This seeding density also provides appropriate absorbance values that fall between 0.2 and 0.6 for these plates.

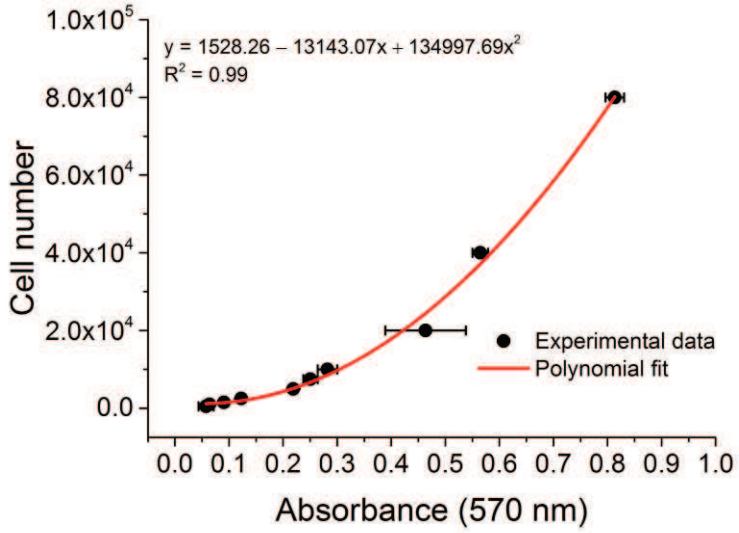

Figure 54. Calibration curve correlating the absorbance with the number of NIH/3T3 cells in 96-well plates.

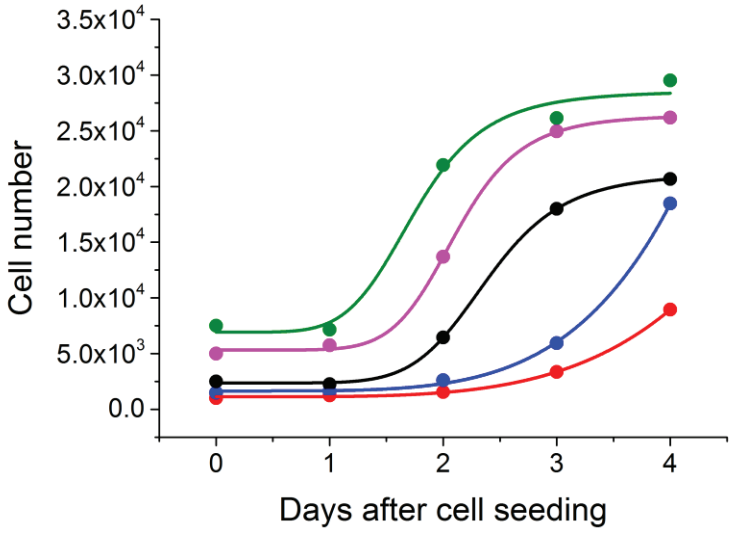

Figure 55. Growth profile curves of NIH/3T3 fibroblasts in 96-well plate for optimization of cytotoxicity protocol. Different initial seeding densities were tested: • 3.1 × 10^3 cells/cm^2, • 4.7 × 10^3 cells/cm^2, • 7.8 × 10^3 cells/cm^2, • 1.6 × 10^4 cells/cm^2 and 2.3 × 10^4 cells/cm^2 corresponding to 1000, 1500, 2500, 5000 and 7500 cells/well, and represented with the respective Logistic fits.

We then evaluated the effect of pure polymer solutions and cross-linked micelles on the viability and proliferation of mouse fibroblasts (Figure 56). This cell line was selected to study the nanomaterial cytotoxicity because fibroblasts are found in the matrix and connective tissue throughout the body, and they have been widely used to assess cellular cytotoxicity, genotoxicity and morphological transformations of a series of nanomaterials.[238-241]

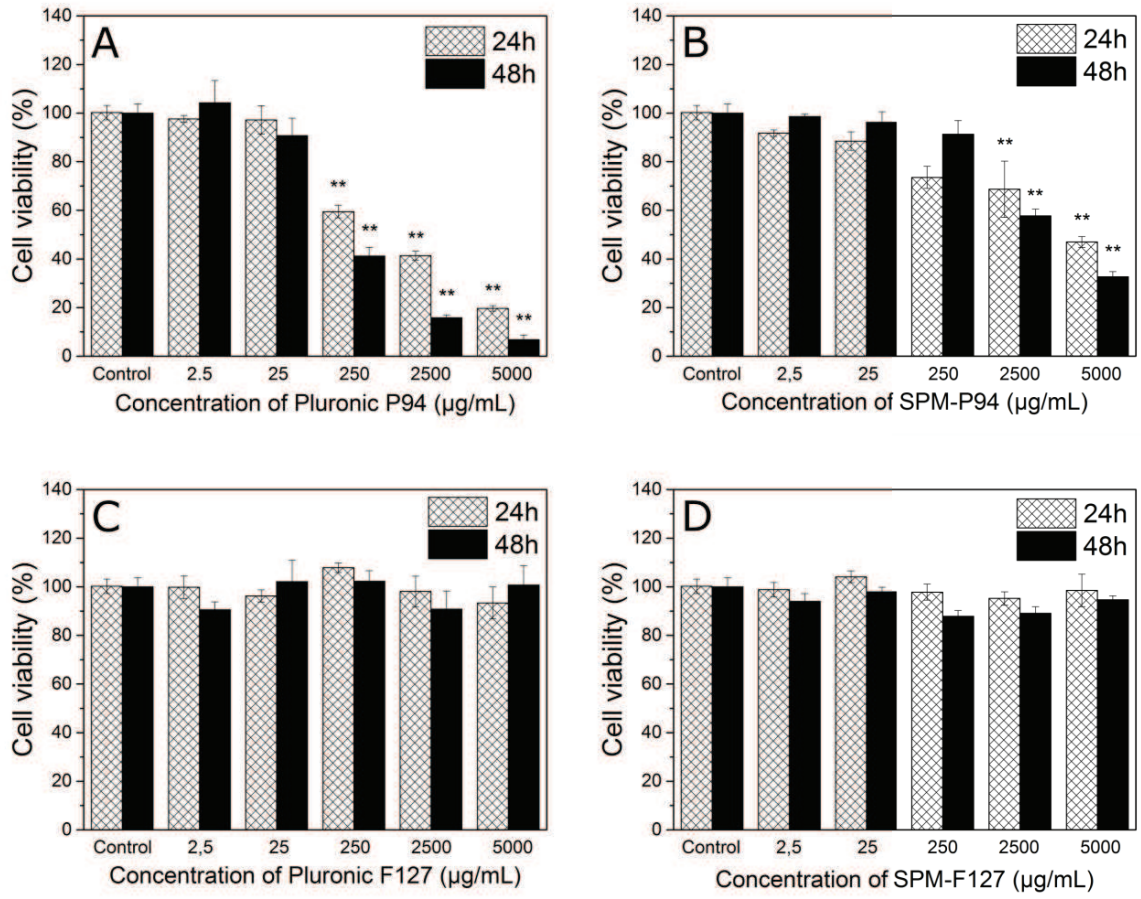

Figure 56. Effect of pure Pluronic solutions and cross-linked Pluronic micelles on the cellular viability of mouse fibroblasts after exposure to different sample concentrations for 24h and 48h: (A) Pure Pluronic P94, (B) SPM-P94, (C) Pure Pluronic F127 and (D) SPM-F127 (**p<0.001).

The toxicity of pure polymer solutions and stabilized Pluronic micelles was evaluated by exposing mouse fibroblasts to increasing sample concentrations up to 5000 µg/mL (0.5 wt%) for 24 and 48h and determining cell viability using the MTT colorimetric cell proliferation assay as previously described.

In the case of pure polymer solution of Pluronic P94, we observe a cytotoxic effect which is dependent on the polymer concentration (Figure 56A). Until the concentration of 25 μg/mL, there is no alteration in the cellular viability. However, an abrupt decrease on the fibroblasts viability was observed at higher concentrations. Interestingly, the cross-linked micelles of Pluronic P94 did not display the same cytotoxic effect (Figure 56B). Despite the fact that the IC50 determination was not possible, the SPM-P94 only displayed a toxic effect at concentrations higher than 250 μg/mL. Moreover, on the highest concentration of SPM-P94 tested (5000 μg/mL), approximately 30-50% of the cells were still viable, while less than 10-20% of the cells survived after exposure to the same concentration of pure P94 polymer solution.

To our knowledge, the toxicity of Pluronic P94 has not been studied before, and the toxicity observed is consistent with previous studies using other Pluronics with high PPO content. The biological effects of Pluronics with high hydrophobic content have been associated with their ability to incorporate in the cellular membrane altering its microviscosity, and also to reduce the intracellular ATP concentration.[98, 227] The cytotoxicity results indicate that the toxic potential of the Pluronic P94 may be related to the unimers and not to the micelles. In fact, the different biological effects of more hydrophobic Pluronic unimers in contrast to their respective micelles have also been reported,[42, 49, 96, 98] showing that unimers are potentially more toxic than their respective micelles. Based on these results, we can understand the less harmful effect obtained with the cross-linked P94 micelles in comparison with the polymer unimers. However, a cytotoxic effect was still observed with the Pluronic P94 stabilized micelles, which might be associated to the presence of free unimers, or it can be an indication of the intracellular degradation of the cross-linked micelles with the consequent release of polymer unimers. In the case of Pluronic F127, we confirmed the nontoxicity and biocompatible properties of pure Pluronic F127 (Figure 56C). For the stabilized micelles of Pluronic F127, there was no alteration in the cellular viability (Figure 56D).

The cytotoxicity evaluation and comparison with the raw polymer solutions demonstrates that the presence of PETA does not induce cellular toxicity. Even after more than two populations doubling time (48 h), the presence of the PETA network did not induce a cytotoxic response.

In parallel, a qualitative evaluation of the fibroblast morphology was performed by microscopy examination. Cells were observed for visible signs of toxicity in response to the tested nanomaterials. In Figure 57 (controls), confluent monolayers of mouse fibroblasts cells can be observed. This is the appearance of the typical fibroblast morphology and the evidence of a noncytotoxic response. As the concentration of cross-linked and pure Pluronic P94 increases (Figure 57), we can observe alterations in the proliferation rate as well as the presence of floating dead cells. The extensive empty areas between cells indicate that extensive cell lysis has occurred. In more detail, we can observe cytoplasmic shrinkage and the appearance of grainy cellular components. In contrast, exposure to pure polymer solutions or cross-linked micelles of Pluronic F127 did not induce any alteration in the fibroblast morphology or proliferation. No toxic effect or any morphological alterations in all the concentrations tested was observed (images not shown).

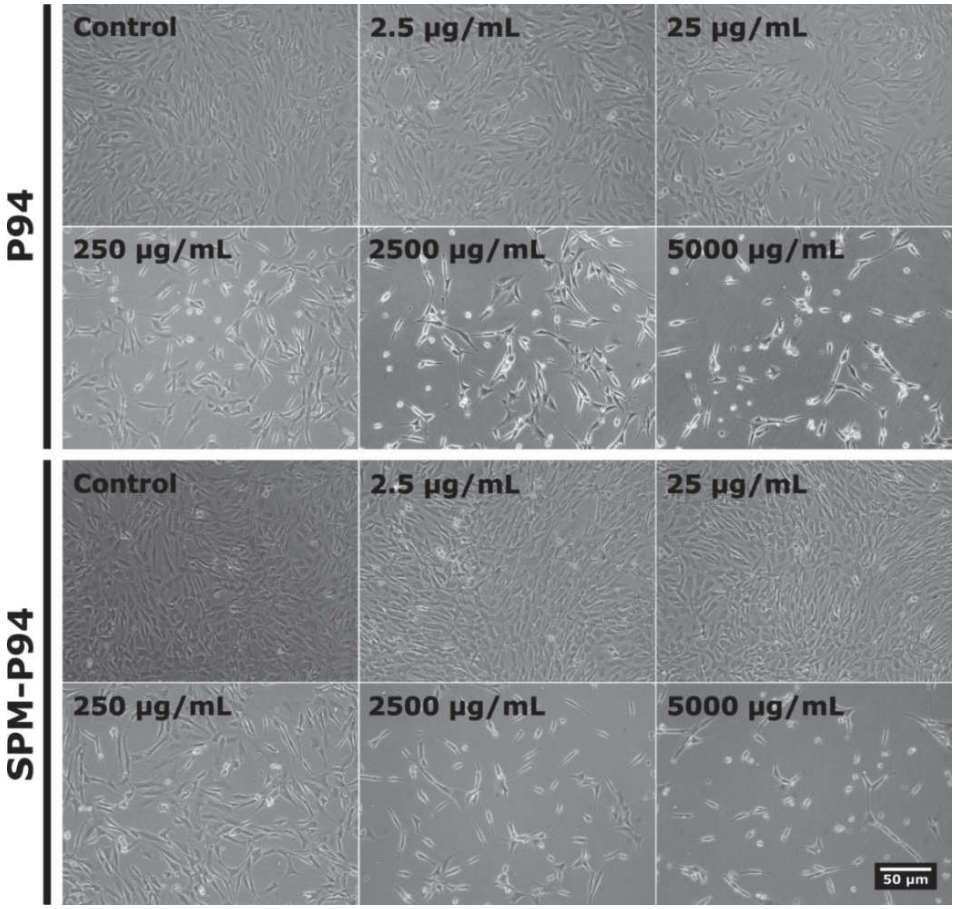

Figure 57. Photomicrographs of the fibroblasts after 24h and 48h incubation with increasing concentrations of Pluronic P94 and stabilized Pluronic P94 micelles.

4.3.1.3 Internalization of stabilized micelles loaded with Nile Red and co-localization with mitochondria in NIH/3T3 fibroblasts

The ability of core cross-linked micelles to incorporate hydrophobic molecules in the core and transport them across the cell membrane was evaluated. Nile Red was loaded in pre-stabilized micelles of Pluronic P94 (SPM-P94) and Pluronic F127 (SPM-F127) (described in Chapter 3 section 3.3.4) and incubated with NIH/3T3 mouse fibroblasts. The intracellular distribution of Nile Red at different incubation times was studied by confocal microscopy (Figure 58). The chosen concentration of stabilized micelles was 250 µg/ml as no cytotoxic effects were observed with both formulations at this concentration (section 4.3.1.2).

Red fluorescence corresponding to the Nile Red was seen inside the cells irrespective of the stabilized Pluronic P94 or F127 micelles. This was observed as early as 30 min after incubation. Moreover, there is a time-dependent internalization as we observed an increase in the red fluorescence intensity as the incubation time increased.

The red fluorescence was mainly observed in localized fluorescence spots, which were more evident as the incubation time increased (4h). This can be an indication of accumulation of micelles in endocytic compartments. However, it can also be that the stabilized micelles released Nile red, and that free Nile Red inside the cytoplasm stained lipid compartments inside the cells. Previous researchers have also shown that free Nile red in the cell medium is not internalized in the same manner as when it is associated to nanocarriers,[242, 243] which means that the localized red fluorescence observed corresponds most probably to fluorescent probe transported by the stabilized micelles. To avoid this pitfall, fluorescent covalent attachment was also performed and the internalization experiments are described in the following sections.

Although the mechanisms of delivery of Nile Red into cells incorporated in stabilized Pluronic micelles are not yet fully clarified, the stabilized micelles have the potential to incorporate hydrophobic molecules and deliver them through the cell membrane.

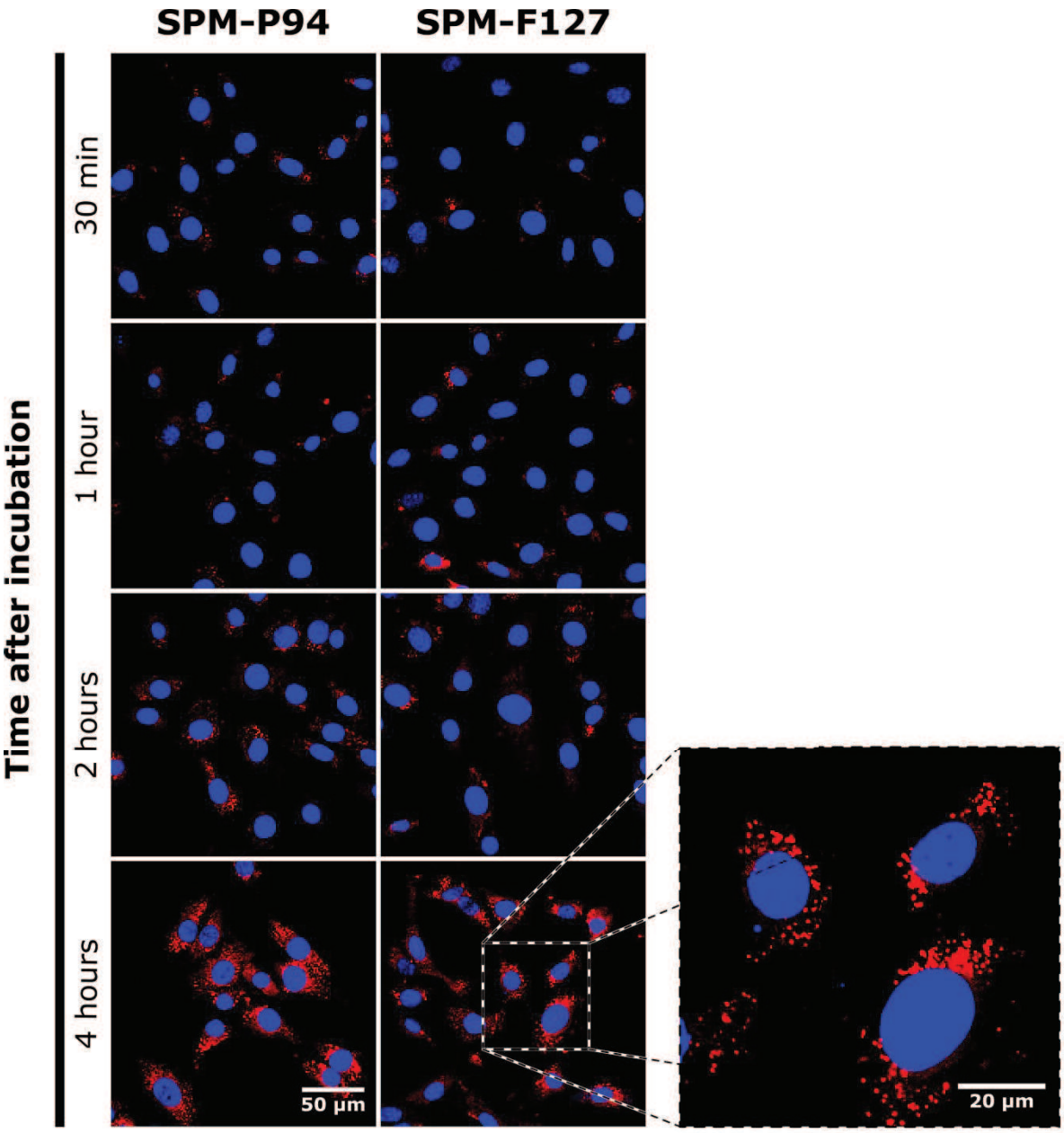

Figure 58. Time-dependent cellular internalization of Nile red-loaded stabilized Pluronic Micelles. Cells were exposed to 250 µg/mL of SPM-P94 or SPM-F127 and imaged by confocal microscopy. The cell nuclei (blue) were labelled with Hoescht 33342.

It has been shown that Pluronic unimers and micelles can localize within different cellular organelles. For example, some Pluronic unimers have been shown to associate with the mitochondria, which leads to depletion of the ATP synthesis and the so-called sensitizing effects in MDR cells.[96] Here, we aimed to verify whether the loaded hydrophobic molecules in cross-linked Pluronic micelles co-localized with the mitochondria (Figure 59). We used a green fluorescent stain (MitoTracker® Green FM) to mark the mitochondria, and the dye-loaded stabilized micelles. We can clearly see the well-defined mitochondrial structures as well as the defined spots of the fluorescent stabilized micelles as observed previously in Figure 58. No co-localization of the micelles with the mitochondria was observed suggesting that the hydrophobic loading in cross-linked Pluronic micelles is not transported to the mitochondria and is either associated to the micelles, released in the cytoplasm or associated to endocytic vesicles.

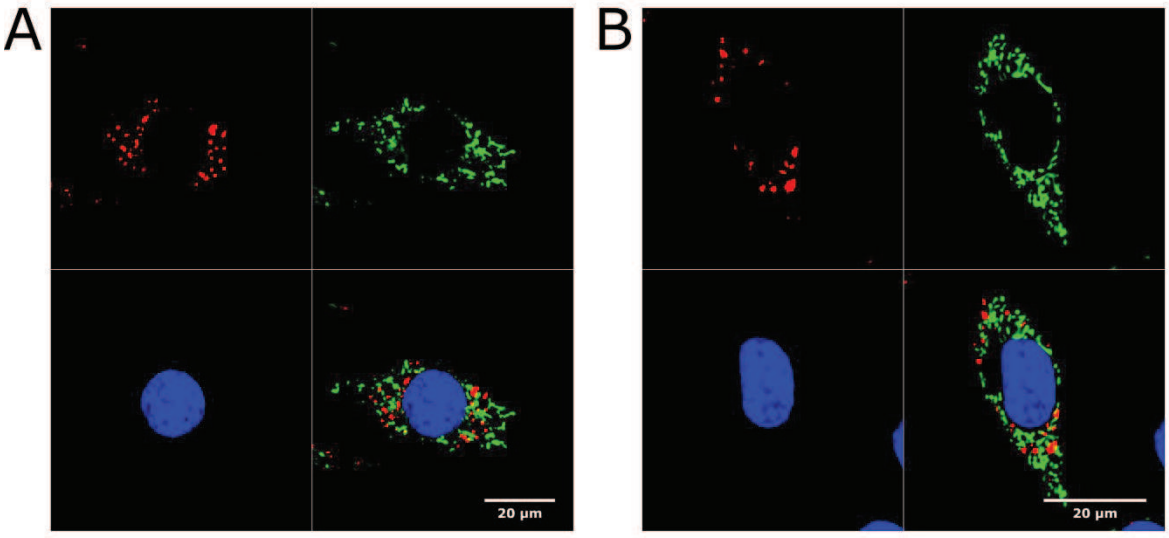

Figure 59. Confocal images of NIH/3T3 cells after incubation with Nile Red-loaded (A) SPM-P94 and (B) SPM-F127 and co-localization with the mitochondria. Cells were visualized in the red channel (top left) for visualization of the Nile Red dye, in the green channel (top right) to observe the mitochondrial network stained with MitoTracker® Green, and in the blue channel (bottom left) to localize the nuclei which was labelled with Hoescht 33342. Co-localization was analyzed in the merged channel (bottom right).

4.3.1.4 Internalization of FITC-labeled nanocarriers and co-localization with lysosomes in HeLa and U87 cells

The internalization mechanisms and intracellular distribution in cervical cancer HeLa and glioblastoma U87 cancer cells were investigated for both Pluronic unimers and cross-linked micelles. Figure 60 and Figure 61 show the confocal images of HeLa and U87 cells respectively after incubation with FITC-labelled Pluronic unimers (F127 and P94) and cross-linked micelles (SPM-F127 and SPM-P94). After 4 hours incubation, a strong green fluorescence was observed intracellularly for all the nanocarriers studied showing that both Pluronic unimers and stabilized micelles were internalized by both cell types.

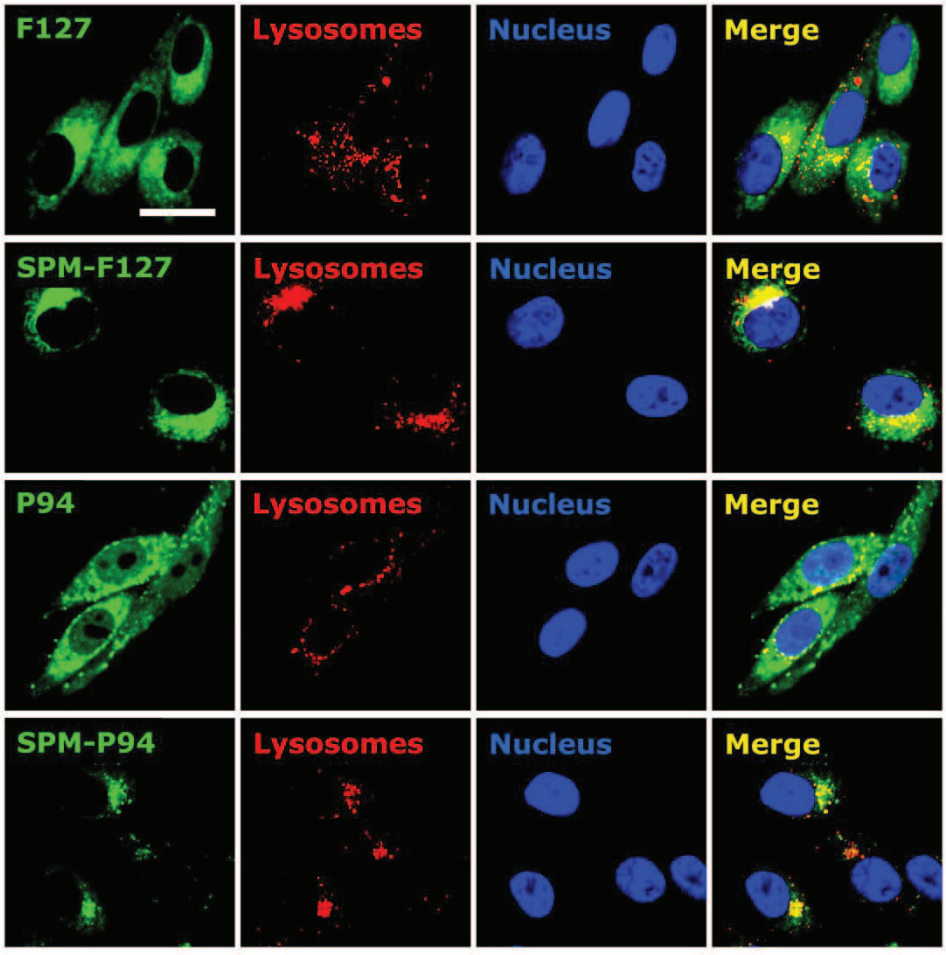

Figure 60. Internalization and intracellular localization of FITC-labelled Pluronic unimers (F127 and P94) and cross-linked micelles (SPM-F127 and SPM-P94) after incubation with U87 cells for 4 hours at a concentration of 250 μg/mL. The lysosomes were marked with LysoTracker Red and the nuclei were stained with DAPI. Scale bar is 20μm.

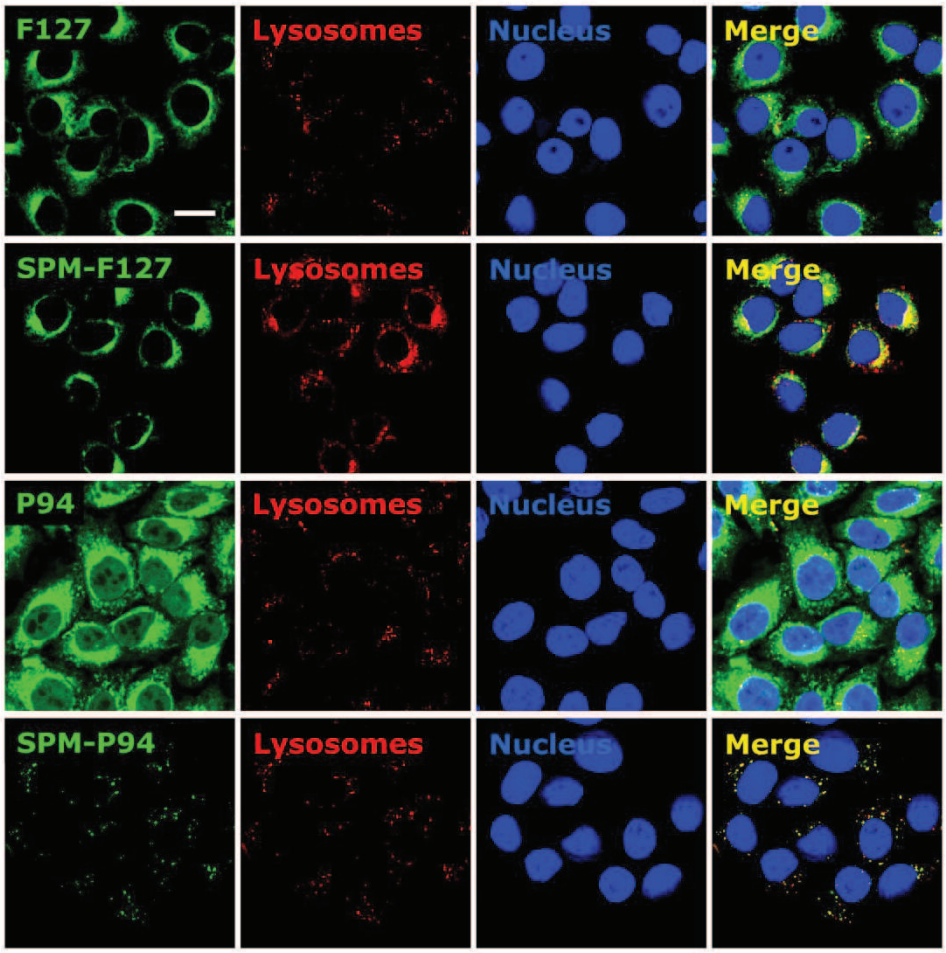

Figure 61. Internalization and intracellular localization of FITC-labelled Pluronic unimers (F127 and P94) and cross-linked micelles (SPM-F127 and SPM-P94) after incubation with HeLa cells for 4 hours at a concentration of 250 μg/mL. The lysosomes were marked with LysoTracker Red and the nuclei were stained with DAPI. Scale bar is 20μm.

The Pluronic unimers fluorescence was distributed throughout the whole cell: dispersed in the cytoplasm or localized around (for F127 and P94) or even inside the nucleus (for P94). Lower magnification images can better translate the differences between F127-FITC and P94-FITC unimers (Figure 62).

The nuclear translocation of P94 unimers in HeLa and U87 cells was observed by a diffuse green fluorescence in the nucleus, whereas F127 unimers remained around the nucleus in HeLa cells (Figure 61 and Figure 62) or diffused in the cytoplasm of U87 cells (Figure 60).

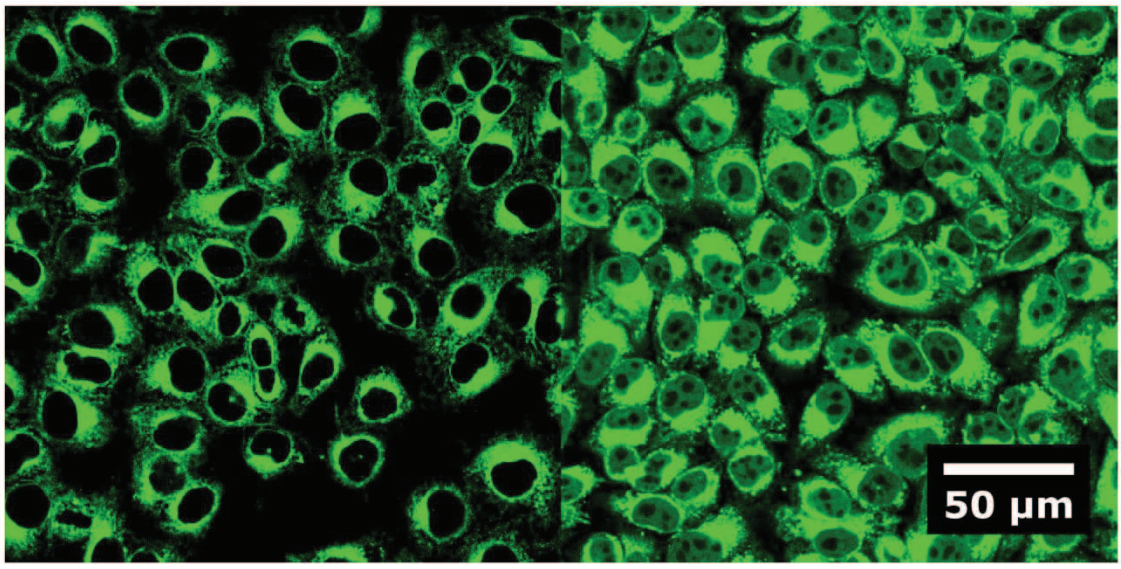

Figure 62. Lower magnification of HeLa cells after incubation with F127-FITC (left) and P94-FITC (right) unimers for 4 hours at 250 µg/mL.

It has been shown that molecules smaller than ≈ 5 nm in diameter can cross the nuclear pore complexes by passive diffusion.[244] This is a very well-defined cut-off for passive diffusion as it has been observed that gold nanoparticles with less than 5 nm diameter enter the nucleus, while particles with 5.5 nm are excluded.[245] Given the hydrodynamic diameter of P94 (4.2 nm) and F127 unimers (5.8 nm) (Table 6), we can therefore expect that P94 unimers can diffuse into the nucleus, whereas higher molecular weight unimers (F127) are excluded. The nuclear translocation observed for Pluronic P94 has been observed previously for other Pluronics: P105 (Mw=6500, $PEO_{37}PPO_{56}PEO_{37}$)[50] and P85 (Mw=4600, $PEO_{26}PPO_{40}PEO_{26}$)[49] which have molecular weights and PEO/PPO compositions very similar to P94 (Mw=5000, $PEO_{26}PPO_{48}PEO_{26}$). Further studies are required to elucidate the effects of low molecular weight Pluronics in the nucleus, and whether the toxicity observed previously for low molecular weight Pluronics can also be related to their nuclear localization and interaction with the nuclear DNA.

The cross-linked Pluronic micelles appeared more localized in small spots or regions, which was an indication that micelles could concentrate in specific organelles such as the lysosomes. To confirm, the lysosomes were stained

with LysoTracker Red and the green fluorescence images (corresponding to the micelles) and the red fluorescence images (corresponding to the lysosomes) were overlaid (Figure 60 and Figure 61). We observed that Pluronic micelles were mostly co-localized with the lysosomes. In both cell types, the lysosomal vesicles containing the SPM-F127 appear to associate with the Golgi complex. However, the localization of the lysosomes containing the SPM-P94 depended on the cell type: they remained dispersed in the cytoplasm of HeLa cells (Figure 61) and associated with the Golgi complex of U87 cells (Figure 60). This indicates that the cellular uptake was associated with the formation of endocytic vesicles that fused with the lysosomes. Moreover, no nuclear localization was observed for both stabilized micelles which is attributed to their larger size compared to the unimers.

The most common internalization pathway of nanomaterials is through endocytosis where the nanocarrier first attaches to the cell membrane through specific (e.g. targeting agents) or non-specific (e.g. electrostatic) interactions, and then is enclosed by the cell membrane forming a membrane-bound vesicle. Endocytosis can be divided into phagocytosis (for nanomaterials larger than 0.5 μm) and pinocytosis (for nanomaterials smaller than 0.2 μm).[47, 246] Pinocytosis is the most common internalization pathway of nanocarriers and can be further classified as: macropinocytosis, clathrin-mediated endocytosis, caveolin-mediated endocytosis, and clathrin/caveolin-independent endocytosis.[45, 247, 248] In the clathrin-mediated endocytosis (Figure 63), the membrane interaction with the nanomaterial leads to the formation of a clathrin-coated vesicle, which evolves into an early endosome in the cytoplasm. The early endosome acidifies and fuses with pre-lysosomal vesicles becoming then a late endosome and finally a lysosome. The lysosome constitutes a vesicle with hydrolytic enzymes in an acidic environment (pH 4.5-5.5) aiming at the digestion of the internalized nanomaterial. The caveolae-mediated endocytosis starts with the formation of a caveolar vesicle that is delivered to a caveosome - a flask-shape pit rich in proteins and lipids - avoiding the nanomaterial degradation by the acidic environment and enzymes present in the lysosome (Figure 63).[45, 246]

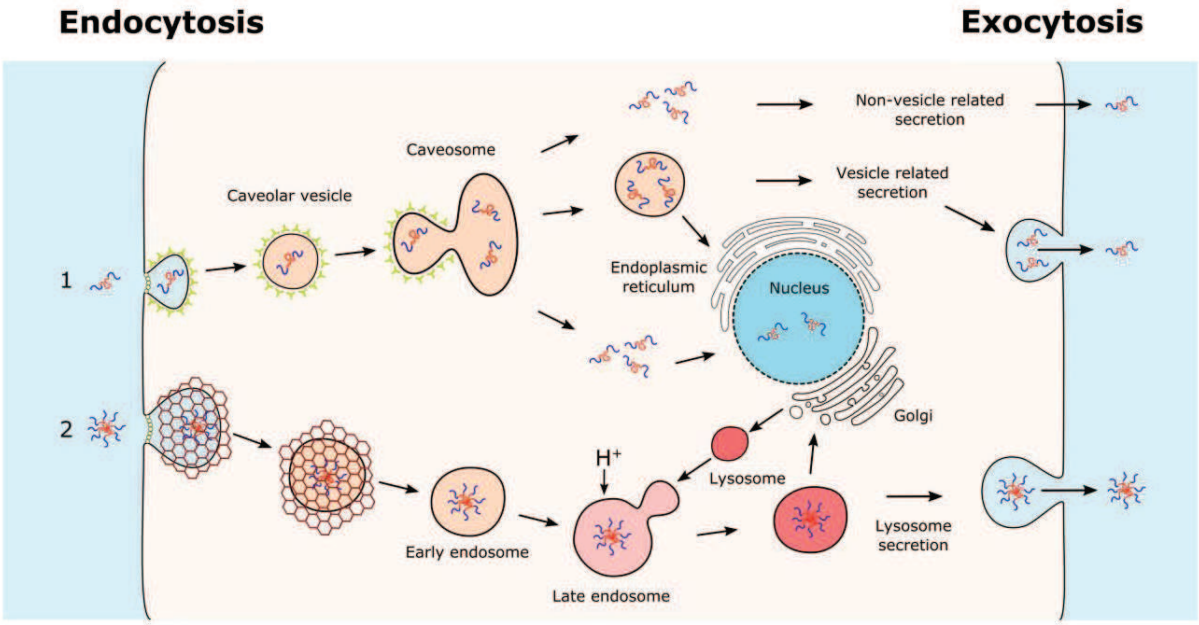

Figure 63. Endocytosis and exocytosis of Pluronic nanocarriers. Internalization of Pluronic unimers is mainly driven by caveolin-mediated endocytosis (1) and further transported to the endoplasmic reticulum *via* the caveosomes or released in the cytoplasm, where they can reach the cell nucleus. Pluronic stabilized micelles undergo internalization through clathrin-mediated endocytosis (2) where they are processed *via* the endosome-lysosome pathway and transported to the Golgi complex or remain trapped in the lysosomes. Exocytosis of Pluronic unimers occurs mainly through vesicle and non-vesicle secretion, while stabilized micelles are excreted through the lysosomes.

Our observation revealed that the most likely internalization pathway for cross-linked Pluronic micelles is through clathrin-mediated endocytosis with the formation of the lysosomes that later fuse with the Golgi complex or stay dispersed in the cytoplasm (Figure 60 and Figure 61). On the contrary, the predominant entry pathway for Pluronic unimers is through caveolae-mediated endocytosis with the caveosomes travelling to the endoplasmic reticulum or releasing the unimers in the cell cytoplasm. Our observations are in good agreement with previous studies using pathways inhibitors.[225-227] The unimers can thereafter reach the nucleus through passive diffusion if their size is smaller than the nuclear pore complex (Figure 60 and Figure 61). Moreover, it has been shown that caveolae trafficking leads to the endoplasmic reticulum and further to the mitochondria,[249] which can also explain the observed

sensitizing effects (specially ATP depletion) observed previously for other Pluronics in MDR cells.

Even though similar nanocarriers possess the same internalization pathway, we show that their ultimate intracellular localization depends on the nanocarriers composition and the cell line used. This is particularly important when defining new applications for each of the nanosystems. For example, the higher molecular weight Pluronic (F127) localized mostly in the perinuclear region, while the shorter one (P94) could diffuse into the cell nucleus. Due to the fact that the caveolae pathway escapes intralysosomal degradation, both Pluronics can be used to efficiently deliver chemotherapeutic drugs when they are covalently bonded to the block copolymers. On the one hand, Pluronic F127 can be potentially used to deliver paclitaxel to target the microtubules. On the other hand, drugs that have a mechanism of action in the cell nucleus (e.g. doxorubicin) can be more efficiently delivered by Pluronic P94. Both molecular systems are also very promising for siRNA therapy applications.[250]

4.3.1.5 Cellular uptake and exocytosis in HeLa Cells

Understanding the cellular internalization and subcellular localization is important to unveil potential intracellular applications. However, the amount of nanocarriers uptake is also crucial for certain therapeutic applications,[250] especially when a biological effect is expected from the nanocarriers.[102]

The quantification of cellular uptake in HeLa cells was determined by radiolabeling the DTPA-functionalized nanocarriers with the gamma-emitter ^{111}In and quantifying by scintillation as previously described in Chapter 3.

The nanocarriers with shorter PEO block (P94 and SPM-P94) were internalized at a higher level than the carriers with larger PEO length (F127 and SPM-F127), regardless of their aggregation state (Figure 64). It is commonly accepted that hydrophilic nanomaterials are less efficiently internalized, whereas hydrophobic nanocarriers are internalized in higher amounts.[230] The extensive hydration of the thick PEO block in the Pluronic F127 unimers and on the SPM-F127 surface (PEO ≈ 4250 g/mol) inhibited the adhesion of the carriers to the cell membrane reducing therefore their uptake (Figure 64). The shorter PEO block in the Pluronic P94 unimers and on the SPM-P94 surface

(PEO ≈ 1100 g/mol) led to an incomplete protection against cell adhesion and a higher uptake of these colloidal carriers by the target cells.

Regarding the aggregation state, although there were no significant differences between F127 and SPM-F127, the P94 unimers exhibited higher internalization than the SPM-P94 (Figure 64) showing that both the PEO block length and aggregation state play a role in the internalization.

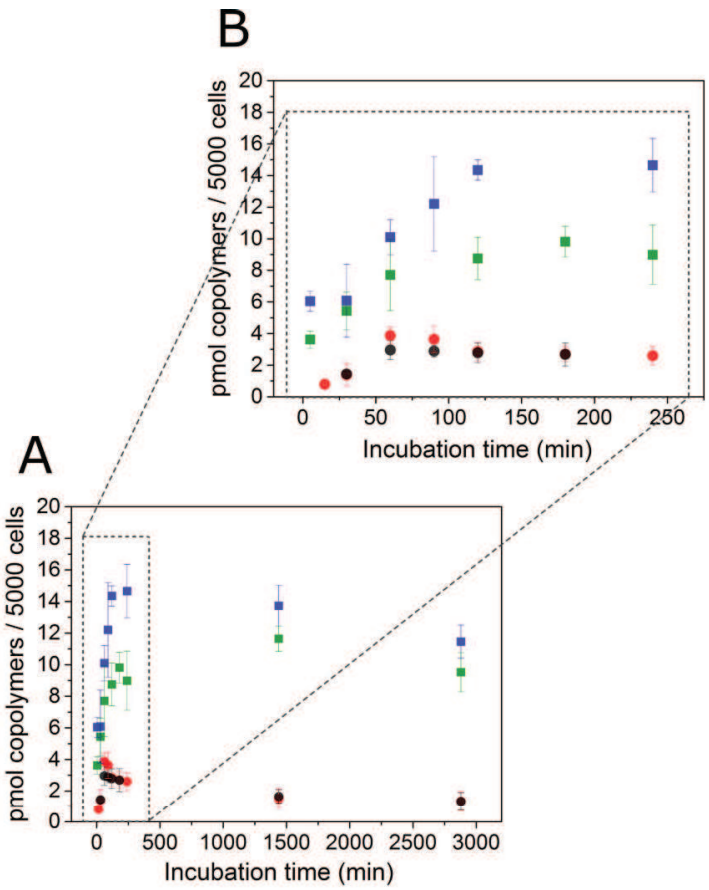

Figure 64. *In vitro* (A) cellular uptake of ^{111}In-radiolabeled Pluronic unimers and cross-linked micelles in HeLa cells as a function of incubation time (up to 48h), and (B) magnification of uptake at early time points (■ P94-DTPA-^{111}In, ■ SPM-P94-DTPA-^{111}In, ● F127-DTPA-^{111}In, ● SPM-F127-DTPA-^{111}In).

The total uptake at 48 hours varied between 0.7 to 2.6% from the total amount of radiolabeled sample incubated with the cells. Although the % of total uptake is relatively small, the maximum uptake of P94 and F127 unimers corresponds to 1.6×10^9 and 5×10^8 unimers per cell respectively, considering that the medium is evenly distributed and all cells internalize the same amount of nanocarriers.

This order of magnitude for the total percentage of uptake in monolayer cultures is consistent with other internalization studies where 0.5 to 3% of PEO-PCL micelles[251] and Pluronic P105[41] were internalized. The free DTPA-^{111}In complex was used as control as this small complex is practically not internalized by the cells and a total average uptake of 0.06% ± 0.02 at 48 hours was observed. After approximately 2 hours of incubation time (Figure 64), the uptake of nanocarriers appears to be complete and an apparent equilibrium between the internalized and the remaining nanocarriers in the cell medium is established.

The nanocarriers should also display high retention in diseased cells to increase the effectiveness of therapies. Thus, it is crucial to study the cellular retention of the nanocarriers after internalization by the cells. After cell uptake, the nanomaterials have three possible fates: degradation in lysosomes, exocytosis or accumulation inside the cells leading to cell toxicity and eventual death.[246] The exocytosis of the nanocarriers was studied by incubating the cells with the radiolabeled samples for 24 hours, and then replacing the cell medium with fresh one. Exocytosis was quantified by measuring the amount of ^{111}In activity retained in the cells after refreshing the medium (Figure 65).

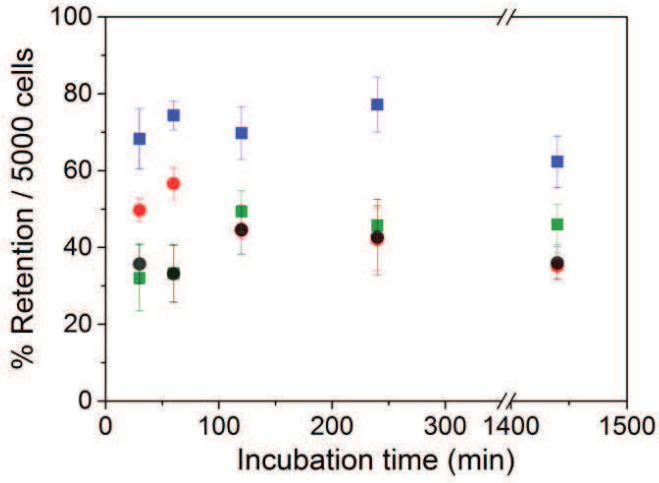

Figure 65. *In vitro* cellular retention of ^{111}In-radiolabeled Pluronic unimers and cross-linked micelles in HeLa cells. Cells were incubated with the radiolabeled samples for 24 hours, the cell medium was replaced with fresh medium, and the % of total activity retained in the cells was measured as a function of time up to 24 hours (■ P94-DTPA-^{111}In, ■ SPM-P94-DTPA-^{111}In, ● F127-DTPA-^{111}In, ● SPM-F127-DTPA-^{111}In).

We observed that the nanocarriers were released from the cells into the new medium, and that exocytosis is a very fast process - within 30 minutes equilibrium between the intracellular and extracellular radioactivity is reached. As verified in the uptake experiments (Figure 64), the nanocarrier with shorter PEO block (P94) was also retained more efficiently by the HeLa cells, i.e. ≈ 70% of the internalized Pluronic P94 unimers were retained. For all the other nanocarriers the retention was approximately 40%, within the level of experimental accuracy.

While the exocytosis of SPM-P94 was higher than P94 unimers, the exocytosis of F127 based nanocarriers was similar in both aggregation states (F127 and SPM-F127). Although we did not observe a direct effect of the aggregation state, the P94 unimers displayed a higher retention capacity over all the nanocarriers studied. Since the major exocytosis mechanisms are related to lysosome secretion, vesicle-related secretion, and non-vesicle-related secretion[252] (Figure 63), the less efficient exocytosis of P94 unimers can be related to their nuclear localization (Figure 60 and Figure 61). The reported toxicity[253] and the MDR effects observed previously with short and relatively hydrophobic Pluronics[227] can also be related to their higher cellular retention.

4.3.1.6 Clonogenic assay

Since internalization studies with Pluronic P94-FITC unimers revealed the nuclear translocation of this polymer, we investigated the potential use of Pluronic P94 for therapy using the Augers electrons emitted by the ^{111}In decay (see Chapter 1 section 1.3.1 for details on these effects). The radiolabeled P94-DTPA-^{111}In was incubated with HeLa cells and its clonogenic potential assessed by the colony-forming assay (Figure 66). While a cell may still reproduce a few times after exposure to toxic nanomaterials, they are considered dead if they can only go through one or two mitoses. A healthy cell that is not reproductively dead will proliferate and form a large colony of cells in a few days.[62] The clonogenic cell survival assay allows this evaluation because it tests the ability of a single cell to proliferate and to grow into a colony that can be visualized with the naked eye.

The clonogenic assay revealed that radiolabeled P94-DTPA-^{111}In is more toxic than non-radiolabeled P94-DTPA and the radiolabeled control DTPA-^{111}In (Figure 66). The complex DTPA-^{111}In was one of the controls because this complex is not internalized by HeLa cells and any observed effect not related to the Auger electrons would be related to external gamma-radiation toxicity. Although cells were still able to divide after exposure to 10 MBq of P94-DTPA-^{111}In, the appearance of cells is typical of apoptosis induction: membrane blebbing and cell shrinkage. This shows that P94-DTPA-^{111}In can be potentially used for Auger therapy.

Lower tested dose-activities (0.1 and 1 MBq) of either P94-DTPA-^{111}In or DTPA-^{111}In did not present significant alteration on the cells morphology or colony formation as compared to the control ones (images not shown).

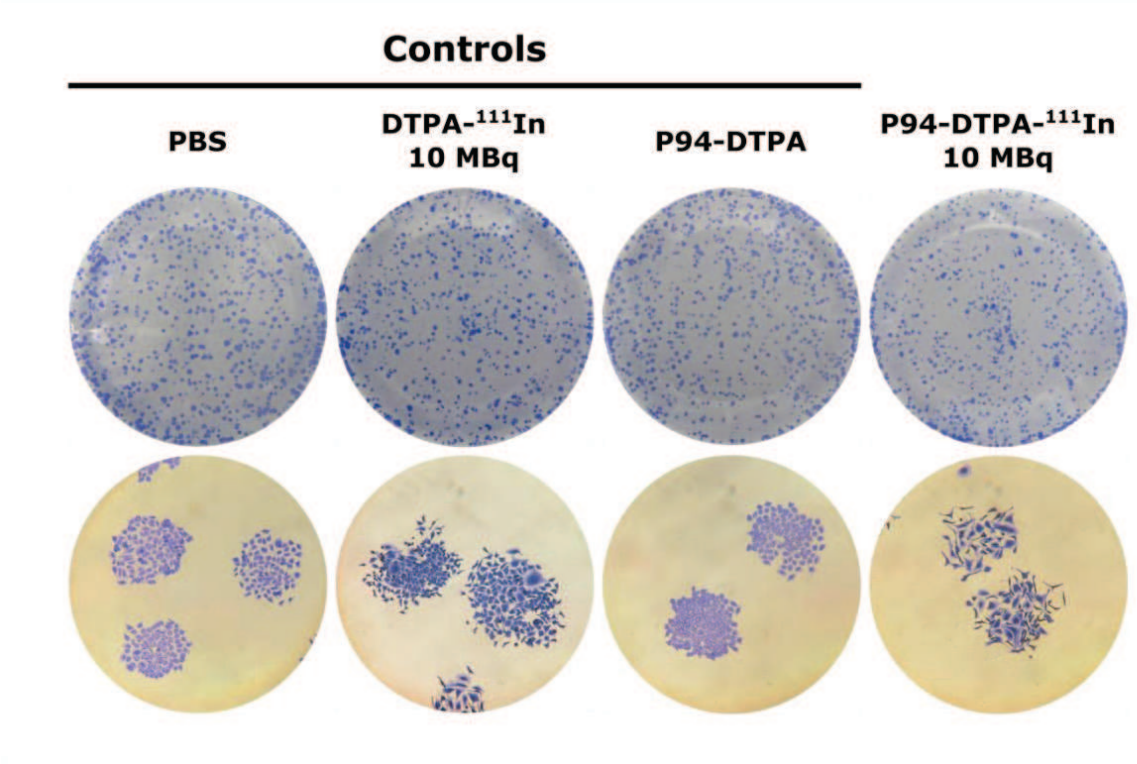

Figure 66. Colony formation assay used to assess the clonogenic potential of P94-DTPA-^{111}In nanocarriers for Auger therapy. Top are naked eye views pictures of the wells, and bottom are microscopy microphotographs of the colonies after exposure to the different carriers.

4.3.2 *In vitro* 3D studies

We showed that different intracellular distributions, internalization pathways, uptake and exocytosis are at play according to the composition (PEO block length) and aggregation state of Pluronic block copolymers. However, the high tumor cell density and the elevated interstitial fluid pressure of solid tumors[254] are the major obstacles for an efficient delivery of the nanocarriers into the tumor interstitium, and therefore for an efficient therapeutic effect.

In vitro spheroids are a much more suitable model to study the potential of nanocarriers for solid tumor therapy due to their similar phenotype. The actively dividing *in vivo* tumors resemble tumor spheroids because the cells located in the spheroid periphery are actively dividing such as the tumor cells adjacent to the blood capillaries, while cells in the center are quiescent, apoptotic or necrotic.[231, 232] These 3D cell culture models can better translate clinical efficacy predictions.

The cellular organization and morphology of the spheroids was analyzed by optical and confocal microscopy (Figure 67). We can observe that optical microscopy is not able to provide sufficient information regarding the structure of the spheroids but is rather usefull to determine their size. Therefore, we labelled the cells nuclei with a nuclear dye and observed the spheroids using confocal microscopy at a penetration depth of 80-100 µm and a section thickness of 10 µm. These images were then analyzed using ImageJ and the *Shape Index Map* option. This enables visualization of defined edges which in our case correspond to single cell nucleus. We can easily then verify the density and organization of cells in a spheroid with around 500-600 µm. The spheroid size is of utmost importance and determines the response to the nanocarriers. A small spheroid (<150 µm in diameter) can exhibit cell to cell and cell to matrix interactions and may also show an altered expression profile as compared to 2D cultures. However, the radial proliferative pathophysiological inward and outward gradients may not yet be found. To develop the chemical gradients (e.g. oxygen, nutrients, and catabolites), spheroids should have diameter between 200 and 500µm, and central necrosis will typically form at sizes >600µm. The establishment of these gradients and

the development of central necrosis varies with the cell line but is comparable to avascular tumors, micro-metastases and micro-regions of solid tumors.[233]

The generation of appropriate 3D multicellular aggregates of HeLa and U87 cells enabled then the study of the penetration and toxicity of the different nanocarriers.

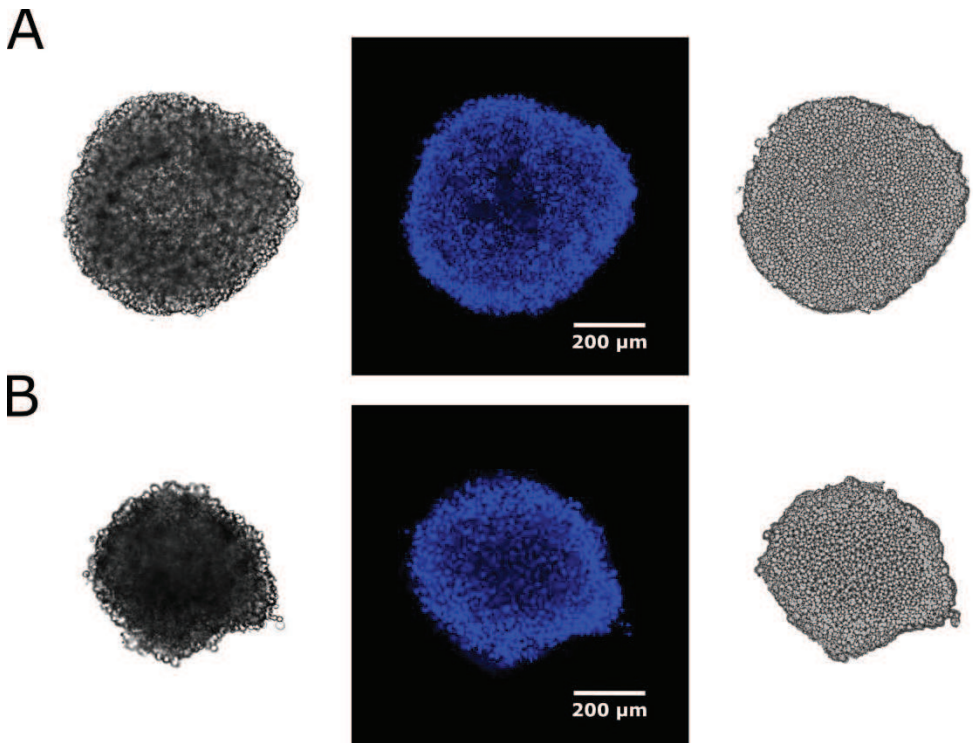

Figure 67. Tumor spheroids of (A) HeLa and (B) U87 cells labelled with Hoescht 33342. From left to right: optical microscope images, confocal images and analyzes of the confocal images using imageJ.

The biocompatible F127-based nanocarriers (F127 and SPM-F127)[253] were used to study the effect of copolymers aggregation state on the tumor penetration. The cytotoxicity exhibited by the P94-based nanocarriers (P94 and SPM-P94)[253] did not allow the study of their penetration due to the disintegration of the spheroids during their transfer to the confocal analysis chambers. Instead, the potential of P94-based nanocarriers to induce spheroid cytotoxicity was investigated.

4.3.2.1 Penetration of F127-based nanocarriers in tumor spheroids

The penetrating capacity of F127 unimers and SPM-F127 was observed after incubation of the FITC-functionalized samples with HeLa (Figure 68) and U87 (Figure 69) spheroids for different periods. Both nanocarriers penetrated the tumor spheroids, yet the penetrating and internalization capacity depended considerably on the aggregation state of the copolymers. The cross-linked micelles (SPM-F127) penetrated the spheroids more efficiently than the unimers (F127). Considering 20 μm as the average diameter of a HeLa cell (as measured by confocal microscopy), we observed that the penetration of F127 unimers was limited to three cell layers in HeLa spheroids (Figure 68) and five cell layers in U87 spheroids (Figure 69), while SPM-F127 reached up to seven cell layers in both spheroids types. Moreover, the area under the fluorescence curves showed that also the quantity of SPM-F127 that penetrated the spheroids was higher than the F127 unimers, and increased considerably overtime.

It has been reported that the penetration of molecules into the tumor interstitium is directly related to their diffusion coefficient, which decreases as the molecular weight increases.[255] Since the diffusion coefficient of the F127 unimers is higher than SPM-F127 due to their smaller size, the above results show that mere diffusion in the extracellular matrix (ECM) is not the dominant mechanism. This suggests that the penetration into the spheroids depends mainly on intracellular mechanisms. The internalization and subsequent exocytosis of the nanocarriers (transcellular transport) from one cell layer to another appear to be the mechanisms governing the penetration depth of the carriers. Very recently, Lu *et al.* showed that cross-linked p(HPMA-co-MAA)-b-PMMA micelles penetrated deeper into pancreatic spheroids compared to the uncross-linked micelles. The same group used collagen micro-spheroids to evaluate micelle diffusion ability in collagen to mimic the ECM and observed that the maximum penetration of micelles was limited to 20-30 μm.[256] Our results suggest that this mechanism of transcellular transport of the nanocarriers to reach the spheroids interstitium appears to be independent of nanocarriers composition.

One can expect that the rate of this mechanism will depend on many factors such as the cellular binding affinity, cellular uptake and exocytosis, cell density and spheroid compactness.[254, 257, 258] Indeed, we observed that the internalization kinetics of the nanocarriers varied in the 2D and 3D systems. In the 2D cell system, the uptake was independent of the aggregation state of the F127 copolymers, and reached an apparent equilibrium after few hours of incubation. In the 3D model, the penetration depended on the aggregation state of the copolymers, and the fluorescence intensity increased with time for several days. These results suggest the involvement of different uptake mechanisms in the 2D and 3D cell systems, and demonstrate the importance of selecting a suitable *in vitro* model according to the desired application.

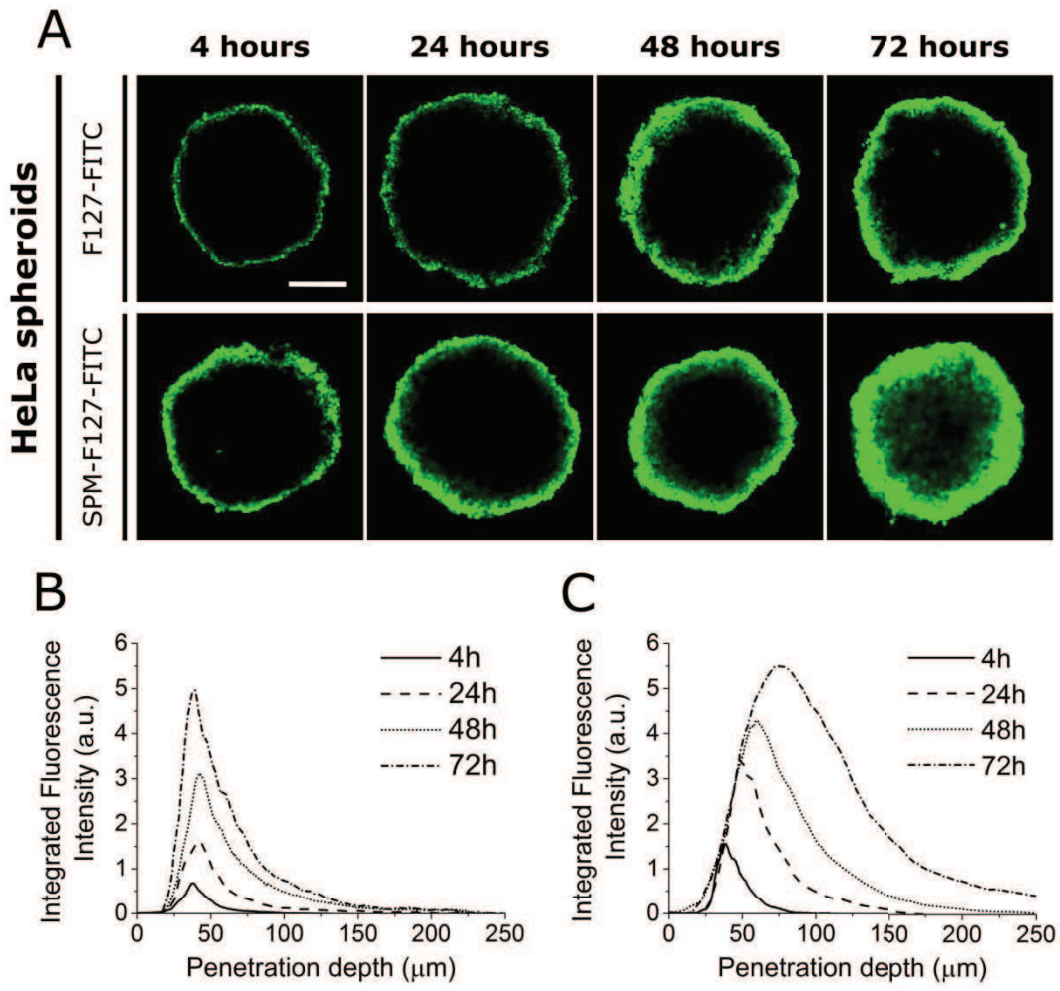

Figure 68. Penetration of Pluronic nanocarriers into HeLa spheroids. (A) Representative confocal laser scanning images of HeLa spheroids after incubation for different times with F127-FITC and SPM-F127-FITC, and radial fluorescence intensity profiles of (B) F127 and (C) SPM-F127-FITC at increasing incubation times. Confocal cross-sections of 10μm were acquired at a penetration depth of 80-100μm. Scale bar is 200μm.

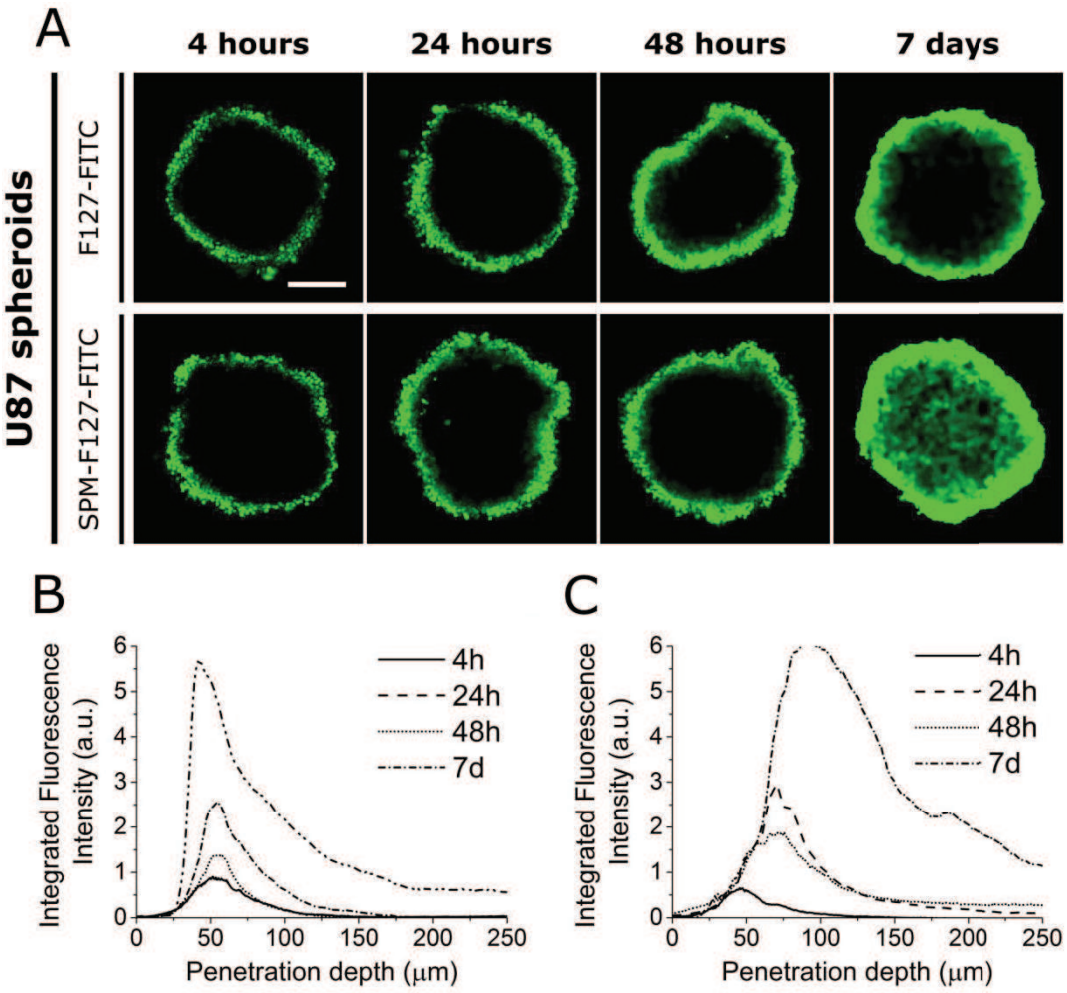

Figure 69. Penetration of Pluronic nanocarriers into U87 spheroids. (A) Representative confocal laser scanning images of U87 spheroids after incubation for different times with F127-FITC and SPM-F127-FITC, and radial fluorescence intensity profiles of (B) F127-FITC and (C) SPM-F127-FITC at increasing incubation times. Confocal cross-sections of 10μm were acquired at a penetration depth of 80-100μm. Scale bar is 200μm.

4.3.2.2 Spheroids toxicity in the presence P94 and SPM-P94

Pluronics with higher PPO content have shown to exert significant sensitizing effects in MDR tumors and can therefore represent an important advancement for the clinical treatment of MDR tumors when administered concomitantly with chemotherapeutic drugs. Moreover, while many chemotherapies present high efficacy in 2D cell models, their efficacy is reduced in the 3D cultures due to the higher MDR of cells in the 3D environment.[232]

We investigated the potential toxicity of the hydrophobic nanocarriers (P94 and SPM-P94) in 3D tumor spheroids using the previously observed toxic concentration in 2D cell cultures of NIH/3T3 fibroblasts (2500 µg/mL) (see section 4.3.1.2). The nanocarriers were able to induce significant toxicity in the 3D cell model (Figure 70). However, the observed effects depended on the cell line used. In the case of U87 spheroid, the exposure to P94 and SPM-P94 resulted in the decrease of the spheroid size, while the morphology was altered in the HeLa spheroids.

In the U87 spheroids, the size reduction can be explained by the progressive penetration of the nanocarriers into the tumor spheroids. The internalization and consequent cytotoxicity of the compounds to the peripheral cell layers results in their detachment from the spheroid surface, and the progressive overall decrease of the spheroid volume with increasing incubation time (Figure 70C). It is noteworthy that the incubation time required to achieve minimum spheroids growth inhibition was ≈48 hours. On the other hand, significant cytotoxicity was only observed at higher incubation times (> 48 hours), oppositely to the monolayer cultures of NIH/3T3 which required less than 48 hours.

The morphology of the HeLa spheroids is substantially affected. The cells become very loosely attached to each other's and the well-defined spheroid rim is lost as the incubation time increases in comparison to the control spheroid, which presents a well-defined spherical and compact structure (Figure 70A and B). The obtained results can be explained based on the different spheroids architecture such as the cell aggregates density and the available interstitial fluid space.[259-261] The aggregation state of the nanocarriers does not appear to significantly influence their toxicity.

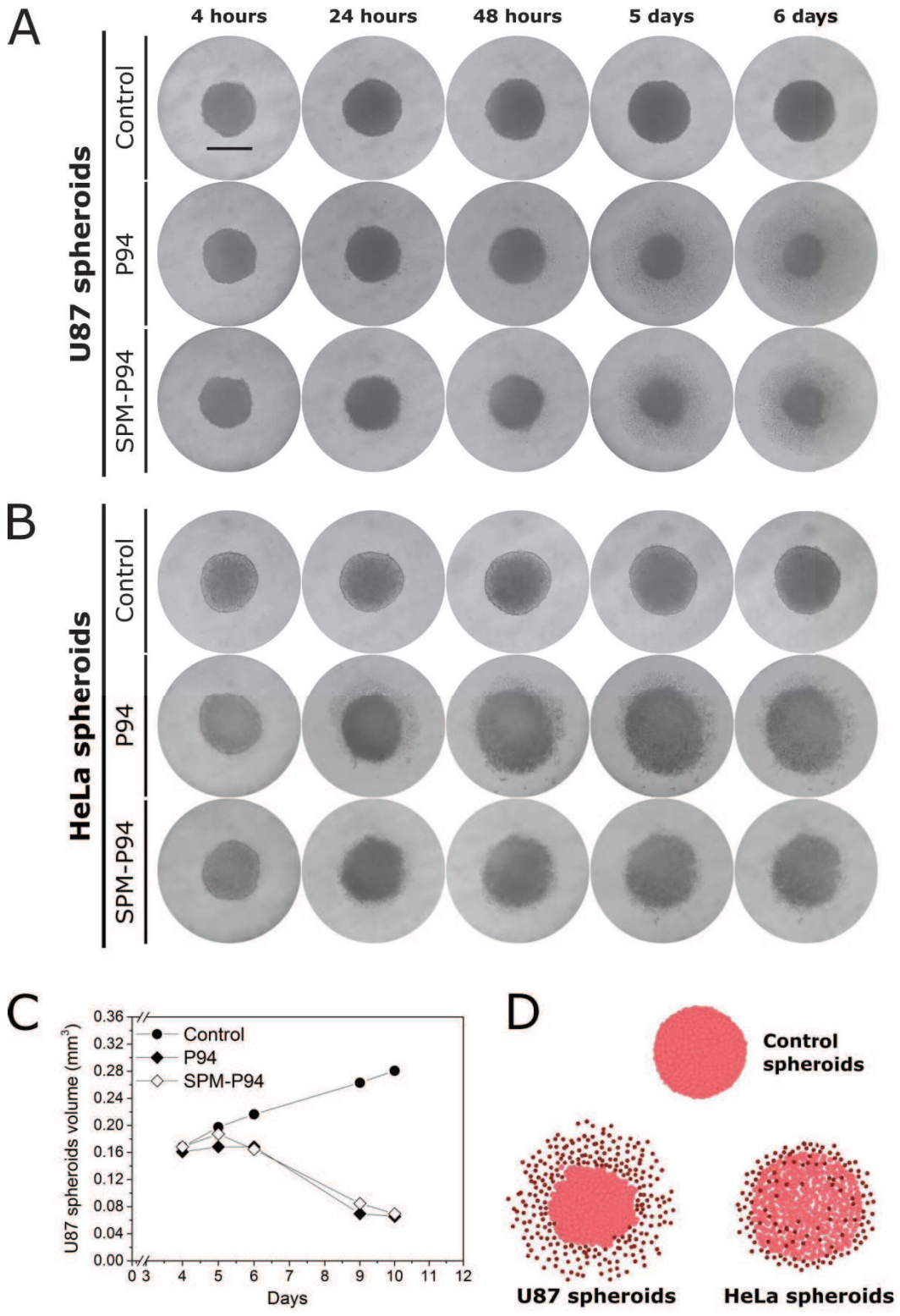

Figure 70. Representative optical images of (A) U87 and (B) HeLa tumor spheroids after exposure to a concentration of 2500 µg/mL of Pluronic P94 unimers and cross-linked P94 micelles (SPM-P94) for different incubation times; (C) evolution of U87 spheroids volume after exposure to the different samples compared to the non-exposed control, and (D) schematic representation of the morphological alterations of the spheroids according to the spheroid composition. Scale bar is 500µm.

4.4 Conclusions

Unmodified Pluronic unimers and cross-linked micelles were evaluated *in vitro* with healthy NIH/3T3 fibroblasts in relation to their cytotoxicity, and ability to load hydrophobic molecules and transport them across the cellular membrane. These cytotoxicity experiments demonstrated that the presence of PETA in the micelles core does not induce cellular toxicity in comparison to the respective pure polymer solutions. Furthermore, stabilized micelles of Pluronic P94 were shown to be less toxic than the polymer itself, and the biocompatibility properties of Pluronic F127 were kept after micelle stabilization.

The internalization studies with NIH/3T3 mouse fibroblasts revealed that the stabilized micelles were able to physically incorporate hydrophobic molecules (e.g. Nile Red), and deliver the hydrophobic components across the cellular membrane. Moreover, we showed that the encapsulated components are dispersed in the cytoplasm (either free or associated to endocytic vesicles) and do not associate with the mitochondria. Overall, these results indicate that Pluronic micelles stabilized by core cross-linking are capable of delivering hydrophobic components physically entrapped in the micelles, thus making them a potential candidate as a delivery platform for cancer therapy.

The chemical functionalized Pluronic unimers and cross-linked micelles with a fluorescent probe (FITC) and hydrophilic chelator (DTPA) linked to the PEO end group were used to visualize and quantify the nanocarriers in cancer cells. Particularly, the tracking of the nanocarriers with FITC and the cellular labelling of the lysosomes and nuclei allowed to accurately monitor their internalization and to probe their internalization pathways and intracellular localization. Our results revealed that the internalization pathways and ultimate cellular localization of the Pluronic nanocarriers depended largely on both the PEO block length and aggregation state of the block copolymers. On the one hand, Pluronic unimers presented distinct intracellular distribution patterns being dispersed in the cytoplasm, and around or even inside the nucleus. On the other hand, the cross-linked micelles were retained in the endolysosomal compartments as visualized by co-localization with the lysosomes. The nuclear translocation observed with the low molecular weight Pluronic P94 suggests that low molecular weight unimers can be potentially

used for Auger or gene-therapy applications. The clonogenic potential of P94-DTPA-^{111}In for Auger-therapy was therefore analyzed and significant alteration in the cells morphology and on the colonies was observed. Pluronic P94 unimers might be therefore very promising for radiation therapy, particularly when considering intratumoral therapy.

The radiolabeling of the carriers with ^{111}In also enabled the quantification of their uptake and exocytosis kinetics. The carriers with shorter PEO length (P94 and SPM-P94), and therefore relatively more hydrophobic, were internalized in higher amounts by HeLa cells. Particularly, the smallest nanocarriers (P94 unimers, R_H~2 nm) displayed the highest cellular uptake and retention.

3D tumor spheroids of HeLa and U87 cells were used to study the penetration capacity and toxicity potential of the nanocarriers. Results revealed that cross-linked F127 micelles penetrated deeper and were therefore delivered more efficiently across the tumor spheroids compared to the corresponding F127 unimers. The results also suggest that the transcellular transport of the nanocarriers (endocytosis and exocytosis) governs their penetration depth. Finally, the remarkable toxicity of Pluronic P94-based nanocarriers (both unimers and cross-linked micelles) observed in the tumor spheroids endows great potential of these formulations for tumor therapy applications. However, the toxic effect is significantly influenced by the spheroid cellular type.

In this chapter we showed that by varying the physicochemical properties of Pluronics copolymers, such as the PEO block length, relative hydrophobicity and aggregation state, it is possible to activate different internalization pathways, reach distinct intracellular compartments, tune and optimize the uptake and exocytosis, and ultimately increase tissue penetration and toxicity. We also demonstrate how nanocarriers display different behaviors depending on the 2D and 3D nature of the *in vitro* model.

Understanding the effects of the physicochemical properties of the nanocarriers on the cellular interactions is essential in the design and development of nanoengineered polymeric nanocarriers to target specific diseases.

CHAPTER 5

Biodistribution of Pluronic nanocarriers

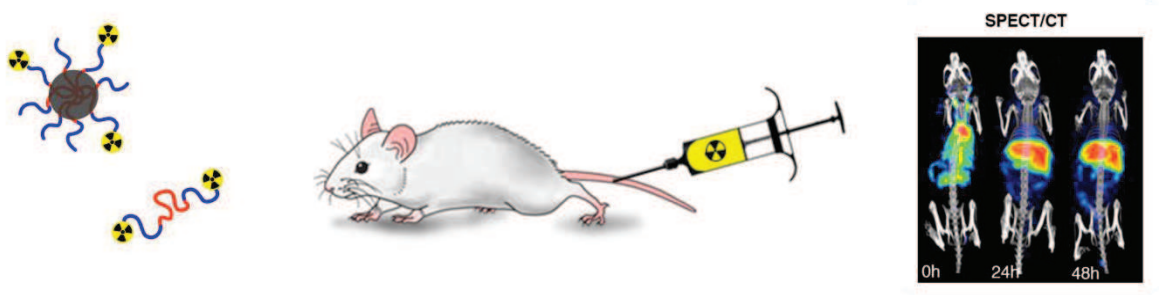

Pluronic block copolymers have largely been used for clinical applications. However, an appropriate assessment of the biodistribution of Pluronic nanocarriers with different composition and aggregation state has not yet been reported. In this chapter, we present the biodistribution of the Pluronic nanocarriers with different PEO block length and aggregation state (unimers *versus* stabilized micelles) developed in Chapter 3. The nanocarriers radiolabeled with the diagnostic isotope ^{111}Indium were used to evaluate the *in vivo* distribution of the different nanocarriers after intravenous injection by SPECT/CT imaging in healthy A/J mice.

This study shows that the renal and liver clearances of Pluronic nanocarriers can be tuned by varying the PEO block length and aggregation state. The assessment of the critical parameters determining their elimination is a necessary step towards the design of more efficient nanocarriers.

5.1 Introduction

To our knowledge, despite the broad use of Pluronics in pharmaceutical formulations, most *in vivo* studies carried out so far have evaluated the pharmacokinetics of the drugs incorporated in the nanocarriers rather than the biodistribution of the nanocarriers themselves. Moreover, drugs can rapidly disassociate from the nanocarriers once in circulation if they are not covalently attached and the pharmacokinetics might reflect poorly the biodistribution of the nanocarriers. Therefore, the design of more efficient nanocarriers requires specific studies dedicated to the evaluation of their biodistribution prior to their functionalization.

Very few groups have studied the *in vivo* biodistribution of Pluronic nanocarriers.[56, 229, 262, 263] Kabanov *et al.* studied the effect of the aggregation state on the biokinetics of Pluronic ^{3}H-P85 (M_n=4600 g/mol, $PEO_{26}PPO_{40}PEO_{26}$) using different polymer doses. They showed that the biodistribution between unimers and micelles did not differ significantly, and renal filtration was the main clearance mechanism for both systems. However, the circulation time depended on the aggregation state varying from 60-70 hours for the low concentrations (0.02%) and up to 90h for the highest concentrations (1%).[56] The biodistribution of Pluronics F68[229, 262] (Mn=8400, $PEO_{76}PPO_{29}PEO_{76}$) and F38[263] (Mn=4700, $PEO_{19}PPO_{17}PEO_{19}$) showed a fast initial renal clearance (≈40% of the ID was recovered after 24 hours in the urine of dogs) followed by a gradual decrease of the Pluronic concentration in the blood. The tissues with the highest concentration of ^{14}C-F68 were the kidneys, liver, spleen, bladder, gastrointestinal tract and lungs.[229] They also reported maximum uptake of Pluronic ^{3}H-F68 in the liver and bile 24 hours post-injection.[262] In rats, 94% ID of Pluronic ^{14}C-F38 was excreted in the urine in 3 days, and the remaining 6% appeared in the feces.[263] Previous studies have also shown that Pluronics accumulate mostly in the kidneys and liver but do not induce any nephro- or hepato-toxicity.[229, 264]

In this chapter, we assessed the biodistribution of Pluronic nanocarriers with different PEO block length and aggregation state (unimers *versus* stabilized micelles). Two Pluronic copolymers (P94 and F127) with different molecular weight and PEO length were used, and Pluronic micelles were stabilized against temperature and dilution effects as described in Chapter 3. The functionalization of Pluronic unimers with the hydrophilic chelator DTPA, also described in Chapter 3, enabled radiolabeling of the nanocarriers with the gamma-emitting radioisotope ^{111}Indium (^{111}In). This gamma emitting isotope was selected as a molecular imaging agent due to its prolonged physical half-life (2.8 days) which allows the non-invasive imaging for a long period after the administration of the radioactive compounds. This makes this isotope suitable for imaging of compounds with prolonged blood circulation.

Monitoring of longitudinal *in vivo* biodistribution of the nanocarriers after intravenous injection was achieved by Single-Photon Emission Computed Tomography (SPECT)[265] (Figure 71) in healthy A/J mice. In addition, the early biokinetics of the most frequently applied Pluronic (F127) was also investigated using a fast dynamic SPECT scan 15 min immediately after injection.[266]

A dedicated ultra-high-sensitivity small animal pinhole collimator was used to enable high image resolution with small amounts of activity (Figure 71).[266] The resolution of the pinhole collimator was determined using ^{99m}Tc phantom scans (Figure 72). The smallest visible rod diameter for 30 min acquisition was 0.85 mm, while in 5 min acquisitions only 1.1 mm rods can be seen for all activities used.[266]

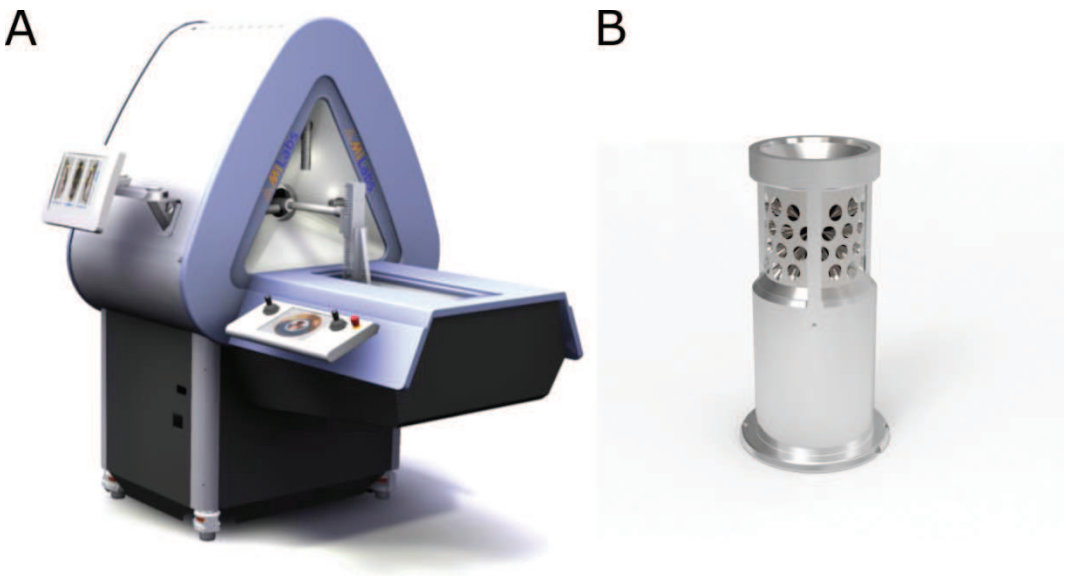

Figure 71. (A) U-SPECT^{+}/CT scanner and (B) ultra-high-sensitivity mouse pinhole collimator (MILabs, The Netherlands) used in the *in vivo* studies of Pluronic nanocarriers.

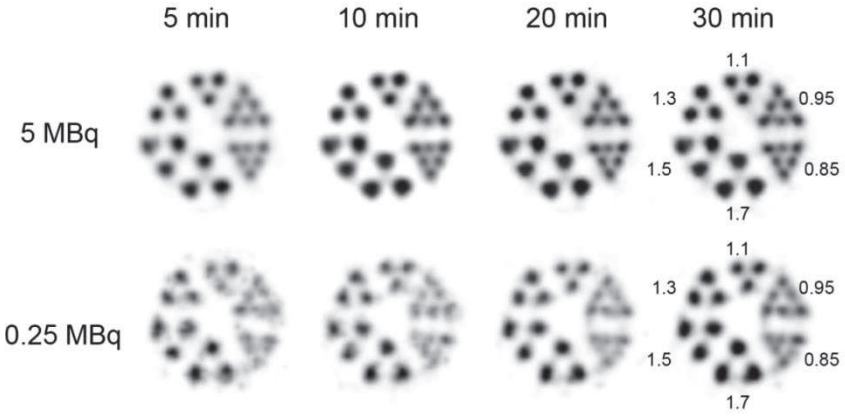

Figure 72. ^{99m}Tc resolution phantom scans (5 and 0.25 MBq) for different acquisition times (5, 10, 20, and 30 min).[266]

5.2 Experimental section

5.2.1 Preparation of radiolabeled nanocarriers

Functionalized Pluronic unimers (F127-DTPA and P94-DTPA) and stabilized micelles (SPM-F127-DTPA and SPM-P94-DTPA) were radiolabeled by diluting in 1X PBS buffer (pH 7.4) and adding 75 MBq of $^{111}InCl_3$ to each sample at room temperature and incubating for 30 min. Quality control of radiochemical purity was evaluated by TLC using EDTA:NH_4Ac (1:1) (v:v) (0.1 M, pH 5.5) as the eluent (see Chapter 3 section 3.3.6).

Samples presenting a labelling efficiency of more than 95% were used without further purification (P94 and F127). Samples with a lower coupling efficiency (SPM-P94 and SPM-F127) were further purified by addition of free DTPA to the labelling mixtures and by subsequent elution through a prepacked PD10 column using 1X PBS as the eluent as described in in Chapter 3 section 3.3.6.4. The purification efficiency for the eluted fractions was also evaluated by TLC. After radiolabeling and purification when required, all samples presented > 95% of radiochemical purity.

5.2.2 Animal handling

Animal experiments were performed with A/J mice according to protocols approved by the Animal Ethical Committee of the UMC Utrecht and in accordance with Dutch Law on Animal experimentation.

SPECT/CT imaging was used as a noninvasive method to access circulation dynamics and tissue deposition of ^{111}In-labelled compounds. Eight mice were divided into four study groups of 2 animals and assigned for imaging with F127-DTPA-^{111}In, SPM-F127-DTPA-^{111}In, P94-DTPA-^{111}In and SPM-P94-DTPA-^{111}In. All animals were anesthetized with isoflurane and injected with the radioactive compounds in the tail vein. Average injected activities were 3.6 MBq and 0.014 g/kg of compound. In detail, 2.2 MBq of F127-DTPA-^{111}In (220 µg, 0.008 g/kg), 3.5 MBq of SPM-F127-DTPA-^{111}In (480 µg, 0.017 g/kg), 5.2 MBq of P94-DTPA-^{111}In (450 µg, 0.016 g/kg) and 3.6 MBq of SPM-P94-DTPA-^{111}In (420 µg, 0.015 g/kg) were injected.

Total body SPECT/CT scans of 30 minutes were acquired at 0 (immediately after injection), 24 and 48 hours post-injection (p.i.). Early stage dynamics of F127-DTPA-^{111}In and detailed information on late-stage biodistribution of the compounds in the abdominal area and liver of the animals were obtained following specific protocols.

For the early stage dynamics of F127-DTPA-^{111}In, one mouse from the F127-DTPA-^{111}In study group was anesthetized and a tail vein catheter was applied. The animal was injected with the compound just after the start of the dynamic SPECT acquisition with 15-second frames.

After the end of the 48 hours p.i. total body scans, an additional 30 minutes scan was performed focusing on the abdominal area to acquire information on late-stage biodistribution in the spleen and liver. After the end of imaging sequence, all animals were sacrificed via cervical dislocation.

5.2.3 SPECT/CT imaging and data analyzing

Animals were imaged in U-SPECT^{+}/CT scanner (MILabs, the Netherlands) (Figure 71). This system is equipped with three stationary scintillator detectors that are arranged in triangular setup and an integrated X-ray micro-CT scanner.[265]

The SPECT scans were acquired in list-mode data format. An ultra-high-sensitivity mouse pinhole collimator was used.[266] After this, SPECT image reconstructions were carried out with a Pixel-based Order-Subset Expectation Maximization (POSEM)[267] algorithm that included resolution recovery and compensation for distance-dependent pinhole sensitivity.[268] All reconstructions were performed with the use of 4 subsets, 12 iterations and an isotropic 0.4-mm-voxel grid. Triple-energy-window based Compton scatter correction according to King et al.[269] with 4% background windows and a 20% photo-peak energy window centered at 171 keV was performed. Effects of gamma-attenuation in the animal and bed were corrected, after which absolute quantification of SPECT images was enabled using a scaling factor that was obtained from scanning a small ^{111}In source with known activity.[270]

Corresponding total body CT scans were acquired with a tube setting of 55 kV and 615 µA. In total 2 frames of 182 projections over 360° were acquired in step and shoot rotation mode. The acquired CT projection data was reconstructed using SkyScan NRecon software to generate a 3D CT image on 0.1693x0.1693x0.1695mm voxel grid. After this, reconstructed SPECT images were co-registered to CT images (U-reg-v1.26c, MILabs, The Netherlands).

To calculate the uptake of radiolabeled micelles in the organs of interest, the registered and quantitative 3D SPECT images were analyzed using biomedical image analyzing software (PMOD 3.6, Zurich, Switzerland). A 3D region-of-interest (ROI) was manually drawn to encompass the radioactivity uptake in the organ whose boundary was delineated in the 3D CT images. Separate ROI's were drawn for the radioactivity uptakes in the heart, liver, spleen, left and right kidneys, and lungs. The % of injected dose (ID) per mL of tissue volume (ID/mL) value was calculated for every imaging time point using Equation 19:

Equation 19
$$\text{ID/mL of tissue [\%]} = \frac{\text{Total activity in the ROI (MBq)}}{\text{Volume of the ROI (mL) x Total injected dose (MBq)}} \text{x}100$$

For visual representation in the text, reconstructed volumes were filtered with 1.2 mm FWHM 3D Gaussian filter, after what maximal intensity projections (MIPs) were generated. Bladder of the animal was manually cropped out from the early stage SPECT scans (0 hours post injection time point) of all animals. Time-activity curves (TACs) derived from dynamic SPECT scans were generated from manually drawn 3D ROI's, using decay-corrected but otherwise unprocessed images, reconstructed as a dynamic frame sequence.

In vivo imaging was performed as a hands-on formation to SPECT supervised by the project partner O. Ivashchenko at MILabs (Utrecht, The Netherlands) under the framework of the "TRACE'nTREAT" project. Image analysis and reconstruction was also performed by the project partner.

5.3 Results and Discussion

After functionalization of the nanocarriers with the chelator DTPA and radiolabeling with the gamma-emitter ^{111}In, we studied their biodistribution as a function of PEO block length and aggregation state. The PEO block length in F127 nanocarriers is four times larger than in Pluronic P94 carriers (see Table 8). The development of a process to stabilize the Pluronic micelles (see Chapter 3 section 3.3.1) enabled the study of the effect of aggregation state by comparing the molecular (F127 and P94) and supramolecular carriers (SPM-F127 and SPM-P94).

Samples were administered below the cmc, i.e. the final concentration in the blood pool was ≤0.025% to assure comparison of molecular and supramolecular nanocarriers, considering a maximum of 20-time dilution of the injected dose in the blood.

During imaging, it is important to optimize animal health status and anesthesia. Monitoring under anesthesia is carried out by evaluating cardiovascular system (pulse rate, ICG and blood pressure), respiratory system (respiratory rate, $PaCO_2$ and PaO_2), and central nervous system (temperature and depth of anesthesia).

5.3.1 Biodistribution in healthy mice

The total activity remaining in the animal body after 30 min, 24 and 48h post-injection (p.i.) was analyzed using quantitative SPECT scans (Table 11) that were corrected for photon attenuation and scatter.

Table 11. Total body activity retention of Pluronic nanocarriers in the body of the animal 30 min, 24 and 48h post-injection (p.i.), measured from total body SPECT scans and expressed as the % of initially injected dose (ID).

	Total body retention in % ID		
Compound	**30 min**	**24 h**	**48 h**
F127-DTPA-^{111}In	81.3±2.5	72.1±2.3	66.1±2.0
SPM-F127-DTPA-^{111}In	80.9±1.6	70.9±1.8	60.5±2.3
P94-DTPA-^{111}In	67.7±2.4	46.8±2.3	40.2±1.5
SPM-P94-DTPA-^{111}In	62.3±2.5	34.1±2.1	33.6±1.9

Figure 73 and Figure 74 represent top view maximal intensity projections (MIPs) on total body SPECT/CT scans at various time points after administration of ^{111}In radiolabeled Pluronic nanocarriers. For better visualization, the activity in the bladder during early stage scans (0h post-injection) was manually cropped from the SPECT images. The corresponding uptake in different organs, expressed as % of injected dose per mL of tissue volume (ID/mL) at different time points was determined after image analysis and is shown in Table 12.

Initial renal clearance

A fraction of the radiolabeled compounds was excreted into the bladder almost immediately after i.v. administration of the radiolabeled compound (Table 11).

The P94 unimers showed higher initial clearance when compared to the F127 unimers. Both Pluronic unimers are close to the renal cut-off, which is 30 kDa for linear PEG[271] or 5.5 nm[4], and the renal filtration observed here depended on their PEO block length and therefore different molecular weight: ≈20% of the injected dose (ID) of Pluronic F127 (12 kDa, 2.9±0.2 nm) and ≈30% ID of Pluronic P94 (5 kDa, 2.1±0.2 nm) were eliminated 30 min p.i..

The stabilized micelles (SPM-F127-DTPA-^{111}In and SPM-P94-DTPA-^{111}In) also presented initial renal clearance, which was faster for the SPM-P94-DTPA-^{111}In. High initial clearance of polymeric micelles and small nanoparticles with DTPA-^{111}In chelates in the surface is not uncommon.[212, 272, 273] Here, the fast clearance of SPM-P94-DTPA-^{111}In (Table 11) could be attributed to its lower stability in serum (Figure 48) and could correspond solely to the elimination of ^{111}In-protein complexes. Thus, increased instability of the complexes *in vivo* could also explain the initial fast clearance of the three other nanocarriers.

After the initial renal clearance, Pluronic unimers and micelles follow general pharmacokinetics with specific organ biodistribution.

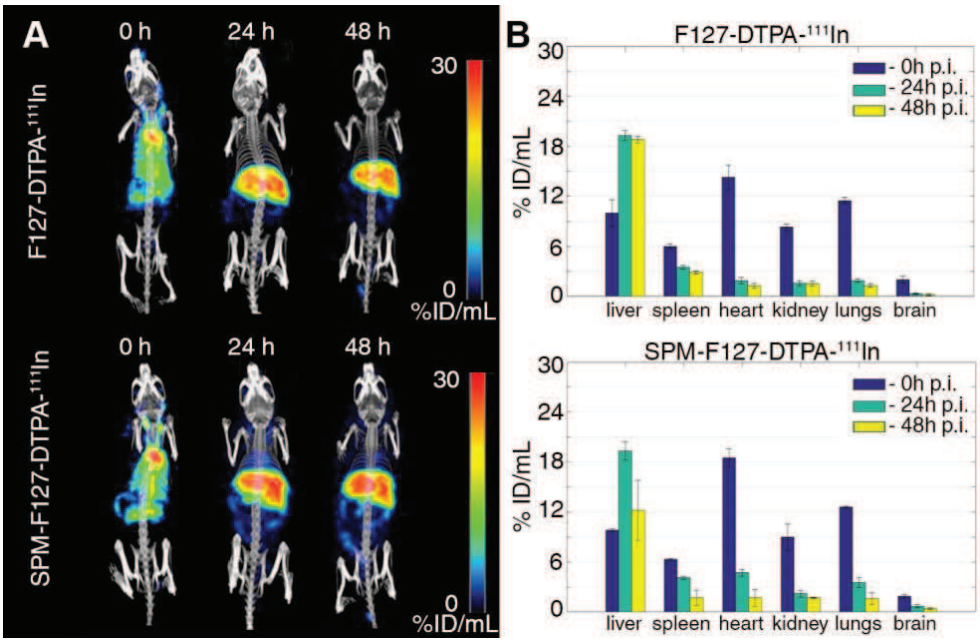

Figure 73. (A) Maximal intensity projections of total body SPECT/CT scans, acquired at 0, 24 and 48 hours post injection of F127-DTPA-^{111}In (top) and SPM-F127-DTPA-^{111}In (bottom). (B) Quantified uptake of the carriers in the selected organs of interest.

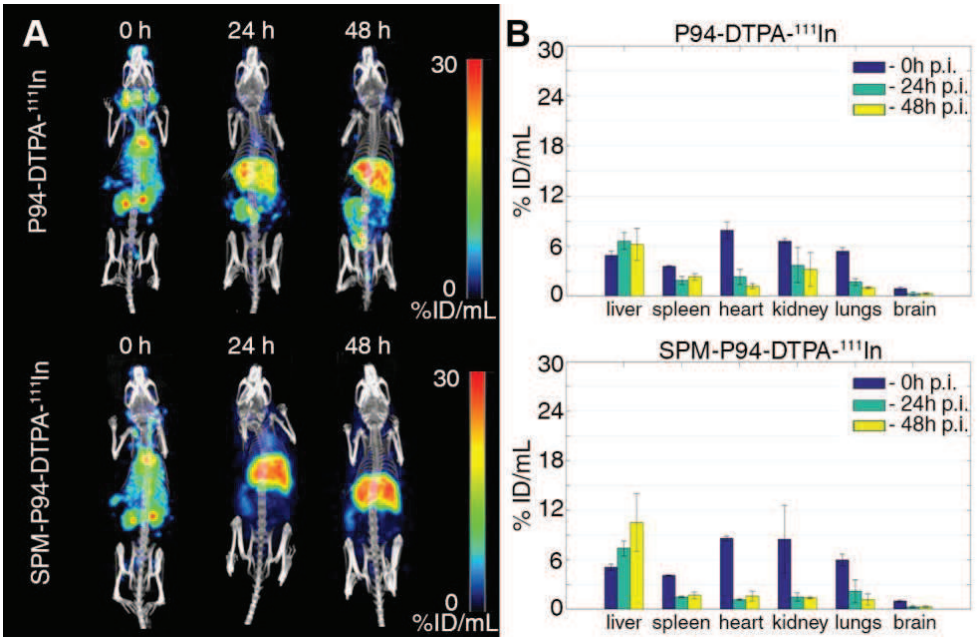

Figure 74. (A) Maximal intensity projections of total body SPECT/CT scans, acquired at 0, 24 and 48 hours post injection of P94-DTPA-^{111}In (top) and SPM-P94-DTPA-^{111}In (bottom). (B) Quantified uptake of the carriers in the selected organs of interest.

Table 12. Accumulation rates of ^{111}In-labelled Pluronic nanocarriers in the heart, liver, spleen, lungs, kidney and brain of the animals at 0, 24 and 48 hours post-injection (p.i.) time points, expressed as % injected dose per mL of tissue volume (ID/mL).

	Heart			**Liver**			**Spleen**		
	ID/mL [%]			ID/mL [%]			ID/mL [%]		
Compound	0h	24h	48h	0h	24h	48h	0h	24h	48h
F127-DTPA-^{111}In	14.3±1.5	1.9±0.4	1.3±0.3	10.0±1.6	19.3±0.6	18.8±0.3	6.0±0.3	3.5±0.2	2.9±0.2
SPM-F127-DTPA-^{111}In	18.5±1.1	4.7±0.4	1.8±1.0	9.8±0.2	19.3±1.1	12.2±2.5	6.3±0.1	4.1±0.2	1.7±0.9
P94-DTPA-^{111}In	7.9±1.0	2.3±0.9	1.2±0.3	4.9±0.5	6.6±1.0	6.2±1.9	3.6±0.1	1.9±0.5	2.3±0.4
SPM-P94-DTPA-^{111}In	8.6±0.3	1.2±0.1	1.6±0.6	5.1±0.4	7.4±0.9	10.5±3.5	4.1±0.1	1.5±0.1	1.7±0.4

Continuation of Table 12. Accumulation rates of $^{111In\text{-}labelled}$ Pluronic nanocarriers in the heart, liver, spleen, lungs, kidney and brain of the animals at 0, 24 and 48 hours post-injection (p.i.) time points, expressed as % injected dose per mL of tissue volume (ID/mL).

	Lungs			**Kidney**			**Brain**		
	ID/mL [%]			ID/mL [%]			ID/mL [%]		
Compound	0h	24h	48h	0h	24h	48h	0h	24h	48h
F127-DTPA-^{111}In	11.5±0.4	1.9±0.2	1.3±0.2	8.3±0.4	1.6±0.3	1.5±0.3	2.0±0.4	0.3±0.1	0.2±0.1
SPM-F127-DTPA-^{111}In	12.6±0.1	3.5±0.6	1.6±0.7	9.0±1.6	2.2±0.4	1.7±0.1	1.9±0.2	0.7±0.2	0.4±0.1
P94-DTPA-^{111}In	5.4±0.4	1.7±0.4	1.0±0.1	6.6±0.3	3.7±2.1	3.2±2.0	0.9±0.2	0.3±0.2	0.3±0.1
SPM-P94-DTPA-^{111}In	6.0±0.7	2.2±1.4	1.2±0.7	8.5±4.1	1.5±0.5	1.4±0.1	1.0±0.1	0.3±0.1	0.3±0.1

Hepatobiliary distribution

We can verify that the organ with the highest uptake of the radioactive compounds is the liver (see Figure 73, Figure 74 and Table 12). In particular, ≈20% ID/mL of F127-DTPA-^{111}In nanocarriers were accumulated in the liver at 48 hours p.i..

Nanomaterials can accumulate in the liver through internalization by the hepatocytes, the liver sinusoidal endothelial cells, or by Kupffer cells. The endothelium of the liver sinusoids presents fenestrations of around 140 nm in mice,[274] which allow the entry of blood components in the perisinusoidal space and thereafter in the liver parenchyma composed by the hepatocytes. The hepatocytes are responsible for metabolizing and excreting foreign material into the bile which is then eliminated through the intestinal tract. The Kupffer cells are macrophages located at the lining of the liver sinusoids and are highly specialized in phagocytizing components that were previously opsonized in the circulation. While nanomaterials processed by Kuppfer cells can only be degraded intracellularly and, if not, they remain within the cells and retained in the body, metabolisation by hepatocytes will lead to their elimination through the bile and intestinal tract.[34, 275, 276] Given the size of the endothelial fenestrations in the liver, materials smaller than the fenestrations cut-off can leave the systemic circulation and be internalized by the hepatocytes.

The liver uptake of the F127 unimers and cross-linked micelles (SPM-F127 and SPM-P94) increased approximately two times from 0 to 24h (Table 12) revealing that recognition by the reticuloendothelial system (RES) was delayed. In the case of P94 unimers, the uptake in the liver did not increase significantly during the 48h suggesting that the elimination of P94 unimers occurs mainly through other pathways, e.g. renal filtration. In fact, the accumulation of P94-DTPA-^{111}In in the kidney was consistently higher than any of the other nanocarriers. The retention in the liver at 48h was influenced by the aggregation state of the copolymers. In particular, SPM-P94-DTPA-^{111}In were more retained (10.5±3.5% ID/mL) than the respective P94 unimers (6.2±1.9% ID/mL), while SPM-F127-DTPA-^{111}In were more efficiently excreted (12.2±2.5% ID/mL) than the corresponding F127 unimers (18.8±0.3% ID/mL) (Figure 12).

Therefore, high uptake in the liver was associated with a higher PEO block length, while the retention was influenced by the aggregation state of the copolymers and either increased or decreased according to the polymer composition.

The abdominal area of the animals was further analyzed on fused late-stage SPECT/CT slices through the coronal and axial areas of the animals (Figure 75). The obtained coronal sections are presented in Figure 76.

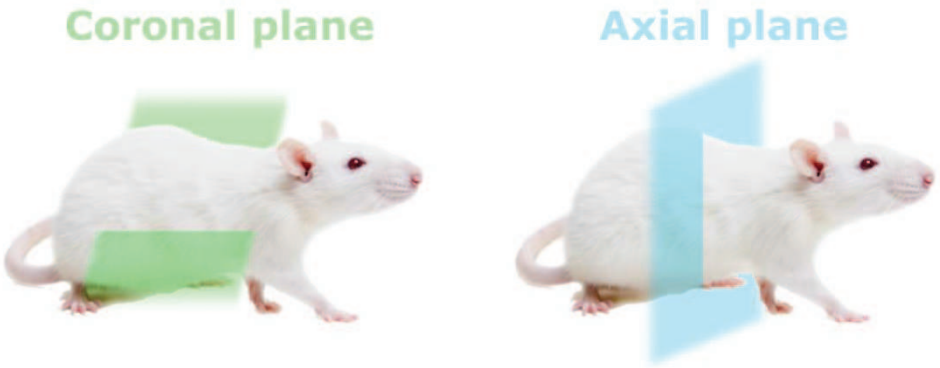

Figure 75. Abdominal coronal and axial planes for focused SPECT/CT scans.

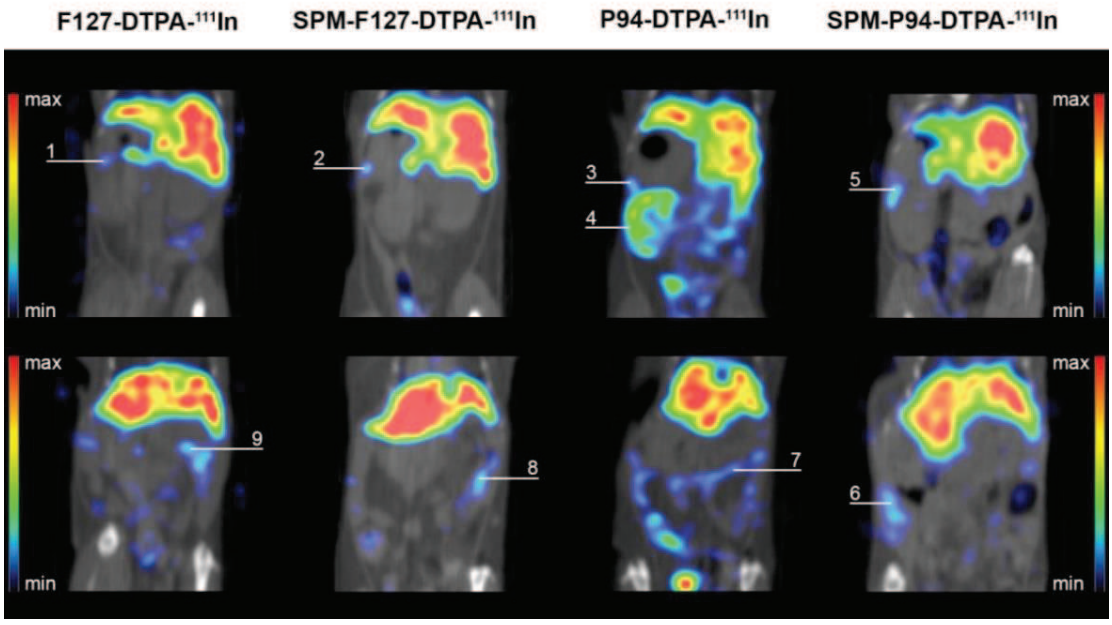

Figure 76. Abdominal area of the 48 hours p.i. scans of mice injected with F127-DTPA-^{111}In, SPM-F127-DTPA-^{111}In, P94-DTPA-^{111}In and SPM-P94-DTPA-^{111}In. Images illustrate uptake in the spleen (1-3,5) and the intestines (6-9) for all compounds tested. At the same time, only P94-DTPA-^{111}In showed minor trapping of the compound in the renal cortex of the animal (4).

We observed at late time points (24 and 48 hours) activity in the intestines for all compounds tested (Figure 76), showing that the nanocarriers were excreted via the hepatobiliary system and therefore metabolized by the hepatocytes.

A higher spreading of the P94 unimers into the surrounding tissues of the gastrointestinal tract was observed (Figure 76). Since the corresponding cross-linked micelles (SPM-P94) presented much lower tissue spreading, we hypothesize that P94 unimers spreading and retention in the tissues is related to both its small size and high hydrophobicity. The usual pore size of intact endothelium is about 5 nm, which is very close to the size of P94 unimers and smaller than the size of F127 unimers (Table 6). The accumulation and retention of P94 unimers in the intestinal tract might contribute to their diffusion through the endothelia and, afterwards, to their spreading through the tissues. The toxicity of some Pluronics reported previously depends on their molecular weight and hydrophilic/hydrophobic balance. The higher systemic toxicity of Pluronic P94 (0.6 g/kg) compared to Pluronic F127 (2.5 g/kg)[87] might thus be related to its spreading in the tissues.

Detailed aspects of liver uptake were investigated in axial planes (Figure 75) and are presented in Figure 77. The unimers with larger PEO length (F127) and cross-linked micelles (SPM-F127 and SPM-P94) presented a homogeneous distribution in the liver tissue consistent with distribution throughout the liver vessels and penetration into the parenchyma. On the other hand, P94 unimers with shorter PEO block length were localized in specific areas, which might also indicate retention in the endothelial vessels and internalization by cells from the RES (Kuppfer cells). High penetration into the liver parenchyma and uptake by hepatocytes has also been observed with small colloids (≤ 50 nm).[277]

To avoid uptake by the Kuppfer cells, it is necessary to avoid opsonization in the systemic circulation. Opsonization by plasma proteins depends strongly on the surface properties of the nanomaterials, namely the presence of PEO is known to greatly reduce protein adsorption. In the case of polymeric micelles, the chain length of the PEO is not the only parameter that influences the adsorption of plasma proteins. For a low opsonization, long PEO chains as well as a high PEO surface density are necessary. For example, the presence of

PEO on the surface of liposomes increased their circulation half-time life to 5 hours in mice,[278] while PEGylated polymersomes exhibited longer half-time lives of approximately one day.[279] The difference observed is associated with the PEO density on their surface, which is much denser on the polymersomes ("brush" conformation) than on the liposomes ("mushroom" conformation). Corona chains in Pluronic micelles are often referred to have a "mushroom" conformation,[280, 281] associated with a lower density of PEO chains and larger fluctuations of the local PEO concentration. These facilitate the adsorption onto the hydrophobic core of plasma proteins[282] that can subsequently be recognized by the RES cells. Therefore, all the referred processes (metabolization by hepatocytes, internalization by endothelial cells, and phagocytosis by Kuppfer cells) contribute to the observed liver uptake. In any case, the % ID/mL in the liver is still significantly low compared to other nanocarriers (≈50% ID/mL).[220, 221]

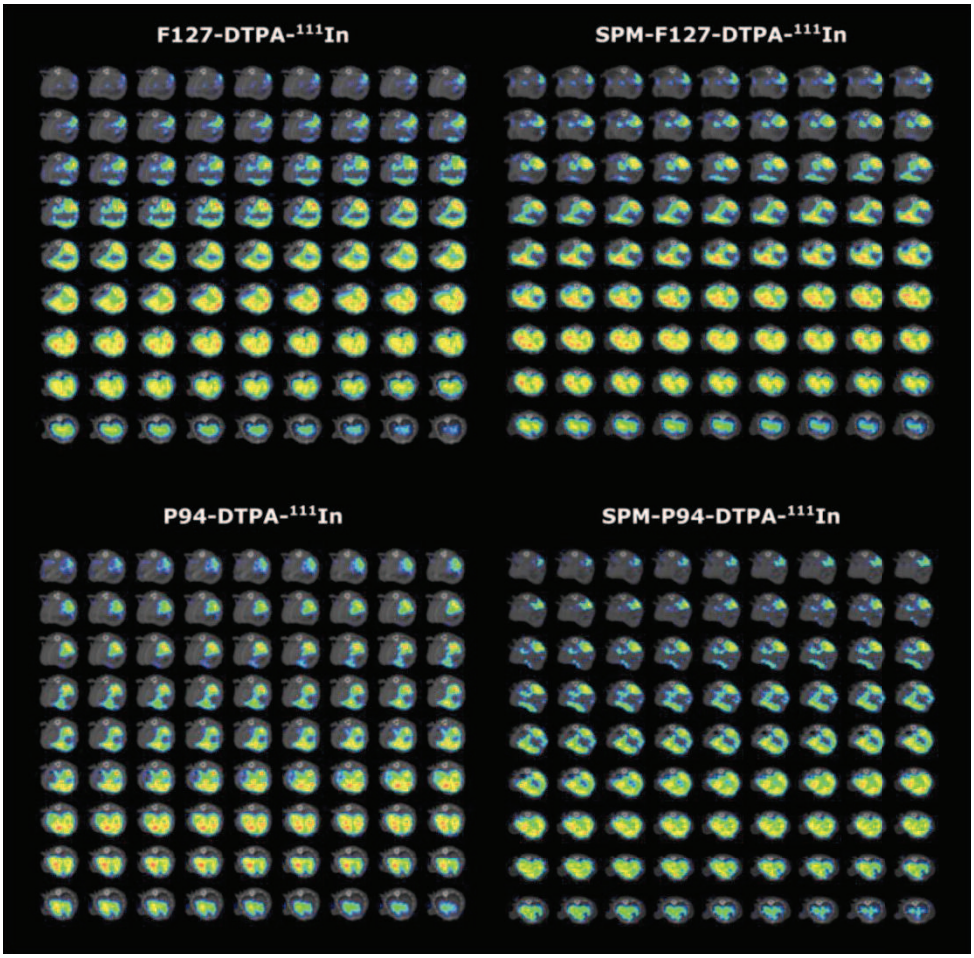

Figure 77. Axial slices (thickness 0.4 mm) of late-stage mouse SPECT/CT scans focusing on abdominal area at 48 hours p.i. of the different nanocarriers.

Biodistribution in other organs

The spleen uptake of all nanocarriers studied was low and decreased overtime indicating no retention in the tissue (Table 12). No significant differences in the spleen uptake between the molecular and supramolecular structures were also observed. High retention in the spleen is usually observed for nanocarriers with high rigidity, elongated or irregular shapes and/or large size.[34] Previous results obtained with polymersomes and liposomes showed increased uptake for sizes larger than 70-90 nm.[221, 283, 284] None of the nanocarriers studied in this work possess any of these properties, which explains their circulation without retention in the spleen sinusoidal sieve. The ability of our nanocarriers to surpass the spleen clearance mechanisms suggests that they should achieve good biocompatibility and should not trigger immunogenic reactions.[285]

Carriers with high size and rigidity tend to be trapped in the lung capillaries, whereas small and deformable carriers return to the heart and are delivered to the systemic circulation. None of the carriers studied in this work were retained in the lungs as observed by the low uptake in this organ at 48h (<1.5% ID/mL) (Table 12).

No accumulation of radioactivity was in general detected in any other organ, especially no retention was observed in the brain (Table 12).

The % of ID/mL in the heart and lungs (Table 12) decreases overtime for all the nanocarriers which suggest circulation of the compounds in the systemic circulation up to 48 h.

5.3.2 Dynamic scan of F127-DTPA-^{111}In

To get insight on the early stage tissue uptake dynamics, we performed a dynamic scan of F127-DTPA-^{111}In.

Pluronic F127 is approved by the FDA for i.v. administration in humans and currently used in the formulation SP1049C (further details on Chapter 1 section 1.5.4). However, the initial clearance using dynamic scans or even biodistribution of labelled Pluronic F127 has never been evaluated *in vivo*.

The time-activity curves (TACs) are presented in Figure 78. The uptake in the investigated organs (heart, kidneys, liver, lungs and spleen) is almost immediate and distribution is achieved about 1 min after i.v. injection of the compound. The renal clearance of the compound also starts 1 min p.i., and the accumulation of activity in the bladder increases during the scan.

The circulation of the compound in the systemic circulation is clear throughout the scan due to high activity in the heart and arteries that is constant during the 15 min scan. Particularly in the lungs, the % of ID/mL decreased from 25% to 11.5% in 30 min (Table 12 and Figure 78). This high activity observed immediately after injection is associated with the high perfusion of this organ (8 mL/min) over the lower blood flow in other organs such as liver (1.8 mL/min), spleen (0.09 mL/min) and kidneys (1.3 mL/min).[34] After injection of the compounds, they were transported to the heart and the entire cardiac output passed through the pulmonary circulation (first barrier).

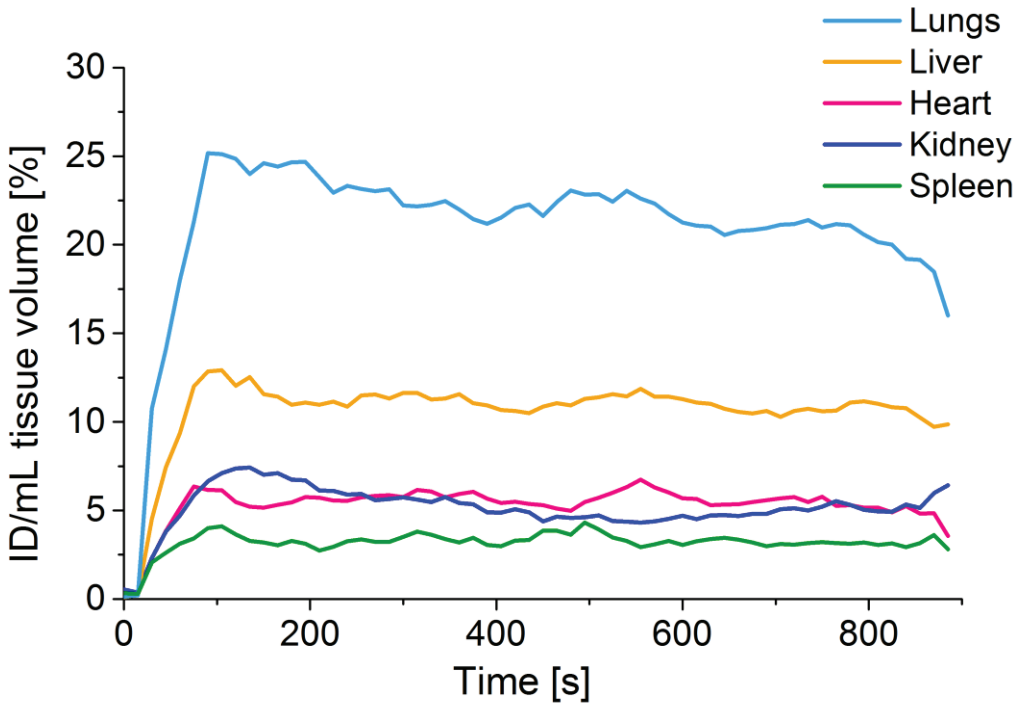

Figure 78. Time-activity curves of F127-DTPA-^{111}In show the uptake during first 15 min after the intravenous injection. The graph shows % of ID/mL uptake values for selected organs of interest in the mouse.

5.4 Conclusions

We developed a new strategy that enabled the *in vivo* comparison of molecular and core-stabilized supramolecular nanocarriers based on Pluronics. This new approach eliminates the recurrent limitation associated with the dynamic nature of copolymer micelles and allows us to use similar concentrations of both types of nanocarriers, which yields a more meaningful comparison of their biodistribution. After labelling the nanocarriers with the gamma-emitter ^{111}In (Chapter 3 section 3.2.10), their biodistribution was evaluated in healthy mice using SPECT/CT imaging. The effects of varying the PEO block length and aggregation state of Pluronic copolymers were then assessed.

All tested nanocarriers showed fast uptake in the studied organs (heart, kidneys, liver, lungs and spleen) followed by a steady elimination mainly through the hepatobiliary tract and renal filtration. The uptake in the different organs was found to decrease in two steps. The first one occurred in short times of the order of 1h and can be mostly attributed to the molecular weight in the case of the unimers, and to the transchelation of ^{111}In to serum proteins and renal elimination of the complexes for the cross-linked micelles. The second step was observed on time scales of the order of several hours and contributes to the significant decrease of the uptake at 24h p.i. in all studied organs, except the liver. This second step is mainly associated with metabolization of the nanocarriers in the liver followed by elimination through the hepatobiliary tract, with an additional direct renal clearance for the smallest P94-DTPA-^{111}In carriers. Retention of the nanocarriers in the liver at late-stage was influenced by the aggregation state of the carriers. Thus, we can conclude that the PEO block length affected the initial renal clearance and the uptake of the nanocarriers in the liver, while the aggregation state influenced the retention of the carriers in the liver.

Our results suggest that varying the PEO block length, molecular weight and aggregation state can lead to significant variations in the biodistribution profile of Pluronic copolymers. Further work is in progress to evaluate their theranostic potential in EPR-based cancer therapies.

General conclusions and future perspectives

This work was performed in the framework of the "TRACE'nTREAT" project whose objective was to develop new molecular technology for nuclear imaging and radionuclide therapy. In this context, we aimed at designing better nanocarriers based on copolymer self-assembly.

In Chapter 1, general concepts were introduced to enable a clear understanding of the different subjects explored in this thesis. We focused on the importance of developing higher molecular weight agents (nanocarriers) than the conventional low molecular weight drugs. However, many parameters affect the nanocarriers performance and their optimum physicochemical properties (e.g. molecular weight, size, shape, hydrophobic/hydrophilic ratio, blocks size, charge) are still far from being completely understood.

We have selected well-known triblock copolymers of PEO-PPO-PEO (Pluronics) which have been extensively used in academic studies as well as for biomedical applications. These copolymers can be used as single polymer chains, or they can aggregate and be used as spherical or elongated micelles. Therefore, they provide a versatile platform for the development of molecular and supramolecular nanostructures, and for the comparison of their biological effects among other many possibilities.

We started by the fundamental study of the sphere-to-rod transition kinetics of Pluronic copolymers with constant PEO (40%) and modest increases of the molecular weight (Chapter 2). The cmT was decreased to room temperature using a water structure maker salt (NaCl), and the kinetics of transformation from spherical to elongated morphology were tracked using non-standard time-resolved multiangle dynamic light scattering. This allowed us to identify multiple competing kinetic pathways for the sphere-to-rod transformation and eventual morphological control in various formulations.

The main new conclusion is that, in most experimental conditions, none of these kinetic pathways can be neglected if one wants to understand the final

morphology of the aggregates. Moreover, even for modest increases of molecular weight in the Pluronic series, equilibration of the micelles population becomes very difficult on the time scale of weeks, and the structure of the solutions becomes dependent on the specific thermal history of the sample.

These results helped us to better select the Pluronic composition if a spherical or elongated morphology is intended. Moreover, this kinetic study showed the necessity to stabilize the core-shell structure of the micelles to allow them to withstand their dilution in the blood flow.

In Chapter 3, we presented new methods for the development and functionalization of molecular (unimers) and supramolecular (spherical micelles) nanocarriers based on Pluronic copolymers. We showed how stabilization of Pluronic spherical micelles can be achieved by the incorporation of a interpenetrated network composed of poly(PETA). Although this strategy was not successful to stabilize the wormlike micelles, it revealed to be very effective to stabilize spherical micelles and prevent their disassembly below the cmc and cmT. It also stabilized the micelles in the presence of serum proteins, and upon freeze-drying and redispersion in organic and aqueous solvents. Moreover, it still allowed incorporation of hydrophobic molecules in the micelles core after micelles stabilization.

We then developed innovative approaches to functionalize the molecular and supramolecular systems with fluorescent probes and metallic chelators by covalent attachment. We further discussed the radiolabeling of the nanocarriers and the different aspects that need to be taken into account when characterizing the radiolabeling efficiency and purification of the radiolabeled carriers. We established the corresponding protocols for the preparation and purification of samples ready for *in vitro* and *in vivo* use.

Moreover, the new strategies and techniques herein described can be generalized to create a great versatility of nanocarriers with other functionalities by combining appropriate molecular modifications and/or load. This lets envision the coupling of specific active targets to the molecular nanocarriers. For instance, this can include targeting of extracellular receptors like hormones (e.g. somatostatin), neuropeptides and growth factors, or intracellular targets such as specific metabolic pathways or the DNA/RNA. On

the other hand, the supramolecular nanocarriers can be very useful to deliver hydrophobic drugs through their incorporation in the micelles core. This incorporation can be achieved via electrostatic interactions, by covalent linking to the copolymer using biodegradable bonds, or can even be through incorporation in the cross-linked interpenetrated network of poly(PETA). The latter can eventually provide a controlled drug release as micelles are metabolized by the lysosomes.

Chapter 4 was dedicated to the assessment of the *in vitro* interactions of the nanocarriers using 2D and 3D cell cultures. The aim of this research was to investigate the influence of the PEO block length and aggregation state parameters on the interactions with healthy and cancer cells. We concluded that the presence of the interpenetrating polymer network of poly(PETA) does not increase cytotoxicity, and delivering physically incorporated hydrophobic content is still possible.

By varying the nanocarriers properties, different internalization pathways were activated, which ultimately lead to different intracellular localization. The molecular nanocarriers entered *via* caveolae-mediated endocytosis and, if they were smaller than the nuclear pore complexes (≈5 nm), they were able to enter the nucleus by passive diffusion. The supramolecular carriers were processes by the clathrin-mediated pathway and were therefore retained in acidic compartments as verified by co-localization with the lysosomes. The uptake and exocytosis kinetics profiles were also influenced by the physicochemical properties of the carriers, with a higher internalization and retention associated to the molecular nanocarriers with the shortest PEO block length. As far as we know, this is the first demonstration of the possibility to select the intracellular localization by tuning simple molecular parameters of the Pluronic copolymers without changing their chemical nature.

In this chapter we also concluded that cross-linked nanocarriers penetrate more efficiently into cellular aggregates, and nanocarriers composed by hydrophobic Pluronic copolymers can significantly alter the morphology of tumor spheroids. All these features open new possibilities for the clinical applications of Pluronic-based nanocarriers such as the delivery of chemotherapeutic drugs and/or gene therapy.

Chapter 5 focused on the *in vivo* behavior of the developed nanocarriers in healthy mice. Radiolabeling of the nanocarriers with ^{111}In allowed the non-invasive *in vivo* monitoring of the nanocarriers and the preclinical assessment of their efficacy. A more thorough understanding of the key parameters that determine the *in vivo* fate of the carriers was therefore obtained. Both the PEO block length and the aggregation state influenced the biodistribution, and the early and late clearances of the carriers. A higher PEO block length was associated to higher liver uptake, and the retention in the liver was influenced by the aggregation state of the copolymers. We also observed that the stability of the DTPA-^{111}In complexes in the nanocarriers surface can be affected by the interactions with the biological fluids, which can compromise the assessment of the nanocarriers biodistribution. Likewise, the functionalization with other moieties can have a significant influence on their biodistribution.

The results from this thesis demonstrate that a rational design needs to be performed for the development of Pluronic nanocarriers, including fundamental studies from the kinetics of micelles formation up to a thorough *in vitro* and *in vivo* evaluation. Varying the physicochemical properties and functionalization moieties can be used to limit the interactions with the biological barriers, target specific intracellular organelles, enhance the nanocarriers uptake and exocytosis kinetics, and/or increase the penetration and toxicity into tumors.

We observed that predicting the optimal characteristics of an ideal nanocarrier is not straightforward, and balancing the copolymer composition for efficient delivery while keeping low toxicity profile is challenging. Moreover, following the rational design, additional fine-tuning is required to balance the benefits and drawbacks of each additional chemical modification.

Further work is in progress by the project partners to evaluate the potential use of the herein developed systems on cancer theranostics based on the EPR effect. The approach, the methods and protocols developed in this work can be applied as well to a large variety of amphiphilic block copolymers based on PEO, and can further allow the future design of advanced nanomedicines.

Appendix I: DLS data analysis

Analysis of $P(\tau_i)$ and parameter definition

The $P(\tau_i)$ resulting from CONTIN analysis was fitted to a sum $S(\tau)$ of Gaussian functions on the logarithmic scale of the grid points:

$$S(\tau) = \sum_k a_k \, exp\left(-\frac{(log(\tau) - log(\tau_k))^2}{\sigma_k^2}\right)$$

using a non-linear least-squares method implementing the Levenberg-Marquardt algorithm. The number k and the initial positions τ_k of the Gaussian peaks used in the fit were determined automatically by the second derivative algorithm, which was very efficient in this case because the CONTIN method produces naturally smooth $P(\tau_i)$ curves. If the fit completed successfully, the results were considered as satisfying if they met all the following criteria: i) $a_k > 0$, ii) number of iterations for fit convergence smaller than 30, iii) relative errors on a_k, τ_k, and σ_k smaller than 200%. Otherwise the results were discarded and not considered for further analysis.

For satisfying results we defined then for each peak the apparent hydrodynamic radius R_k following Equation 5 in Chapter 1 and the associated peak area $A_k = \sqrt{\pi} a_k \sigma_k$. We note that this peak area definition takes into account that $P(\tau_i)$ is already a discretization on a logarithmic scale of the normalized distribution of relaxation times $p(\tau)$. It ensures that A_k is proportional to the relative contribution I_k of decay mode k to the total scattering intensity I_{tot}. Thus:

$$\tilde{g}^{(1)}(0) = \sum_{i=1}^{N_g} P(\tau_i) = \sum_{k=1}^{N_p} A_k$$

$$I_k = \frac{A_k}{\sum A_k} I_{tot}$$

where N_p is the number of peaks. These definitions were used to split the total scattering intensity into the intensities contributed by each decay mode.

Relative errors on the parameters R_k, A_k and I_k were defined from the relative errors $\delta\tau_k$, δa_k, $\delta\sigma_k$, and the correlation factor C_k between a_k and σ_k obtained in the non-linear fitting as:

$$\delta R_k = \delta\tau_k$$
$$\delta A_k = [(\delta a_k)^2 + (\delta\sigma_k)^2 + 2C_k\delta a_k\delta\sigma_k]^{1/2}$$
$$\delta I_k = \delta A_k + \frac{\sum A_k\delta A_k}{\sum A_k} + \frac{\Delta I_{tot}}{\sqrt{255}I_{tot}}$$

where the numerical factor $1/\sqrt{255}$ comes from the fact that we use the standard error on the time-averaged I_{tot} to compute the errors on the time-averaged I_k. When plotting I_{tot}, we use ΔI_{tot} as error bars to give an idea about the amplitude of time fluctuations in the scattering intensities. For all other intensity plots, we use error bars defined by the previous equations.

Figure 79shows typical results obtained during the analysis. These consecutive measurements show how CONTIN output can depend on data noise. The fitting algorithm found (Figure 80) two peaks in measurement 0027 and only one in measurement 0028, where the small features at $t \leq 0.5\,ms$ were skipped by the fit because they correspond to a too weak relative contribution. The small peak at $t \approx 0.1\,s$ was excluded from the fitting range because it is obviously not corresponding to any decay in the data. This contribution is however influencing $P(\tau_i)$ at smaller t.

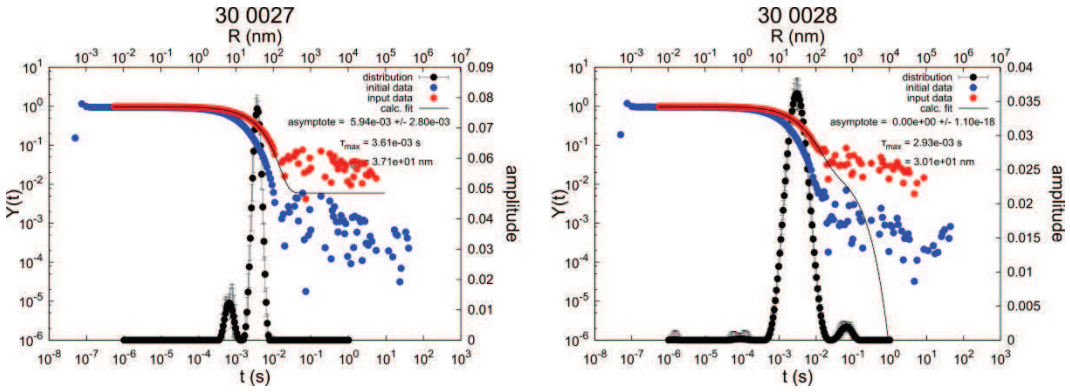

Figure 79. Two typical examples of CONTIN outputs. Sample P94 at 28ºC and θ=30º, (●) $\boldsymbol{g^{(2)}(t)-1}$; (●) $\boldsymbol{\tilde{g}^{(1)}(t)}$; (●) $\boldsymbol{P(\tau_i)}$. The continuous line shows the correlation function corresponding to $\boldsymbol{P(\tau_i)}$.

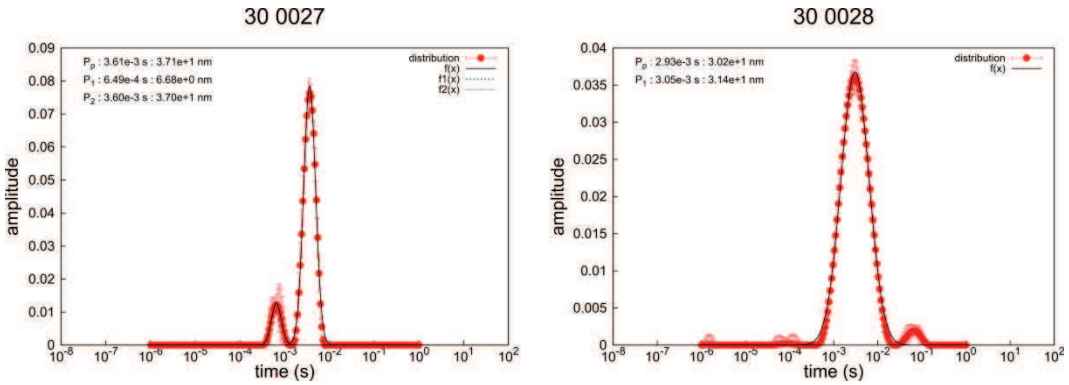

Figure 80. Fits of the CONTIN outputs $\boldsymbol{P(\tau_i)}$ (●) by Gaussian peaks (lines). Same data as in Figure 79.

Automated peak identification and sorting

Due to the experimental noise in the ICFs, the CONTIN analysis can produce spurious peaks in the $P(\tau_i)$ that should be discarded. To do this in an automated way, we first discarded peaks with $A_k/A_{max} < 0.005$, where A_{max} is the peak area of the major contribution in $P(\tau_i)$. The remaining contributions were then sorted by plotting an histogram of all R_k values as shown in Figure 81.

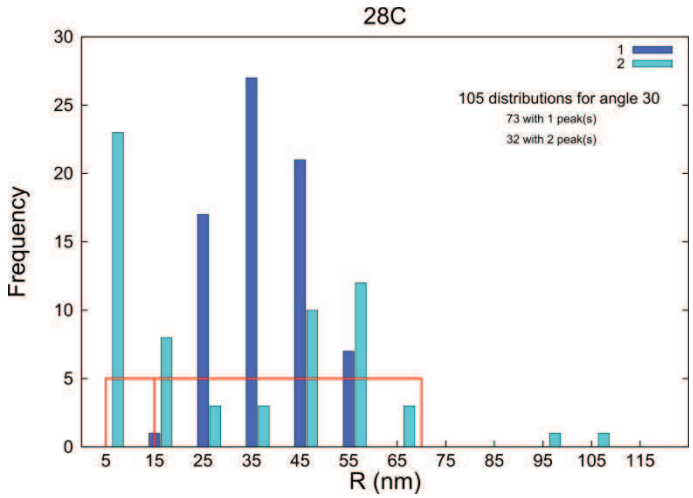

Figure 81. Histogram of the $\boldsymbol{R_k}$ values measured for P94 at T=28ºC and θ=30º in monomodal (●) or bimodal (●) $\boldsymbol{P(\tau_i)}$. Bins are 10 nm wide and located at the center of the class, i.e., the bar at $\boldsymbol{R = 5\,nm}$ corresponds to the frequencies for $\boldsymbol{0 < R \leq 10}$. The red lines shows we defined two classes in this example: fast decay mode for $\boldsymbol{R \leq 15\,nm}$ and slow decay mode for $\boldsymbol{15 < R \leq 70}$. The two occurrences at $\boldsymbol{R > 90\,nm}$ were rejected as non-typical after a closer look at the data.

This typical example shows that, depending on the experimental noise, CONTIN either resolved two peaks with positions $R_k \approx 5\,nm$ and $R_{k+1} \approx 55\,nm$ or merged them in a broader peak at position $R_a \approx 35\,nm$ with $R_k < R_a < R_{k+1}$. Decision on the next step was achieved by comparing the relative frequencies of solutions with 1 or 2 peaks. The solutions with the largest frequency were usually considered as the most representative and we defined accordingly R intervals to assign the experimental R_k and I_k values to the fast or the slow components.

In the present example, although the solutions with a monomodal $P(\tau_i)$ outnumber the ones with a bimodal $P(\tau_i)$, we kept the bimodal description because it is consistent with the behavior at larger scattering angles.

When $P(\tau_i)$ with distinct peaks were in the minority, a merged contribution was calculated for them as:

$$I_a = I_k + I_{k+1}$$

$$I_a \delta I_a = I_k \delta I_k + I_{k+1} \delta I_{k+1}$$

$$R_a = \frac{R_k I_k + R_{k+1} I_{k+1}}{I_k + I_{k+1}}$$

$$(R_a \delta R_a)^2 = \frac{[(R_a - R_k)^2 + (R_k \delta R_k)^2] I_k + [(R_a - R_{k+1})^2 + (R_{k+1} \delta R_{k+1})^2] I_{k+1}}{I_k + I_{k+1}}$$

Depending on the respective weights I_k and I_{k+1}, R_a can be located in either the fast or the slow component class and the associated errors can be large, producing large fluctuations and error bars in the final plots. However, we preferred to keep these values rather than to cherry-pick "good results".

The amplitude of the fluctuations in the results helps one to appreciate how much confidence should be given to the existence of small decay modes at given temperature and scattering angle. The quality of mode splitting and its evolution with time can be further evaluated by plotting $I_k(R_k)$ with color coding of the decay modes (Figure 82). In the present example, the definition of the two classes in Figure 81 produces two distinct clouds of points, confirming that distinguishing two classes is meaningful. The elongated shape of these clouds is associated with the time evolution of $P(\tau_i)$. Here the ratio of intensities I_{slow}/I_{fast} is about 10 and the ratio of radii R_{slow}/R_{fast} about 5.

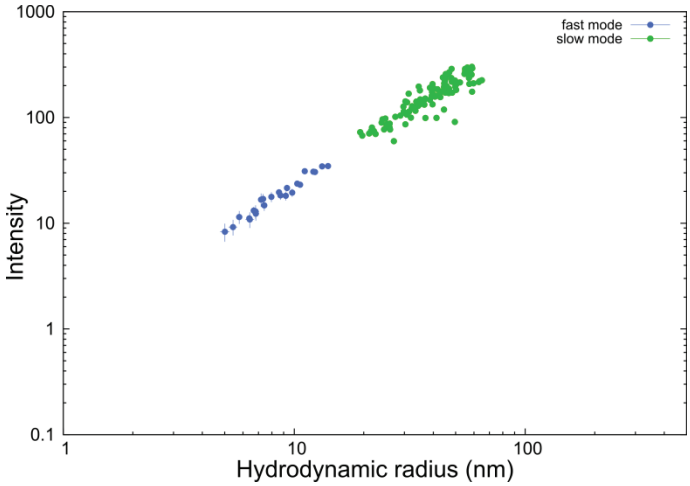

Figure 82. Plot of the intensity vs. the associated hydrodynamic radius for all the peaks in $\boldsymbol{P(\tau_i)}$ obtained for sample P94 at T=28ºC and θ=30º.

Specific results

Angular dependence of slow decay mode intensity for P84 at T=32, 33º

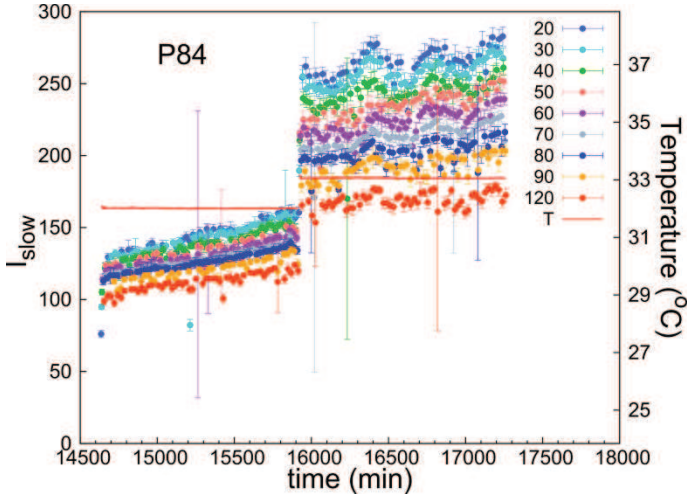

Figure 83. Time evolution of $\boldsymbol{I_{slow}}$ for all measured scattering angles. Sample P84 at T=32,33º.

Angular dependence of slow decay mode for P94 at T=29, 30º

In Figure 84 it can be seen that the scattering intensity I_{slow} starts increasing rapidly at $t \approx 13000\,min$ for the larger angles. At about the same time, R_{slow} stops increasing at the smallest scattering angles. As a consequence, the angular dissymmetry is decreasing and the range of R_{slow} values measured at the different θ values shrinks. This behavior marks the crossover to the semidilute regime for the wormlike micelles. At T = 30º, the crossover is achieved, the further increase in I_{slow} is much smaller and R_{slow} becomes independent of θ (Figure 85).

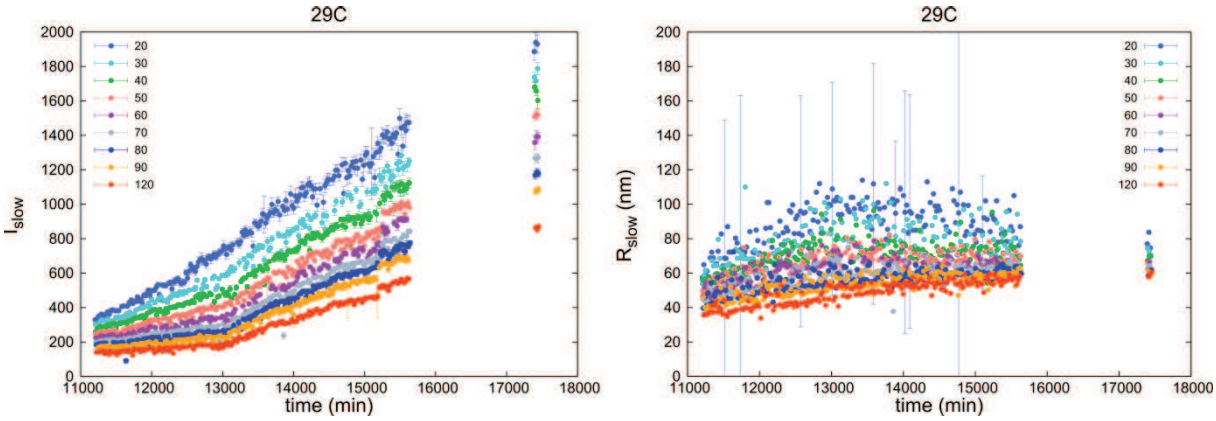

Figure 84. Time evolution of I_{slow} and R_{slow} for all measured scattering angles. Sample P94 at T=29º. The time gap corresponds to unattended failure of the acquisition software.

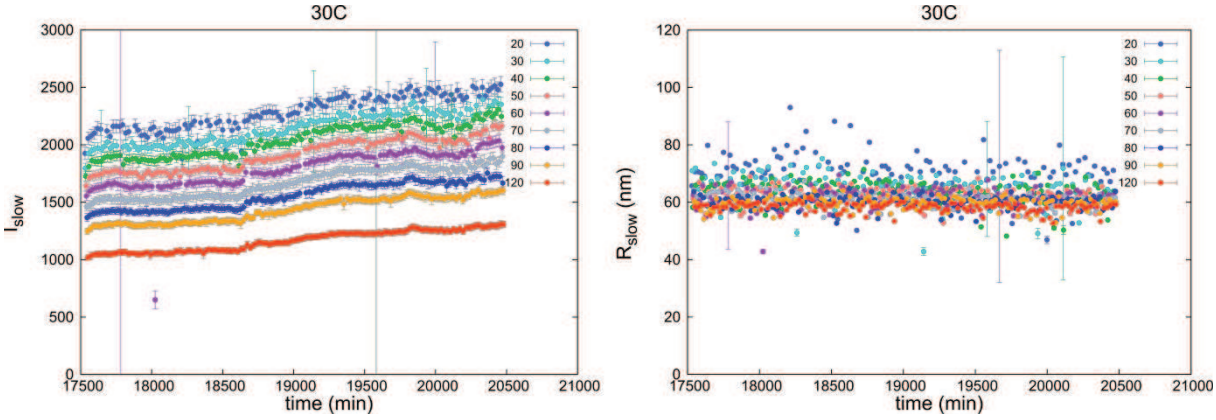

Figure 85. Time evolution of I_{slow} and R_{slow} for all measured scattering angles. Sample P94 at T=30º.

Angular dependence of fast and slow decay mode for P104 at T=34º

Figure 86 shows the time evolution of the angular dependence of the two decay modes for P104 sample at T=34º. For the fast mode, a q-dependence starts to show up for the smallest scattering angles in both the scattering intensity and the apparent hydrodynamic radius. For the slow mode, the intensity is plotted on a logarithmic scale to emphasize that it is increasing in time with no change in the q-dependence, i.e., at constant average radius of gyration. Values for the corresponding AHRs are strongly dependent on scattering angle and nearly independent of time within experimental accuracy.

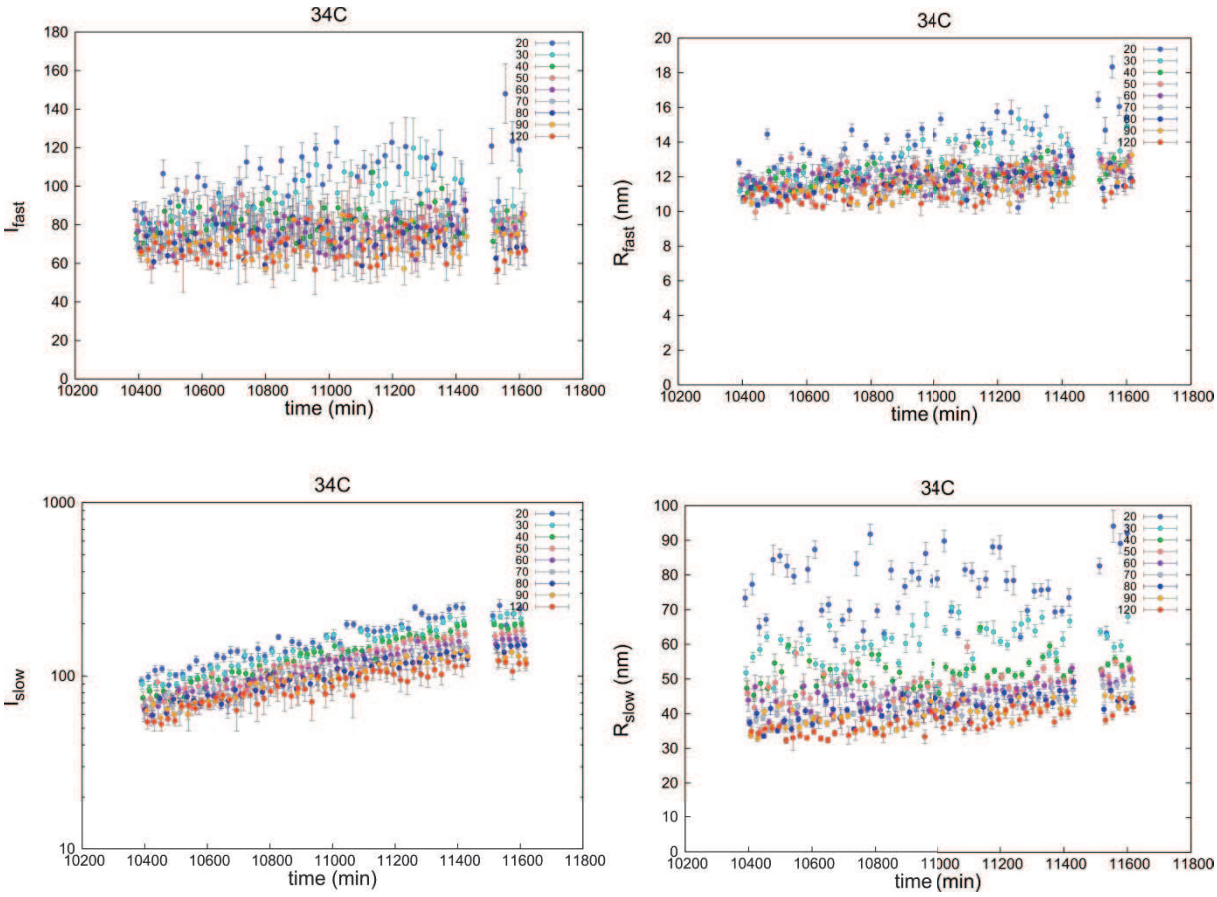

Figure 86. Time evolution of the angular dependence of the fast (above) and slow (below) decay modes for all measured scattering angles. Sample P104 at T = 34º.

Appendix II: Trials to stabilize wormlike micelles

The study carried out in Chapter 2 opens new possibilities on the use of Pluronic systems as nanomedicines with different shapes, specifically elongated micelles.

The Pluronic P84 appears very promising due to its fast kinetic transition upon small temperature variations. However, the stability of the elongated micelles is very short once the system is brought to the spherical micelles temperature.

The Pluronic P94 has a much slower transition kinetics, but the kinetic stability of the elongated micelles is much higher.

The Pluronic P104 forms aggregates of spherical micelles at high temperatures, thus it is not adequate if the elongated morphology is intended.

Taken into account these observations, two approached were tried to stabilize wormlike Pluronic micelles: via the formation of a IPN of poly(PETA) or through an emulsion technique.

The first trials were through the creation of an IPN of poly(PETA) as described in Chapter 3. Two methods were tested: either by stabilization after formation of the wormlike micelles, or inducing the sphere-to-rod transition by solubilization of increasing concentrations of PETA.

We first formed the wormlike micelles as described in Chapter 2: Pluronic P84 or P94 were dissolved in 2M NaCl and the temperature was increased to 40ºC for different periods (Table 13). Then, PETA dissolved in ethanol was added to the solution, and cross-linked for one hour. From these series of trials, we verified it is critical to add the PETA before micelles formation so that it is adequately incorporated in the micelles core. When PETA is added after micelle formation, the stabilization is not possible and the solution becomes turbid after temperature decrease (see Figure 24 from Chapter 3). Therefore, this strategy was abandoned.

The second method was reported by Petrov et al..[286] The authors reported they cross-linked Pluronic P123 (M_w=5800, $PEO_{20}PPO_{70}PEO_{20}$) wormlike micelles using increasing concentrations of PETA (from 3.5% to 21%).

We tried to cross-link Pluronic P94 with increasing concentrations of PETA ranging from 3 to 24% (Table 13) and, after purification by diafiltration, the size of the micelles remained constant in all the concentrations tested. None of these trials were successful and only spherical micelles with similar hydrodynamic size as the ones reported in Chapter 3 (Table 6) were obtained. We hypothesize this is associated to the presence of PETA in the core from the spherical stage, which hinders their aggregation and evolution into the elongated morphology.

Table 13. Trials performed to stabilize wormlike Pluronic micelles using Pluronic P84 and P94.

%P84	%P94	Solvent	%PETA	**Incubation**		**Cross-linking**	
				Temp [ºC]	Time [h]	Temp [ºC]	Time [h]
0.5		2M NaCl	6	40	1	40	1
2.5		2M NaCl	6	40	1	40	1
	2.5	2M NaCl	6	40	3	40	1
	0.5	2M NaCl	6	40	3	40	1
	2.5	2M NaCl	6	40	24	40	1
	0.5	2M NaCl	6	40	24	40	1
	2.5	H_2O	3	60	1	60	1
	2.5	H_2O	6	60	1	60	1
	2.5	H_2O	12	60	1	60	1
	2.5	H_2O	24	60	1	60	1

To confirm this method does not enable formation of wormlike micelles, we also tried to cross-link the more hydrophobic Pluronic (P123).[286] We tested increasing PETA concentrations from 1.5 to 12% and cross-linking in the presence of 8% ethanol with or without added salt (KCl) (Table 14) as it has been reported to induce the formation of wormlike micelles (see Figure 10 on Chapter 1 section 1.5.4). Irradiation was performed using gamma-rays from a Cobalt-60 source (0.1 kGy/h on 01/01/2015) at room temperature. In the absence of salt at high PETA concentrations (12%), the size of the micelles was $R_{H,15^oC}$=13.5±0.7 nm. With added salt at 12% PETA, only a small increase of the hydrodynamic radius was observed ($R_{H,15^oC}$=21±0.8 nm).

Table 14. Trials performed to stabilize wormlike Pluronic micelles using Pluronic P123.

%P123	Solvent	%PETA	**Incubation**		**Cross-linking**	
			Temp	Time [h]	Temp	Time [h]
4	8% etOH	1.5	RT	5	RT	5
4	8% etOH	3	RT	5	RT	5
4	8% etOH	6	RT	5	RT	5
4	8% etOH	12	RT	5	RT	5
4	8% etOH + 2M KCl	1.5	RT	5	RT	5
4	8% etOH + 2M KCl	3	RT	5	RT	5
4	8% etOH + 2M KCl	6	RT	5	RT	5
4	8% etOH + 2M KCl	12	RT	5	RT	5

Finally, an emulsion technique was tested using water and chloroform. The Pluronic P94 and the fluorescent dye Nile Red were dissolved in chloroform and a small amount of the organic solution was added to the aqueous phase to achieve a final concentration of 10% Pluronic P94 and a ratio chloroform:water of 1:100.

The solution was stirred to disperse the chloroform droplets and the solution imaged by confocal microscopy (Figure 87). In the beginning, we see the droplets of chloroform containing the Nile Red and the Pluronic. After few minutes, the surface of the droplets becomes destabilized and very flexible wormlike structures are formed, which appear to be wormlike vesicles. After 2-3 minutes, the wormlike structures shrink into spherical structures. We also tried different concentrations of NaCl in the aqueous phase, which prevented the formation of the wormlike structures as the salt concentration increased (Figure 88).

Due to the short stability of the wormlike structures and/or formation of unwanted structures in the tested conditions, this strategy was abandoned.

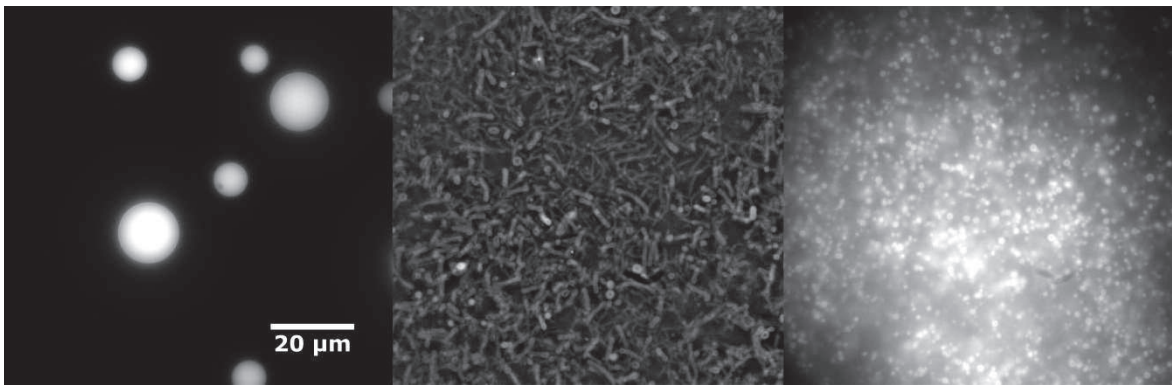

Figure 87. Overtime confocal images of a solution of chloroform:water (1:100) containing Pluronic P94 and Nile Red dissolved in the chloroform phase. Formation of emulsion droplets (left), destabilization and formation of elongated structures (center), which evolve into spherical structures (right).

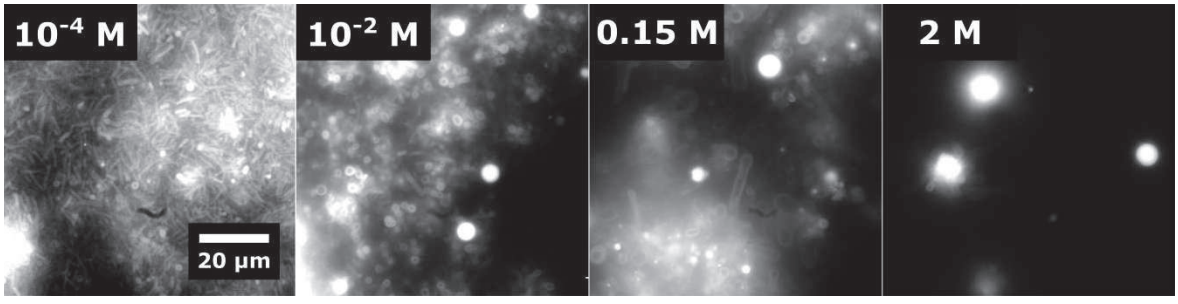

Figure 88. Confocal images of Pluronic P94 and Nile Red dissolved in chloroform dispersed in the aqueous phase with increasing concentrations of NaCl. Images were acquired ≈1 min after mixing the organic and aqueous phases.

Appendix III: Cross-linking efficiency

Determining the efficiency of the cross-linking process of Pluronic micelles is very challenging. Due to the large contribution of the stabilized micelles to the scattered light intensity, the detection of the unimers by DLS is very difficult. Moreover, due to the problems in separating both peaks, quantifying the unimers and micelles is almost impossible. Therefore, a technique that is able to separate both species in solution and quantify them individually is needed.

Asymmetric Flow Field Flow Fractionation (A4F) is a chromatographic technique without a stationary phase that enables separation of species according to their size in aqueous conditions. The separation requires several steps (Figure 89A). During injection and focusing, the flow enters from both sides of the channel to concentrate the sample. The fractionation of the species is obtained by using a crossflow and a direct laminar flow. The crossflow forces the sample towards the membrane, but due to their Brownian motion they diffuse back into the channel. Smaller species (unimers) will move faster to the center of the channel, while larger species (stabilized micelles) will stay closer to the channel wall. Due to the effect of the direct laminar flow, particles in the center of the channel will be eluted faster and larger particles will be eluted later. Due to the conjugation of both flows, an optimization for each sample is required, which can even involve the use of different crossflows during the same analyses. The different components are then collected and analyzed by different detectors (e.g. UV, DLS).

Preliminary analysis of a sample containing cross-linked F127 micelles and 6% PETA is presented in Figure 89B. Three peaks were identified: the first corresponds to small unimers or impurities (contaminants), the second peak to the F127 unimers, and the third one to the cross-linked F127 micelles. In proportion, the first and second peaks account for 84.2%, while the stabilized micelles correspond to the remaining 15.8%. This analysis was carried out in a more than six months old sample that was not purified. The low efficiency observed here can thus be related to degradation overtime. In any case, this technique enables a characterization of the cross-linking method and the qualitative as well as quantitative comparison of the unimers and micelles present in the sample.

Further work is in progress to characterize the efficiency after micelles preparation with different concentrations of cross-linking agent, and their long-term stability.

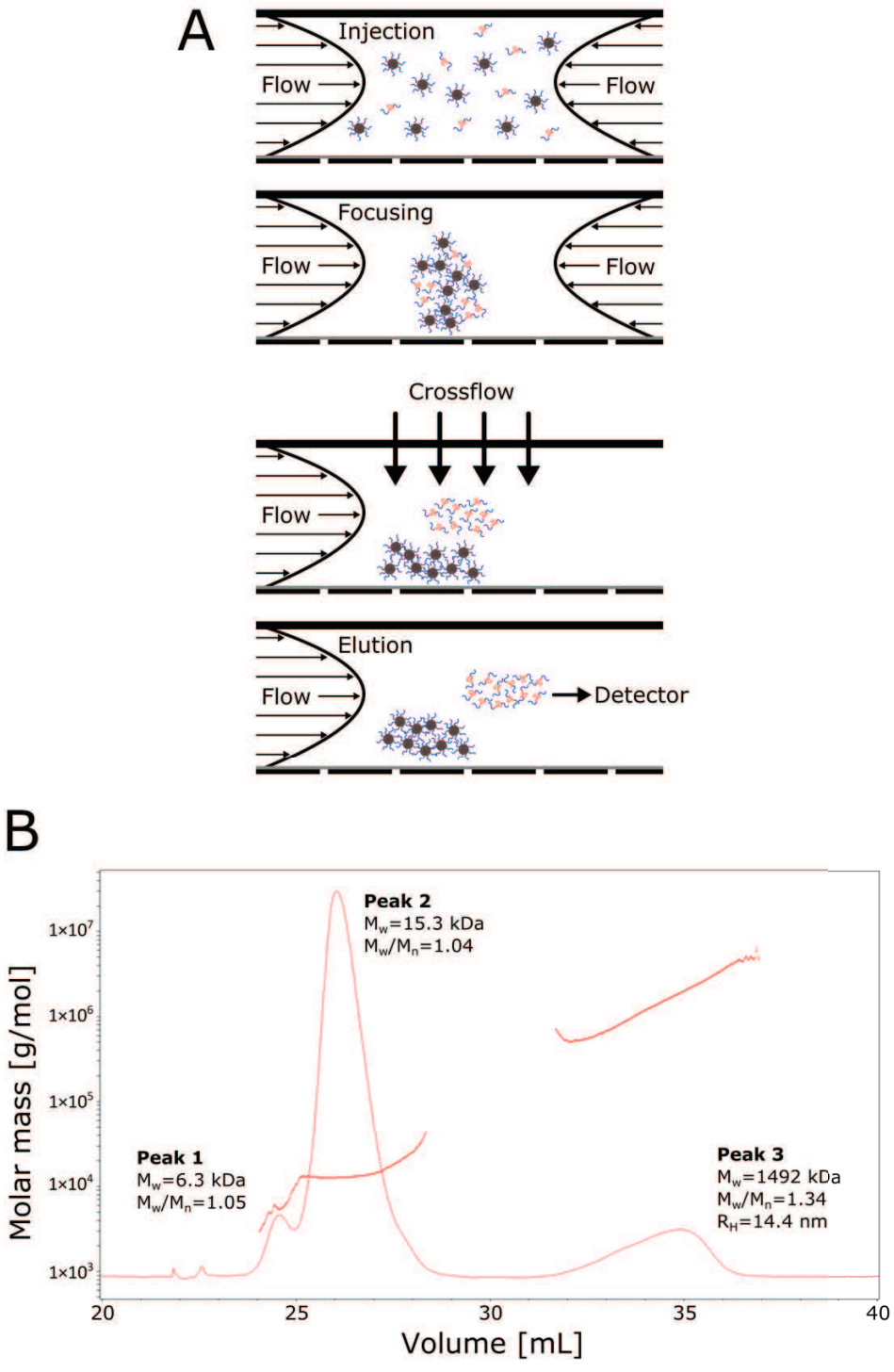

Figure 89. (A) Scheme of the Asymmetric Flow Field Flow Fractionation steps used to characterize the cross-linking efficiency of Pluronic micelles by an IPN of poly(PETA), and (B) preliminary results obtained in one sample of F127 cross-linked micelles (SPM-F127).

References

1. T. Lammers, F. Kiessling, W. E. Hennink and G. Storm, *J Control Release*, **2012**, 161, 175-187.
2. R. Duncan and R. Gaspar, *Mol Pharm*, **2011**, 8, 2101-2141.
3. T. Lammers, V. Subr, P. Peschke, R. Kühnlein, W. E. Hennink, K. Ulbrich, F. Kiessling, M. Heilmann, J. Debus, P. E. Huber and G. Storm, *Br J Cancer*, **2008**, 99, 900-910.
4. H. Soo Choi, W. Liu, P. Misra, E. Tanaka, J. P. Zimmer, B. Itty Ipe, M. G. Bawendi and J. V. Frangioni, *Nat Biotech*, **2007**, 25, 1165-1170.
5. T. Lammers, W. E. Hennink and G. Storm, *Br J Cancer*, **2008**, 99, 392-397.
6. X. Duan and Y. Li, *Small*, **2013**, 9, 1521-1532.
7. V. Sainz, J. Conniot, A. I. Matos, C. Peres, E. Zupančič, L. Moura, L. C. Silva, H. F. Florindo and R. S. Gaspar, *Biochem Biophys Res Commun*, **2015**.
8. A. Gabizon, H. Shmeeda and Y. Barenholz, *Clin Pharmacokinet*, **2003**, 42, 419-436.
9. S. Nakamura, H. Iwata, Y. Funato, K. Ito and Y. Ito, *Gan To Kagaku Ryoho*, **2015**, 42, 447-455.
10. S. Sofou, *Int J Nanomedicine*, **2008**, 3, 181-199.
11. A. B. de Barros, A. Tsourkas, B. Saboury, V. N. Cardoso and A. Alavi, *EJNMMI Res*, **2012**, 2, 2-39.
12. M. R. Stratton, P. J. Campbell and P. A. Futreal, *Nature*, **2009**, 458, 719-724.
13. J. M. Irish, N. Kotecha and G. P. Nolan, *Nat Rev Cancer*, **2006**, 6, 146-155.
14. R. Liu, B. K. Kay, S. Jiang and S. Chen, *MRS Bulletin*, **2009**, 34, 432-440.
15. P. P. Di Fiore, J. H. Pierce, T. P. Fleming, R. Hazan, A. Ullrich, C. R. King, J. Schlessinger and S. A. Aaronson, *Cell*, **1987**, 51, 1063-1070.
16. L. E. Kelemen, *Int J Cancer*, **2006**, 119, 243-250.
17. J. Albanell, J. Codony, A. Rovira, B. Mellado and P. Gascon, *Adv Exp Med Biol*, **2003**, 532, 253-268.
18. F. Danhier, O. Feron and V. Preat, *J Control Release*, **2010**, 148, 135-146.
19. D. B. Kirpotin, D. C. Drummond, Y. Shao, M. R. Shalaby, K. Hong, U. B. Nielsen, J. D. Marks, C. C. Benz and J. W. Park, *Cancer Res*, **2006**, 66, 6732-6740.
20. D. W. Siemann, *Cancer Treat Rev*, **2011**, 37, 63-74.
21. H. Maeda, H. Nakamura and J. Fang, *Adv Drug Deliv Rev*, **2013**, 65, 71-79.
22. M. I. Koukourakis, S. Koukouraki, A. Giatromanolaki, S. Kakolyris, V. Georgoulias, A. Velidaki, S. Archimandritis and N. N. Karkavitsas, *Acta Oncol*, **2000**, 39, 207-211.
23. M. I. Koukourakis, S. Koukouraki, I. Fezoulidis, N. Kelekis, G. Kyrias, S. Archimandritis and N. Karkavitsas, *Br J Cancer*, **2000**, 83, 1281-1286.
24. K. J. Harrington, S. Mohammadtaghi, P. S. Uster, D. Glass, A. M. Peters, R. G. Vile and J. S. Stewart, *Clin Cancer Res*, **2001**, 7, 243-254.
25. J. Fang, H. Nakamura and H. Maeda, *Adv Drug Deliv Rev*, **2011**, 63, 136-151.

26. M. K. Danquah, X. A. Zhang and R. I. Mahato, *Adv Drug Deliv Rev*, **2011**, 63, 623-639.

27. J. Ehling, B. Theek, F. Gremse, S. Baetke, D. Mockel, J. Maynard, S. A. Ricketts, H. Grull, M. Neeman, R. Knuechel, W. Lederle, F. Kiessling and T. Lammers, *Am J Pathol*, **2014**, 184, 431-441.

28. S. K. Hobbs, W. L. Monsky, F. Yuan, W. G. Roberts, L. Griffith, V. P. Torchilin and R. K. Jain, *Proc Natl Acad Sci U S A*, **1998**, 95, 4607-4612.

29. F. Yuan, M. Dellian, D. Fukumura, M. Leunig, D. A. Berk, V. P. Torchilin and R. K. Jain, *Cancer Res*, **1995**, 55, 3752-3756.

30. B. Theek, F. Gremse, S. Kunjachan, S. Fokong, R. Pola, M. Pechar, R. Deckers, G. Storm, J. Ehling, F. Kiessling and T. Lammers, *J Control Release*, **2014**, 182, 83-89.

31. T. Lammers, *Adv Drug Deliv Rev*, **2010**, 62, 203-230.

32. K. Riehemann, S. W. Schneider, T. A. Luger, B. Godin, M. Ferrari and H. Fuchs, *Angew Chem Int Ed Engl*, **2009**, 48, 872-897.

33. W. R. Sanhai, J. H. Sakamoto, R. Canady and M. Ferrari, *Nat Nano*, **2008**, 3, 242-244.

34. N. Bertrand and J. C. Leroux, *J Control Release*, **2012**, 161, 152-163.

35. P. Decuzzi, B. Godin, T. Tanaka, S. Y. Lee, C. Chiappini, X. Liu and M. Ferrari, *J Control Release*, **2010**, 141, 320-327.

36. E. A. Simone, T. D. Dziubla and V. R. Muzykantov, *Expert Opin Drug Deliv*, **2008**, 5, 1283-1300.

37. H. S. Choi, B. I. Ipe, P. Misra, J. H. Lee, M. G. Bawendi and J. V. Frangioni, *Nano Lett*, **2009**, 9, 2354-2359.

38. Y. Geng, P. Dalhaimer, S. Cai, R. Tsai, M. Tewari, T. Minko and D. E. Discher, *Nat Nano*, **2007**, 2, 249-255.

39. X. Huang, L. Li, T. Liu, N. Hao, H. Liu, D. Chen and F. Tang, *ACS Nano*, **2011**, 5, 5390-5399.

40. J. Fang, H. Nakamura and H. Maeda, *Adv. Drug Delivery Rev.*, **2011**, 63, 136-151.

41. N. Rapoport, A. Marin, Y. Luo, G. D. Prestwich and M. D. Muniruzzaman, *J Pharm Sci*, **2002**, 91, 157-170.

42. G. Sahay, D. Y. Alakhova and A. V. Kabanov, *J Control Release*, **2010**, 145, 182-195.

43. N. Oh and J. H. Park, *Int J Nanomedicine*, **2014**, 1, 51-63.

44. R. Sakhtianchi, R. F. Minchin, K.-B. Lee, A. M. Alkilany, V. Serpooshan and M. Mahmoudi, *Adv Colloid Interface Sci*, **2013**, 201–202, 18-29.

45. H. Hillaireau and P. Couvreur, *Cell Mol Life Sci*, **2009**, 66, 2873-2896.

46. S. E. A. Gratton, P. A. Ropp, P. D. Pohlhaus, J. C. Luft, V. J. Madden, M. E. Napier and J. M. DeSimone, *Proc Natl Acad Sci U S A*, **2008**, 105, 11613-11618.

47. M. Zhu, G. Nie, H. Meng, T. Xia, A. Nel and Y. Zhao, *Acc Chem Res*, **2013**, 46, 622-631.

48. Z. Mao, X. Zhou and C. Gao, *Biomater Sci*, **2013**, 1, 896-911.

49. G. Sahay, E. V. Batrakova and A. V. Kabanov, *Bioconjug Chem*, **2008**, 19, 2023-2029.

50. M. Muniruzzaman, A. Marin, Y. Luo, G. D. Prestwich, W. G. Pitt, G. Husseini and N. Y. Rapoport, *Colloids Surf B Biointerfaces*, **2002**, 25, 233-241.

51. A. Mahmud and A. Lavasanifar, *Colloids Surf B Biointerfaces*, **2005**, 45, 82-89.

52. Z. Zhang, Q. Qu, J. Li and S. Zhou, *Macromol Biosci*, **2013**, 13, 789-798.

53. Y. Kim, M. H. Pourgholami, D. L. Morris, H. Lu and M. H. Stenzel, *Biomater Sci*, **2013**, 1, 265-275.

54. Y. Kim, M. H. Pourgholami, D. L. Morris and M. H. Stenzel, *Biomacromolecules*, **2012**, 13, 814-825.

55. B. Hoang, R. M. Reilly and C. Allen, *Biomacromolecules*, **2012**, 13, 455-465.

56. E. V. Batrakova, S. Li, Y. Li, V. Y. Alakhov, W. F. Elmquist and A. V. Kabanov, *J Control Release*, **2004**, 100, 389-397.

57. J. Liu, F. Zeng and C. Allen, *Eur J Pharm Biopharm*, **2007**, 65, 309-319.

58. J. van den Eijnde and M. Schouwenburg, *Practical Radiation Protection*, Syntax Media, Utrecht, **2013**.

59. https://de.wikipedia.org/wiki/Nuklidkarte, (accessed 06-09-2015).

60. F. Buchegger, F. Perillo-Adamer, Y. M. Dupertuis and A. B. Delaloye, *Eur J Nucl Med Mol Imaging*, **2006**, 33, 1352-1363.

61. T. M. Behr, M. Behe, M. Lohr, G. Sgouros, C. Angerstein, E. Wehrmann, K. Nebendahl and W. Becker, *Eur J Nucl Med*, **2000**, 27, 753-765.

62. J. Wang, P. Chen, Z.-F. Su, K. Vallis, J. Sandhu, R. Cameron, A. Hendler and R. M. Reilly, *Nucl Med Biol*, **2001**, 28, 895-902.

63. L. Bodei, A. I. Kassis, S. J. Adelstein and G. Mariani, *Cancer Biother Radiopharm*, **2003**, 18, 861-877.

64. C. A. Boswell and M. W. Brechbiel, *J Nucl Med*, **2005**, 46, 1946-1947.

65. I. Verel, G. W. Visser and G. A. van Dongen, *J Nucl Med*, **2005**, 46, 164S-171S.

66. W. Branderhorst, F. van der Have, B. Vastenhouw, M. A. Viergever and F. J. Beekman, *Phys Med Biol*, **2012**, 57, 717-732.

67. F. M. Nortier, S. J. Mills and G. F. Steyn, *Appl Radiat Isot*, **1990**, 41, 1201-1208.

68. T. J. Wadas, E. H. Wong, G. R. Weisman and C. J. Anderson, *Chem Rev*, **2010**, 110, 2858-2902.

69. C. F. Meares, M. J. McCall, D. T. Reardan, D. A. Goodwin, C. I. Diamanti and M. McTigue, *Anal Biochem*, **1984**, 142, 68-78.

70. M. S. Cooper, E. Sabbah and S. J. Mather, *Nat. Protocols*, **2006**, 1, 314-317.

71. M. L. Adams, A. Lavasanifar and G. S. Kwon, *J Pharm Sci*, **2003**, 92, 1343-1355.

72. S. Movassaghian, O. M. Merkel and V. P. Torchilin, *Wiley Interdiscip Rev Nanomed Nanobiotechnol*, **2015**.

73. P. Alexandridis and T. Alan Hatton, *Colloids Surf A Physicochem Eng Asp*, **1995**, 96, 1-46.

74. Y. Yu and A. Eisenberg, *J Am Chem Soc*, **1997**, 119, 8383-8384.

75. L. Liu, X. Gao, Y. Cong, B. Li and Y. Han, *Macromol Rapid Commun*, **2006**, 27, 260-265.

76. H. Shen and A. Eisenberg, *Macromolecules*, **2000**, 33, 2561-2572.

77. S. Jain and F. S. Bates, *Macromolecules*, **2004**, 37, 1511-1523.

78. T. Ohta and K. Kawasaki, *Macromolecules*, **1986**, 19, 2621-2632.

79. G. Wanka, H. Hoffmann and W. Ulbricht, *Macromolecules*, **1994**, 27, 4145-4159.

80. W. Loh, *Journal*, **2002**.

81. J. A. Faucher, *J Polym Sci, Part B: Polym Phys* **1965**, 3, 143-145.

82. P. G. de Gennes, *Solid State Physics*, Academic Press, New York, **1978**.

83. L. Zhang and A. Eisenberg, *Science*, **1995**, 268, 1728-1731.

84. D. Y. Alakhova and A. V. Kabanov, *Mol Pharm*, **2014**, 11, 2566-2578.

85. D. A. Chiappetta and A. Sosnik, *Eur J Pharm Biopharm*, **2007**, 66, 303-317.

86. A. Pitto-Barry and N. P. E. Barry, *Polym Chem*, **2014**, 3291–3297.

87. S. C. Rodriguez and E. J. Singer, in *Nonionic Surfactants: Polyoxyalkylene Block Copolymers*, ed. V. M. Nace, CRC Press, New York, **1996**, vol. 60, pp. 211-241.

88. A. V. Kabanov and V. Y. Alakhov, *Crit Rev Ther Drug Carrier Syst*, **2002**, 19, 1-72.

89. A. V. Kabanov, E. V. Batrakova and V. Y. Alakhov, *J Control Release*, **2002**, 82, 189-212.

90. V. P. Torchilin, *Adv Drug Deliv Rev*, **2006**, 58, 1532-1555.

91. V. P. Torchilin, *J Control Release*, **2001**, 73, 137-172.

92. G. Gaucher, M.-H. Dufresne, V. P. Sant, N. Kang, D. Maysinger and J.-C. Leroux, *J Control Release*, **2005**, 109, 169-188.

93. N. Rapoport, W. G. Pitt, H. Sun and J. L. Nelson, *J Control Release*, **2003**, 91, 85-95.

94. R. A. Petros and J. M. DeSimone, *Nat Rev Drug Discov*, **2010**, 9, 615-627.

95. E. Batrakova, S. Lee, S. Li, A. Venne, V. Alakhov and A. Kabanov, *Pharm Res*, **1999**, 16, 1373-1379.

96. E. V. Batrakova and A. V. Kabanov, *J Control Release*, **2008**, 130, 98-106.

97. E. V. Batrakova, S. Li, W. F. Elmquist, D. W. Miller, V. Y. Alakhov and A. V. Kabanov, *Br J Cancer*, **2001**, 85, 1987-1997.

98. A. V. Kabanov, E. V. Batrakova and V. Y. Alakhov, *Adv Drug Deliv Rev*, **2002**, 54, 759-779.

99. S. Kunjachan, B. Rychlik, G. Storm, F. Kiessling and T. Lammers, *Adv Drug Deliv Rev*, **2013**, 65, 1852-1865.

100. T. Demina, I. Grozdova, O. Krylova, A. Zhirnov, V. Istratov, H. Frey, H. Kautz and N. Melik-Nubarov, *Biochemistry*, **2005**, 44, 4042-4054.

101. T. F. Yang, C. N. Chen, M. C. Chen, C. H. Lai, H. F. Liang and H. W. Sung, *Biomaterials*, **2007**, 28, 725-734.

102. E. V. Batrakova and A. V. Kabanov, *J. Controlled Release*, **2008**, 130, 98-106.

103. D. W. Miller, E. V. Batrakova and A. V. Kabanov, *Pharm Res*, **1999**, 16, 396-401.

104. S. Hvidt, E. B. Joergensen, W. Brown and K. Schillen, *J Phys Chem*, **1994**, 98, 12320-12328.

105. O. Glatter, G. Scherf, K. Schillen and W. Brown, *Macromolecules*, **1994**, 27, 6046-6054.

106. K. Mortensen, W. Brown and B. Nordén, *Phys Rev Lett*, **1992**, 68, 2340-2343.

107. K. Mortensen, *J Phys Condens Matter*, **1996**, 8, A103.

108. R. Ganguly, V. K. Aswal and P. A. Hassan, *J Colloid Interface Sci*, **2007**, 315, 693-700.

109. A. G. Denkova, E. Mendes and M. O. Coppens, *J Phys Chem B*, **2008**, 112, 793-801.

110. J. P. Mata, P. R. Majhi, C. Guo, H. Z. Liu and P. Bahadur, *J Colloid Interface Sci*, **2005**, 292, 548-556.

111. Y. L. Su, X. F. Wei and H. Z. Liu, *J Colloid Interface Sci*, **2003**, 264, 526-531.

112. Y. Kadam, R. Ganguly, M. Kumbhakar, V. K. Aswal, P. A. Hassan and P. Bahadur, *J Phys Chem B*, **2009**, 113, 16296-16302.

113. E. B. Jørgensen, S. Hvidt, W. Brown and K. Schillén, *Macromolecules*, **1997**, 30, 2355-2364.

114. L. Guo, R. H. Colby and P. Thiyagarajan, *Physica B: Condensed Matter*, **2006**, 385–386, Part 1, 685-687.

115. V. Patel, J. Dey, R. Ganguly, S. Kumar, S. Nath, V. K. Aswal and P. Bahadur, *Soft Matter*, **2013**, 9, 7583-7591.

116. B. Bharatiya, C. Guo, J. H. Ma, P. A. Hassan and P. Bahadur, *Eur Polym J*, **2007**, 43, 1883-1891.

117. P. Parekh, K. Singh, D. G. Marangoni and P. Bahadur, *J Mol Liq*, **2012**, 165, 49-54.

118. K. Nakashima and P. Bahadur, *Adv Colloid Interface Sci*, **2006**, 126, 75-96.

119. P. Alexandridis, V. Athanassiou and T. A. Hatton, *Langmuir*, **1995**, 11, 2442-2450.

120. Y. Zhang and P. S. Cremer, *Curr Opin Chem Biol*, **2006**, 10, 658-663.

121. Z. Yang, *J Biotechnol* **2009**, 144, 12-22.

122. J. Dey, S. Kumar, S. Nath, R. Ganguly, V. K. Aswal and K. Ismail, *J Colloid Interface Sci*, **2014**, 415, 95-102.

123. M. Khimani, R. Ganguly, V. K. Aswal, S. Nath and P. Bahadur, *J Phys Chem B*, **2012**, 116, 14943-14950.

124. B. Foster, T. Cosgrove and B. Hammouda, *Langmuir*, **2009**, 25, 6760-6766.

125. P. Parekh, R. Ganguly, V. K. Aswal and P. Bahadur, *Soft Matter*, **2012**, 8, 5864-5872.

126. D. Y. Alakhova, Y. Zhao, S. Li and A. V. Kabanov, *PLoS One*, **2013**, 8.

127. V. Alakhov, E. Klinski, S. Li, G. Pietrzynski, A. Venne, E. Batrakova, T. Bronitch and A. Kabanov, *Colloids Surf B*, **1999**, 16, 113-134.

128. S. E. Jin, H. E. Jin and S. S. Hong, *Biomed Res Int*, **2014**, 2014, 814208.

129. S. Danson, D. Ferry, V. Alakhov, J. Margison, D. Kerr, D. Jowle, M. Brampton, G. Halbert and M. Ranson, *Br J Cancer*, **2004**, 90, 2085-2091.

130. J. W. Valle, A. Armstrong, C. Newman, V. Alakhov, G. Pietrzynski, J. Brewer, S. Campbell, P. Corrie, E. K. Rowinsky and M. Ranson, *Invest New Drugs*, **2011**, 29, 1029-1037.

131. D. Sutton, N. Nasongkla, E. Blanco and J. Gao, *Pharm Res*, **2007**, 24, 1029-1046.

132. M. Talelli, C. J. F. Rijcken, W. E. Hennink and T. Lammers, *Curr Opin Solid State Mater Sci*, **2012**, 16, 302-309.

133. D. A. Christian, S. Cai, O. B. Garbuzenko, T. Harada, A. L. Zajac, T. Minko and D. E. Discher, *Mol Pharm*, **2009**, 6, 1343-1352.

134. N. Nishiyama, *Nat Nano*, **2007**, 2, 203-204.

135. S. C. Owen, D. P. Y. Chan and M. S. Shoichet, *Nano Today*, **2012**, 7, 53-65.

136. G. Waton, B. Michels and R. Zana, *J Colloid Interface Sci*, **1999**, 212, 593-596.

137. G. Waton, *J Phys Chem B*, **1997**, 101, 9727-9731.

138. G. Waton, B. Michels and R. Zana, *Macromolecules*, **2001**, 34, 907-910.

139. Y. Rharbi, *Macromolecules*, **2012**, 45, 9823-9826.

140. G. Landazuri, V. V. A. Fernandez, J. F. A. Soltero and Y. Rharbi, *J Phys Chem B*, **2012**, 116, 11720-11727.

141. A. G. Denkova, E. Mendes and M.-O. Coppens, *Soft Matter*, **2010**, 6, 2351-2357.

142. E. A. G. Aniansson and S. N. Wall, *J Phys Chem*, **1974**, 78, 1024-1030.

143. A. G. Denkova, E. Mendes and M. O. Coppens, *J Phys Chem B*, **2009**, 113, 989-996.

144. B. J. Berne and R. Pecora, *Dynamic Light Scattering with Applications to Chemistry, Biology, and Physics*, Wiley Interscience, New York, **1976**.

145. M. Doi and S. F. Edwards, *The Theory of Polymer Dynamics*, Oxford University Press, Oxford, **1986**.

146. P. Lindner and T. Zemb, *Neutrons, X-rays and Light: Scattering Methods Applied to Soft Condensed Matter*, **2002**.

147. T. Nicolai, O. Colombani and C. Chassenieux, *Soft Matter*, **2010**, 6, 3111-3118.

148. R. Lund, L. Willner and D. Richter, in *Controlled Polymerization and Polymeric Structures*, eds. A. Abe, K. S. Lee, L. Leibler and S. Kobayashi, Springer International Publishing, **2013**, vol. 259, pp. 51-158.

149. M. Kahlweit, *Pure Appl Chem*, **1981**, 53, 2069-2081.

150. B. Michels, G. Waton and R. Zana, *Langmuir*, **1997**, 13, 3111-3118.

151. M. Kahlweit, *J Colloid Interf Sci*, **1982**, 90, 92-99.

152. M. J. Kositza, C. Bohne, P. Alexandridis, T. A. Hatton and J. F. Holzwarth, *Langmuir*, **1998**, 15, 322-325.

153. E. E. Dormidontova, *Macromolecules*, **1999**, 32, 7630-7644.

154. R. Zana, C. Marques and A. Johner, *Adv Colloid Interface Sci*, **2006**, 123–126, 345-351.

155. M. J. Kositza, C. Bohne, P. Alexandridis, T. A. Hatton and J. F. Holzwarth, *Macromolecules*, **1999**, 32, 5539-5551.

156. T. Thurn, S. Couderc-Azouani, D. M. Bloor, J. F. Holzwarth and E. Wyn-Jones, *Langmuir*, **2003**, 19, 4363-4370.

157. A. Halperin and S. Alexander, *Macromolecules*, **1989**, 22, 2403-2412.

158. E. Hecht and H. Hoffmann, *Colloids Surf A Physicochem Eng Asp*, **1995**, 96, 181-197.

159. I. Goldmints, J. F. Holzwarth, K. A. Smith and T. A. Hatton, *Langmuir*, **1997**, 13, 6130-6134.

160. I. LaRue, M. Adam, M. Pitsikalis, N. Hadjichristidis, M. Rubinstein and S. S. Sheiko, *Macromolecules*, **2006**, 39, 309-314.

161. R. Ganguly, M. Kumbhakar and V. K. Aswal, *J Phys Chem B*, **2009**, 113, 9441-9446.

162. R. Ganguly, K. Kuperkar, P. Parekh, V. K. Aswal and P. Bahadur, *J Colloid Interf Sci*, **2012**, 378, 118-124.

163. L. A. Fielding, J. A. Lane, M. J. Derry, O. O. Mykhaylyk and S. P. Armes, *J Am Chem Soc*, **2014**, 136, 5790-5798.

164. M. Duval, G. Waton and F. Schosseler, *Langmuir*, **2005**, 21, 4904-4911.

165. K. Mortensen and W. Brown, *Macromolecules*, **1993**, 26, 4128-4135.

166. S. E. Burke and A. Eisenberg, *Langmuir*, **2001**, 17, 8341-8347.

167. R. Lund, L. Willner, D. Richter, P. Lindner and T. Narayanan, *ACS Macro Letters*, **2013**, 2, 1082-1087.

168. I. Echavarri Franco, P. Lorchat, J. P. Lamps, M. Schmutz, A. Schröder, J. M. Catala, J. Combet and F. Schosseler, *Langmuir*, **2012**, 28, 4815-4828.

169. Z. Zhou, B. Chu and D. G. Peiffer, *Macromolecules*, **1993**, 26, 1876-1883.

170. R. Klucker, J. P. Munch and F. Schosseler, *Macromolecules*, **1997**, 30, 3839-3848.

171. V. V. Fernandez, J. F. Soltero, J. E. Puig and Y. Rharbi, *J Phys Chem B*, **2009**, 113, 3015-3023.

172. Z. Zhou and B. Chu, *Macromolecules*, **1987**, 20, 3089-3091.

173. U. Holzgrabe, B. W. Diehl and I. Wawer, *J Pharm Biomed Anal*, **1998**, 17, 557-616.

174. J. U. Izunobi and C. L. Higginbotham, *J Chem Educ*, **2011**, 88, 1098-1104.

175. A. Postma, T. P. Davis, A. R. Donovan, G. Li, G. Moad, R. Mulder and M. S. O'Shea, *Polymer*, **2006**, 47, 1899-1911.

176. S. Saeki, N. Kuwahara, M. Nakata and M. Kaneko, *Polymer*, **1977**, 18, 1027-1031.

177. P. G. de Gennes, *Scaling Concepts in Polymer Physics*, Cornell University Press, Ithaca, New York, **1979**.

178. R. Lund, L. Willner, V. Pipich, I. Grillo, P. Lindner, J. Colmenero and D. Richter, *Macromolecules*, **2011**, 44, 6145-6154.

179. P. Alexandridis, J. F. Holzwarth and T. A. Hatton, *Macromolecules*, **1994**, 27, 2414-2425.

180. L. Willner, A. Poppe, J. Allgaier, M. Monkenbusch and D. Richter, *EPL (Europhysics Letters)*, **2001**, 55, 667.

181. Y.-Y. Won, H. T. Davis and F. S. Bates, *Macromolecules*, **2003**, 36, 953-955.

182. R. Lund, L. Willner, D. Richter and E. E. Dormidontova, *Macromolecules*, **2006**, 39, 4566-4575.

183. R. Lund, L. Willner, J. Stellbrink, P. Lindner and D. Richter, *Phys Rev Lett*, **2006**, 96, 15.

184. R. Lund, L. Willner, D. Richter, H. Iatrou, N. Hadjichristidis and P. Lindner, *J Appl Crystallogr* **2007**, 40, s327-s331.

185. S.-H. Choi, T. P. Lodge and F. S. Bates, *Phys Rev Lett*, **2010**, 104, 047802.

186. R. Lund, L. Willner, J. Stellbrink, P. Lindner and D. Richter, *Phys Rev Lett*, **2010**, 104, 049902.

187. T. Zinn, L. Willner, R. Lund, V. Pipich and D. Richter, *Soft Matter*, **2012**, 8, 623-626.

188. J. Lu, F. S. Bates and T. P. Lodge, *ACS Macro Letters*, **2013**, 2, 451-455.

189. N. R. B. Boase, I. Blakey and K. J. Thurecht, *Polym Chem*, **2012**, 3, 1384-1389.

190. T. Krasia-Christoforou and T. K. Georgiou, *J Mater Chem B*, **2013**, 1, 3002-3025.

191. N. Rapoport, *Colloids Surf B*, **1999**, 16, 93-111.

192. C. F. van Nostrum, *Soft Matter*, **2011**, 7, 3246-3259.

193. E. S. Read and S. P. Armes, *Chem Commun*, **2007**, 3021-3035.

194. R. K. O'Reilly, C. J. Hawker and K. L. Wooley, *Chem Soc Rev*, **2006**, 35, 1068-1083.

195. J. D. Pruitt, G. Husseini, N. Rapoport and W. G. Pitt, *Macromolecules*, **2000**, 33, 9306-9309.

196. G. A. Husseini, D. A. Christensen, N. Y. Rapoport and W. G. Pitt, *J Control Release*, **2002**, 83, 303-305.

197. J. L. Nelson, B. L. Roeder, J. C. Carmen, F. Roloff and W. G. Pitt, *Cancer Res*, **2002**, 62, 7280-7283.

198. P. Petrov, M. Bozukov and C. B. Tsvetanov, *J Mater Chem*, **2005**, 15, 1481.

199. K. Yoncheva, P. Calleja, M. Agüeros, P. Petrov, I. Miladinova, C. Tsvetanov and J. M. Irache, *Int J Pharm*, **2012**, 436, 258-264.

200. G. Niu, A. B. Djaoui and D. Cohn, *Polymer*, **2011**, 52, 2524-2530.

201. J.-Y. Kim, W. I. Choi, Y. H. Kim, G. Tae, S.-Y. Lee, K. Kim and I. C. Kwon, *J Control Release*, **2010**, 147, 109-117.

202. W. I. Choi, G. Tae and Y. H. Kim, *J Mater Chem*, **2008**, 18, 2769-2774.

203. K. H. Bae, Y. Lee and T. G. Park, *Biomacromolecules*, **2007**, 8, 650-656.

204. M. Di Biase, P. de Leonardis, V. Castelletto, I. W. Hamley, B. Derby and N. Tirelli, *Soft Matter*, **2011**, 7, 4928-4937.

205. N. Abdullah Al, H. Lee, Y. S. Lee, K. D. Lee and S. Y. Park, *Macromol Biosci*, **2011**, 11, 1264-1271.

206. D. H. Nguyen, J. W. Bae, J. H. Choi, J. S. Lee and K. D. Park, *J Bioact Compat Polym*, **2013**, 28, 341-354.

207. R. P. Brinkhuis, K. Stojanov, P. Laverman, J. Eilander, I. S. Zuhorn, F. P. J. T. Rutjes and J. C. M. van Hest, *Bioconjugate Chem*, **2012**, 23, 958-965.

208. B. Hoang, H. Lee, R. M. Reilly and C. Allen, *Mol Pharm*, **2009**, 6, 581-592.

209. A. Arranja, A. Schroder, M. Schmutz, G. Waton, F. Schosseler and E. Mendes, *J Control Release*, **2014**, 13, 87-95.

210. Z. Lu and T. Hirt, **2012**, US Patent 2012/0121518A1.

211. H. F. Lu, W. S. Lim, J. Wang, Z. Q. Tang, P. C. Zhang, K. W. Leong, S. M. Chia, H. Yu and H. Q. Mao, *Biomaterials*, **2003**, 24, 4893-4903.

212. B. Hoang, H. Lee, R. M. Reilly and C. Allen, *Mol Pharm*, **2009**, 6, 581-592.

213. Y.-Y. Won, A. K. Brannan, H. T. Davis and F. S. Bates, *J Phys Chem B*, **2002**, 106, 3354-3364.

214. K. Mortensen and Y. Talmon, *Macromolecules*, **1995**, 28, 8829-8834.

215. X. Ye, J. Zhang, H. Chen, X. Wang and F. Huang, *ACS Appl Mater Interfaces*, **2014**.

216. H. Tan, N. S. Liu, B. He, S. Y. Wong, Z.-K. Chen, X. Li and J. Wang, *Chem Commun*, **2009**, 6240-6242.

217. S. M. Moghimi, A. C. Hunter and J. C. Murray, *Pharmacol Rev*, **2001**, 53, 283-318.

218. M. N. Lub-de Hooge, J. G. W. Kosterink, P. J. Perik, H. Nijnuis, L. Tran, J. Bart, A. J. H. Suurmeijer, S. de Jong, P. L. Jager and E. G. E. de Vries, *Br J Pharmacol*, **2004**, 143, 99-106.

219. D. J. Hnatowich, *Int J Rad Appl Instrum B*, **1986**, 13, 353-358.

220. R. R. Patil, J. Yu, S. R. Banerjee, Y. Ren, D. Leong, X. Jiang, M. Pomper, B. Tsui, D. L. Kraitchman and H.-Q. Mao, *Mol Ther*, **2011**, 19, 1626-1635.

221. R. P. Brinkhuis, K. Stojanov, P. Laverman, J. Eilander, I. S. Zuhorn, F. P. J. T. Rutjes and J. C. M. van Hest, *Bioconjug Chem*, **2012**, 23, 958-965.

222. W. R. Harris, Y. Chen and K. Wein, *Inorg Chem*, **1994**, 33, 4991-4998.

223. J. Fang, H. Nakamura and H. Maeda, *Adv Drug Deliv Rev*, **2011**, 63, 136-151.

224. G. Sahay, D. Y. Alakhova and A. V. Kabanov, *J. Controlled Release*, **2010**, 145, 182-195.

225. G. Sahay, E. V. Batrakova and A. V. Kabanov, *Bioconjugate Chem.*, **2008**, 19, 2023-2029.

226. M. Muniruzzaman, A. Marin, Y. Luo, G. D. Prestwich, W. G. Pitt, G. Husseini and N. Y. Rapoport, *Colloids Surf., B*, **2002**, 25, 233-241.

227. E. V. Batrakova, S. Li, V. Y. Alakhov, D. W. Miller and A. V. Kabanov, *J Pharmacol Exp Ther*, **2003**, 304, 845-854.

228. E. V. Batrakova, S. Li, Y. Li, V. Y. Alakhov, W. F. Elmquist and A. V. Kabanov, *J. Controlled Release*, **2004**, 100, 389-397.

229. J. M. Grindel, T. Jaworski, O. Piraner, R. M. Emanuele and M. Balasubramanian, *J Pharm Sci*, **2002**, 91, 1936-1947.

230. N. S. Melik-Nubarov, O. O. Pomaz, T. Y. Dorodnych, G. A. Badun, A. L. Ksenofontov, O. B. Schemchukova and S. A. Arzhakov, *FEBS Lett.*, **1999**, 446, 194-198.

231. F. Hirschhaeuser, H. Menne, C. Dittfeld, J. West, W. Mueller-Klieser and L. A. Kunz-Schughart, *J Biotechnol*, **2010**, 148, 3-15.

232. N. R. Patel, B. S. Pattni, A. H. Abouzeid and V. P. Torchilin, *Adv Drug Deliv Rev*, **2013**, 65, 1748-1762.

233. J. Friedrich, R. Ebner and L. A. Kunz-Schughart, *Int J Radiat Biol*, **2007**, 83, 849-871.

234. T. Lammers, F. Kiessling, W. E. Hennink and G. Storm, *J. Controlled Release*, **2012**, 161, 175-187.

235. https://en.wikipedia.org/wiki/MTT_assay, (accessed 06-09-2015).

236. M. Kahm, G. Hasenbrink, H. Lichtenberg-Frate, J. Ludwig and M. Kschischo, *J Stat Softw*, **2010**, 33(7), 1-21.

237. R. I. Freshney, *Culture of Animal Cells: A Manual of Basic Technique and Specialized Applications*, John Wiley & Sons, Inc., **2010**.

238. R. Coradeghini, S. Gioria, C. P. García, P. Nativo, F. Franchini, D. Gilliland, J. Ponti and F. Rossi, *Toxicol Lett*, **2013**, 217, 205-216.

239. D. M. Ridolfi, P. D. Marcato, D. Machado, R. A. Silva, G. Z. Justo and N. Durán, *J Phys Conf Se*, **2011**, 304, 012032.

240. M. Safi, H. Sarrouj, O. Sandre, N. Mignet and J. F. Berret, *Nanotechnology*, **2010**, 21, 145103.

241. J. Ponti, F. Broggi, V. Mariani, L. De Marzi, R. Colognato, P. Marmorato, S. Gioria, D. Gilliland, C. Pascual Garcia, S. Meschini, A. Stringaro, A. Molinari, H. Rauscher and F. Rossi, *Nanotoxicology*, **2013**, 7, 221-233.

242. R. Sun, Q. Luo, C. Gao, Y. Wang, L. Gao, H. Du, Y. Huang, X. Li, Z. Shen and W. Zhu, *Polym Chem*, **2014**, 5, 4879-4883.

243. S. L. Demento, N. Bonafe, W. Cui, S. M. Kaech, M. J. Caplan, E. Fikrig, M. Ledizet and T. M. Fahmy, *J Immunol*, **2010**, 185, 2989-2997.

244. R. Kapon, B. Naim, D. Zbaida, R. Nevo, O. Tsabari and Z. Reich, *Nucleus*, **2010**, 1, 475-480.

245. E. Oh, J. B. Delehanty, K. E. Sapsford, K. Susumu, R. Goswami, J. B. Blanco-Canosa, P. E. Dawson, J. Granek, M. Shoff, Q. Zhang, P. L. Goering, A. Huston and I. L. Medintz, *ACS Nano*, **2011**, 5, 6434-6448.

246. Z. Mao, X. Zhou and C. Gao, *Biomater. Sci.*, **2013**, 1, 896-911.

247. C. Brandenberger, C. Muhlfeld, Z. Ali, A. G. Lenz, O. Schmid, W. J. Parak, P. Gehr and B. Rothen-Rutishauser, *Small*, **2010**, 6, 1669-1678.

248. S. D. Conner and S. L. Schmid, *Nature*, **2003**, 422, 37-44.

249. K. A. McMahon, M. Zhu, S. W. Kwon, P. Liu, Y. Zhao and R. G. Anderson, *Proteomics*, **2006**, 6, 143-152.

250. M. Videira, A. Arranja, D. Rafael and R. Gaspar, *Nanomedicine*, **2014**, 10, 689-702.

251. A. Mahmud and A. Lavasanifar, *Colloids Surf., B*, **2005**, 45, 82-89.

252. N. Oh and J. H. Park, *Int. J. Nanomed.*, **2014**, 1, 51-63.

253. A. Arranja, A. Schroder, M. Schmutz, G. Waton, F. Schosseler and E. Mendes, *J. Controlled Release*, **2014**, 13, 87-95.

254. C. L. Waite and C. M. Roth, *CRC Crit Rev Bioeng*, **2012**, 40, 21-41.

255. A. Pluen, Y. Boucher, S. Ramanujan, T. D. McKee, T. Gohongi, E. di Tomaso, E. B. Brown, Y. Izumi, R. B. Campbell, D. A. Berk and R. K. Jain, *Proc Natl Acad Sci U S A*, **2001**, 98, 4628-4633.

256. H. Lu, R. H. Utama, U. Kitiyotsawat, K. Babiuch, Y. Jiang and M. H. Stenzel, *Biomater Sci*, **2015**.

257. F. Yuan, A. Krol and S. Tong, *Ann Biomed Eng*, **2001**, 29, 1150-1158.

258. R. K. Jain, *Adv Drug Deliv Rev*, **2001**, 46, 149-168.

259. A. S. Mikhail, S. Eetezadi, S. N. Ekdawi, J. Stewart and C. Allen, *Int J Pharm*, **2014**, 464, 168-177.

260. R. Grantab, S. Sivananthan and I. F. Tannock, *Cancer Res*, **2006**, 66, 1033-1039.

261. S. McGuire and F. Yuan, *Nanomedicine*, **2012**, 8, 1088-1095.

262. M. L. Willcox, M. M. Newman and B. C. Paton, *J Surg Res*, **1978**, 25, 349-356.

263. Z. Y. Wang and I. J. Stern, *Drug Metab Dispos*, **1975**, 3, 536-542.

264. E. V. Batrakova, Y. Zhang, Y. Li, S. Li, S. V. Vinogradov, Y. Persidsky, V. Y. Alakhov, D. W. Miller and A. V. Kabanov, *Pharm Res*, **2004**, 21, 1993-2000.

265. F. van der Have, B. Vastenhouw, R. M. Ramakers, W. Branderhorst, J. O. Krah, C. Ji, S. G. Staelens and F. J. Beekman, *J Nucl Med*, **2009**, 50, 599-605.

266. O. Ivashchenko, F. van der Have, M. C. Goorden, R. M. Ramakers and F. J. Beekman, *J Nucl Med*, **2015**, 56, 470-475.

267. W. Branderhorst, B. Vastenhouw and F. J. Beekman, *Phys Med Biol*, **2010**, 55, 2023-2034.

268. F. van der Have, B. Vastenhouw, M. Rentmeester and F. J. Beekman, *IEEE Trans Med Imaging*, **2008**, 27, 960-971.

269. M. A. King, S. J. Glick, P. Hendrik Pretorius, R. Glenn Wells, H. C. Gifford, M. V. Narayanan and T. Farncombe, in *Emission Tomography*, ed. M. N. W. N. Aarsvold, Academic Press, San Diego, **2004**, pp. 473-498.

270. C. Wu, J. R. de Jong, H. A. Gratama van Andel, F. van der Have, B. Vastenhouw, P. Laverman, O. C. Boerman, R. A. Dierckx and F. J. Beekman, *Phys Med Biol*, **2011**, 56, N183-193.

271. T. Yamaoka, Y. Tabata and Y. Ikada, *J Pharm Sci*, **1994**, 83, 601-606.

272. A. I. Jensen, T. Binderup, P. Kumar Ek, A. Kjær, P. H. Rasmussen and T. L. Andresen, *Biomacromolecules*, **2014**, 15, 1625-1633.

273. Z. Yang, S. Zheng, W. J. Harrison, J. Harder, X. Wen, J. G. Gelovani, A. Qiao and C. Li, *Biomacromolecules*, **2007**, 8, 3422-3428.

274. E. Wisse, F. Jacobs, B. Topal, P. Frederik and B. De Geest, *Gene Ther*, **2008**, 15, 1193-1199.

275. H. Soo Choi, W. Liu, P. Misra, E. Tanaka, J. P. Zimmer, B. Itty Ipe, M. G. Bawendi and J. V. Frangioni, *Nat Biotechnol*, **2007**, 25, 1165-1170.

276. M. Longmire, P. L. Choyke and H. Kobayashi, *Nanomedicine (Lond)*, **2008**, 3, 703-717.

277. K.-i. Ogawara, M. Yoshida, K. Higaki, K. Toshikiro, K. Shiraishi, M. Nishikawa, Y. Takakura and M. Hashida, *J Control Release*, **1999**, 59, 15-22.

278. A. L. Klibanov, K. Maruyama, V. P. Torchilin and L. Huang, *FEBS Lett*, **1990**, 268, 235-237.

279. D. E. Discher and F. Ahmed, *Annu Rev Biomed Eng*, **2006**, 8, 323-341.

280. J. Bhattacharjee, G. Verma, V. K. Aswal, V. Patravale and P. A. Hassan, *RSC Adv*, **2013**, 3, 23080-23089.

281. S. M. Moghimi, *FEBS Lett*, **2003**, 540, 241-244.

282. D. E. Owens, 3rd and N. A. Peppas, *Int J Pharm*, **2006**, 307, 93-102.

283. H. Harashima and H. Kiwada, *Adv Drug Deliv Rev*, **1996**, 19, 425-444.

284. D. C. Litzinger, A. M. J. Buiting, N. van Rooijen and L. Huang, *Biochim Biophys Acta*, **1994**, 1190, 99-107.

285. M. A. Dobrovolskaia and S. E. McNeil, *Nat Nanotechnol*, **2007**, 2, 469-478.

286. P. Petrov, J. Yuan, K. Yoncheva, A. H. E. Müller and C. B. Tsvetanov, *J Phys Chem B*, **2008**, 112, 8879-8883.

Résumé en Français

Plan de Thèse

Ce projet de thèse a été financé par le *People Programme (Marie Curie Actions)* du septième programme-cadre de l'Union européenne (FP7/2007-2013) dans le cadre du projet "TRACE'nTREAT". Ce réseau de formation initiale regroupe plusieurs partenaires académiques et industriels de différents pays avec une grande variété d'expertises complémentaires.

Le travail présenté dans cette thèse est le résultat de trois années de recherche réalisée principalement à Strasbourg (Institut Charles Sadron, Université de Strasbourg), mais aussi pendant 6 mois à l'étranger à Delft (Réacteur Institut de Delft, de l'Université technique de Delft) et à Utrecht (MILabs). Les discussions fructueuses de la collaboration entre les différents partenaires, les périodes de recherche à l'étranger, et la formation pluridisciplinaire intense étaient cruciales pour l'élaboration de cette thèse.

Les objectifs principaux du projet "TRACE'nTREAT" sont la production de radionucléides pour l'imagerie nucléaire et/ou la radiothérapie, leur incorporation dans des nouveaux véhicules moléculaires et supramoléculaires polymériques, et leur évaluation préclinique.

Dans le cadre de ce projet, l'objectif principal de cette thèse est le développement, la caractérisation et l'évaluation préclinique des nanovéhicules polymères moléculaires et supramoléculaires. Ces véhicules sont élaborés à partir de copolymères triséquencés commerciaux de type Pluronic

Les objectifs spécifiques de cette thèse sont:

(i) Acquérir une meilleure compréhension fondamentale des phénomènes de croissance et de décroissance des micelles de Pluronic, quand ils évoluent à partir des unimères simples à des morphologies structurées complexes.

(ii) Développer des nanovéhicules à partir des copolymères de Pluronic. Ces copolymères seront fonctionnalisés par des marqueurs fluorescents ou radioactifs et utilisés sous forme d'unimères dissociés ou sous forme de micelles stabilisées par réticulation. Nous varierons également le poids moléculaire et la composition des copolymères utilisés.

(iii) Comprendre l'effet de ces paramètres physico-chimiques sur les interactions cellulaires avec les modèles *in vitro* 2D et 3D, et sur la biodistribution *in vivo*.

La thèse est organisée comme suit:

Le Chapitre 1 présente les concepts généraux nécessaires à une meilleure compréhension des différents aspects abordés dans cette thèse. Nous introduisons l'importance de la nanomédecine et des technologies d'imagerie, les propriétés des copolymères séquencés à base de Pluronics, et nous terminons avec quelques concepts utiles sur la diffusion de lumière dynamique.

Le Chapitre 2 explore la cinétique de la transition de la forme sphérique à la forme cylindrique des copolymères Pluronic avec un poids moléculaire croissant et un ratio hydrophobe/hydrophile constant.

Le Chapitre 3 décrit le développement des nanovéhicules moléculaires (unimères) et supramoléculaires (micelles stabilisées) avec différentes longueurs du bloc de PEO. Nous décrivons aussi la fonctionnalisation des véhicules avec un marqueur fluorescent et un chélatant appropriés pour l'imagerie et la quantification.

Le Chapitre 4 analyse les interactions *in vitro* des différents véhicules en utilisant la culture cellulaire 2D et 3D. On étudie spécifiquement la cytotoxicité, la cinétique d'internalisation et la rétention dans les cultures cellulaires 2D, tandis que les sphéroïdes de tumeur 3D sont utilisés pour évaluer la pénétration et la toxicité potentielle des véhicules.

Le chapitre 5 se concentre sur l'évaluation *in vivo* de la biodistribution des nanovéhicules radiomarqués dans les souris saines, et l'évaluation de l'influence des différents aspects physico-chimiques (longueur du bloc de PEO et l'état d'agrégation).

Un résumé général des conclusions dans chaque phase du projet et les perspectives futures sont présentés à la fin de la thèse.

Chapitre 1

Introduction

Le développement de nanomédicaments a suscité un intérêt croissant à cause de leur potentiel pour l'imagerie, le diagnostic et le traitement de plusieurs maladies, en particulier dans le domaine de l'oncologie. Les premières générations d'agents chimio-thérapeutiques présentent plusieurs inconvénients en raison de leur faible poids moléculaire et de leur forte hydrophobie. Ces caractères entraînent leur élimination rapide du corps et leur dégradation enzymatique, en même temps que leur distribution généralisée dans le corps associe toxicité pour les tissus sains et faible accumulation dans les sites ciblés.

Pour surmonter ces obstacles, d'autres véhicules à base de polymères, micelles, liposomes, ou nanoparticules ont été développés. Ils ont un volume de distribution réduit conduisant à une accumulation plus faible dans les tissus sains et générant donc moins d'effets secondaires. De plus, ils s'accumulent de préférence dans les zones qui présentent un endothélium vasculaire poreux et un drainage lymphatique défectueux, comme les tumeurs solides. Cet effet de perméabilité et de rétention renforcées est connu sous le nom d'effet «EPR», pour *Enhanced Permeability and Retention*.

Le développement de véhicules à base de polymères (3-10 nm) et de micelles polymères (10-80 nm) est particulièrement intéressant, car ils peuvent être conçus avec des fonctionnalités adaptées aux besoins et ainsi délivrer plus efficacement leur contenu.

Malgré ces avantages, l'administration intraveineuse de véhicules de poids moléculaire plus élevé présente également plusieurs limitations dues à une série de barrières biophysiques. Le principal obstacle est la circulation sanguine où les nanomatériaux sont exposés aux composants spécifiques du sang (opsonines) qui peuvent se lier à leur surface (opsonisation). Cela permettra d'activer le système immunitaire et d'augmenter leurs mécanismes d'élimination. Par conséquent, une forte accumulation des nanovéhicules dans les principaux organes d'élimination (foie et rate) est souvent observée.

Pour visualiser et quantifier leur biodistribution, la stratégie plus courante consiste à utiliser des modalités d'imagerie qui permettent la surveillance non invasive de leur biodistribution spatiale et temporelle. Les techniques d'imagerie les plus utilisées sont la tomographie par émission de positons (PET) et la tomographie d'émission monophotonique (SPECT). Ces techniques reposent sur l'utilisation des radioéléments qui se décomposent et émettent des rayonnements pour permettre leur détection. Ces radioéléments sont conjugués à différents véhicules en fonction de l'application désirée (imagerie ou thérapie). Par exemple, le radioisotope Indium-111 a une demi-vie prolongée de 2.83 jours (67.9 h) qui permet la détection de véhicules avec long temps de circulation, émet deux photons gamma pour permettre la détection, et émet également des électrons Auger qui ont un potentiel élevé d'endommager l'ADN.

Les véhicules développés à partir de Pluronics sont probablement les plus largement utilisés et étudiés. Les Pluronics sont des copolymères amphiphiles triséquencés poly(oxyde d'éthylène)-b-poly(oxyde de propylène)-b-poly(oxyde d'éthylène) (PEO-PPO-PEO). Ils sont très intéressants pour l'imagerie ou pour le transport et la libération de médicaments en raison de leur disponibilité commerciale dans une très large gamme de compositions et de poids moléculaire, de leur biocompatibilité, de leur capacité à intégrer des composés hydrophobes, et de leur approbation par les organismes de réglementation (FDA) pour l'utilisation dans des formulations pharmaceutiques. Selon leur composition, ils peuvent également présenter des effets cytotoxiques importants dans les cellules cancéreuses résistantes à la polychimiothérapie. En raison de leurs propriétés amphiphiles, les chaînes libres de copolymères (unimères) peuvent s'agréger et s'auto-assembler en micelles composées d'un cœur hydrophobe de PPO et d'une couronne hydratée hydrophile de PEO. L'agrégation a lieu au-dessus de la température (cmT) et de la concentration (cmc) micellaires critiques et dépend donc de ces paramètres ainsi que de l'utilisation d'additifs.

Chapitre 2

Effets du poids moléculaire sur la cinétique de croissance et de décroissance de micelles de Pluronics

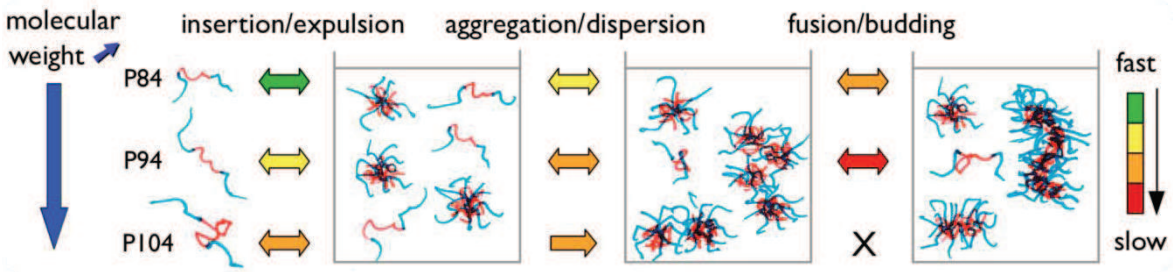

La première partie de cette thèse est focalisée sur l'étude de la croissance et de la décroissance de micelles à base de Pluronics. Nous étudions en particulier l'effet du poids moléculaire du polymère. Les copolymères Pluronics peuvent s'auto-assembler sous forme de sphères ou de cylindres, selon leur poids moléculaire et leur composition. Les micelles formées à partir de copolymères de ratio PEO/PPO intermédiaire présentent à température élevée une transition de la forme sphérique à la forme cylindrique quand leur diamètre de cœur est voisin de la taille du segment PPO entièrement étiré. Toutefois, l'effet du poids moléculaire sur la transition de morphologie de ces copolymères n'a pas été complètement étudié, en particulier du point de vue de la cinétique de cette transition.

Nous avons caractérisé les transitions micellaires d'une série de copolymères Pluronic avec un ratio PEO/PPO constant et un poids moléculaire croissant (P84, P94 et P104) par diffusion de lumière statique et dynamique. Nous avons observé que la croissance et la décroissance des agrégats micellaires dépendaient fortement du poids moléculaire du copolymère et présentaient des voies cinétiques distinctes. Au-dessus de la cmT, la fonction d'autocorrélation de l'intensité diffusée présente un seul mode de relaxation qui correspond à la diffusion Brownienne de micelles sphériques d'environ 8 nm de rayon. Au-dessus d'une certaine température critique, l'intensité totale de la lumière diffusée augmente et la fonction d'autocorrélation de l'intensité présente deux modes de relaxation (rapide et lent), traduisant ainsi l'apparition d'agrégats micellaires de taille plus élevée.

Nous avons suivi l'évolution de ces deux modes de relaxation en fonction du temps écoulé pour caractériser la cinétique de croissance et de décroissance des agrégats micellaires après des sauts de température.

Le polymère P84 montre un ajustement rapide de la taille micellaire en deux étapes après chaque saut de température (T-steps) et forme des cylindres allongés à l'équilibre thermodynamique. Cette croissance micellaire traduit un échange rapide des unimères et des mécanismes de fusion/fission facilités par le faible poids moléculaire du P84. Pour le copolymère P94, de poids moléculaire plus important, ces processus sont ralentis et une croissance continue d'agrégats micellaires allongés est observée. La cinétique de croissance est dominée par une fusion/fission bien plus lente, qui rend l'équilibre thermodynamique problématique. Finalement, dans le cas du Pluronic P104, les processus de fusion/fission deviennent tellement difficiles que les agrégats de micelles ne se transforment plus en micelles cylindriques et restent sous forme sphéroïdale. On observe seulement une très faible croissance des micelles sphériques par le processus d'échange des unimères. Pour tous les copolymères, on observe une coexistence de micelles sphériques avec les agrégats de plus grande taille.

Après refroidissement des solutions vers le régime des micelles sphériques, les micelles allongées de P84 reviennent très rapidement à leur état de micelles sphériques, tandis que les agrégats micellaires de P94 et P104 restent plusieurs jours dans l'état atteint à haute température, micelles allongées pour le P94 et sphéroïdes pour le P104.

Ces résultats sont expliqués par plusieurs processus élémentaires qui fonctionnent simultanément pour équilibrer la population des assemblages micellaires après une augmentation de la température, à savoir l'insertion/l'expulsion des unimères, l'agrégation/dissociation des agrégats micellaires, et la fusion/bourgeonnement des agrégats micellaires. Les cinétiques de ces processus élémentaires dépendent fortement du poids moléculaire du copolymère. Ces résultats ont motivé le choix du P94 comme polymère de base pour la conception de nos nanovéhicules.

Chapitre 3

Développement et fonctionnalisation de nanovéhicules à base de copolymères Pluronic

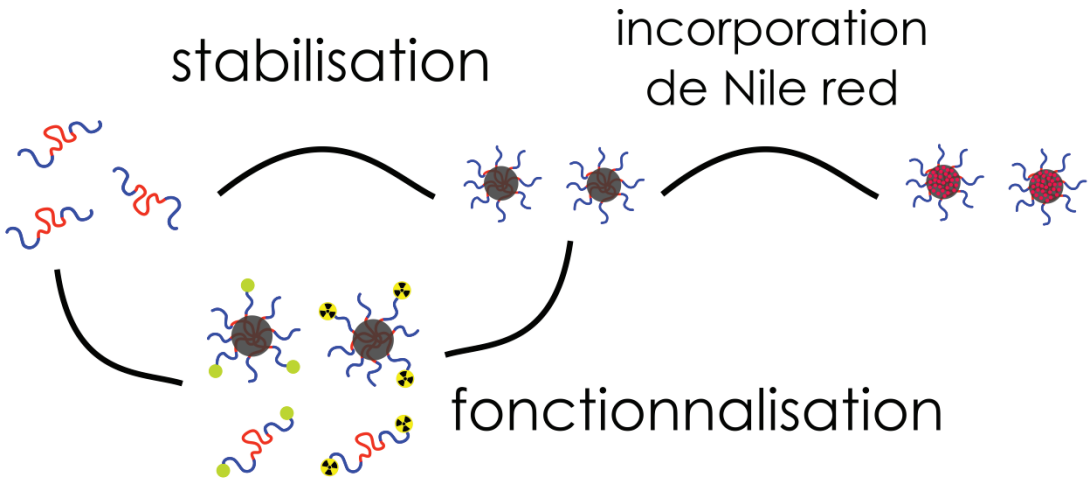

Dans ce chapitre, nous avons présenté le développement et la fonctionnalisation de nanovéhicules moléculaires et supramoléculaires à base de copolymères Pluronic. Deux copolymères de poids moléculaire et de composition PEO/PPO différents ont été sélectionnés (Pluronics P94 et F127) pour obtenir des nanovéhicules avec différentes longueurs du bloc de PEO.

Nous avons développé des véhicules moléculaires et supramoléculaires à base de copolymères de Pluronic (P94 ou F127). Les nanovéhicules supramoléculaires sont obtenus par la stabilisation des micelles dynamiques via réticulation dans le cœur. Les véhicules moléculaires (unimères) présentent des diamètres moyens de 4 à 6 nm et les supramoléculaires (micelles stabilisées) de 28 à 36 nm. Les masses des blocs PEO augmentent (1100 g/mol pour les véhicules basés sur le P94, et 4250 g/mol pour les véhicules basés sur le F127) et la masse du bloc PPO est constante (~3000 g/mol).

Les systèmes moléculaires et supramoléculaires ont été fonctionnalisés par fixation covalente d'un marqueur fluorescent ou d'un chélateur hydrophile pour le radiomarquage avec le radioisotope Indium-111.

Stabilisation de micelles sphériques par un réseau polymère interpénétré

En raison de la nature dynamique des micelles Pluronic, elles peuvent rapidement se désagréger au-dessous de la température (cmT) et de la concentration (cmc) micellaires critiques, ce qui représente un problème pour leur utilisation *in vivo* à cause de l'extrême dilution dans le sang après injection intraveineuse. La désagrégation des micelles affecte la biodistribution et l'internalisation cellulaire des véhicules. Pour cette raison, les micelles de Pluronic F127 et P94 ont été stabilisées par l'incorporation et la polymérisation d'un monomère tétrafonctionnel photo-réticulable hydrophobe (tétraacrylate de pentaérythritol). Ce monomère est solubilisé dans le cœur des micelles et polymérisé pour créer un réseau polymère interpénétré avec les segments de PPO. Ainsi on prévient les échanges de copolymères avec la solution environnante et on gèle la dynamique micellaire. Les principaux paramètres qui régissent le processus de réticulation ont été identifiés. Après la réaction de réticulation, les solutions sont filtrées pour éliminer les unimères non-incorporés, et elles sont caractérisées par diffusion de lumière, cryo-microscopie électronique en transmission, microscopie électronique à balayage et microscopie à force atomique.

La stabilité des micelles sphériques réticulées a été évaluée au-dessous et au-dessus de la cmT et cmc, en présence de milieu de culture cellulaire et de protéines sériques, et après lyophilisation et dispersion dans différents solvants. La diffusion de lumière a révélé l'intégrité des micelles dans ces conditions, aucune adsorption des protéines à la surface des micelles et aucune agrégation n'ayant été observées. Les micelles stabilisées sont également stables après lyophilisation et dispersion dans des solvants aqueux et organiques (eau, acétone, tétrahydrofuranne et chloroforme).

Capture physique d'un colorant hydrophobe dans les micelles stabilisées

Pour vérifier le potentiel des micelles réticulées à traverser les membranes cellulaires et libérer leur contenu hydrophobe, une molécule hydrophobe fluorescente (Nile red) a été physiquement incorporée dans des micelles pré-stabilisées pour imiter un médicament chimio-thérapeutique.

Fonctionnalisation covalente des unimères et des micelles stabilisées

Les véhicules moléculaires (unimères) et supramoléculaires (micelles réticulées) de Pluronics P94 et F127 ont également été modifiés chimiquement avec une sonde fluorescente hydrophile (isothiocyanate de fluorescéine: FITC) ou un chélateur (S-2-(4-benzyl isothiocyanate) pentaacétique-diéthylènetriamine: *p*-SCN-Bn-DTPA). Pour cela, les copolymères ont été d'abord modifiés avec des amines primaires sur les groupes terminaux des séquences PEO par les partenaires du projet. La fonctionnalisation a ensuite été obtenue par réaction des amines primaires avec les groupes isothiocyanate réactifs dans le FITC et le p-SCN-Bn-DTPA pour former des complexes de thiourée très stables.

Le chélateur fixé aux nanovéhicules fonctionnalisés a été complexé avec le radioisotope Indium-111. L'efficacité de la conjugaison du chélateur aux nanovéhicules et du radiomarquage des nanovéhicules moléculaires et supramoléculaires a été déterminée par la radio-TLC après le radiomarquage par l'indium-111. La purification des micelles stabilisées a été réalisée pour obtenir une haute pureté radiochimique appropriée pour les études *in vitro* et *in vivo*.

Chapitre 4

Interactions cellulaires de nanovéhicules basés sur les copolymères Pluronic

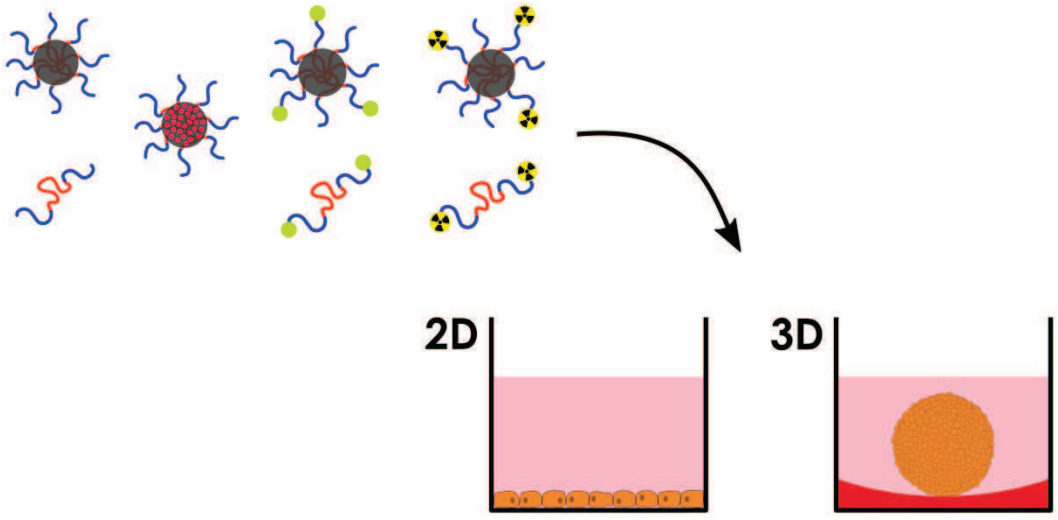

Des cultures cellulaires modèles bidimensionnelle (2D) et tridimensionnelle (3D) ont été utilisées pour étudier les interactions cellulaires avec les nanovéhicules de Pluronic en fonction de la longueur des séquences PEO et de l'état d'agrégation (unimères et micelles stabilisées). Les cultures en couche monocellulaire ont été utilisées pour étudier la cytotoxicité des véhicules, leur capacité à transporter des molécules hydrophobes, leur localisation intracellulaire, leur absorption et leur exocytose, ainsi que leur potentiel clonogénique. La pénétration et la toxicité des différents nanovéhicules ont été étudiées dans les sphéroides de tumeur 3D.

Ce chapitre montre comment les propriétés physico-chimiques des copolymères séquencés influence considérablement leurs interactions avec les cellules saines et cancéreuses, en monocouche ou en sphéroide, et comment différentes applications cliniques peuvent être envisagées.

Etudes in vitro 2D d'unimères et de micelles stabilisées

Cytotoxicité

La cytotoxicité des micelles réticulées a été évaluée *in vitro* avec une lignée de cellules saines (fibroblastes NIH/3T3) et comparée avec les copolymères bruts par le test MTT. La culture cellulaire de NIH/3T3 fibroblastes a été optimisée en vue de l'évaluation de la cytotoxicité de nanovéhicules. La viabilité cellulaire après exposition à différentes concentrations d'échantillon pendant 24h ou 48h a montré que les micelles réticulées ne sont pas plus toxiques que les copolymères bruts. De plus, nous avons observé une toxicité du P94 à des concentrations élevées, tandis que le F127 n'est pas toxique à toutes les concentrations testées.

Internalisation de micelles stabilisées avec un colorant hydrophobe (Nile red) et colocalisation avec les mitochondries

Les fibroblastes NIH/3T3 ont été incubés avec les micelles réticulées fluorescentes. Une fluorescence correspondant au colorant a été vue à l'intérieur des cellules pour les deux types de micelles stabilisées (SPM-P94 ou SPM-F127). Ceci montre que les composés sont incorporés. Les résultats ne permettent pas de décider s'ils restent associés aux micelles, s'ils sont libérés dans le cytoplasme ou associés à des vésicules d'endocytose. Par contre, le transport ne s'effectue pas jusque dans les mitochondries. Ces résultats démontrent que ces nanoparticules peuvent incorporer des molécules hydrophobes et les libérer à travers la membrane cellulaire.

Internalisation

La fonctionnalisation avec FITC a permis de visualiser la localisation intracellulaire de P94-FITC, F127-FITC, SPM-P94-FITC et SPM-F127-FITC dans des cellules cancéreuses (cellules d'adénocarcinome cervical HeLa et de glioblastome U87) par microscopie confocale. Les résultats montrent que les unimères ne sont pas retenus dans les lysosomes, et se distribuent dans toute la cellule: dispersés dans le cytoplasme, et autour (F127) ou même à l'intérieur (P94) du noyau. Au contraire, les micelles stabilisées sont plus localisées en petites taches à l'intérieur du cytoplasme de la cellule.

Le marquage des lysosomes avec une coloration appropriée a révélé la co-localisation des micelles réticulées avec les lysosomes, ce qui indique une internalisation cellulaire associée à la formation de vésicules d'endocytose qui fusionnent avec des lysosomes. Aucune localisation nucléaire n'a été observée pour les deux micelles stabilisées, ce qui a été attribué à leur grande taille.

La modification chimique avec l'agent chélatant DTPA a permis le marquage radioactif des véhicules avec l'émetteur gamma ^{111}In. Ainsi, il a été possible de quantifier l'internalisation et l'exocytose cellulaire, d'évaluer le potentiel thérapeutique *in vitro* par thérapie Auger, et d'évaluer la biodistribution des véhicules *in vivo*.

Quantification de l'internalisation et l'exocytose dans les cellules HeLa

Les résultats révèlent que les véhicules avec un bloc PEO plus grand (F127 et SPM-F127) sont moins internalisés que ceux avec un bloc PEO plus court (P94 et SPM-P94). De plus, l'exocytose des véhicules diminue quand l'hydrophobie et la taille des véhicules diminue.

Test clonogénique

Le radio-isotope ^{111}In émet également des électrons Auger. Ceux-ci sont très intéressants parce que, bien que leur énergie soit faible (<25 keV), ils disposent d'un transfert d'énergie linéaire (LET) très élevé similaire à celui des particules α. Cependant, tandis que le rayonnement α peut atteindre 40 à 80 µm dans le tissu, la pénétration des électrons Auger est bien inférieure à 1 µm. Cela signifie que les cellules doivent internaliser ces radionucléides pour que les électrons Auger exercent leur toxicité, en particulier les radionucléides doivent pénétrer le noyau pour un effet maximum. Avec les études de localisation intracellulaire, nous avons observé que le Pluronic P94 peut se translocaliser vers le noyau cellulaire. Par conséquent, nous avons également évalué l'utilisation potentielle de Pluronic P94 pour la thérapie Auger avec un test clonogénique. Les cellules HeLa ont été exposées à P94-DTPA-^{111}In et nous avons observé qu'il est plus toxique que le P94 non-radiomarqué et que le complexe moléculaire DTPA-^{111}In. Par conséquent, les unimères de P94 pourraient être particulièrement prometteurs pour la thérapie par rayonnement.

Etudes in vitro 3D d'unimères et de micelles stabilisées

Le développement de sphéroïdes tumoraux tridimensionnels des cellules HeLa et des cellules U87 a permis une autre approche de la pénétration et de la toxicité des unimères et des micelles réticulées. Ces agrégats multicellulaires imitent le contexte cellulaire et les gradients physiopathologiques de tumeurs *in vivo* et on s'attend donc à ce que le comportement des véhicules *in vitro* en présence de ces sphéroïdes tumoraux reflète mieux le comportement *in vivo* que les études *in vitro* sur cultures monocouches bidimensionnelles classiques. Les résultats obtenus par microscopie confocale ont révélé que les micelles réticulées (SPM-F127-FITC) sont capables de pénétrer plus profondément dans la tumeur *in vitro* que les unimères (F127-FITC). Les véhicules plus hydrophobes (SPM-P94 et P94) ont induit une toxicité vérifiée par microscopie optique. Cette toxicité se traduit par la diminution de la taille des sphéroïdes (U87) et des changements de leur morphologie (HeLa). Ce sont donc des véhicules prometteurs pour les applications d'imagerie et de thérapie.

Chapitre 5

Biodistribution de nanovéhicules basés sur les copolymères Pluronic

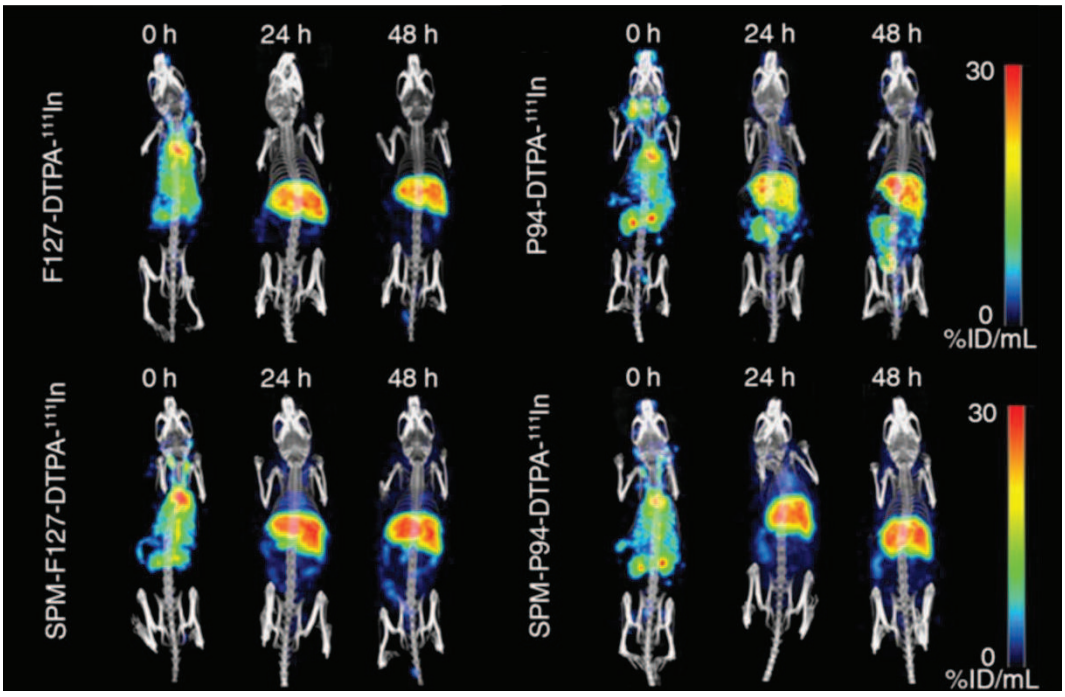

La dernière partie de cette thèse a porté sur l'évaluation de la biodistribution des véhicules en fonction de la longueur des séquences PEO et de l'état d'agrégation (unimères et micelles stabilisées). La biodistribution des véhicules radiomarqués avec ^{111}In a été visualisée après injection intraveineuse dans les souris A/J sains par tomographie d'émission monophotonique (SPECT) couplée à la tomodensitométrie (SPECT/CT).

Cette étude a montré que l'élimination par les vois hépatique et rénale peut être modifiée par la longueur du bloc PEO et l'état d'agrégation. La compréhension des paramètres déterminant l'élimination des nanovéhicules est une étape nécessaire vers la conception de nanovéhicules plus efficaces.

Les nanovéhicules à base de Pluronic F127 ont montré une accumulation plus importante dans le foie, tandis que les véhicules à base de Pluronic P94 avaient une élimination rénale initiale plus élevée. Contrairement à la majorité des véhicules supramoléculaires développés jusqu'ici, pour lesquels une accumulation importante dans les tissus non ciblés (foie et rate) est souvent observée, les micelles réticulées de Pluronics ne s'accumulent pas dans la rate.

L'état d'agrégation a influencé principalement la rétention des véhicules dans le foie où les micelles stabilisées à base du Pluronic plus hydrophobe (SPM-P94) ont été retenues plus longtemps que les unimères correspondants (P94). Par ailleurs, les micelles stabilisées préparées avec le polymère plus hydrophile (SPM-F127) ont été éliminés de manière plus efficace que les unimères correspondants (F127).

Nos résultats montrent la nécessité de choisir avec plus de précautions les paramètres qui déterminent la biodistribution des nanovéhicules (composition, longueur de séquence PEO, état d'agrégation) et comment de petites variations peuvent aboutir à des effets biologiques très différents.

Conclusions et perspectives

Dans le cadre du projet "TRACE'nTREAT" dont l'objectif était de développer de nouvelles technologies moléculaires pour l'imagerie moléculaire nucléaire et la thérapie par radionucléides, nous avons développé des nanovéhicules à partir de copolymères séquencés, auto-assemblés ou sous forme d'unimères.

Nous avons caractérisé la cinétique de formation, de croissance et de décroissance des micelles formées à partir d'une série de copolymères séquencés de poids moléculaires différents et de composition PEO/PPO constante. Cela nous a permis d'identifier plusieurs voies cinétiques concurrentes pour la transition de la forme sphérique à la forme cylindrique. La principale conclusion est que, dans ces conditions expérimentales, aucune des voies cinétiques ne peut être négligée si on veut comprendre la morphologie finale des agrégats. De plus, l'équilibrage de la population des micelles devient très difficile sur des temps de l'ordre de la semaine même pour de légères augmentations de poids moléculaire des copolymères, et la structure des solutions devient dépendante de l'histoire thermique spécifique de l'échantillon.

En raison de l'effet marqué du poids moléculaire sur le poids respectif des voies cinétiques, nous comprenons pourquoi un consensus sur les mécanismes d'équilibrage de micelles de copolymère a été difficile à réaliser jusqu'à présent à partir de résultats obtenus avec des copolymères de nature, composition, architecture ou poids moléculaire différents.

A partir de cette étude cinétique, nous avons choisi les Pluronics P94 et F127 pour le développement de nouveaux nanovéhicules et cette étude a montré aussi la nécessité de stabiliser la structure des micelles pour éviter leur désintégration dans le flux sanguin. En raison de la nature dynamique des micelles de Pluronics, les auto-assemblages supramoléculaires ont été photo-réticulés par incorporation d'un monomère réticulable hydrophobe dans le cœur des micelles. Les monomères et les micelles stabilisées ont été caractérisés et, en particulier, nous avons vérifié la très bonne stabilité des micelles dans différentes conditions.

Nous avons développé de nouvelles méthodes pour fonctionnaliser les systèmes moléculaires et supramoléculaires avec des marqueurs fluorescents ou des chélateurs pour permettre leur imagerie *in vitro* et *in vivo*. Nous avons discuté le radiomarquage des nanovéhicules et les différents aspects qui doivent être pris en compte pour la caractérisation de l'efficacité de radiomarquage. Nous avons établi les protocoles correspondants pour la préparation et la purification d'échantillons prêts à leur utilisation *in vitro* et *in vivo*. Les nouvelles stratégies et techniques décrites ici peuvent être généralisées pour créer de nouveaux nanovéhicules polyvalents avec d'autres fonctionnalités, en combinant des modifications et/ou des molécules appropriées.

La cytotoxicité et la capacité d'incorporation de molécules hydrophobes ont été évaluées *in vitro*. La localisation intracellulaire, la cinétique d'internalisation et d'exocytose cellulaire, la pénétration et la toxicité dans des sphéroides tumoraux et le potentiel thérapeutique par des électrons Auger ont été testés *in vitro* avec deux lignées de cellules tumorales. Enfin, la biodistribution *in vivo* des nanovéhicules radiomarqués a été évaluée dans des souris saines par imagerie SPECT/CT.

Ces résultats ont montré que la longueur du bloc de PEO et l'état d'agrégation modifient les interactions avec les cellules et la biodistribution. En particulier, différentes voies d'internalisation ont été activées *in vitro*, et l'élimination initiale et finale par voies rénale et hépatique des véhicules varie avec ces paramètres. Une plus grande longueur du bloc de PEO est associée à l'augmentation de l'absorption dans le foie, et la rétention dans cet organe dépend également de l'état d'agrégation des copolymères.

Les résultats de cette thèse démontrent qu'une approche rationnelle est nécessaire à l'élaboration des nanomédicaments, depuis l'étude fondamentale de la cinétique de formation des micelles jusqu'aux études approfondies *in vitro* et *in vivo*. La variation des propriétés physico-chimiques et des fonctionnalités peut être utilisés pour limiter les interactions avec les barrières biologiques, cibler des organites intracellulaires spécifiques, améliorer la cinétique d'absorption et d'exocytose, et/ou augmenter la pénétration et la toxicité dans les tumeurs.

Globalement, cette thèse présente le développement complet de nanovéhicules composés de copolymères Pluronics depuis les premières étapes de la caractérisation physico-chimique fondamentale jusqu'à l'évaluation de leur intérêt pour les applications d'imagerie et de thérapie.